Advanced technologies and applications based on Polydimethylsiloxane (PDMS)

Dissertation
zur Erlangung des akademischen Grades
Doktoringenieurin
(Dr.-Ing.)

Von

M.Sc. Liubov Bakhchova
geb. am 09.August 1993
in Berdyansk, Ukraine

genehmigt durch die Fakultät für Elektrotechnik und Informationstechnik der
Otto-von-Guericke-Universität Magdeburg (OvGU)

Gutachter:
Prof. Dr.-Ing. Ulrike Steinmann, OvGU
Prof. Dr. Andreas Hierlemann, ETH Zürich

Einreichungsdatum 29.08.2023
Verteidigungsdatum 19.02.2024

Zusammenfassung

Diese Dissertation präsentiert Forschungsergebnisse im Bereich der mikrofluidischen Chips und ihre Anwendungen im biomedizinischen Bereich. Grundlage für diese Chips ist dabei das vielseitige Material Polydimethylsiloxan (PDMS). PDMS ist bekannt für seine Transparenz, Gasdurchlässigkeit, Biokompatibilität und Dehnbarkeit. Aus der Kombination von PDMS mit anderen Polymeren und Glas, lassen sich maßgeschneiderte Lösungen für Gewebetechnik und Einzelzellexperimente herleiten. Im Gegensatz dazu bieten handelsübliche Mikrofluidikgeräte oft nicht die benötigte dedizierte Anpassungsfähigkeit zur Untersuchung spezieller, hochkomplexer biologischer Fragestellungen. In der vorliegenden Arbeit werden drei mikrofluidische Chips vorgestellt, die jeweils für eine spezifische Anwendung zugeschnitten sind.

Erstens, wird eine Struktur mit zwei mikrofluidischen Kanälen, die durch eine poröse Polyester-Membran getrennt sind und speziell für die Anwendung eines Stomach-on-Chip entwickelt wurden, beschrieben. Zur Realisierung dieses Chips wurde eine neuartige Klebebindungstechnik auf Basis von flüssigem PDMS vorgeschlagen, entwickelt und in der vorliegenden Arbeit beschrieben. Das vorgeschlagene Verfahren ermöglicht eine zuverlässige Verbindung von beliebigem porösem Material mit PDMS. Dies eröffnet weitreichende Möglichkeiten für die Herstellung von mehrschichtigen Chips aus verschiedenen Materialien. Darüber hinaus ermöglicht diese neuartige Klebebindungstechnik die Steuerung der Haftfestigkeit und hält den mikrofluidischen Chip unter kontinuierlichen Flussbedingungen über Wochen funktionsfähig. Zudem ist es möglich, den Chip zu zerlegen und die Membran mit kultivierten Zellen für die anschließende Analyse auszustoßen. Als ein Anwendungsfall ist exemplarisch die Kultivierung von Magenkrebszelllinien unter dynamischen Bedingungen durchgeführt worden. Zur weiteren Untersuchung der kultivierten Magenkrebszelllinien ist außerdem ein umfängliches System aus druckgesteuerter Pumpe und Incucyte-Fluoreszenz-Automatenmikroskop entworfen und gebaut worden. Diese Vorrichtung ermöglicht eine geringe Durchflussrate des Zellkulturmediums von $0.5\,\mu l/min$ und die Detektion der Zellapoptose für chemotherapeutische Medikamentenforschung.

Zweitens, wurde eine spezielle 3D-Mikrofluidikstruktur (ImmunoChip) entwickelt. Der Immunochip ermöglicht es Immun-$CD4^+$-T-Zellen zu charakterisieren und ihren Transport zu den von Leishmanien infizierten Makrophagen zu untersuchen. Diese Struktur besteht aus 378 miteinander verbundenen Kanälen. Dafür wurde zunächst ein mikrofluidischer Chip sorgfältig entworfen, um sowohl Makrophagen effektiv von T-Zellen zu trennen, als auch eine kontrollierte Interaktion zwischen diesen Zelltypen zu ermöglichen. Daher wurde in dieser Dissertation eine neuartige, sich in zwei Schritte gliedernde Prozessierungsmethodik entwickelt, um das 3D-hochintegrierte Mikrofluidiksystem mit Nanopräzision zu fertigen. Auf Basis der weichen Lithographie werden zunächst drei "große" Kanäle realisiert und anschließend unter Verwendung des Femtosekunden-Direktschreibprozess extrem feine

senkrechte $6\,\mu m \times 4\,\mu m \times 30\,\mu m$ Kanäle hergestellt. Dieses innovative Design dient als ein wichtiges Werkzeug zur Förderung des menschlichen Verständnisses der Immunsignalgebung, ein entscheidender Faktor bei der Behandlung und Heilung zahlreicher Krankheiten.

Drittens, wurde in dieser Arbeit ein maßgeschneiderter mikrofluidischer Chip entwickelt, um den Einfluss heterogener Umgebungen auf die Bewegung von Chlamydomonas, einzelnen grünen Mikroalgen-Mikroschwimmern, zu untersuchen. Chlamydomonas verfügen über eine Sehkraft, die es ihnen ermöglicht, phototaktisches Verhalten zu zeigen. D.h. sie reagieren auf Lichtreize und ermitteln eine optimale Umgebung für die Photosynthese. Diese grünen Mikroschwimmer reagieren stark auf die Umgebungsbedingungen und könnten in Zukunft für ökologische Studien von Nutzen sein. Dafür ist es jedoch unerlässlich zunächst ihr Verhalten unter sich verändernden Umgebungen besser zu verstehen. Daher enthält der vorgeschlagene Chip mikrostrukturierte PDMS-Kanäle, die als eine künstliche poröse Umgebung dienen (LabyrinthChip). Der aus PDMS und Glas hergestellte mikrofluidische Chip realisiert verschiedene Konfigurationen von mikrostrukturierten Labyrinthen, die die Untersuchung des Bewegungsverhaltens der Mikroschwimmer ermöglichen. Zylindrische und elliptische Strukturen sind schachbrettartig in der Mitte jedes Kanals angeordnet und stellen Hindernisse für die Mikroschwimmer dar. Etwaige Reflexions- und Transmissionsereignisse der Chlamydomonas verursacht durch diese Hindernisse werden analysiert.

Mikrofluidische Chips benötigen Sensoren zur genauen Überwachung des Zustands der Zellkultur innerhalb des Kanals. Dies kann entweder optisch oder elektronisch erfolgen. In dieser Arbeit wurden mehrere solcher Sensoren für eine optimale Überwachung implementiert. Zur Detektion von Krebszellen wird sich etwa die unterschiedliche Sauerstoffverbrauchsrate im Vergleich zu gesunden Zellen zu Nutze gemacht. Ein Lumineszenzsensor integriert in einen mikrofluidischen Chip ermöglicht so die Messung der *in-situ* Sauerstoffkonzentration. In dieser Arbeit wurde eine Methodik für Sauerstoffkonzentrationsmessungen in Mikrofluidik-Kanälen vorgeschlagen und die Auslesung untersucht.

Des Weiteren wurden transepitheliale Widerstandselektroden (TEER) bestehend aus Gold in einen flexiblen mikrofluidischen Chip implementiert, um die Konfluenz der Zellen zu erfassen. Der gemessene Widerstand steigt 12 Stunden nach Aussaat der Zellen an und bestätigt die Gewebebildung. Die auf das elastische PDMS aufgedampfte Metallstruktur weist Falten auf, die den Widerstand der Elektroden beeinflussen. Erstmals wurde der Einfluss der PDMS-Härte und -Dicke auf die Faltenbildung erforscht. Hervorzuheben ist ebenfalls der durch die Falten ermöglichte Selbstheilungseffekt, der für die Stabilität der Metallelektroden auf elastischem Substrat äußerst vorteilhaft ist.

Alle in dieser Arbeit vorgeschlagenen Ansätze stellen neuartige Lösungen im Bereich der Mikrostrukturierung für maßgeschneiderte mikrofluidische Chips mit integrierten Sensoren zur Überwachung im Kanal dar. Die neuartigen Lösungen ermöglichen Erforschung hochkomplexer interdisziplinärer Fragestellungen im Bereich der Biomedizin und können einen wesentlichen Beitrag zu einer besseren Gesundheitsversorgung und Ökologie leisten.

Abstract

This thesis presents a pioneering exploration into the realm of microfluidic chip development, with a profound emphasis on their applications in the medical domain, leveraging the versatile Polydimethylsiloxane (PDMS) as a core material. PDMS, known for its transparency, gas-permeability, biocompatibility, and stretchability within the silicone group, forms the basis of these cutting-edge micro-sized structures tailored for tissue engineering and single-cell experiments, in combination with other polymers and glass. Since biology is a very complex science, particular biological questions require individual customized solution. Hence, commercial off-the-shelf microfluidic devices, are often incapable to address complex biological questions.

First, a structure with two microfluidic channels divided by a porous polyester membrane, designed specifically for Stomach-on-Chip (Gastric Cell culture on-Chip) application, is described. To implement this device, a novel adhesive bonding technique based on liquid PDMS was proposed, developed and described here. Developed technology enables a reliable bonding of any porous material to PDMS, what opens a wide perspectives for multi-material chip fabrication. Moreover, it allow control of the bonding strength and keeps the chip stable under continuous flow conditions over weeks. Furthermore, it is possible to disassemble the chip and extrude the membrane with cultured cells for the following analysis. Gastric NCI cell line were cultured in the proposed microfluidic chip under dynamic conditions. Furthermore, a full custom designed microfluidic system was built around the proposed chips in combination with a pressure-driven pump and Incucyte fluorescence automatic microscope. This setup enables meager cell culture medium flow rate of 0.5 µl/min and detection of the cell death during the chemotherapeutic drug screening.

Second, to investigate the immune $CD4^+$ T cells and study their route towards macrophages infected by Leishmania, a dedicated 3D microfluidic structure (ImmunoChip), consisting of 378 interconnected channels was developed in this thesis. Initially, a microfluidic device was meticulously designed with a dual purpose: firstly, to effectively segregate macrophages from T cells, and subsequently, to facilitate controlled interaction between these cell types. This innovative design serves as a crucial tool in advancing human comprehension of immune signaling, a pivotal factor in the treatment and cure of numerous diseases. Therefore, a novel technology was developed for obtaining the 3D highly integrated microfluidic system with nano-precision. The master mold fabrication for PDMS was done in two steps: first, soft lithography for big micro-channels (two channels 100 µm and one 150 µm) and second, femtosecond direct write process for 6 µm × 4 µm × 30 µm perpendicular channels. Also, the bottom side of the ImmunoChip is a 170 µm thick glass slide, which allows for cell monitoring by fluorescence and optical microscopy with high resolution.

Third, to study the effect of heterogeneous surroundings on the motion of Chlamydomonas, single-cell green algae microswimmers, a dedicated custom designed microfluidic chip was developed in this work. Chlamydomonas possess an eyesight that enables them to exhibit phototactic behavior, i.e. to react to light stimuli and seek optimal conditions for photosynthesis. These green microswimmers are highly reactive on the environmental conditions and could be beneficial in ecology studies if we understand deeply their behaviour. Therefore, the proposed chip contains microstructured PDMS channels that act as an artificial porous environment (LabyrinthChip). The fabricated microfluidic chip is based on PDMS and glass and implements various configurations of microstructured labyrinths that enables the study of the movement behaviour of the microswimmers. Cylindrical and elliptical structures are arranged in chess-board order in the middle of each channel, posing obstacles for microswimmers to cross. These reflection and transmission events of the Chlamydomonas through the obstacles are recorded and analyzed.

Microfluidic chips need sensors to monitor the state of cell culturing inside the channel. This can be done either by optical or electronic means. Several such sensors were implemented in this work. Cancer cells have a different oxygen-consumption rate compared to that of healthy cells. Therefore, a luminescence sensor was built into a microfluidic device to enable *in-situ* oxygen concentration measurements. This can be potentially used to distinguish between cancerous and healthy cells in the channel. A technological solution how to embed an optical sensor with wireless readout was provided. Additionally, a methodology for oxygen concentration measurements in microfluidic channels is proposed in this work. Furthermore, golden transepithelial resistance electrodes (TEER) were implemented in a flexible microfluidic chip to detect the cells' confluency. The measured resistance grows in 12 hours after cells' seeding, which proves the creation of the tissue. The metal structure sputtered on the elastic PDMS possesses wrinkles, which influence the resistance of the electrodes. The wrinkling behaviour of metal thin films on the elastic materials is a potential research field, which could open a new horizons for sensor development. Therefore, meander-shaped elements on thin freestanding PDMS membranes were designed and studied in depth. At first time the influence of the PDMS hardness and thickness on the wrinkle formation was reported. Moreover, wrinkles ensure a self-healing effect, which is highly beneficial for metal electrode stability on elastic substrate.

All of the techniques proposed in this thesis provide novel solutions in the field of microstructuring for development of custom-designed microfluidic devices with integrated sensors for monitoring inside the channel. These devices enable interdisciplinary research that helps to gain knowledge and develop tools for better healthcare and a better environment.

Contents

List of Acronyms

PDMS Polydimethylsiloxane

DMDCS Dichlor(dimethyl)silane

ISO International Organization for Standardization

PEB Post Exposure Bake

EBR Edge Bead Cleaning

SW Silicon Wafer

GW Glass Wafer

3DLL Three Dimensional Laser Lithography

WEC Offset Wedge Error Compensation Offset

PVD Physical Vapour Deposition

APTES (3-Aminopropyl)triethoxysilan

ID Inner diameter

OD Outer diameter

IP Intraperitoneal

MilliQ water water purified using a Millipore Milli-Q lab water system

CAD Computer-Aided Design

CPT Chemotherapeutic Anticancer Drug

UV Ultraviolet spectrum

VIS Visible spectrum

TEER Transepithelial Electrical Resistance

List of Figures

List of Tables

1 Introduction

> Nature has no separate departments
> of biology, physics, chemistry or art.
> _____
>
> R. Buckminster Fuller

1.1 Motivation

In former times, scientists were able to span their knowledge on a substantial number of subjects and solve complex interdisciplinary problems. These individuals were called polymaths (in German "Universalgelehrter"). One of the ancient examples is Archimedes of Syracuse (born ca. 287 BC), who is regarded as one of the leading scientists in classical antiquity. He was simultaneously a mathematician, physicist, engineer, astronomer, and inventor. Other examples of polymaths, just to name a few, include Leonardo da Vinci (born 1452), who was not only a very famous painter but also a draughtsman, engineer, scientist, theorist, sculptor, and architect; Galileo Galilei (born 1564), who was a philosopher, physicist, mathematician, engineer, and astronomer; Sir Isaac Newton (born 1642) who was a mathematician, physicist, astronomer, theologian, and philosopher, and Thomas Young (born 1773) who made notable contributions to the fields of vision, light, solid mechanics, energy, physiology, language, musical harmony, and Egyptology. Polymaths are also referred to as the "Renaissance man" (a term coined in the 20th century since many great thinkers lived before, during, or after the Renaissance). The idea of multidisciplinary education was essential to achieving polymath ability.

However, the incredible development of science over the last 100 years, propelled by the invention and development of powerful computers, the internet, measurement equipment, emerging new branches of science, and an increasing number of research groups worldwide, led to an exponential growth of scientific publications. For example, IEEE Xplore lists over 5.5 million scientific papers (at the moment this thesis is written), PubMed comprises more than 33 million citations for biomedical literature, and Scopus lists 82.4 million scientific records at the moment. With this huge amount of research results and knowledge, it is simply impossible for a single person to cover a wide range of sciences and read all of the publications in a single science field in a lifetime. Therefore, most scientists specialize their knowledge to a single field of science and focus their research on a narrow part of that subject. For example, in the field of electrical engineering, some groups specialize in power electronics, others in digital design, and others in communication theory, etc.

As an example of the diversity of sub-branches, the Faculty of Electrical Engineering and Computer Sciences at the University of California at Berkeley employs over 190 active academic faculty members (professors), each specializing in different facets of electrical engineering.

Unfortunately, the types of problems that research faces today often require a combination of deep knowledge from various fields of science. For example, in the biomedical field addressed in this thesis, one would need knowledge in the fields of measurement technology, fluid dynamics, micro-structuring, micro-mechanics, optics, materials science, sensor engineering, cellular biology, and specific expert knowledge in medicine, depending on the type of the application (e.g., inner medicine, neurology, immunology, etc.). Obviously, a single scientist (a "Renaissance man") would not be able to solve the complex interdisciplinary problems of today, even with aid of the most powerful computers. Therefore, interdisciplinary research teams in academia and industry must work together to address these problems. The problems become ever more multidisciplinary and require many researchers, each bringing different skills into the collaborative project.

This work focuses on highly interdisciplinary research in the field of biomedical engineering and seeks to bridge the different types of interdisciplinary knowledge involved. The research results and methods are presented in this thesis in an understandable and comprehensive manner for readers from various backgrounds (both medical and engineering).

One example of an interdisciplinary research problem is "tissue engineering." This field encompasses material science, biochemistry, and cellular biology and has the motivation to grow human tissues in-vitro [1]. This involves very complex 3D geometries and the use of novel additive manufacturing tools. Another important example that will be thoroughly discussed in this thesis is the Organ-on-Chip concept. It was developed thanks to extensive research in microfluidics in combination with cellular biology. Organs-on-Chips are microfluidic devices enabling the culture of living cells in continuously perfused, micro-sized chambers. This concept enables the modeling of the physiological functions of tissues and organs. The main advantage of this approach is synthesis of minimal functional units that recapitulate tissue- and organ-level functions and enable investigation of the influence of surroundings, mechanical stress, drug, bacteria, etc.

One of the possible specific Organ-on-Chip variants is the Stomach-on-Chip. It can be used for applications such as drug testing and bacteria co-culture. The microfluidic environment created within the chip is intended to reproduce and emulate human body conditions. Therefore, same as in-vivo, the drug is introduced to the tissue from the basolateral side with a continuous flow. This model opens the possibilities of patient-specific drug screening (Figure 1.1, left) and the synthesis of new drugs (Figure 1.1, right). In the first case, cells from one patient are multiplied in several chips; in the second case, cells from different patients are grown in every single chip.

Patient-specific drug screening (Figure 1.1, left) is highly important for cancer cases.
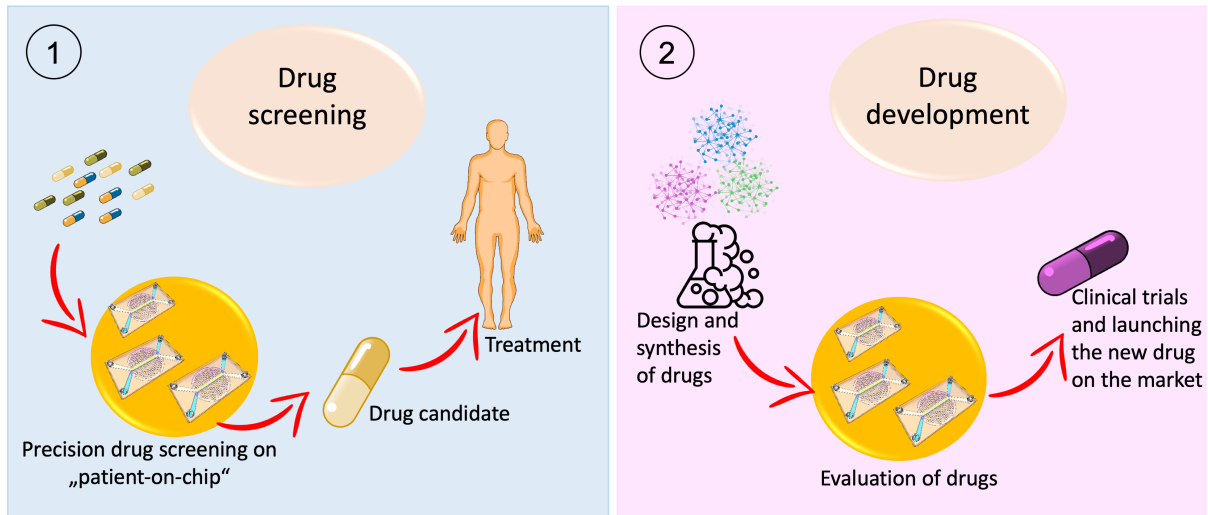
Figure 1.1: Motivation to use microfluidic devices for cellular biology and pharmacology.

According to worldwide statistics published in 2020 in CA: A Cancer Journal for Clinicians [2], 19.3 million new cancer cases and 10 million cancer deaths were registered. Stomach cancer is in 5th position with 5.6 % of new cases and a 7.7 % death rate. The number of new cancer cases is growing yearly, and the global cancer burden is expected to be 28.4 million cases in 2040, a 47 % rise from 2020. Therefore, working on devices that can open a new path in cancer study and drug testing is highly important. Essentially, due to the personal nature of cancer, personalized drug testing can open new treatment horizons. The premise is that the patient's own cells are best suited to provide relevant information about the drug's efficiency for that person. Stomach-on-Chip (as part of Organ-on-Chip interdisciplinary research) is a major and revolutionary research area that can provide a promising solution for personalized drug testing. Drug testing on chips saves a person from taking unnecessary medicaments and provides a fast and reliable answer to the question: "Which solution is the most effective for this cancer type and this person's genetic peculiarities." Moreover, Organ-on-Chip is a promising alternative to animal experiments, which are cruel, unnecessary and, due to the genetic differences, are not reliable.

Particular motivation to create Stomach-on-chip is seen in drug screening and bacteria co-culture in the mucosa layer. This research requires ensuring a continuous flow at the apical side of the cell to avoid the non-body relevant accumulation of the, e.g., H. pillory bacteria. In this field of medical research, microfluidics is fundamental in gaining more knowledge about the reasons for diseases and our physiology. Exactly this motivation leads us to the development of the next two applications addressed in this thesis: ImmunoChip and LabyrinthChip.

Our immune system is a warrior, protecting us daily from thousands of break-ins. Therefore, knowing how immunity works can help us strengthen the immune system and

use it as a weapon against incurable disease. This goal motivates interdisciplinary research. Combining microfluidics and immunology, we designed and fabricated an ImmunoChip, in which T cells find and attack macrophages infected by Leishmania. Leishmaniasis is a disease caused by a parasite inherited from a mosquito bite. It develops into non-healing wounds all over the body and causes pain and discomfort for the patient. An estimated 700 000 to 1 million new cases occur annually. By means of the ImmunoChip, we hope to gain more insight about the T cells response to this parasite and find a way to strengthen it.

Last but not least, a microfluidic chip for studying the behavior of Chlamydomonas is investigated. Green Algae has similarities with the plant-animal common ancestor and probably gave rise to land plants, so they are essential in evolutionary studies. Also, all cells are sensitive to changes in their surroundings. Cellular movement behavior depends on environmental geometry, light, and chemical composition. Therefore, the fundamental study of these creatures leads to a deeper understanding of the evolution of life and can be used in environmental analysis.

1.2 Objectives and thesis outline

In this work, microfluidic chips for three different, but all interdisciplinary applications were designed, fabricated, and concept proven. For each application, a dedicated microfluidic chip was designed, and for each chip a novel technological process was developed to ensure fabrication feasibility and measurement capability. All three devices are based on Polydimethylsiloxane (PDMS). PDMS is already a well-discussed and reviewed material, but there are still technological challenges and the potential for optimization of its structure and application in on-chip systems. This work addresses such questions by focusing on three different research examples:

- Stomach-on-Chip

- ImmunoChip

- LabyrinthChip

All three microfluidic devices are developed for biomedical studies. Stomach-on-Chip is designed for cell culture and recreating human tissue. ImmunoChip and LabyrinthChip are developed for single cells motion experiments. Moreover, sensor development and integration into the microfluidic chip are discussed and presented in this thesis. The Stomach-on-Chip device was chosen for sensor embedding, as this application has the highest need for monitoring functionality.

The first part of this thesis focuses on PDMS's material properties, state-of-the-art microfluidic devices for biomedical studies and fabrication methods, which report optimized

process parameters, determined empirically in this work. Chip design, fabrication results, and proof-of-concept experiments are presented in Chapters 4, 5, 6. Furthermore, Chapter 7 reports on embedding of a commercially available luminescence sensor into Stomach-on-Chip. Additionally, it presents a self-developed transepithelial resistance sensor. Moreover, Subsection 7.3, discusses a thin PDMS membrane functionalized with thermo-electric elements for microfluidics. The structure of this thesis is shown schematically in Figure 1.2.
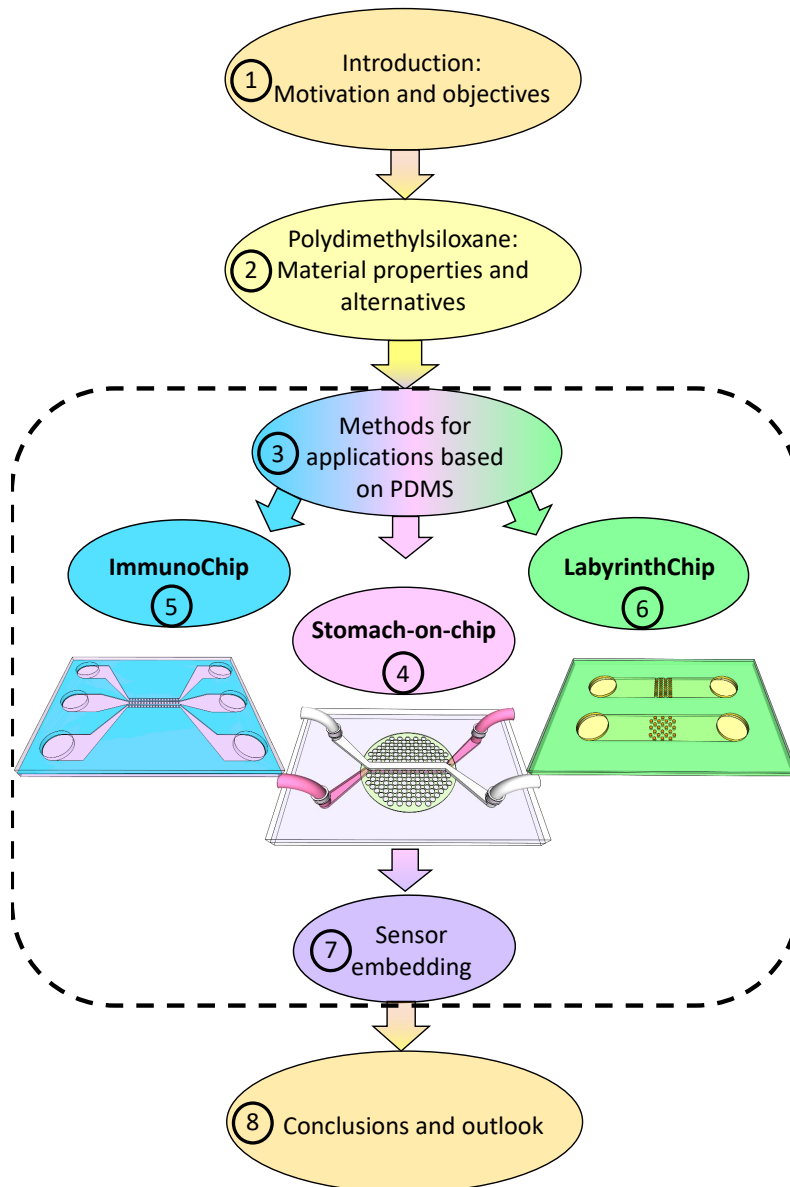
Figure 1.2: Thesis structure and outline.

2 Polydimethylsiloxane – material properties and based on it microfluidics

Polydimethylsiloxane (PDMS) is a synthetic polymer, also known as silicon rubber, used for in-vivo and in-vitro applications. Such properties as biocompatibility, transparency, gas permeability, flexibility and comparably easy structuring justify the high use of this material. A polymer material is comprised of many simple molecules that are replicating structural units named monomers. The PDMS backbone consists of $[SiO(CH_3)_2]$ monomers. The presence of carbon atoms in a backbone is an indication for organic polymers. The carbon atom has four valence electrons each of which can form a covalent bond to another carbon atom or to a foreign atom. The molecular structure of the Polydimethylsiloxane is shown in the Figure 2.1.
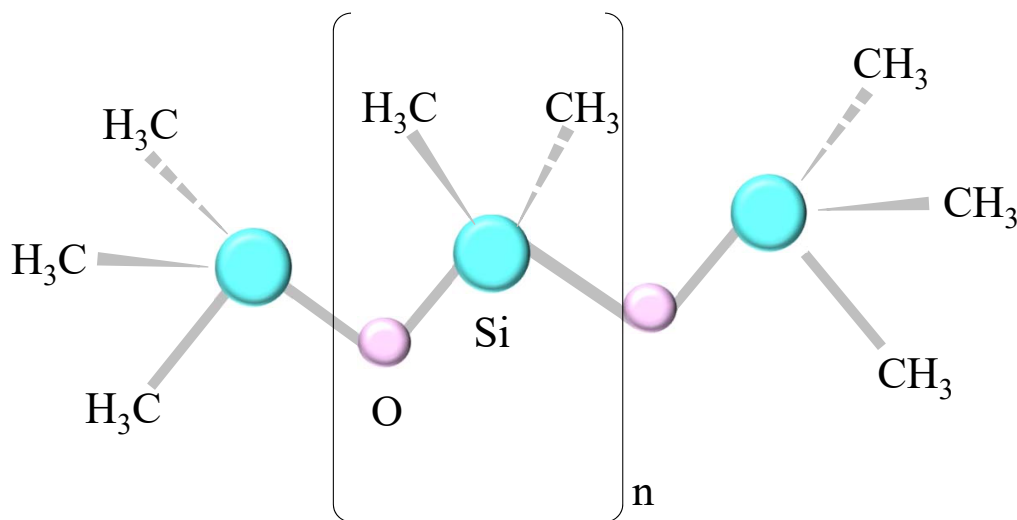
Figure 2.1: Molecule of Polydimethylsiloxane.

Usually, PDMS is represented in a liquid phase, with short polymer chains which are highly moveable. The material is inexpensive and easy to fabricate in large amounts. The basic components are Dichlor(dimethyl)silane (DMDCS, $(CH_3)_2SiCl_2$) and water. The first component is synthesized by passing methyl chloride (CH_3Cl) through heated silicon powdered in the presence of a catalyst CuCl at $300\,°C$. In its turn, the CH_3Cl is a colorless highly volatile poisonous gas, which can be produced by heating a mixture of methanol, sulfuric acid, and sodium chloride. The schematics of PDMS synthesis are shown in Figure 2.2. During the hydrolysis of the (Dichlor(dimethyl)silane), an atom of

chlorine is replaced by oxygen and hydrogen from water. The electron on the oxygen is then able to form a bond with the silicon atom of another DMDCS molecule, releasing another chlorine atom. The reaction is repeating; the DMDCS polymerizes with other of the same molecules, and the PDMS polymer chains are thus created.
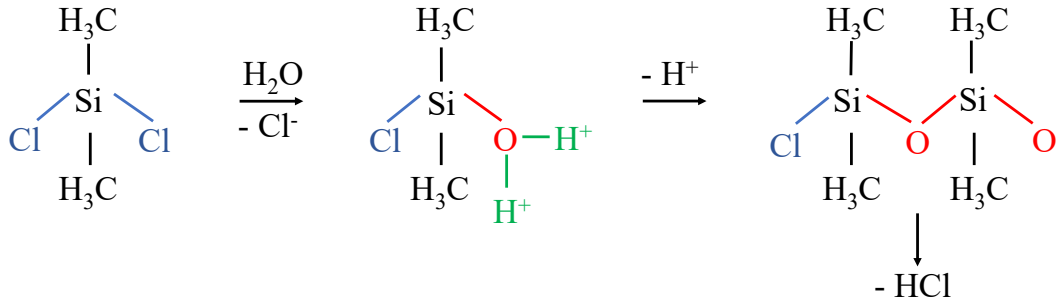
Figure 2.2: PDMS synthesis by the DMDCS hydrolyze polymerization.

Usually, PDMS is stored in a liquid phase when the polymer chains are highly movable. To create structures based on PDMS, the material has to be transferred to the solid phase. Therefore, the polymer chains become interconnected with each other and the high movability is lost (Figure 2.3).

Branched polymer   Cross-linked polymer
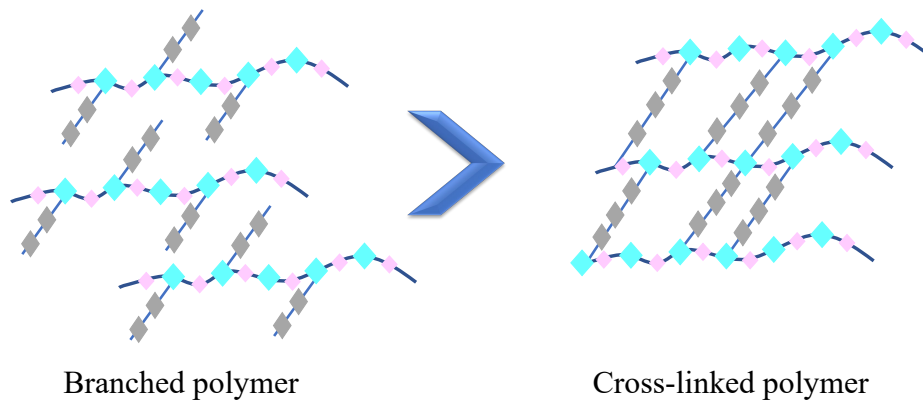
Figure 2.3: Schematic description of the PDMS in a liquid phase (left) and cross-linked solid phase (right).

This process, called the hardening of the polymer, is done by cross-linking and requires a cross-linker or curing agent (marked in blue color in Figure 2.4) [3].

Two of the most widely used curing mechanisms of silicone are condensation mechanism [5] and platinum based catalysis [6]. The condensation crosslinking mechanism is
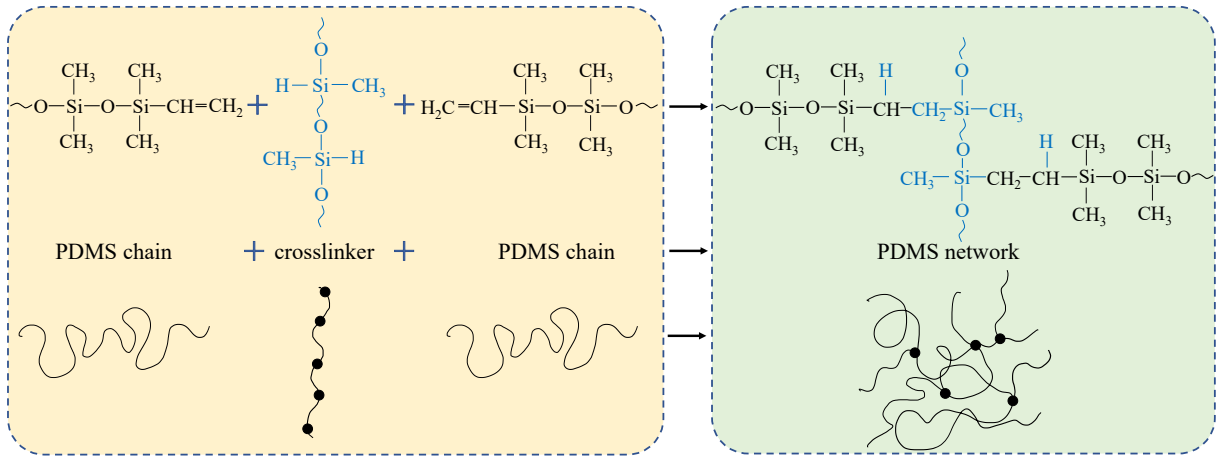
Figure 2.4: Crosslinking or curing mechanism of the PDMS (adopted from [4]).

the simplest and requires only a crosslinker and PDMS base. Curing takes place at room temperature, with the process finishing in 48 hours. The main challenge is a fine mixing of these two components so that the reaction is homogeneous. To speed up the crosslinking of PDMS, higher temperatures can be used. As an example, the curing process can be completed after 2 hours at 60 °C. Once PDMS is cured, the polymer chains form a network, but due to their flexibility, the material is solid, flexible and gas permeable. Curing of PDMS can be done with additional components to tune the material properties [7].

Another way to cross-link PDMS is via the platinum catalysis crosslinking system [8]. The scheme of the curing system with the platinum catalyst is shown in Figure 2.5. The catalyst is used to reduce the activation energy of the reaction. In this particular case, Pt has a high affinity to a hydrogen atom and helps to break a C=H bond.
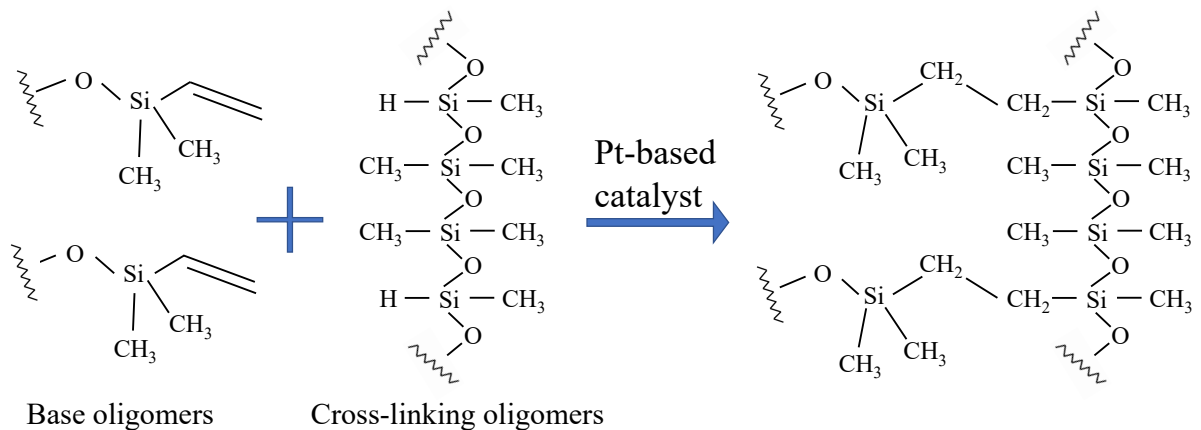
Figure 2.5: PDMS crosslinking process within the platinum-based catalysis system (adopted from [4,6]).

Combined with platinum, other chemical components can be used to improve the pot-life time at room temperature and stability of the system. In this case, the platinum

catalyst consists of alcohol, xylene, divinylsiloxanes, or cyclic vinylsiloxanes. There are two main parts of the system: part A is vinylsiloxane with Pt (5–10 ppm) and part B is a hydrosiloxane with inhibitor (0.01–50 ppm). Additional components, named moderators and inhibitors, can slow Pt catalysis or stop the reaction. Platinum catalysts are volatile and decomposed by heat or light (UV) [8]. Both curing mechanisms are advantageous and can be applied according to the needs of the structuring process and resulting material properties.

2.1 PDMS material properties

All the PDMS properties listed in this chapter are important to consider when designing and fabricating microfluidic devices for biomedical applications. Parameters such as biocompatibility, optical transparency, gas permeability, mechanical and surface properties can directly affect cells in microfluidic channels and, likewise, the development process of the microfluidic structures.

2.1.1 Biocompatibility

PDMS is a highly used material in many aspects of life. It is present in shampoos, lubricants, caulks, sealants, implants, wearable electronics (as an insulator and packaging material), in biomedical microelectromechanical systems (bio-MEMS) and even Silly Putty. It is advantageous for these applications due to its biocompatibility. This property is ensured by the presence of the carbon atom in the PDMS backbone. To use PDMS as a material for implants, though, its surface has to be modified to avoid foreign body reactions [9]. There are several techniques such as coating with antifibrosis drugs, surface micro-structuring, plasma treatment, etc. to accomplish this. However, at the smooth PDMS surface, a layer of bacteria was often created. With plasma surface modification, complete eradication of the bacterial layer for several implants was observed [10]. There are many works on implantable PDMS structures and devices, but it is beyond the scope of this work to review them all. Here we focus on the in-vitro applications based on PDMS, where biocompatibility also plays a significant role. The main challenge in the cell culture is to emulate the body conditions to ensure the cell's functionality. Therefore, biocompatibility, in combination with flexibility and gas permeability, is beneficial. According to the statement for measurements of the International Organization for Standardization ISO [11], PDMS is a non-toxic and biocompatible material. Test system configurations for cytotoxicity measurement are shown in Figure 2.6.

- Extracting device material and then exposing cells to the extracted substances (Level 1 in Figure 2.6);

- Direct cytotoxicity testing, which can be done if the device material can be placed directly onto cells without causing damage (Level 2 in Figure 2.6);

- Indirect testing, which can be done by placing the device material onto a cushioning layer above cells (Level 3 in Figure 2.6).
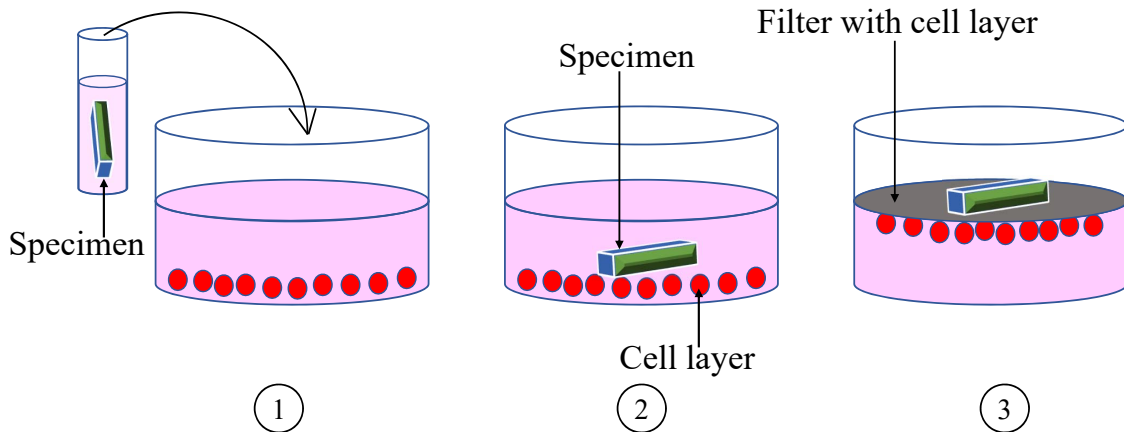
Figure 2.6: Measurement of the level of biocompatibility. Level 1 - Specimen is immersed in the medium, which is poured then on the cell layer; Level 2 - Material block is placed onto the cell layer; Level 3 - Test sample is located on the porous material with cell layer (adopted from [11]).

Moreover, it is important to mention that, dependent on the curing temperature and time, the biocompatibility of PDMS can differ. There is leaching of uncrosslinked oligomers, which can be reduced by curing the material overnight instead of 2 h, regardless of the curing temperature (60 °C or 80 °C). This result demonstrates the importance of the PDMS curing parameters [12]. Moreover, PDMS is soluble in solvents like diisopropylamine, pentane, ethanol, etc. [13]. While choosing the solvent for microfluidic chip sterilization or performing cell-based experiments, it is important to consider PDMS swelling in organic solvents, to avoid chip deformation and release of oligomers into the medium.

2.1.2 Gas permeability: solubility and diffusion of the molecules

The permeability of the chip material is an important parameter for cell culture and biological experiments in microfluidic structures. Cells in the channels receive necessary gases (e.g., CO_2) only from the surrounding medium, which in this case is a μ-volume. In turn, the cell culture medium has to receive gas molecules from the atmosphere with gas exchange proceeding through the walls of the microfluidic chip. Gas permeability is most beneficial for applications like immunology and single-cell analysis, where experiments last over hours and pumping is absent. Figure 2.7 schematically shows the three different mechanisms involved in permeation: the solution of the gas molecules at the polymer/gas

interface, diffusion through the membrane, and finally, the evaporation out of the membrane.
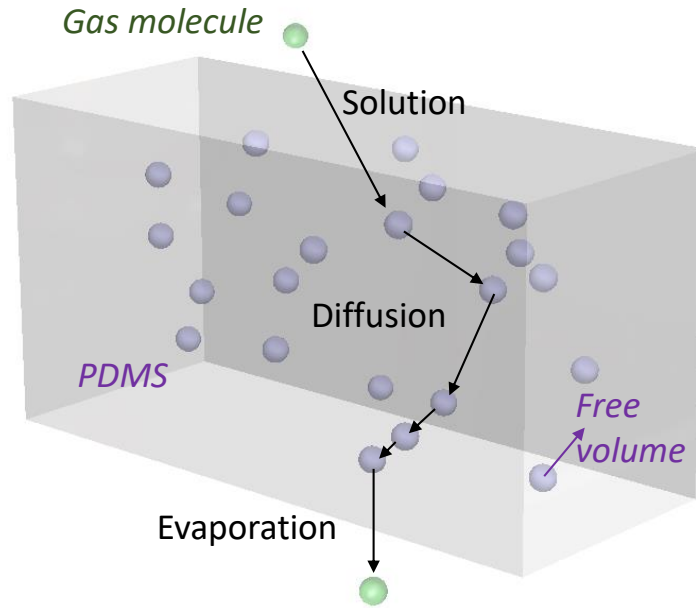
Figure 2.7: Schematic description of the permeability mechanism in the PDMS. It consists of three steps: Solubility (Solution), Diffusion, and Evaporation (adopted from [14]).

The permeation rate is a specific function of a given gas and rubber, and it depends on both solubility and the diffusion rate. The permeability versus thickness relation is predicted by Fick's law:

$$P = \left(D(C_0 - C_1)\right)/L, \tag{2.1}$$

where,

- D is a diffusion coefficient;

- C_0 and C_1 are concentrations of the particular gas on opposite sides of the PDMS layer or membrane;

- L is a PDMS layer thickness.

The high flexibility of the silicon–oxygen Si—O chains in silicones provides "openings", which are free volumes that allow gas diffusion inside the network. Free volumes, often named "holes", thermally generate and disappear with the movement of polymer chains. The diffusion of gas molecules in the rubber membrane is a process in which the gas molecules migrate from "hole" to "hole" [15]. Furthermore, PDMS permeability depends on the material's stiffness, which is conditioned by the mixing ratio of the base and curing

agent. The polymer chains are less interconnected and easily movable for soft versions of the PDMS (e.g., 20:1 mixing ratio). Therefore, molecules can effortlessly drift through the PDMS layer. The dependency of the PDMS permeability on the mixing ratio is shown in Figure 2.8.
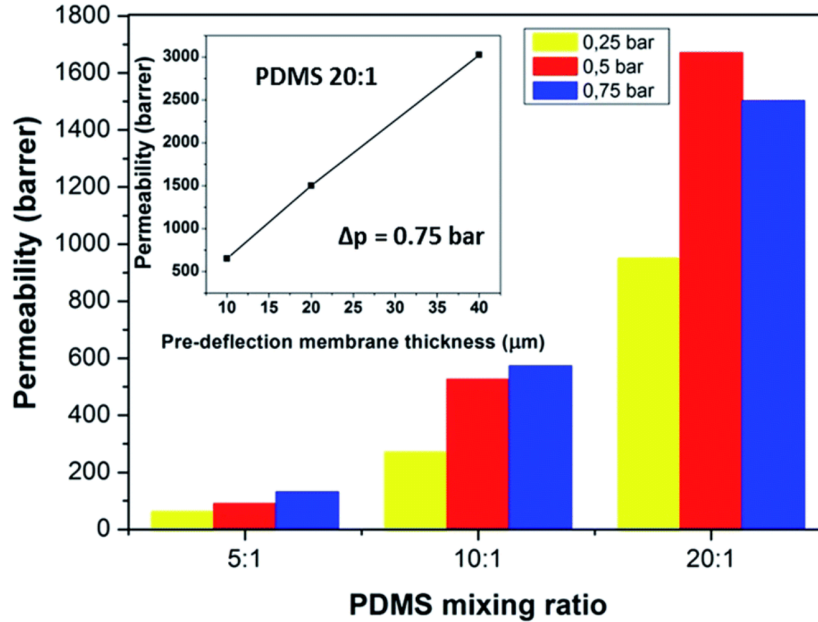
Figure 2.8: Graphical representation of the permeability dependency on PDMS mixing ratio (base and curing agent), pressure difference at membrane's opposite sides. The inset shows PDMS permeability as a function of the pre-deflection membrane thickness [14].

Furthermore, PDMS's gas permeability depends on many parameters, most of which are processing and application-dependent, including:

- Thickness of PDMS layer;

- Curing temperature;

- Ratio between polymer base and curing agent;

- Effective diffusion area;

- Partial pressure;

- Properties of the penetrating component.

2.1.3 Optical transparency

Because microscopy is one of the main analytical tools in cellular biology, optical transparency is another essential material property for cell-based applications. PDMS is

amorphous silicone and, thus, transparent in the wavelength spectrum from 240 nm to 1100 nm [16, 17]. As shown in Figure 2.9, the transmittance of the PDMS is approximately 90 %. Therefore, the remaining 10 % is distributed between absorption and reflection. The PDMS surface is usually planar as the system seeks minimum energy of the materials, and the dominant mechanism is specular reflection, compared to diffuse reflection and light absorption. Moreover, the light transmittance through PDMS and glass is equivalent [18]. Therefore, PDMS is a beneficial material for Lab-on-Chip biomedical applications. As shown in Figure 2.9, thermally-treated PDMS transmittance differs from untreated PDMS. One possible reason lies in the influence of thermo-mechanical expansion on the amorphicity of silicone. Every polymer consists of amorphous and crystalline areas, and after thermal treatment, presumably, the amount of crystalline islands in PDMS increases, rendering it less transparent.
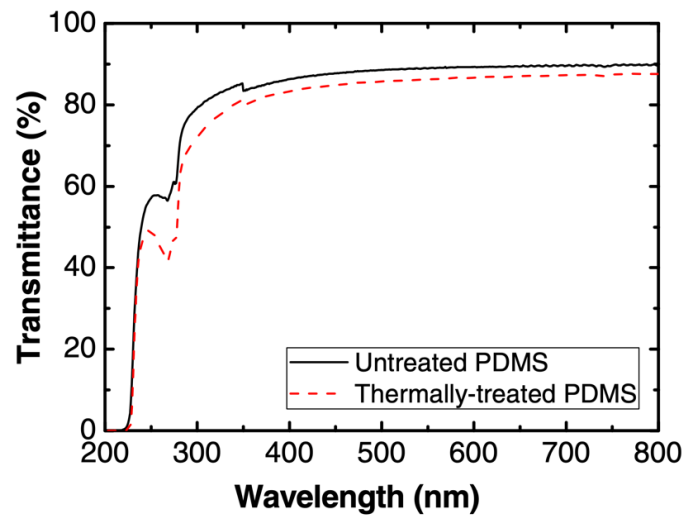
Figure 2.9: Transmittance of the untreated and thermally-treated PDMS (at 300 °C, 30 min) in the near UV and VIS spectrums [19].

Furthermore, PDMS has a high linear negative thermo-optical coefficient. The refractive index varies with the temperature at constant pressure, and optical properties are sensitive to temperature changes [20, 21]. As temperature increases, PDMS undergoes thermal expansion, causing the polymer chains to stretch and the material to become less dense. This leads to a decrease in the refractive index of PDMS, making it more transparent to light. Conversely, at lower temperatures, PDMS contracts and becomes more dense, increasing the refractive index and reducing transparency. The linear change in the refractive index of PDMS due to temperature variations is shown in Figure 2.10. This effect makes possible the development of PDMS-based high-resolution optical sensors for temperature measurements. Authors in [20] achieved a temperature sensor based on thermo-mechanical PDMS expansion with a sensitivity of 384 pm/°C in the range of 25 °C - 80 °C. Also, the

transparency of PDMS can be controlled by adjusting the temperature, making it a useful material for optical devices that require temperature-sensitive optical properties [22].
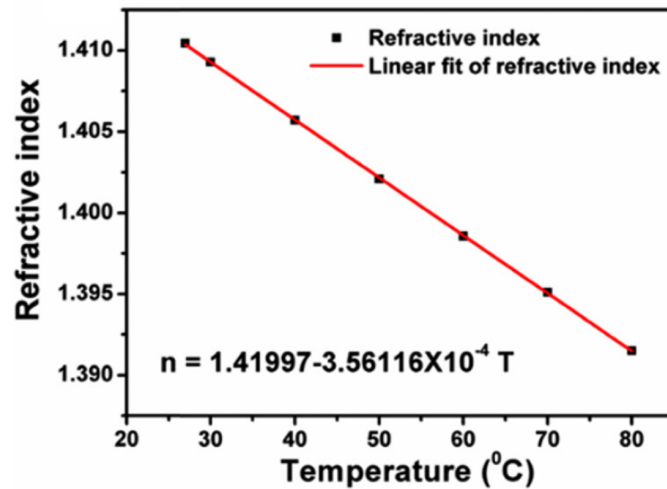
Figure 2.10: Variation of the PDMS refractive index with temperature change [21].

Often, to create complex devices, other materials and layers (e.g., metal to realize electrodes) need to be structured on top of PDMS. A promising technique for structuring these materials and layers is laser ablation. However, one has to consider material degradation. The transmittance can be significantly reduced by pulsed laser irradiation. Light absorption increases due to the chemical transformation in the PDMS volume. In particular, the intermolecular bonds in the entire irradiated area are broken [23]. Besides, PDMS possesses autofluorescence. It absorbs energy in the form of invisible light and emits the energy as longer-wavelength, lower-energy light [24]. Lines of length 552 nm were used to excite the autofluorescence of the PDMS. The emission was detected in the spectral range 581–695 nm [25]. These properties must be considered while developing PDMS-based devices or executing measurements.

2.1.4 Mechanical properties: flexibility, stretchability, and robustness

As mentioned previously, PDMS is an elastic, flexible, and robust polymer. The elasticity and flexibility of this polymer are a result of the Si—O bond in the main chain. The interatomic distance between the bonded atoms exceeds that observed in a C—C bond. This is due to the presence of a double bond within the Si—O group, which results in a bond angle of 143 °C that is significantly larger than the standard tetrahedral angle of 110 °C. The bond angle is highly flexible and can undergo deformation up to 180 °C, resulting in a torsional potential that is much higher than that of a C—C bond. Furthermore, the double bond influences the bond dissociation energy, which is notably higher at 460 kJ/mol than that of a C—O bond (345 kJ/mol) [26, 27]. Young's modulus of this material also

depends on the curing temperature and mixing ratio. According to the literature, it can be in the range from 0.36 MPa to 2.97 MPa [28]. The differentiation in the Young's modulus of PDMS due to the curing temperature at 10:1 mixing ratio is shown in Figure 2.11.
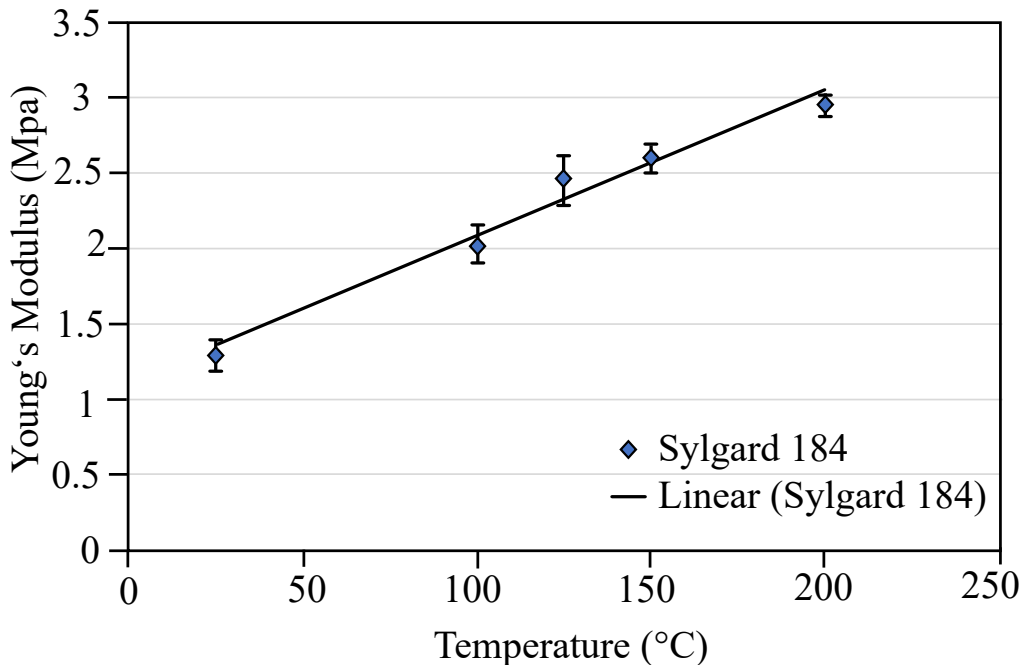
Figure 2.11: Graph representing the differences in PDMS's Young's modulus due to the curing temperature (adopted from [28]).

Furthermore, by changing the mixing ratio of the PDMS base and curing agent, it is also possible to tune Young's modulus of the material [29]. Thus, the mechanical properties of PDMS are highly dependent on the processing parameters, especially temperature and time. This is an advantage of this silicone for the development of novel sensors, actuators, and structures. Nevertheless, Young's modulus of PDMS can change over time as well. The reason for this effect is thermal degradation [30, 31]. At temperatures higher than 250 °C, thermal cleavage of the Si—O bonds can occur via a homolytic process, in which the bond breaks and generates a silicon-centered radical and a free radical on the oxygen atom. These radicals can then further react with each other, leading to cross-linking, or react with other polymer chains, leading to chain scission and the formation of smaller cyclic oligomers. The reaction is shown in Figure 2.12. Although the C—Si bond is the weakest bond in PDMS, at $78 \, \text{kcal} \times \text{mol}^{-1}$, the formation of cyclic oligomers during decomposition suggests that the Si—O bond, at $108 \, \text{kcal} \times \text{mol}^{-1}$, breaks instead. Therefore, PDMS depolymerization can be attributed to its molecular structure and kinetics rather than to bond energies. Additionally, at very high temperatures, PDMS can undergo further degradation via pyrolysis, in which the polymer decomposes into smaller molecules, including volatile products such as dimethylsilane and other hydrocarbons. The

decomposition of PDMS is almost complete at about 460 °C [30, 32]. Furthermore, in the presence of oxygen, additional reactions take place in two distinct stages. The first stage occurs up to 339 °C, while the second stage commences at 400 °C. The resulting reaction products from these stages consist of oligomers, water, and CO_2. Upon reaching a temperature of 500 °C, the residual matter comprises silica [30].
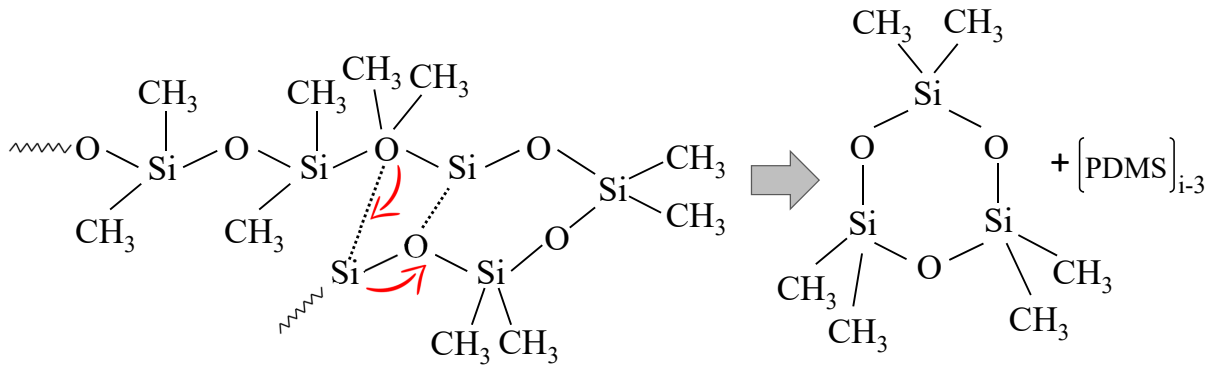
Figure 2.12: Chemical reaction of the PDMS thermal degradation and creation of the cyclic oligomers (adopted from [31]).

The thermal conductivity of PDMS is 0.27 W/m°K, is lower than that of water (0.5918 W/m°K). Thus, heat is not well distributed in this polymer. The reason for this may be the variable cross-section of the polymer chain, which prevents the polymer from packing efficiently and prevents heat energy transport. Subsequently, the dilution entropy and the excess volume deviate from the theoretically determined values, and the gas permeability is very high. The glass transition temperature is −125 °C [27]. Overall, the mechanical properties of silicon-based polymer PDMS are complex, highly interdependent and tunable by the processing parameters. Understanding these mechanisms is important for designing, developing and using Lab-on-Chip PDMS in biomedical applications. In addition, material degradation during processing and use must be considered.

2.1.5 Surface properties

The most important PDMS surface properties for biomedical applications are hydrophobicity/hydrophilicity, protein and particle absorption and roughness. PDMS is a highly hydrophobic material with a water drop contact angle >100 °C [33]. However, the inherent hydrophobic nature and low surface energy of PDMS prevent its direct use in many applications. The disadvantage of this characteristic is low surface wetting, which leads to an absence of capillary forces in microfluidic structures made of PDMS. As a result, liquid can only be introduced to the channel with applied pressure, which requires a pipette or pump. Such a flow of water-based solutions in a hydrophobic channel can create air bubbles, which are critical for most biomedical applications. There are several ways to change the hydrophobic surface to hydrophilic which will allow a capillary liquid flow.

One approach is an oxygen plasma surface treatment. During this process, OH groups are created on the surface instead of CH_3, as shown in Figure 2.13.
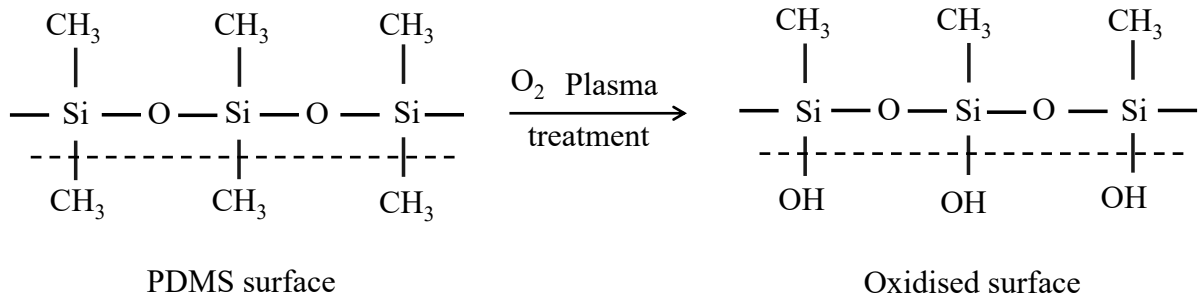
Figure 2.13: PDMS chemical formula before (left) and after (right) plasma surface treatment (adopted from [34]).

The main parameter to be controlled during the plasma treatment is time. The surface energy of PDMS rises to the maximum in the first 30 seconds of the treatment, while a longer process only results in surface degradation, as shown in Figure 2.14.
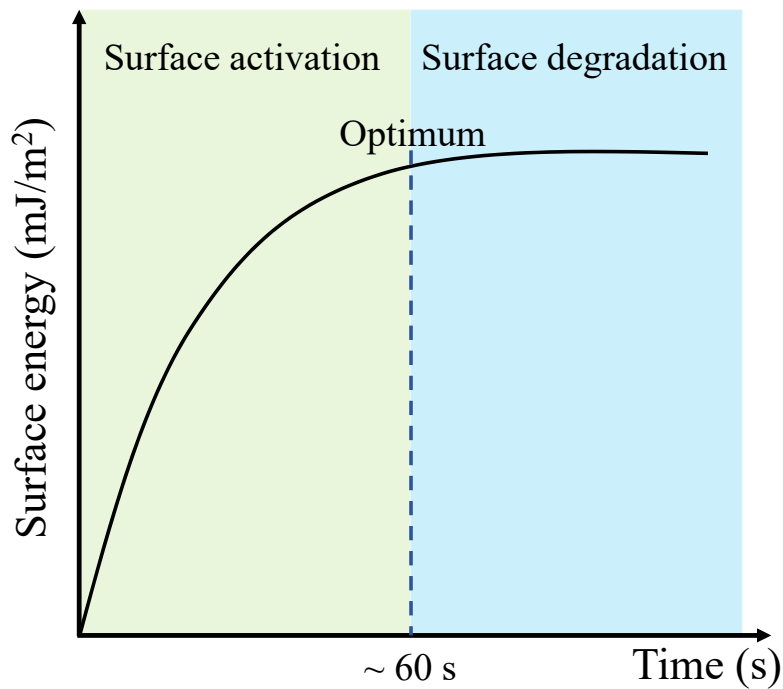
Figure 2.14: Graphical representation of the surface energy and plasma treatment time dependency.

This effect is also clearly seen in the dependence on the water drop contact angle on the plasma treatment time (Figure 2.15). The contact angle of the drop on PDMS reaches its minimal value after one minute of the plasma treatment. Subsequently, the angle value stays the same with longer plasma activation, but the surface degrades. Therefore, the optimal time for the plasma surface treatment is 60 seconds. Once activated, the

surface stays hydrophilic for over 12 hours, thereafter returning slightly to its hydrophobic properties.
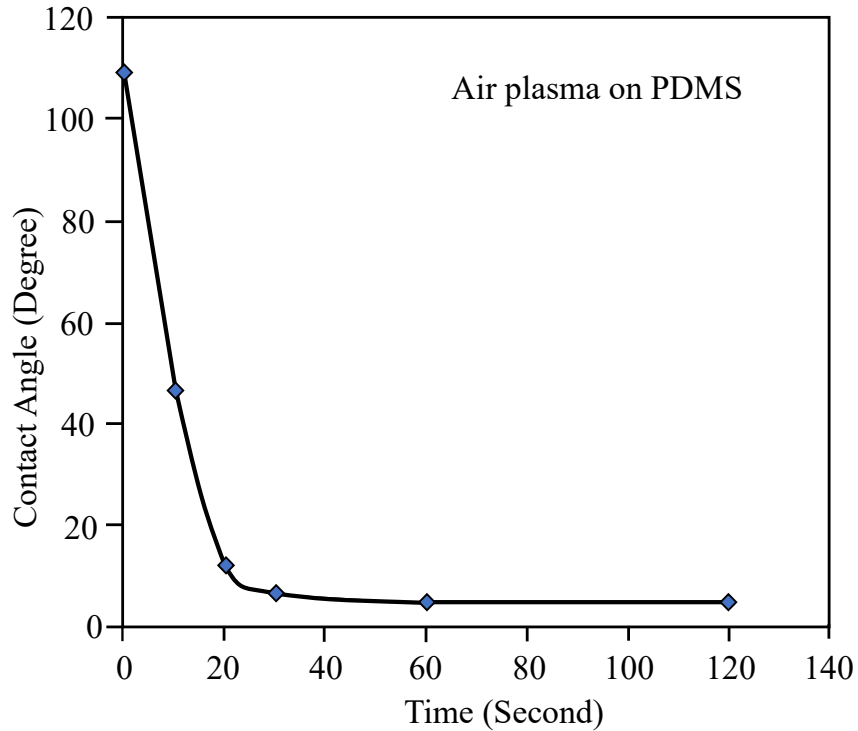
Figure 2.15: Water drop contact angle on a PDMS surface as a function of the plasma treatment time (adopted from [35]).

Thus, plasma surface treatment is a useful process for functionalizing the PDMS surface with proteins, e.g., collagen or BSA. The channel must be filled with the liquid protein solution directly after oxygen or air plasma treatment. In this case, wetting of the surface is high and liquid covers even the smallest nano-sized areas homogeneously with capillary forces. Also, this prevents bubble formation even after long duration use of the chip since a PDMS surface that has been functionalized with proteins stays hydrophilic.

A second way to make a PDMS surface hydrophilic is to add supplementary components before curing. In work [36], authors modified the PDMS surface with dimethylsiloxane-(60-70 % ethylene oxide) block copolymer (PDMS-PEG BCP). Copolymer comprised of poly(ethylene glycol) (PEG) due to the shortage of the polymer chains accumulates close to the PDMS surface during the curing process. When facing an aqueous solution, the copolymer self-organizes and creates a stable hydrophilic PDMS property. This concept is useful not only in changing hydrophobic properties to hydrophilic, but helps also in preventing the absorption of the proteins by PDMS.

2.1.6 Alternative materials to PDMS

In spite of all the advantages of PDMS for microfluidics, its disadvantages induce the search for alternative materials. These weak points, as mentioned above, are protein adsorption, difficulties in realization of metal electrodes on its surface and hydrophobicity. Promising candidates for an alternative are glass, Flexdym$^{\text{TM}}$ and Ostemer$^{©}$.

Glass is a standard material for microfluidic applications, is also transparent, and has the lowest ability to adsorb proteins and drugs. It has a solid crystal structure and serves as a good substrate for a wide range of materials [37]. Nevertheless, glass structuring is expensive and requires cleanroom facilities. This limits its use for microfluidic applications and opens a need for easier-to-structure materials like polymers.

The nearest alternative to PDMS based on its properties is Flexdym$^{\text{TM}}$ [38]. This polymer material was recently developed and has the main benefit of not requiring plasma treatment for bonding [39]. Nevertheless, this polymer exhibits a significantly lower gas permeability compared to PDMS [40]. Also, it is distributed in already prepared layers. Therefore, the only way to structure channels in this material is by hot embossing. Furthermore, same as PDMS, this material adsorbs biological components and drugs.

Another candidate is Ostemer$^{©}$. This polymer can be structured by soft lithography, hot embossing, imprint lithography, and milling [41]. Its structuring also requires lithography facilities [42]. Compared to PDMS and glass, its transparency is much lower, and the material is semi-transparent.

All above mentioned materials are biocompatible, and cell layers can be cultured in microfluidic devices made from them. Nevertheless, the selection of the appropriate material for constructing a microfluidic structure with optimal properties remains imperative for each biomedical application in order to address specific biological questions.

2.2 Current status of microfluidics and sensor integration for medical applications

There is a significant number of microfluidic approaches for cellular biology. Some are developed for single-cell analysis [43], protein assembly, and understanding their behavior [44], synthesis, screening, and sorting of libraries of variants of a specific enzyme [45], etc. In this work, we focus on microfluidic platforms for multiple cell cultures and analyses. Therefore, the state-of-the-art research described in this chapter will mainly focus on the latest achievements in microfluidics for cell culture and tissue engineering.

2.2.1 Tissue engineering and microfluidics

The field of tissue engineering took its beginning in the 20$^{\text{th}}$ century. Many intelligent scientists wished to improve upon cell culturing in the Petri dish and believed that new

approaches would light up many ways to improve human health. Therefore, Robert Langer and Joseph P. Vacanti published their first works on tissue engineering on 3D-shaped scaffolds [46], as it is chronologically depicted in Figure 2.16.
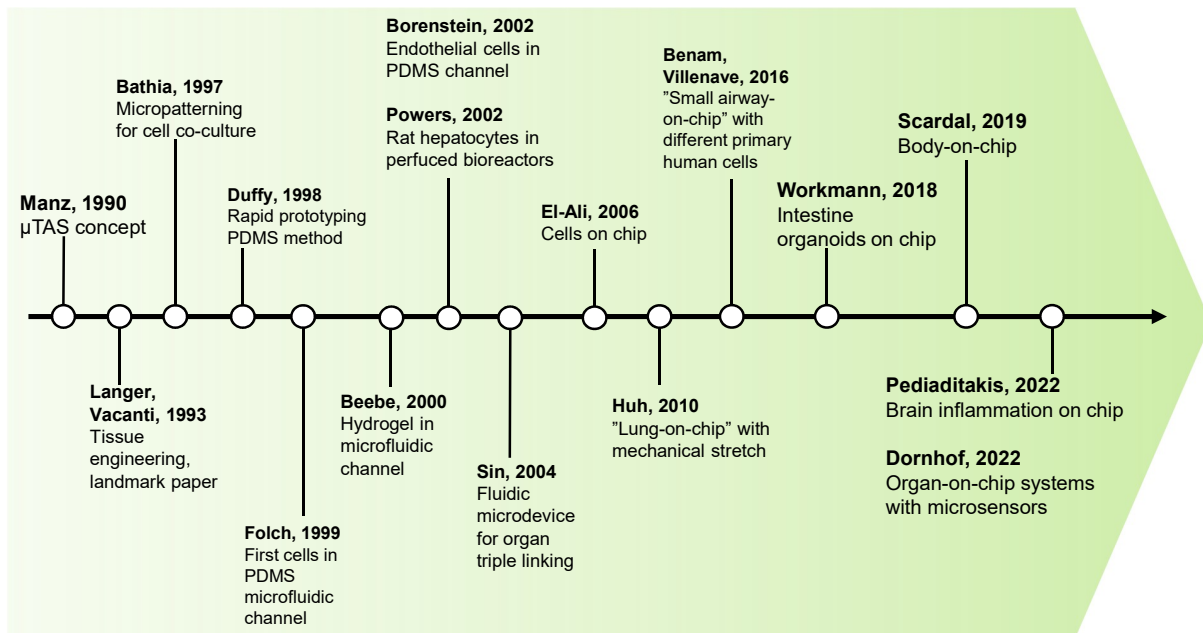
Figure 2.16: The development of the microfluidics into an Organ-on-Chip concept.

Authors believed that tissue engineering would help to replace dysfunctional organs. Their research even progressed to the first animal trials. Still, the human organism is an extremely complex system, and the goal of organ replacement by an artificial one has yet to be achieved. At the same time, chemistry, materials science, microsystem technology, and measurement technology were all progressing significantly. Thus, Duffy et al. in 1998 [47] and Folch et al. [48] in the year 1999 demonstrated deep (more than 25 μm) molding technology for Polydimethylsiloxane and with that launched the era of PDMS microfluidics for cell culturing. In the subsequent years, many research groups continued to work on PDMS microfluidics and cell culture [49], [50], [51], [52]. The next milestone, which is essential to mention, was the development of the first Organ-on-Chip model by the group of Donald Ingber at Harvard University [53]. It was the first "breathing" model of the human lungs. As shown in Figure 2.17, human epithelial and endothelial cells are located on opposite sides of the membrane, and the vacuum channels (grey color) enable the "breathing" motion. The described chip membrane is 50 μm thick with a pore size of 10 μm, giving room for this model's improvement. Nevertheless, the concept of two microfluidic channels divided by a porous membrane was groundbreaking and became widely utilized. Next, based on this structure but with different channel sizes and membranes, many different Organs-on-Chip were developed. By culturing different cell types in the chip, various Organs-on-Chip can be created, e.g. Placenta-on-Chip [54], Muscle-on-Chip [55],

Heart-on-Chip [56, 57], Gut-on-Chip [1, 58], Brain-on-Chip [59], Kidney-on-Chip [60], Blood-Brain-Barrier [61], Liver-on-Chip [62, 63], etc.

1. Epithelial Channel
2. Human Epithelial Cells
3. Vacuum Channel
4. Membrane
5. Human Endothelial Cells
6. Endothelial Channel
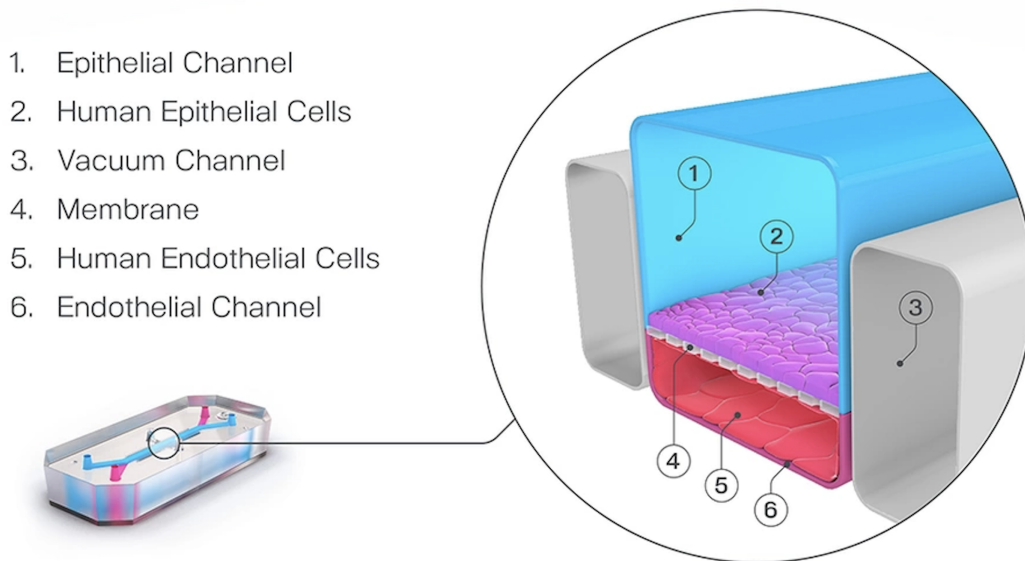
Figure 2.17: The schematic view on first Lung-on-Chip model [53].

To answer a specific biological question, in many cases a chip with specific geometry has to be designed and developed. Today, most PDMS chips are fabricated by replicating a master mold made by Photo and Soft Lithography [64]. Since the microfabrication field has significantly advanced and new technologies have appeared, Organ-on-Chip fabrication has become faster and more precise, and microfluidics can be reproducibly obtained with sub-micron sizes [65]. Even with such advanced technologies, humans have not found the ideal material suitable for all medical and cellular biological experiments. In microfluidic devices, we recapitulate part of the organ to find answers about human nature or to perform drug screening experiments. The development of 3D printing launched the 3D bioprinting technologies [66], where Matrigel is mixed with living cells and printed in the shape of an organ. But up to now, neither 3D bioprinting nor Organs-on-Chip can create an organ replacement as intended by Robert Langer and Joseph P. Vacanti in the 90ˢ.

2.2.2 Sensor integration in microfluidics for cell culture

Since researchers have achieved significant advances in technological approaches for microfluidics which have been successfully applied in cellular biology, the next step will be in-situ measurement. This entails the integration of sensors into microfluidic systems to enable measurements in the vicinity of the cells. By means of the embedded sensors it would be possible to detect short-life proteins [67], the bio-environment and physiological conditions of the cell culture [68], [69] released from the cell's proteins, biomarkers

or hormones [70], etc. The primary sensor types for integration into microfluidics are amperometric, voltammetric, impedimetric, and optical [69].

Optical and electrochemical sensors are usually developed and utilized to measure the oxygen concentration in microfluidic devices for cell culture or single-cell analysis. Optical sensors commonly have the shape of the sensor spots and are based on the luminophore (a compound that is responsible for its luminescent properties) [71]. This material could be combined with a polymer matrix or nanoparticles [72], [73]. Nevertheless, the state of the art shows equal sensor characteristics to commercially available sensor spots. Nevertheless, electrochemical sensors often consume oxygen, which is a significant disadvantage for biomedical applications [71]. Some of the latest achievements towards sensor miniaturization and implementation into microfluidics are shown in Figure 2.18. One research point of interest is the cell's mechanical properties [74]. Urbanska et al. published research on cell deformability measurements in microfluidics by constriction-based deformability cytometry (cDC), shear flow deformability cytometry (sDC) and extensional flow deformability cytometry (xDC) [75].
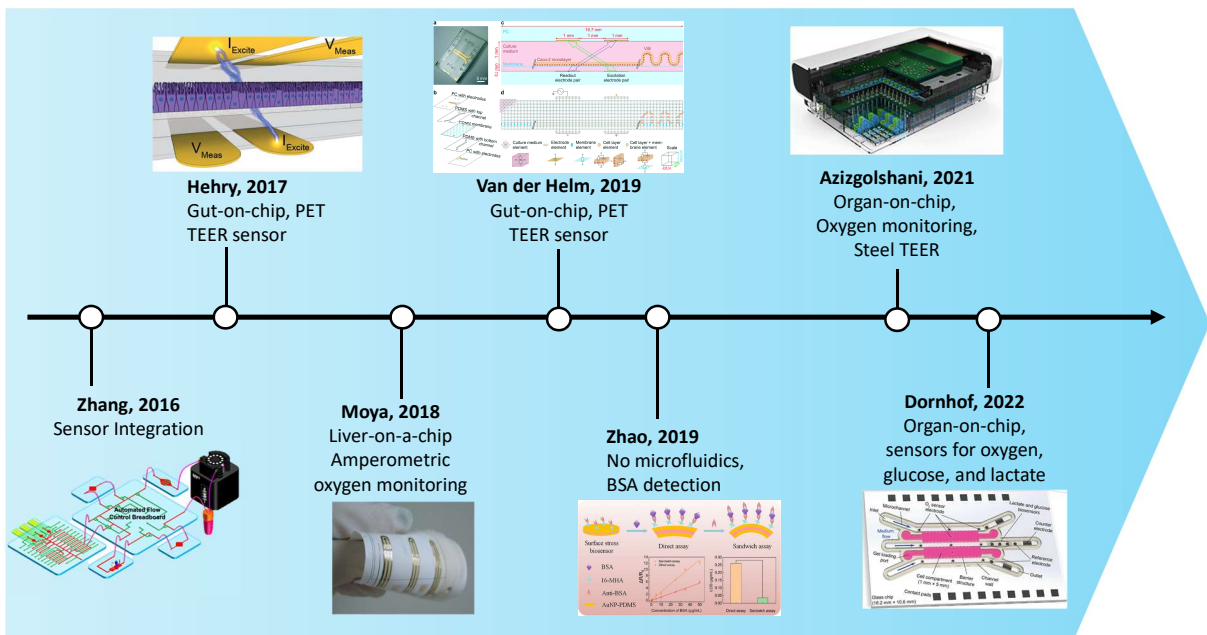
Figure 2.18: State-of-the-art schematic representation of sensor integration in microfluidics for cell culture.

Other components of interest are oxygen concentration [76], glucose, lactate [77], etc. The measured physiological parameters are temperature, the flow rate of the cell culture medium, pH [78], and transepithelial electrical resistance (TEER) [61, 79, 80]. TEER measurements can be performed at DC or using an AC signal at low-frequencies. The latter technique provides information about a complex bioimpedance. Based on these measurements, one can implement an impedance camera for cell distribution monitoring [81].

A significant amount of research on sensor integration into the Organ-on-Chip is based on semi-flexible and transparent, but not stretchable and gas-permeable polymers or glass. These materials have an essential parameter for cellular experiments – transparency. TEER measurements provide the information about a cell layer confluence. The cell itself could be represented as a capacitor (C_c) in an equivalent circuit (Figure 2.19), and the tight junctions created between the cells are resistors. Therefore, by measuring resistance between the electrodes in the upper and bottom compartments we can detect the increase in resistance, which relates to the tissue development. Once a confluent cell layer is created, further experiments can take place, e.g. drug screening or bacteria co-culture. Recently, most of the cell culture experiments are done in the Petri dishes and Boyden chambers, where TEER is measured by the chopstick electrodes immersed manually into the cell culture medium. This creates a certain level of measurements uncertainty due to the human factor and positioning of the electrodes. Nevertheless, electrodes such as those represented in Figure 2.19 could not be used with microfluidic devices due to their size and the impossibility of insertion into a chip. Therefore, some research groups have integrated the TEER electrodes into microfluidic devices [79], [80], but not into a completely flexible PDMS chip. The material of choice as a substrate for electrodes is glass or polycarbonate, which are not stretchable and not gas permeable. Therefore, further research on electrification and functionalization of the PDMS layers is necessary.
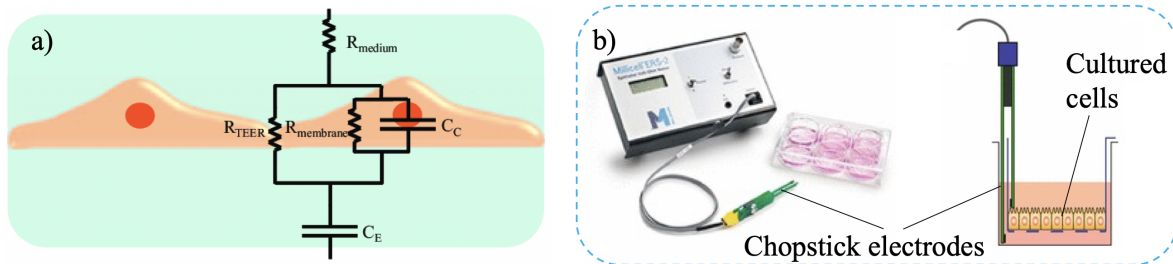
Figure 2.19: Transepithelial electrical resistance (TEER) equivalent circuit of the cell layer (a) and Millicell-ERS (Electrical Resistance System, Merck KGaA) with chopstick electrodes, which are also immersed into Boyden chamber with cultured cell layer (b).

Due to the special properties of this elastic material, which are listed before, sputtering of metal onto PDMS is not a trivial task. This poses additional significant research challenges for micro-structuring, such as micro-cracks, delamination, and potential degradation of electromechanical behavior caused by mechanical deterioration [82]. The deposition of metal films by magnetron sputtering can lead to the formation of wrinkles and grooves on the PDMS surface which are then transferred to the deposited metal [83]. This phenomenon is attributed to the thermo-mechanical expansion of PDMS during metal deposition and subsequent relaxation processes [84].

Previous studies have explored the deposition of metals on elastic PDMS, showing that naturally formed wrinkles' wavelength increases linearly with the metal film thickness, in agreement with continuous elastic theory [84]. Controlled surface modification can also be achieved by pre-stretching PDMS [85], providing the potential for electrode "self-healing" during mechanical movements.

Interestingly, researchers have observed the appearance of wrinkles exclusively near cracks in metal films when applying DC magnetron sputtering on uncured and partially cured PDMS substrates. The manipulation of metal film thickness has revealed distinct ordered wrinkling patterns, such as branched stripes, herringbones, and labyrinths, explained by a non-linear wrinkling model [86]. Moreover, custom-designed wrinkling patterns have been fabricated using specific combinations of metals and thin PDMS [87].

The practical applications of tailored wrinkled soft metalized layers include strain sensors and droplet motion devices. However, despite existing research, there remains no definitive understanding of the mechanism behind wrinkle formation and behavior in large area freestanding metallized soft polymer layers. Additionally, there is a lack of studies investigating the influence of Polydimethylsiloxane's stiffness on wrinkle creation.

Control of the metal wrinkle presence, absence and shape can provide a wide spectrum of opportunities for sensor and actuator research for Lab-on-chip devices. Therefore, in this thesis, the fabrication methodology, electrical and thermo-electrical behavior of Cr/Au sputtered metal structures on thick and thin PDMS with different mixing ratios are presented.

3 Microfluidics with integrated sensors based on Polydimethylsiloxane – processing methods

Polydimethylsiloxane (PDMS) is a relatively easy-to-structure polymer. The main steps for PDMS-based structure preparation are mixing, molding, and bonding. Besides, it is possible to adjust PDMS properties during mixing or curing procedures. Curing is a chemical process that enables the hardening of a polymer material by cross-linking of polymer chains. The cross-linking can be realized by one of the three common systems/mechanisms for silicone resin curing: condensation, platinum-based, or peroxide-based. In the condensation curing mechanism, PDMS consists of siloxane polymers with hydrolyzable groups and a hydrolyzable silane cross-linker [5]. By manipulating the concentration of base and curing agents, we can make PDMS softer and sticky or harder. The desired properties depend on the application. The molding process requires a master mold whose structure will replicate PDMS. Therefore, master structures are usually fabricated by a soft lithography process on silicon substrates, which enables high-resolution and low roughness of the replicas. Alternatively, 3D-printing technology, hot embossing, etching, etc., can be used instead. This chapter describes the processing of PDMS based on the condensation mechanism.

3.1 Master mold fabrication

Master mold fabrication is the most critical process in chip development, as PDMS replicates the geometry of the prepared wafers. A standard soft lithography process is commonly used to create the micro-structured mold for PDMS replication. Soft lithography is a process in which a light-reactive photoresist layer is exposed through a shadow mask to create structures on the wafer. In this work, master molds for the Stomach-on-Chip, ImmunoChip, and LabyrinthChip applications were fabricated with an optimized soft lithography process on silicon and glass 4″ wafers. Optimization targeted the soft bake and post-exposure bake temperatures and cooling to avoid cracks in the photoresist layer and to improve the development process. The main requirements for a master mold are:

- Surface roughness. The intention is to keep it in the less-than-nanometer range in order to ensure a good surface contact for future bonding of the replicated PDMS layers.

- Angle between the wafer and fabricated structures. Ideally, the angle should be 90 degrees. Ensuring this parameter during master structures development, we can

deliver the best resolution to the molded PDMS parts.

- Complete absence of the photoresist residuals. If the master mold development process is incomplete, and the uncured photoresist stays in the corners or in hard-to-reach places, then these defects would be replicated by the PDMS. At the same time, over-development will cause cracks in the photoresist and delamination of the master structures from the wafer.

- Surface wetting. The structure's surface obtained by photo-lithography has to be hydrophilic or low hydrophobic to ensure PDMS can fill all the tiniest places on the master mold.

- Absence of any horizontal barrier. After pouring liquid polymer on the master mold, air bubbles will move upwards and will be naturally removed from PDMS. If any structure creates a barrier, bubbles will stay in the layer, worsening the PDMS structure quality.

- Proper adhesion of the photoresist structures to the Si or Glass wafer. While removing the cured PDMS layers from the master mold, the mold structures face mechanical stress. Therefore, to avoid delaminations at this technological step, sufficient adhesion has to be ensured.

3.1.1 Master mold for Stomach-on-chip

The first generation of fabricated master molds for Stomach-on-Chip contained various micro-structures, varying widths (denoted by w in Figure 3.1) from 0.1 mm to 5 mm and chip body size from $3 \times 4 \, \text{cm}^2$ to $2 \times 3 \, \text{cm}^2$. The design of the shadow mask for the lithography process is shown in Figure 3.1, where the channel length f is 1 mm. Wide structures with $w = 3$ mm and $w = 5$ mm had a length of 3 cm. The inlet and outlet ports are designed to have a diameter a of 1 mm. The soft lithography process utilized the materials listed in Table 3.1 and was based on the parameters listed in Table 3.2.

Table 3.1: Materials for Stomach-on-Chip master mold fabrication by soft lithography.

Amount	Material	Specifications
4	4″ Si-Wafer (SW)	SSP, 100 mm, 525 µm, 1-5 $\Omega \cdot$ cm
16 ml	SU-8-100	Negative photoresist
On-demand	N_2, Aceton, Isopropanol	Process supportive chemicals and gases
800 ml	mr-Dev600	Developer

To enable a larger number of microfluidic devices per wafer, a second generation of the master mold was designed (Figure 3.2) and fabricated. In addition to the above-mentioned requirements, the master contains the optimal number of structures to ensure

Table 3.2: Process parameters for Stomach-on-Chip master mold fabrication realized by soft lithography.

Step	Name	Description
1.	Wafer preparation	Wafers dehydration on a hot plate at 200 °C, 5 min
2.	SU-8 spin-coating on SW	500 rpm − 10 s 1000 rpm − 80 s − photoresist dispensing 4 ml SU-8 Thickness adjustment: 200 μm - 1375 rpm - 30 s; 100 μm - 2500 rpm - 30 s Acceleration: 300 rpm Intermediate step 30 minutes at room temperature
3.	Soft Bake	65 °C - 25 min, 85 °C - 70 min
4.	Edge Bead Cleaning (EBR)	Removing the edge of the thin film: 3000 rpm − 5 s 3000 rpm − 20 s EBR Repeating these steps 3 times 10 min evaporation time
5.	Exposure	Exposure dose SW: 650 mJ/cm² Mask: mm-LB Time: 80 s; Alignment Gap: 150 μm; Exposure type: soft; WEC type: cont; WEC Offs: Off
6.	PEB	13.5 min 65 °C; 95 °C 20 min; slow cooling
7.	Development	In mr-Dev600 (20 min) Rinsing in Isopropanol (2 min)

the effectiveness of the molding process and hold enough area for bonding. Thus, one can fabricate a sufficient number of microfluidic devices for generating statistics from the cell culture experiments. The second generation of the master mold included only a $2 \times 3\,\mathrm{cm}^2$ squares with a channel width of 1 mm, multiplied ten times (Figure 3.2). Same as the first generation mold, the second generation mold was fabricated using the materials described in Table 3.1) and process parameters listed in Table 3.2.

3.1.2 Master mold for ImmunoChip

To realize the master mold for ImmunoChip, two technologies had to be combined, which is a novel way of 3D mold fabrication. The first technology is soft photolithography, and the second one is direct femtosecond laser writing. These two technological approaches compensate for the weaknesses in each other. For the soft lithography process, the challenges are nano-sized structures, spin-coating on the pre-structured wafer, mask alignment for second-layer exposure, and fabrication of the 3-dimensional structures. In its
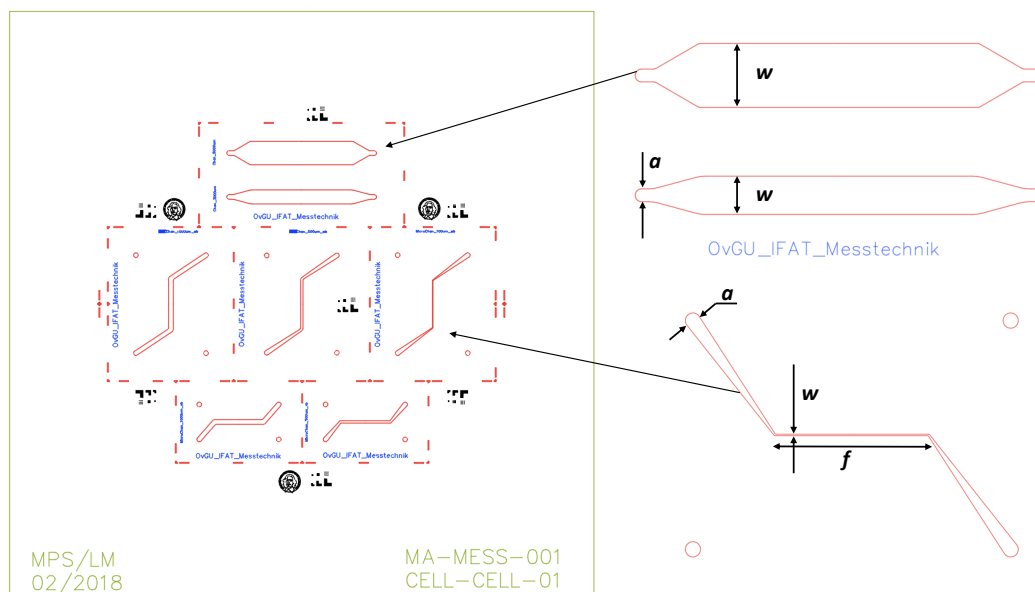
Figure 3.1: Technical drawing of the first-generation mold for Stomach-on-Chip application, designed in AutoCAD®, Autodesk Inc. Master wafer includes seven structures for microfluidics with different channel width w and length f. The diameter of the inlet and outlet ports a is $1\,\text{mm}$.
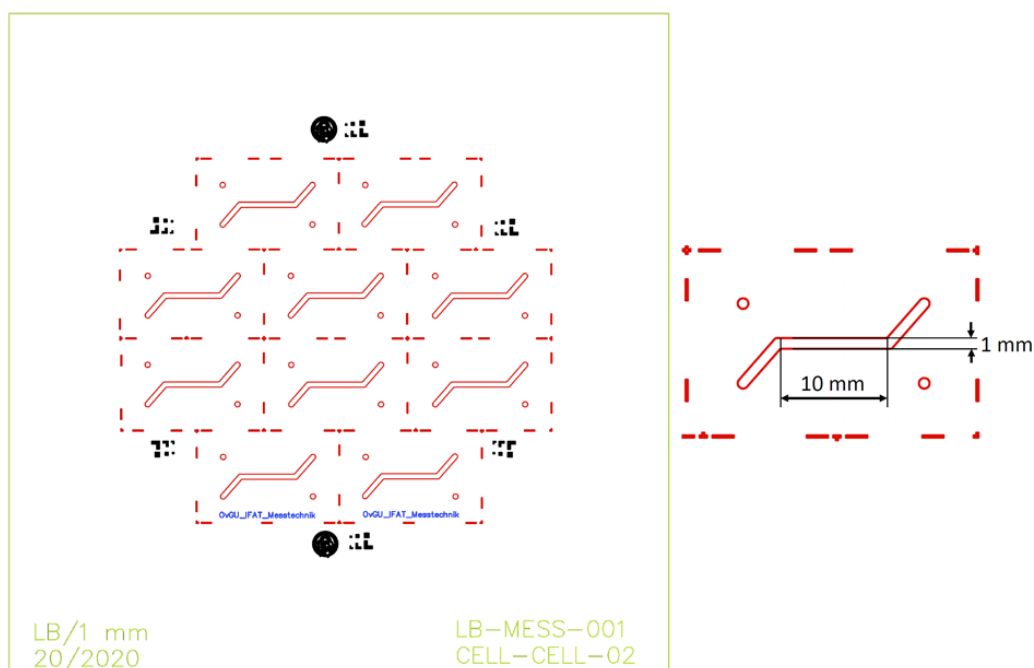
Figure 3.2: Technical drawing of the second-generation mold for Stomach-on-Chip application, designed in AutoCAD®, Autodesk Inc. Sketch includes ten identical parts to one, which is shown in magnification.

turn, the femtosecond laser writing technique is not advantageous in the case of large model structuring (more than a millimeter), which would last hours. Therefore, the combination

and the right sequence of these two technologies can lead to the optimal result. The master mold for ImmunoChip is a 3D structure on a glass wafer with three wide channels (100 µm, 150 µm and 100 µm width) with a height of 40 µm, which are interconnected by 375 perpendicular microchannels (width 6 µm, height 4 µm, length 30 µm).

Soft lithography is the first step in the complex fabrication technology. Optimized process parameters are given in Table 3.3. The geometrical parameters are set by the design of the lithography shadow mask. The sketch is shown in Figure 3.3, where $a = 1.1$ mm, $b = 100$ µm, $c = 150$ µm, $r = 25$ µm, and $d = 30$ µm. The lithography process is designed for a resulting structure thickness of 40 µm.
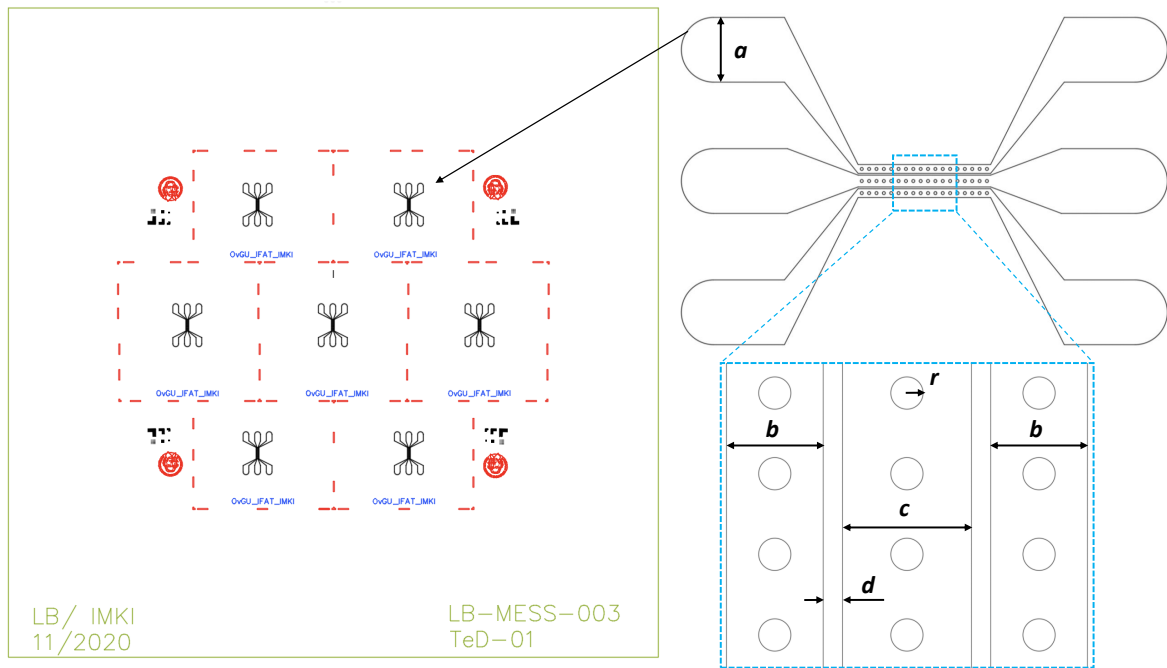
Figure 3.3: Technical drawing of the second-generation mask of ImmunoChip for soft lithography, designed in AutoCAD®, Autodesk Inc. Sketch includes seven identical structures, where a is a width of the inlet and outlet ports of the channels, b is a width of the side channels, c is a width of the middle channel, d is a distance between channel structures reserved for the femtosecond laser structuring of the smaller interconnecting channels, and r is a radius of the circular pillar for mechanical stability.

Table 3.3: Materials for ImmunoChip master mold fabrication by soft lithography.

Amount	Material	Specifications
40	4″ Glass-Wafer with ZnO	DSP, 100 mm, 325 µm thick, Borofloat
4 ml/wafer	SU-8-25	Negative photoresist
On-demand	N_2, Aceton, Isopropanol	Process supportive chemicals and gases
200 ml/wafer	mr-Dev600	Developer

Table 3.4 describes the process parameters for ImmunoChip master mold fabrication. To improve the exposure step, a layer of ZnO nanoparticles has to be spin-coated on the bottom side of the glass wafer. Therefore, ZnO nanoparticles of a size $\leq 50\,\text{nm}$ (Merck KGaA, Germany) were mixed with toluene in the ultrasound bath [88]. Once homogeneous mixing was achieved, $1\,\text{ml}$ of the solution was pipetted on the glass wafer and spin-coated at $3000\,\text{rpm}$ for $30\,\text{s}$. Next, the wafer with the spin-coated ZnO layer was heated to $180\,°\text{C}$ on a hot plate for $10\,\text{min}$. The procedure was repeated four times.

Table 3.4: Process parameters for ImmunoChip master mold fabrication by soft lithography.

Step	Name	Description
1.	Wafer preparation	Wafers dehydration on a hot plate at $200\,°\text{C}$, $5\,\text{min}$
2.	SU-8 Spin-coating on a Glass Wafer (GW)	$500\,\text{rpm}$ - $10\,\text{s}$ $1000\,\text{rpm}$ - $6\,\text{s}$ - photoresist dispensing $4\,\text{ml}$ SU-8 $1600\,\text{rpm}$ - $30\,\text{s}$ - thickness adjustment Acceleration: $300\,\text{rpm}$ Intermediate step $30\,\text{min}$ room temperature
3.	Soft Bake	$65\,°\text{C}$ - $5\,\text{min}$, $85\,°\text{C}$ - $15\,\text{min}$
4.	Edge Bead Cleaning (EBR)	Removing the edge of the thin film: $3000\,\text{rpm}$ - $5\,\text{s}$ $3000\,\text{rpm}$ - $20\,\text{s}$ developer dispensing Repeating these steps 3 times $10\,\text{min}$ evaporation time
5.	Exposure	Exposure dose SW: $220\,\text{mJ/cm}^2$ Mask: LB-MESS-002 Time: $24\,\text{s}$; Alignment Gap: $150\,\text{µm}$; Exposure type: soft; WEC type: cont; WEC Offs: Off
6.	PEB	$2\,\text{min}$ at $65\,°\text{C}$; $10\,\text{min}$ at $95\,°\text{C}$; slow cooling
7.	Development	In mr-Dev600 ($6\,\text{min}$) Rinsing in Isopropanol ($2\,\text{min}$)

The next fabrication step is multiphoton polymerization-based 3D laser lithography (3DLL) using the "Laser Nanofactory" (Femtika Ltd., Vilnius, Lithuania) setup with the femtosecond laser "Carbide" (by Light Conversion). By means of 3DLL, structures that are perpendicular to the pre-structured microfluidic channels are developed. The printing has to be performed through the glass wafer to avoid shadowing by the $40\,\text{µm}$ high channels. Therefore, the wafer was turned structured-side down, and femtosecond-laser direct writing (or 3DLL) was implemented, as is schematically shown in Figure 3.4. The materials utilized (Table 3.5) and process parameters (Table 3.6) are listed in the following tables.

Table 3.5: Materials for ImmunoChip master mold fabrication by 3DLL or femtosecond laser structuring.

Amount	Material	Specifications
5	Pre-structured 4″ Glass-Wafer (PGW)	DSP, 100 mm, 325 µm thickness, Borofloat
0.5 ml/wafer	Photo-polymer SZ20280 with photo-initiator Irgacure 369	Negative photoresist
On-demand	N$_2$, Aceton, Isopropanol	Process supportive chemicals and gases
100 ml/wafer	2-propanol, 4-methyl-2-pentanone and acetone	Developers

Table 3.6: 3DLL or femtosecond laser structuring parameters for ImmunoChip master mold fabrication.

Step	Name	Description
1.	Wafer preparation	Wafers are pre-structured by soft-lithography process
2.	Applying photo-reactive polymer	0.5 ml by the pipet in the center of the prepared SU-8 structures; Intermediate step - 15 min
3.	Soft Bake	2 hours at 50 °C on a hot plate
4.	3DLL	Turn the wafer upside down Femtosecond laser Operation at the second harmonic (λ=515 nm) Power: 10 mW Pulse duration: 250 fs Repetition rate: 20 20 × 0.8 NA objective lens by Zeiss
5.	Development	Development in methyl isobutyl ketone with continuous stirring

In order to realize such a production pipeline, a special procedure has to be followed. First, a drop of pre-polymer material is cast on a lithographically-made master. In the case of this study, this was a hybrid organic-inorganic photopolymer SZ2080 [89]. The sample is subsequently heated at 50 °C for 2 hours. During this process, SZ2080 condenses and becomes a hard gel. Laser exposure follows. The setup used was Laser Nanofactory by Femtika. Detailed description of the setup is available in the literature published by the vendor [90]. For focusing, a 20 × 0.8 NA objective lens by Zeiss was employed. Upon fabrication, the sample was submerged into methyl isobutyl ketone developer to reveal the integrated features.
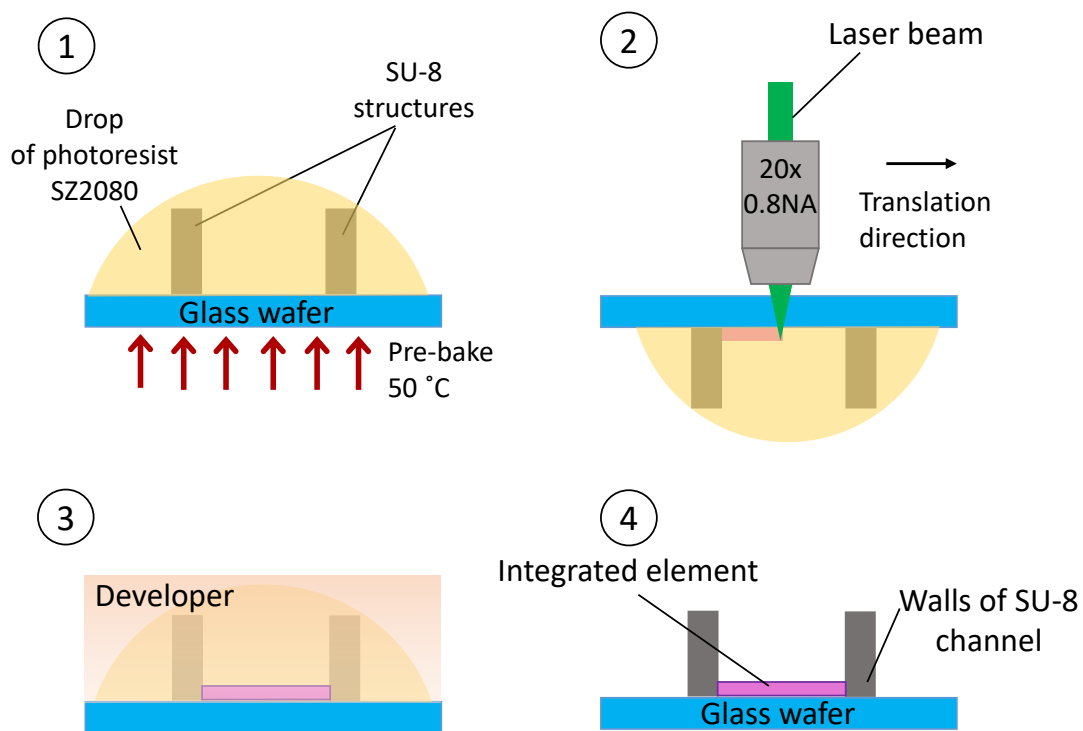
Figure 3.4: Technological steps during component integration in already existing structure using 3DLL. (1) sample preparation, when SZ2080 is drop-casted on the existing structure and pre-baked at 50 °C for 2 hours; (2) writing process. Note that the sample is turned upside-down to allow easier focusing with a laser beam. This is possible because SZ2080 is ahard gel after pre-bake; (3) development, during which unaffected pre-polymer is removed; (4) final structure.

3.1.3 Master mold for LabyrinthChip

A third master mold was fabricated for the Chlamydomonas microfluidic chip using the soft lithography process with optimized parameters. Materials utilized in mold fabrication are listed in Table 3.7 and the main process steps with parameters are given in Table 3.8.

Table 3.7: Materials for LabyrinthChip master mold fabrication by soft lithography.

Amount	Material	Specifications
20	4″ Silicon Wafer (SW)	DSP, 100 mm, 525 µm thickness
4 ml/wafer	SU-8-25	Negative photoresist
On-demand	N_2, Aceton, Isopropanol	Process supportive chemicals and gases
200 ml/wafer	mr-Dev600	Developer

Table 3.8: Soft lithography process parameters for LabyrinthChip master mold.

Step	Name	Description
1.	Wafer preparation	Wafers dehydration on a hot plate at $200\,°C$, $5\,min$
2.	SU-8 Spin-coating on SW	$500\,rpm - 10\,s$ $1000\,rpm - 6\,s$ – photoresist dispensing $4\,ml$ SU-8 $2000\,rpm - 30\,s$ – thickness adjustment Acceleration $300\,rpm$ Intermediate step $30\,min$ room temp
3.	Soft Bake	$65\,°C$ - $3\,min$, $85\,°C$ - $5\,min$
4.	Edge Bead Cleaning (EBR)	Removing the edge of the thin film: 3000 rpm $- 5$ s 3000 rpm $- 20$ s developer dispensing Repeating these steps 3 times 10 min evaporation time
5.	Exposure	Exposure dose SW: $160\,mJ/cm^2$ Mask: MEMS-LB-002 Time: $16.1\,s$ Alignment Gap: $150\,µm$ Exposure type: soft WEC type: contact; WEC Offset: Off
6.	PEB	$2\,minutes$ at $65\,°C$; $5\,minutes$ at $95\,°C$ slow cooling
7.	Development	In mr-Dev600 ($1\,hour\ 35\,minutes$) Rinsing in Isopropanol ($2\,min$)

The master mold for LabyrinthChip was designed using AutoCAD® (Autodesk Inc.). This design was used in lithography shadow mask production. Figure 3.5 shows the schematic of the master mold and dimensions, where $w = 20\,µm$, $l = 80\,µm$, $a = 40\,µm$ and $r = 10\,µm$. The varied parameters are the distance between the prolonged pillars $b_1 = 40\,µm$, $b_2 = 20\,µm$ and distance between the centers of circular pillars $d_1 = 80\,µm$ and $d_2 = 60\,µm$.

The time and temperature for Soft Bake of the LabrynthChip master mold were significantly reduced to ensure the complete development of the cylindrical parts of the structure. Furthermore, before spin-coating of the photoresist, the silicon wafer was pre-cleaned with KOH solution to improve the adhesion force.
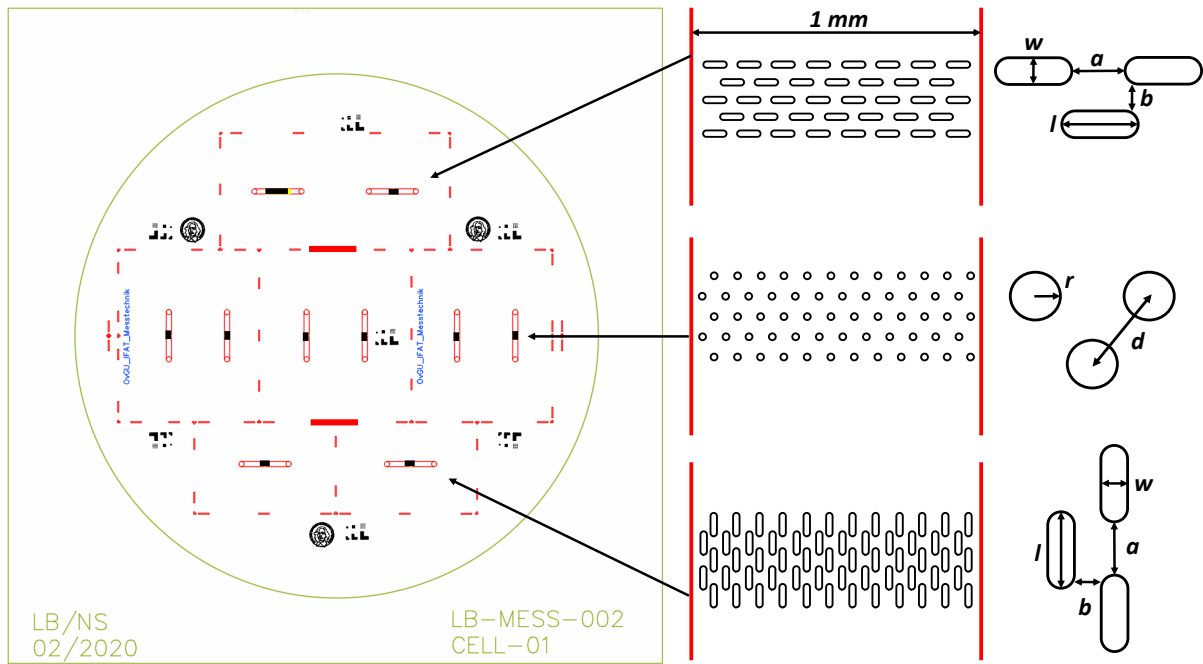
Figure 3.5: Technical drawing of the second-generation mask for soft lithography, designed in AutoCAD®, Autodesk Inc. Sketch includes 10 channels with various geometries of labyrinths (shown left), where w is a pillars' width, l - length, a and b is a distance between prolonged pillars, r is a radius of the circular pillar and d is a distance between the centers of circular pillars.

3.2 PDMS mixing and molding

Commercially available Polydimethylsiloxane is provided as a highly viscous liquid (5100 cP) in two components (DOW Silgard 184): Silicone base and curing agent. The standard mixing ratio is 10:1, respectively. As described in Chapter 2.1, PDMS properties are highly dependent upon the mixing and curing procedure. In this work, PDMS was mixed with the ratio 10:1 for the Stomach-on-chip application and microfluidic chip for single-cell analysis (Chlamydomonas). For the ImmunoChip, the mixing ratio was 20:1 Silicone base to curing agent. Every time the combination was mixed continuously with a magnetic stirrer for over 20 minutes and then poured on the fabricated master mold (Figure 3.6).

Once the material was properly mixed, 10 ml of the solution was poured on the prepared 4″ master mold. This volume of liquid PDMS stays solely on the wafer, and the resulting thickness of the replica is 1 mm. For the Stomach-on-Chip application, the top replica for the microfluidic chip is 3 mm thick, and, therefore, 40 ml of PDMS was poured on a master mold that had been placed Petri dish. The silicon wafer was attached to the plastic dish with a water-soluble wax to prevent the elevation of the wafer to the surface of PDMS.

The wafer with liquid PDMS has to be protected from dust and laid in a level planar position. Gas bubbles generated during mixing move from the bulk to the surface and vanish naturally if obstacles in their way are absent. Furthermore, higher curing temperature
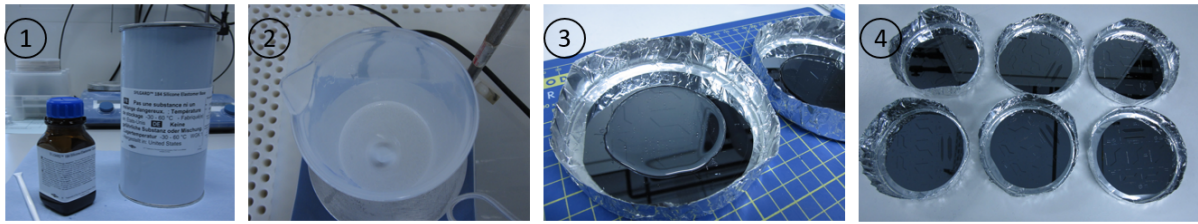
Figure 3.6: Detailed description of the mixing and molding process. Photo (1) shows two PDMS components - silicone base and curing agent, which are mixed with a magnetic stirrer (2), prepared solution poured on the master molds (3) and subsequently cured (4).

reduces process time, and polymer chains connect faster. This reduces the possibility for the natural elimination of the bubbles. In this work, different temperature conditions were tested to speed up the PDMS curing and, simultaneously, to avoid the presence of air defects and to provide the suitable mechanical properties of the material. The regimes are provided in Table 3.9. PDMS layers, poured on master molds for three applications described in this work, were cured at low and room temperatures. Moreover, the liquid PDMS adhesive layers were cured at 100 degrees Celsius for 1 hour.

Table 3.9: Technological approaches and parameters of the PDMS curing process.

Temp (°C)	Time (h)	Necessary conditions	Resulting quality
20	48	Air atmosphere	Material is fully cured, no air bubbles
40	6	Hot plate/oven, air atmosphere or vacuum	Material is fully cured, no air bubbles
60	2	Oven and vacuum	Material is fully cured, air bubbles at μ-structures
80	1.5	Oven and vacuum	Material is fully cured, air bubbles at μ-structures
100	1	Oven and vacuum	Material is fully cured, air bubbles are present, especially at μ-structures

Once PDMS layers are completely cured (crosslinked) on the master mold, they are peeled off and cut. Inlet and outlet holes are punched with 1 mm biopsy punch and prepared parts can be bonded.

3.3 Bonding

Prepared PDMS replicas have to be activated with oxygen plasma to ensure covalent bonding to a glass substrate or other PDMS layer [91–94]. In the case of ImmunoChip and LabyrinthChip, the bottom layer is a microscopy glass slide with a thickness of 0.170 mm ± 0.005 mm (Paul Marienfeld GmbH & Co. KG). The technological steps to fabricate a microfluidic chip for cell culture are listed in Table 3.10.

Table 3.10: Bonding process steps and parameters for Stomach-on-Chip.

Step	Name	Description
1.	Plasma treatment	Bottom replicas 1 minute at 0.5 mbar oxygen atmosphere
2.	Applying adhesive layer	Liquid PDMS (10:1) applied on the plasma treated surface by the "doctor-blade" technique around, but not in the channel area
3.	Plasma treatment	Polyester membrane 20 seconds at 0.5 mbar oxygen atmosphere
4.	Placing the membrane	Plasma treated side onto the replica with applied adhesive layer
5.	Intermediate step	Stack has to be placed on the planar surface for 10 minutes
6.	Plasma treatment	Stack PDMS/Adhesive/Membrane 20 seconds at 0.5 mbar oxygen atmosphere
7.	Applying adhesive layer	Liquid PDMS (10:1) applied by "doctor-blade" technique on plasma treated surface around, but not in the channel area
8.	Intermediate step	PDMS/Adhesive/Membrane/Adhesive Stack has to be placed on the planar surface for 10 minutes
9.	Cross-linking	PDMS/Adhesive/Membrane/Adhesive Stack on the hot plate for 1 hour at 100 °C
10.	Plasma treatment	PDMS/Adhesive/Membrane/Adhesive Stack and top replica 1 min at 0.5 mbar oxygen atmosphere
11.	Alignment	PDMS/Adhesive/Membrane/Adhesive Stack and top replica matching the top and bottom microfluidic channels bring two parts into a contact
12.	Bonding	PDMS/Adhesive/Membrane/Adhesive/PDMS Stack on a hot plate 10 min at 80 °C passive cooling

PDMS replicas and glass slides were treated with the oxygen plasma for 1 minute at a pressure of 0.5 mbar in a plasma oven (ThermoFisher Scientific, International). Next, they were brought into contact and placed on the hot plate. The bonding process lasted for

10 minutes at 80 °C. After the microfluidic chips were removed from the hot plate, they were passively cooled and filled with DI water. The microfluidic chip for Stomach-on-Chip application consists of two mirrored PDMS replicas (1 mm and 3 mm thick) and a polyester membrane (Sterlitech Inc., USA). The inlet and outlet openings were punched only in the thick top PDMS replica.

3.4 Femtosecond laser structuring of the membrane in microfluidic channel

The microfluidic structure technology for Organ-on-Chip applications described in the previous sections utilized commercially available polyester filters. To create different pore geometries and higher porosity, one can obtain a membrane with nano-resolution by femtosecond laser direct writing [95]. Therefore, as schematically described in Figure 3.7, the listed technological steps have to be accomplished.
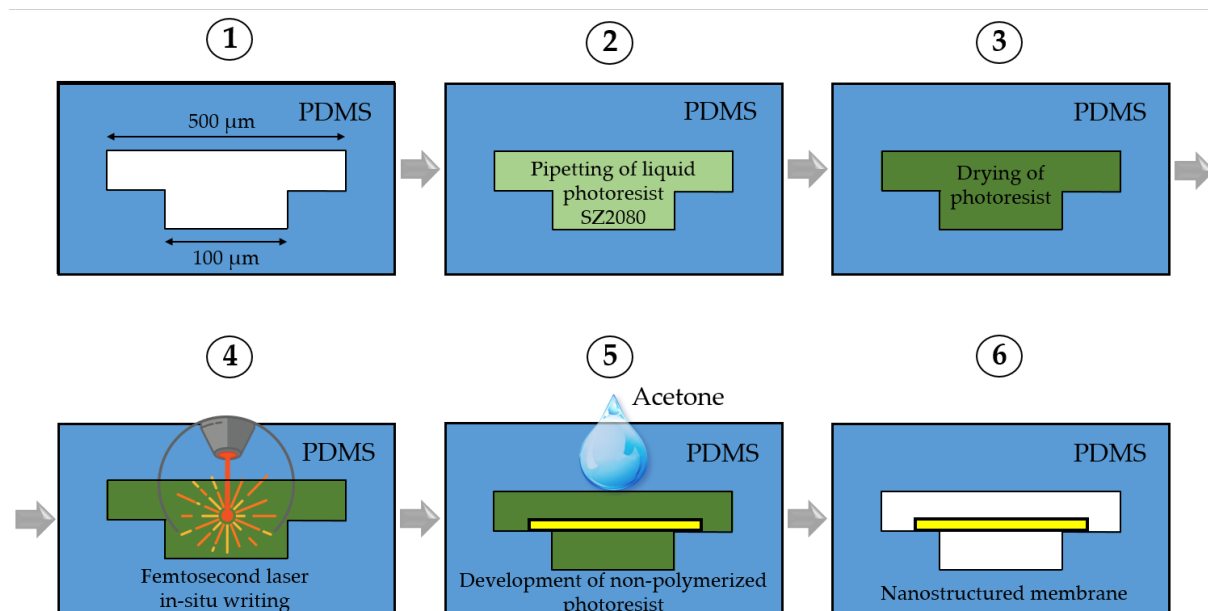
Figure 3.7: Schematic view on the process steps of the membrane structuring in microfluidic channel by femtosecond laser. 1 - microfluidic chip preparation; 2 - pipetting of liquid photoresist in the chip; 3 - Soft Bake of the polymer on a hot plate; 4 - femtosecond laser direct writing in the closed microfluidic structure; 5 - development of the non-polymerized photoresist; 6 - chip is washed with the cell culture medium and is ready to use [25].

Following the procedure shown in the figure, a microfluidic chip was prepared from two replicas, one with 500 μm channel width and the second - with 100 μm. Thus, an artificial stair was created, to which the sides of the membrane are attached. Fabrication technology of the master mold and PDMS-based chip is reported in Chapters 3.1.1, 3.2, 3.3.

Photoresist SZ2080 with photoinitiator Irgacure 369 (developed by IESL—FORTH, Heraklion, Crete, Greece) was pipetted into the channel. Once an homogeneous channel filling was accomplished, the sample was placed on a hot plate and heated to $50\,^\circ$C for 45 min. The photoresist drying time was optimal to avoid creation of air bubbles due to the material shrinkage and to prevent any liquidized phases. Once the third step was completed and the photoresist was completely dried, micro-structuring was performed by a 3DLL technique using the "Laser Nanofactory" (Femtika Ltd.,Vilnius, Lithuania) with femtosecond laser "Carbide" (by Light Conversion) setup [95]. The laser operation was at the second harmonic ($\lambda = 515\,$nm), with the power in the range from 0.1 to 10 mW, and a 250 fs pulse duration. In this work, lenses of $20 \times 0.4\,$NA (1.5 mm focusing distance, Olympus, Tokyo, Japan) and $20 \times 1.4\,$NA (0.32 mm focusing distance, Carl Zeiss AG, Jena, Germany) were tested. The membrane was configured as a pattern of 2.5 µm wide wires with a distance of 1.5 µm in between.

The subsequent step is development. To remove the non-polymerized residuals of the material, three developers were used: 2-propanol, 4-methyl-2-pentanone (24 h by continuous stirring), and acetone (8 h with continuous stirring). After the development, chips with the membranes were dried and washed with the cell culture medium. Samples were analysed by optical microscope (Olympus IX 73, Tokyo, Japan) and confocal microscope (SP8 Confocal Laser Scanning, Leica GmbH).

3.5 Cell culture and analysis

As a proof of concept for the Stomach-on-Chip application, NCI-N87 gastric cancer cells were cultured in a microfluidic channel. First, the microfluidic chip was sterilized by an autoclave. Next, collagen solution was prepared (50 µg/ml in 0.02 % acetic acid), pipetted into microchannels and incubated at $37\,^\circ$C for 1 hour. Then, chips were perfused with the cell culture medium (RPMI 1640 medium supplemented with 10 % FCS and 1 % penicillin-streptomycin). Next, NCI-N87 cells were seeded into the channel with the density of 1800 cells/mm^2. Pumping (MFCS-EZ, Fluigent GmbH, Germany) of the medium at 0.5 µl min was adjusted after 6 hours, when cells have proliferated on the membrane. Permeability was measured by the FITC-dextran fluorescent component, which was added to the medium by pumping through the top channel. The medium was collected at the outlets and measured by the spectrofluorometer with an emission wavelength of 520 nm. When the confluent layer was grown, gastric monolayer on-a-chip was exposed from the basolateral side to a chemotherapeutic drug (CPT) contained in the medium (20 µM). Fluorescence read-out was performed by fluorescence microscopes (Keyence Deutschland GmbH, Germany) and IncuCyte (Essen Bioscience GmbH, Germany) [96]. Experiments were performed at the Institute of Experimental Internal Medicine, Medical Faculty, OvGU Magdeburg.

As a proof of concept for the ImmunoChip application, activated IP macrophages were introduced into the inner channel, while fluorescently marked T cells were filled into both outer channels. In order to monitor T cell movement and location, $CD4^+$ T cells were stained with CellTracker Deep Red (CTDR, purple). Fluorescent staining Fluo-4 was also used to measure the calcium influx and activation (green). Analysis was performed with the Keyence fluorescence microscope (Keyence Deutschland GmbH, Germany). The chemokine CXCL9 was added to the inner channel to facilitate T cell migration and attract $CD4^+$ T cells chemotactically. Experiments were conducted at the Institute for Molecular and Clinical Immunology, Medical Faculty, OvGU Magdeburg.

LabyrinthChip investigated the motion of the Chlamydomonas reinhardtii of the strain SAG11-32a, which were purchased from the culture collection of algae at Goettingen University, Germany. Algal suspensions were then centrifuged at $1000\,g$ for 10 minutes, and the supernatant was discarded. The cells were subsequently re-suspended in a fresh TAP medium and loaded into PDMS channels using a pipette. These channels were sealed at the inlet with grease and placed in water under the same lamp used for cell culturing for several hours. Next, channels were incubated overnight before use. In some instances, the light-switchable adhesion property of Chlamydomonas reinhardtii was utilized to create concentration gradients. Local blue light generated by a halogen lamp with a filter ($\lambda = 480\,\text{nm}$) was applied. Red LED illumination ($\lambda = 628\,\text{nm}$) was used to maintain cell motility throughout the microchannel. Cells that reached the blue spot often transitioned to an adhered state. This condition was maintained for approximately one hour to accumulate adhered cells in the blue spot.

Following this, the red ambient illumination was turned off, and global blue illumination was applied for around 10 minutes using a cold light source (KL2500LCD, Schott AG, Germany) and a blue bandpass filter ($\lambda = 513\,\text{nm}$). This triggered global cell adhesion. While total adhesion was not achieved, a significant gradient of adhered cell concentration was established. The cells reverted to the swimming state after the illumination conditions were switched back to red ambient light and red observation illumination. Videos of Chlamydomonas reinhardtii motion in the patterned microchannels were recorded using an inverted microscope Zeiss (Axio Observer D1, Carl Zeiss AG, Germany), which was equipped with a Canon EOS M6 Mark II (Canon Deutschland GmbH, Germany) digital camera. The analysis and tracking were executed using the Trackmate plugin within Fiji (ImageJ). This involved employing a Laplacian of Gaussians filter for edge detection and a Kalman tracker for trajectory extraction [97]. Experiments were performed at the Department of Nonlinear Phenomena, Faculty of Natural Sciences, OvGU Magdeburg.

3.6 Sensor Integration Technology

Integration of sensors and/or actuators into the Organ-on-Chip structure requires adjustments to the chip fabrication process. The adapted fabrication technology is specified in the following sections.

3.6.1 Integration of the sensor for *in-situ* oxygen concentration measurements

A commercially available oxygen sensor spot SP-PSt3-NAU (PreSense GmbH), which is 40 µm thick and 1 mm in diameter, can be integrated into the microfluidic chip during the molding procedure. Therefore, the self-adhesive disk was attached to the master mold at the channel area. Next, liquid PDMS was poured onto the silicon wafer with photoresist structures and a sensor. After the curing process, which is described in Section 3.2, the following fabrication steps can be done, as described in Section 3.3. The schematic description of the technological steps for oxygen sensor integration is shown in Figure 3.8.
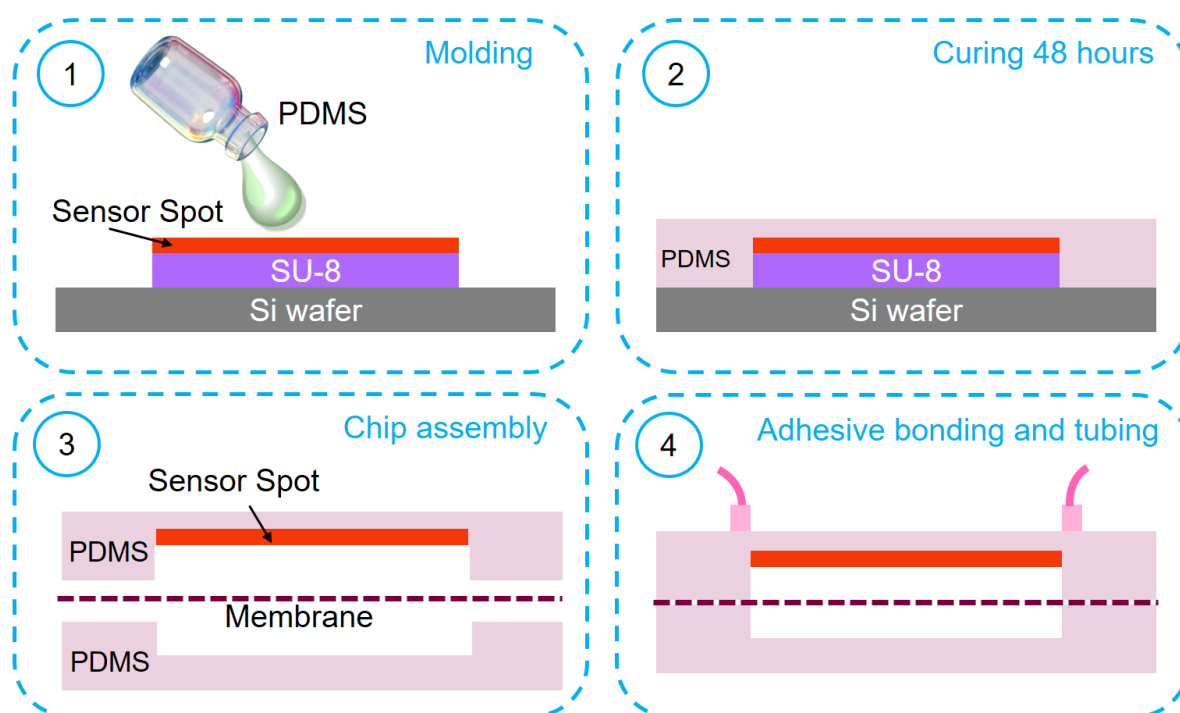
Figure 3.8: Schematic description of the process to embed a luminescence sensor in a microfluidic structure. 1 - Pouring liquid PDMS on structured master mold with PreSense Sensor Spot on it; 2 - Curing; 3 - Releasing, cut of the PDMS layer and chip assembly; 4 - Adhesive bonding with liquid PDMS.

During the plasma treatment, the sensor spot was covered with plastic foil to avoid any influence from the plasma on the material. The PreSens wireless read-out system was utilized for measurements [98] in a beaker and in microfluidic chips with and without a polyester membrane.

Three liquids were tested in these setups: DI water, cell culture medium and medium with additional serum. All of the liquids in the chips were tested under flow conditions. Pumping was enabled by a pressure-driven pump (Fluigent GmbH) with a flow rate of $0.5\,\mu l/min$. Every measurement was performed for 30 seconds with a 1-second step.

Reference measurements were performed with the optical oxygen sensor FireStingO$_2$, manufactured by PyroScience GmbH. Measurements were conducted in a beaker with DI water and cell culture medium.

The PreSens luminescence sensor was calibrated using the software procedure integrated into the readout system. Therefore, the first measurements were done in the oxygen-free liquid (sodium sulfite solution) to set the 0 concentration. Calibration measurement lasted for 3 minutes.

3.6.2 Integration of electrodes for TEER measurements

The chip configuration was modified to integrate electrodes for transepithelial electrical resistance (TEER) measurements in the microfluidic chip for cell culturing, and the number of component layers increased from three (Section 3.3) to five. Instead of molding technology, stamp cutting of the PDMS layers was used. The resulting chip consists of the following layers:

- Layer 1 - 1 mm thick planar PDMS with Cr/Au electrode (Figure 3.9);

- Layer 2 - 100 µm thick PDMS with a stamp cut 1 mm wide opening;

- Layer 3 - Polyester membrane (13 mm diameter and 3 µm pore size);

- Layer 4 - 100 µm thick PDMS with a stamp cut 1 mm wide opening;

- Layer 5 - 1 mm thick planar PDMS with Cr/Au electrode (Figure 3.9).

To fabricate layers 1 and 5, a blank silicon wafer was used as a carrier, on which 10 ml of PDMS was poured and cured. Curing lasted 48 hours at room temperature. Once the material was cross-linked entirely, it was released and cut into a piece of $3 \times 4\,cm^2$. Next, the rectangles were placed on the polycarbonate foil and were oxygen plasma treated for 1 minute. Then, samples with the shadow masks were directly placed in the magnetron sputtering chamber with two targets: Chromium and Gold. Once high vacuum of 5×10^{-7} bar was reached, interval metal deposition occurred. Every deposition step lasted 30 seconds, with 5 minutes of cooling in between. The sputtering rates of Chromium and gold are 50 nm/min (RF 400 W) and 110 nm/min (DC 200 W), respectively. After the metal deposition, the shadow mask was carefully removed, and the next steps for chip assembly were implemented. The fabrication technology of layers 1 and 5 are shown in Figure 3.9.
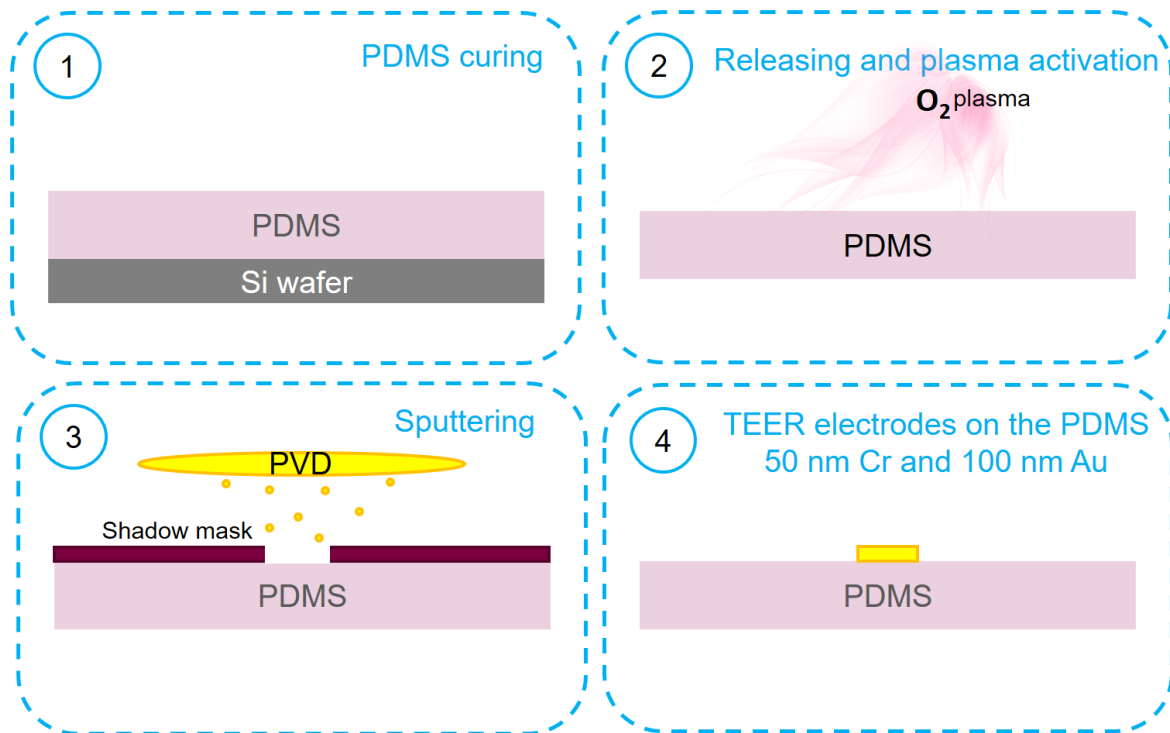
Figure 3.9: Schematic representation of the technology process for fabricating transepithelial resistance Electrodes on PDMS. 1 - Preparation of the PDMS planar layer; 2 - Removing the PDMS layer from the silicon wafer and oxygen plasma treatment of the surface; 3 - Magnetron metal deposition through the shadow mask; 4 - Obtained PDMS layer with 150 nm thick electrode.

To fabricate layers 2 and 4, a stamp-knife was designed and developed. The geometry of the desired structure was identical to the photolithographical one, described in Section 3.1.1, i.e. S-shaped 1 mm wide with a 1 cm long middle part. PDMS was prepared with a mixing ratio of 10:1 (base and curing agent, respectively) and spin-coated on the $4''$ silicon wafer. After 2 hours of curing in the oven in a vacuum (Figure 3.9), the layers were removed from the wafer, placed on the plastic foil, and cut with the stamp-knife. Once all layers were prepared, the process steps described in the Table 3.11 were implemented.

The resistance between two electrodes was measured using the Volt-Ohm Meter EVOM Manual (World Precision Instruments, USA). Blank resistance R_{blank} was measured in the chip filled with the cell culture medium. The measured value was multiplied by the membranes' area, which is $0.1\,cm^2$.

The resistance of the cell layer was calculated as $R_{tissue} = R_{measured}$ - R_{blank}. To report the data in common TEER units, R_{tissue} was multiplied by the membrane effective area: $TEER_{reported} = R_{tissue} \cdot A_{membrane}$ [99]. Measurements were performed at the room temperature.

Table 3.11: Assembly steps of a microfluidic device with electrodes for TEER measurements in Organ-on-Chip application.

Step	Name	Description
1.	Plasma treatment	Layers 1, 2 and 4, 5 1 minute at 0.5 mbar oxygen atmosphere
2.	Bonding	Bring into a contact layer 1 with 2 and 4 with 5 Place on the hot plate, 10 minutes at 80 °C
3.	Plasma treatment	Stack of layers 1+2 1 minute at 0.5 mbar oxygen atmosphere
4.	Applying adhesive layer	Liquid PDMS (10:1) applied by the "doctor-blade" technique on the plasma treated surface around, but not in the channel area
5.	Plasma treatment	Polyester membrane 20 seconds at 0.5 mbar oxygen atmosphere
6.	Placing the membrane	Plasma treated side onto the stack 1+2 with applied adhesive layer
7.	Intermediate step	Stack has to be placed on the planar surface for 10 minutes
8.	Plasma treatment	Stack 1+2 with membrane 20 seconds at 0.5 mbar oxygen atmosphere
9.	Applying adhesive layer	Liquid PDMS (10:1) applied on the plasma treated surface of the membrane by the "doctor-blade" technique around, but not in the channel area
10.	Intermediate step	Stack 1+2 with membrane has to be placed on the planar surface for 10 minutes
11.	Cross-linking	Stack on the hot plate for 1 hour at 100 °C
12.	Plasma treatment	Stack 1+2 with membrane and stack 4+5 1 minute at 0.5 mbar oxygen atmosphere
13.	Alignment	Stack 1+2 with membrane and stack 4+5 matching the top and bottom microfluidic channels and TEER electrodes bring two parts into a contact
14.	Bonding	Stack of 5 layers on the hot plate 10 minutes at 80 °C; passive cooling

3.6.3 Integration of the meander-shaped thermo-electric element on a thin PDMS membrane

A meander-shaped thermo-electric element can be used as an actuator or as a temperature sensor. This study involves various samples with distinct characteristics, including different PDMS thicknesses (20 µm and 40 µm), PDMS mixing ratios (10:1 for soft and 10:4 for hard), and meander lengths (29 mm for short and 48 mm for long).

Figure 3.10 provides a detailed schematic description of the developed technology.
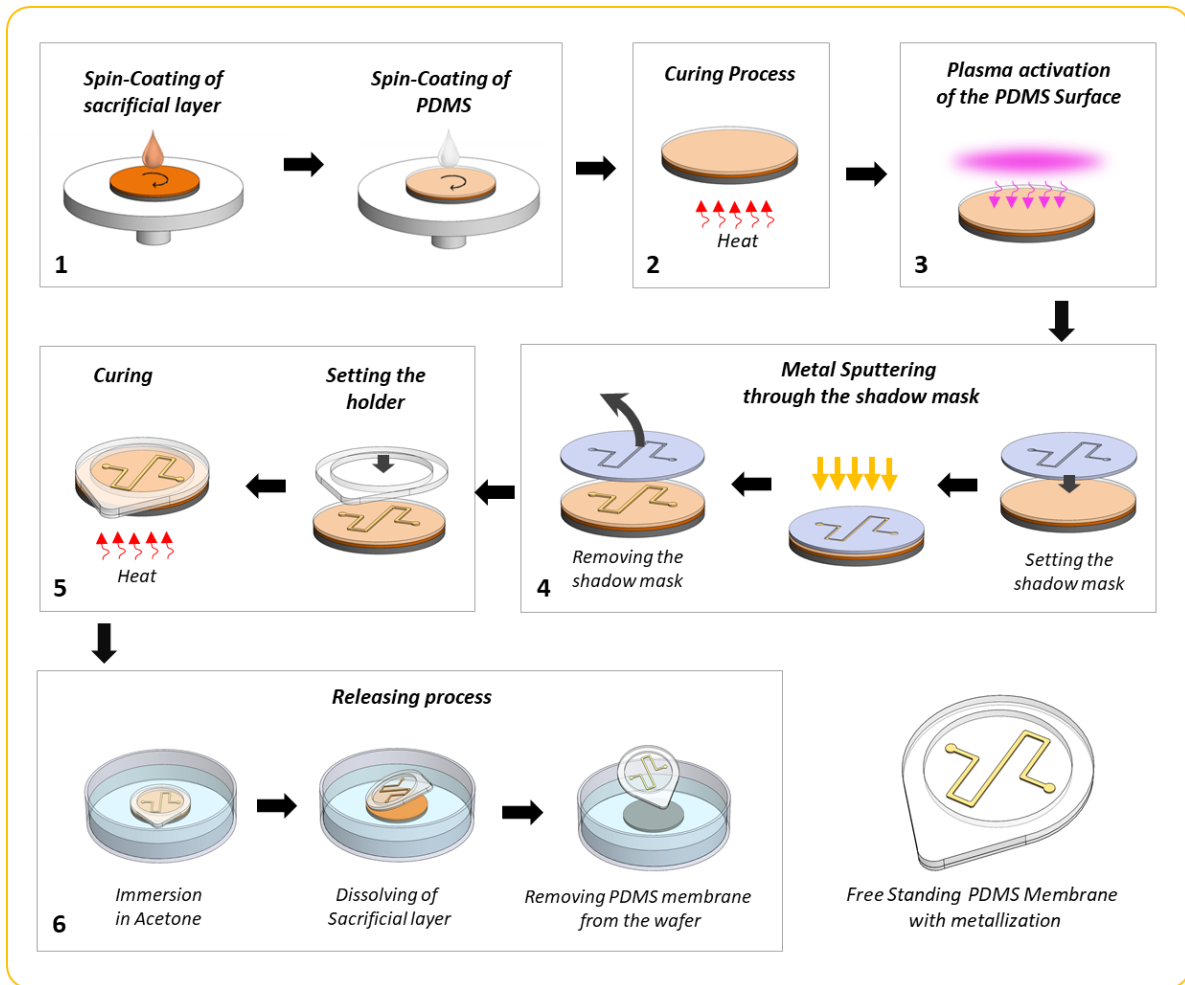
Figure 3.10: The schematic description of the fabrication process for a thermo-electric
meander-shaped element on a thin freestanding PDMS membrane is as follows:
1) sacrificial layer of photoresist is applied by spin coating. Following this, a
layer of PDMS is spin-coated onto the sacrificial layer. 2) The assembly is
then subjected to a curing process in an oven. 3) After curing, the layers are
treated with oxygen plasma to prepare the surface. 4) Metal sputtering is
performed through a shadow mask to create the desired pattern. 5) A ring
holder is attached, and the entire structure is cured in the oven at 60 °C for
3 hours. 6) Finally, the thin freestanding PDMS membrane is released by
rinsing it in acetone, which dissolves the sacrificial layer, leaving the completed
thermo-electric meander-shaped element [100].

To fabricate thin freestanding PDMS membranes, 1 inch silicon wafers were used as
substrates. The process for fabricating these membranes involved several steps, which are
schematically represented in Figure 3.10. Initially, all wafers were thoroughly cleaned by
rinsing them in isopropanol and subsequently dehydrated at 200 °C for 5 min. Next, a
sacrificial layer made of photoresist AZ 1512 (Microchemicals GmbH) was applied.

This sacrificial layer enabled the subsequent release of the PDMS membrane by immersion in acetone. The photoresist was spin-coated onto the wafers using a spin coater (POLOS Spin150i) at 2000 rpm for 20 s to achieve a 2.5 μm thick coating. The coated wafers were then subjected to a soft-bake on a hot plate at 100 °C for 1 min. These silicon substrates with their sacrificial layers served as the foundation for fabrication of all the subsequent samples in this study.

To obtain the PDMS membrane, a solution of PDMS base-polymer (DOW Sylgard 184) with a curing agent was prepared, with mixing ratios of 10:1 and 10:4 (w/w) (base:curing agent). The higher concentration of the curing agent results in a harder material. The solution was spin-coated onto the sacrificial layer, and spin-coating parameters, such as rotation speed and time, were adjusted to achieve PDMS membranes with thicknesses of 20 μm and 40 μm. The thickness of the PDMS layer was measured using a spectrophotometer (Filmmetrix, Inc. F20e-UVX), and the samples were then cured in an oven at 60 °C for two hours.

After curing, the PDMS layers were treated with oxygen plasma using specific parameters (20 s at 70 % power and 0.5 bar gas pressure) with a ThermoFisher Scientific system.

Metallization of the PDMS membrane surface was carried out using magnetron sputtering of Chromium (Cr) and Gold (Au) through a shadow mask. The shadow mask, with a meander-shaped opening, was laser-cut from 300 μm thick magnetic steel and positioned on the sample, held in place by a magnet at the bottom side of the silicon wafer. The metal deposition process involved 14 steps: 2 steps for Chromium at 30 W (100 mA) and 12 steps for Gold at 60 W (100 mA). Argon gas was used as the process gas, and the chamber pressure was maintained at 3.5×10^{-3} bar. Chromium was employed as an adhesive layer.

To handle and release the thin membranes, PDMS-ring holders were fabricated. A 1 mm thick PDMS layer was cured on a 4″ silicon wafer, released, and cut into a circular shape with an inner diameter (ID) of 2 cm and an outer diameter (OD) of 2.7 cm. A small amount of liquid PDMS was applied to the ring holders, which were then placed on the cured membranes and baked in the oven for 1 hour at 60 °C. Finally, the sacrificial photoresist layer (AZ 1512) was removed by immersion in acetone and then rinsing for 1 minute. This process resulted in a freestanding PDMS membrane with the desired meander-shaped metal structure. The ring holder, while serving as support during fabrication, can be cut off if the ultra-thin PDMS membrane is applied to other systems, such as Lab-on-Chip structures.

Measurements and analysis of the meander wires on PDMS membranes were conducted in two configurations: (1) while the layers were still on the silicon wafer and (2) after their release. The characterization was performed using a Teflon block specially designed with a built-in cavity for holding samples and with gold pin contacts (Figure 3.11).
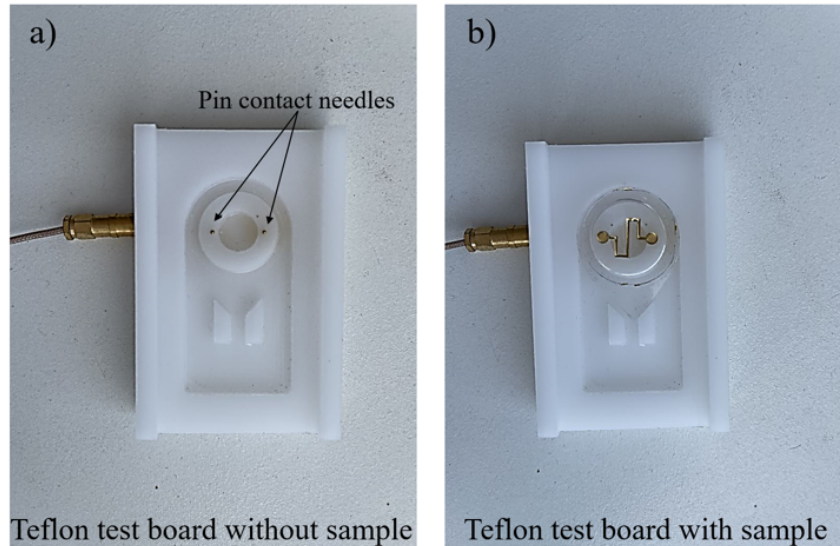
Figure 3.11: Photographs of the Teflon test board for resistance and temperature measurements (a) without sample on it and (b) with sample on it [100].

During the measurements, the sample was positioned on top of spring-pin contacts, ensuring soft mechanical contact with the meanders' contact pads. The resistance of the meanders was determined by applying a current ranging from 20 mA to 180 mA in steps of 20 mA, while recording the corresponding voltage values.

Theoretical resistance values of the modeled and CAD-plotted meanders were calculated based on Pouillet's law, assuming a planar wire without wrinkles. Concurrently, temperature measurements were carried out using a portable infrared camera Hti-Xintai HT-A1 (Dongguan Xintai Instrument Co.,Ltd, China) at 10 seconds after the current was applied in order to achieve thermal equilibrium with the environment.

Surface analysis and wire deformation characterization were conducted using optical microscopy (Keyence VHX – 500F). To assess surface roughness and metal thickness, a 3D profilometer (Keyence Corp., 3D-Profilometer VR-6000) was employed. The adhesion force between the metal and PDMS was evaluated using a pull-off test. For this purpose, the metal on PDMS was glued using epoxy adhesive ("Uhu Plus Endfest 300") to a dolly, and the breaking strength was measured using the XYZTEC Condor Sigma bond tester.

To determine hardness, a digital hardness tester HT-6510C (Precision Scientific Instruments Corp.) was used. PDMS blocks with dimensions of $30 \times 30 \, \text{mm}^2$ and 6 mm thickness were prepared for the hardness measurements, with PDMS base and curing agent mixing ratios of 10:1 and 10:4, respectively.

4 Stomach-on-Chip

4.1 Microfluidic chip for gastric cell culture

Cellular biology research has made impressive progress recently, marking such achievements as self-organizing multicellular 3D cell cultures. These cells, called organoids, are generated from primary tissue or human stem cells. Organoids contain self-renewing progenitor cells, which can be distinguished into various organ-specific cell types upon exposure to certain conditions or components. Therefore, one can use these cells to mimic various human organ functions. This opens a vast field of opportunities to analyze and diagnose numerous diseases, test drugs, and much more.

The human stomach is a very complex organ with no identical counterpart in the animal world due to the complexity of cell types. Animal models can not mimic such complexity. Therefore, it is important to reproduce the body conditions for the human stomach cells for organoid research and bioengineering. Furthermore, the human stomach consists of many types of cells (Figure 4.1).
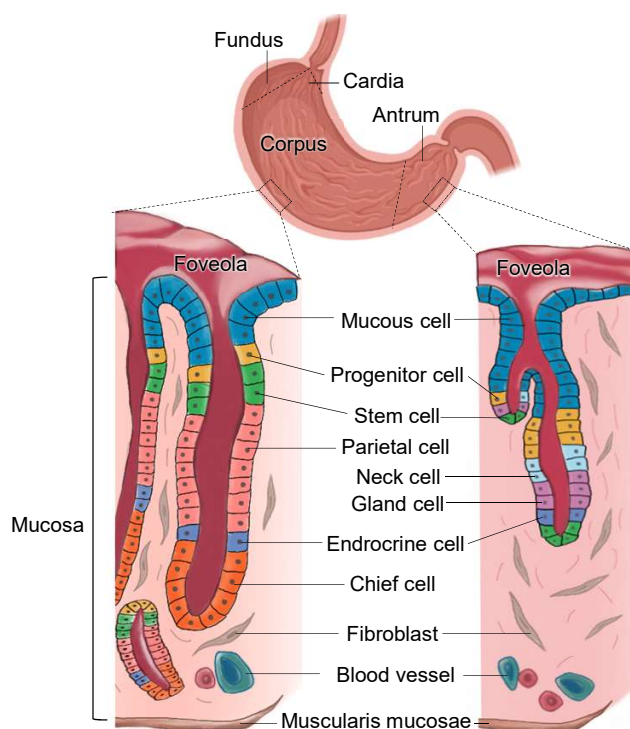
Figure 4.1: The schematic description of the human gastric mucosa and the complexity of its cell types [101].

All of them sense each other's presence and communicate via sending different proteins. Also, cells that are grown together represent the behavior and functionality close to those that are in the human body. The gastric mucosa consists of a simple columnar epithelium, which produces mucus. Growth factors released from mucosal stroma cells enable the maintenance of gastric stem cells. On the surface of the mucosa, funnel-like depressions, or foveolae, are ducts covered by a number of different cell types, which, depending on their localization in the stomach (fundus/corpus, cardia, or antrum), produce, for example, mucus, pepsinogen, hydrochloric acid, or gastrin, as shown in Figure 4.1.

There are several approaches worldwide to emulate part of the human gastrointestinal tract using gastric organoids. To replicate the conditions of the human stomach in-vitro, two widely used cell and organoid culture methods exist: 2D in Boyden chamber (Figure 4.2 a) and 3D in Matrigel (Figure 4.2 b). In a 2D gastric organoid, grown in a Boyden chamber (as shown in Figure 4.2 a), the apical side of the epithelium faces towards the medium. Nevertheless, this is a static model, which does not provide relative body conditions for cell culture. However, in 3D gastric organoids, grown in an extracellular matrix (ECM), shown in Figure 4.2 (b), the apical side of the epithelium faces towards the lumen of the organoid [102]. This is a major disadvantage since the 3D organoids deposit debris from apoptotic cells and mucus in the lumen. In the Boyden chamber, the dead cells are not manually "washed" away either, as could be done automatically in a microfluidic structure. Therefore, operating with 2D organoid in a microfluidic chip is more accurate, more controllable and extends the maximal duration of an experiment [101].
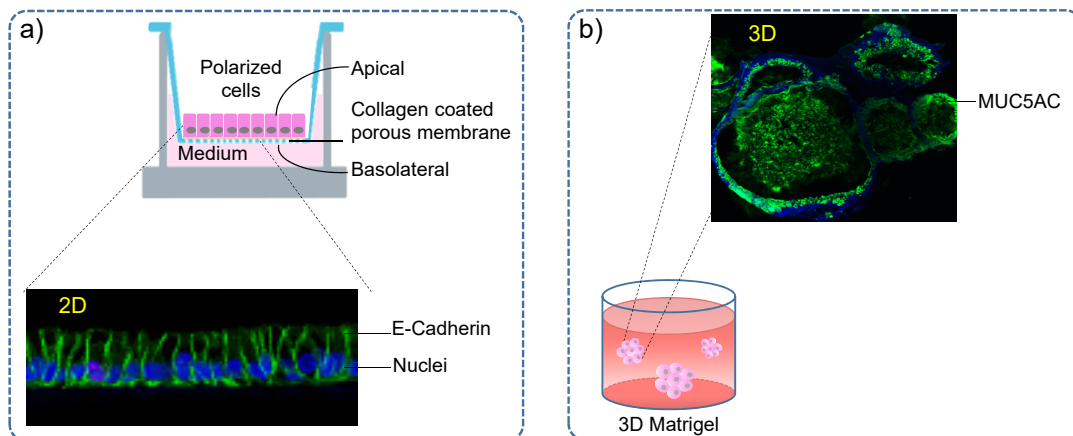
Figure 4.2: 2D gastric organoid grown in a Boyden chamber (a), a hollow plastic chamber in which the monolayers grow on a porous membrane. E-cadherin indicates for the adherens junctions of the columnar polarized cell monolayer. 3D gastric organoid grown in extracellular matrix (Matrigel) (b) [101].

One of the first 3D Stomach-on-Chip approaches was presented by Lee at al [103]. Their work reported on a 3D gastric organoid embedded in Matrigel in a central chamber of a macrofluidic structure. Micro-needles were inserted into opposite sides of the organoid

in order to emulate in vivo luminal flow through the organoid by means of a peristaltic pump, generating luminal flow. This system provides a first attempt at studying gastric physiology and offers potential for drug discovery. However, perfusion was conducted through the organoid, which does not reflect body conditions with sufficient accuracy. As mentioned previously and seen in Figure 4.1, the stomach contains many different cell types and barriers. Therefore, other emulation approaches must be considered, which more reliably and accurately mimic the interplay and interdependence between the various cell types in the tissue. Because of the aforementioned shortcomings of the 3D gastric organoid approach, an alternative device for the culture of 2D monolayer gastric organoids is addressed in detail in this thesis. This approach offers several advantages over 3D organoid culture for analysis of gastric-infection biology and diseases. It can be extended to analyse multiple various types of organoids on-a-chip.

An interesting observation of the experiment conducted in Boyden chamber has been reported in [102]; removal of the liquid medium on top of the 2D monolayer organoid results in an air-liquid interface (ALI) condition, which in turn strongly increases the epithelial morphology. These ALI conditions, which initiate the generation of mucus on the apical side of the epithelial cells, are highly relevant to a large number of biomedical applications. Thus, as mentioned above, a physical implementation of a 2D microfluidic device should be able to implement ALI conditions. Furthermore, a 2D gastric organoid is an excellent model, which enables study of dynamic host-pathogen infection processes. For example, the human pathogen Helicobacter pylori resides and colonizes the apical side of the gastric epithelial cells [102, 104].

The aforementioned organoid cells can be placed into a microfluidic device. This combination is called "organoid-on-a-chip". One of the most common geometries, which could be used for this purpose is the "sandwich" structure. It is a very generic structure that can be used for growing any type of cell, for example, endothelial cells, epithelial cells, fibroblasts, neural cells, etc. Further these cultured or co-cultured monolayers in microfluidic chip can be used to test the effects of medicaments on cells. If, for example, on one side of the membrane neurons are grown and on the other side endothelial cells, one can investigate the "blood-brain-barrier". If the drug under test can flow within the channel containing endothelial cells, this would enable analysis of the effect of medicaments on the brain. The sandwich structure comprises two micro-sized channels divided by a porous membrane, as shown in Figure 4.3. The top view shows the 3D structure. Using highly accurate microfluidic pumps, two different types of liquids (containing cells or medicament) can be pumped in and pumped out via the micro-inlets. Such pumps, e.g., produced by Fluigent, can very accurately control the flow rate and the quantity of the pumped liquid. Figure 4.3 shows two channels, marked by white and pink colors. A cross-section of the 3D structure, showing a cut along line A-B, is shown at the bottom of Figure 4.3. It visualizes the scenario for Organ-on-Chip application, in which the top channel is used

to grow epithelial cells, while the bottom channel is used to grow endothelial cells. The membrane is used to provide a means for the two cultures to communicate with each other. The size of the pores and density of the perforations must be suitable for the particular types of cells that will be grown in these channels.
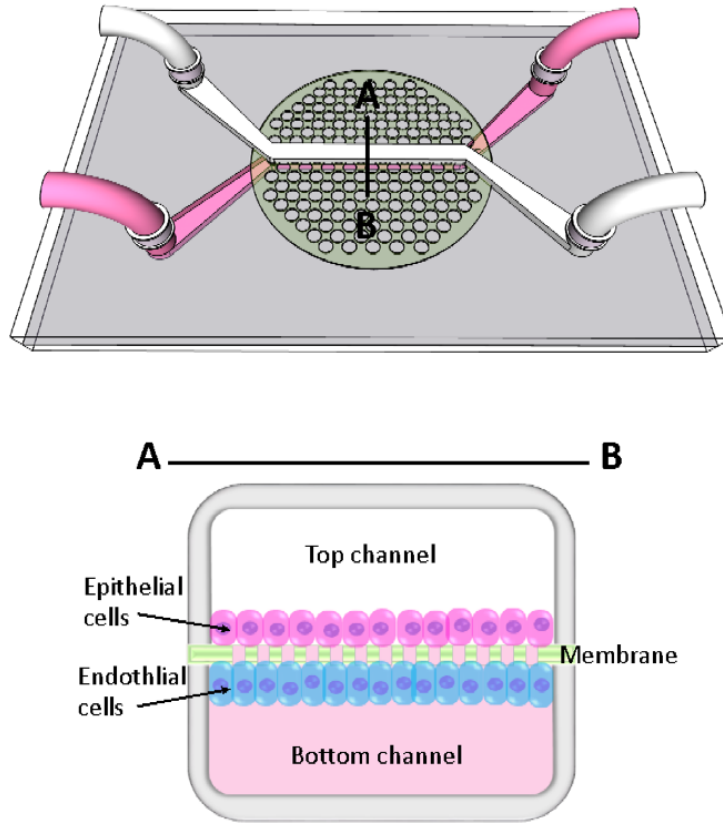
Figure 4.3: 3D design of the microfluidic chip for gastric cell culture [101].

Such microfluidic "sandwich" devices are usually made of polymers. Typical microfabrication steps include soft lithography, injection molding, or 3D printing. Polymers offer several crucial advantages for the realization of such devices and for cell cultures, such as flexibility, transparency, and gas permeability. Organoid-on-chip is an exceptional instrument that enables analysis of human tissue ex-vivo and facilitates new biomedical applications. One of the main biomedical applications analyzed in this dissertation is Stomach-on-Chip, which is investigated utilizing microfluidic device created during the course of this work. Therefore, the following Subsection presents a detailed view on the applicability of PDMS-based microfluidic channels for gastric cell culture. Chapter 4 is structured as follows:

- Section 4.1.1 presents detailed design considerations of microfluidic chips for Stomach-on-Chip applications, providing biomedical insight, discussion of advantages of 2D microfluidic devices and qualitative specifications,

- Section 4.1.2 provides a detailed description of the physical design, layout, and manufacturing of the 2D microfluidic devices,

- Section 4.2 describes the application of the PDMS microfluidic chip manufactured in Section 4.1.2 for 2D Cell Culture and drug testing for gastric organoids,

- Section 4.3 describes further advanced manufacturing techniques for the nano-structuring of the membrane in a microfluidic device for 2D cell culture,

- Section 4.4 summarizes this chapter, provides an outlook into the future and emphasizes the key novel results reported in this chapter.

4.1.1 Chip Design Considerations for Stomach-on-Chip

The proper sequence and conditions for the cell's co-culture play an essential role in reproducing a suitable stomach model for drug testing. As described in the introduction of this thesis, the Organ-on-Chip is a powerful model for personalized medicine and for development of new drugs. The microfluidic chip is designed for 2D gastric organoid culture as well as for gastric epithelial cell culture. To reliably and accurately emulate the body conditions for stomach analysis, the following requirements must be considered and fulfilled by the experimental setup. This can be translated into specifications for the microfluidic chip and impose the following design properties:

- **Dynamic system flow conditions:** the continuous microfluidic flow of the culture medium must be ensured in a specific range from $0.1\,\mu l/min$ to $5\,\mu l/min$. This is a meager flow rate, which is very hard to maintain. This imposes challenges on the design of the system setup and geometry. To achieve such low flow rates, the impact of gravitation and self-induced liquid flow due to height gradients must be avoided by all means. This is to avoid any additional forces that might accelerate the liquid flow, making it uncontrollable and much faster than is suitable for this application. Therefore, the only source for controllable movement of liquids must be a microfluidic pump that guarantees such low specific flow rates. The dynamic conditions for cell culture are highly important for bacteria co-culture and drug screening for Stomach-on-Chip application. As Bochelato et al. presented in their study [102], the bacteria H. Pylori affects the stomach tissues and leads to chronic inflammation with an increased risk of gastric cancer. The authors performed their experiments in the Boyden chamber, which means under static conditions. Therefore, the accumulation of the bacteria overgrowth did not correspond to conditions naturally occurring in the body and the population was overgrown. Using the microfluidic chip, we can study the process of the bacteria co-culture under conditions relevant to the human organism. The continuous flow washes out part of the bacteria population from the stomach. This process can be realized in the microfluidic chip.

- **Possibility to realize Air Liquid Interface (ALI):** this property is required in the scenario when cells are cultured in the upper channel. Once the liquid is pumped away from the upper channel, the grown cell layer, located physically upon the membrane, is exposed with the upper surface to the air. Furthermore, these cells will get nutrition from the bottom channel through the membrane's pores. The exposure of the cell to the air atmosphere is relevant to the body conditions and even increases the oxygen supply into the cell layer or organoid [105].

- **Possibility to feed cells from the basolateral side:** nutrition and drugs must be delivered to the cells from the basolateral side, similar to the case in the human body. It is particularly essential for drug testing to provide the medicament under flow conditions from the basolateral side of the stomach epithelium cells [106]. This mimics drug delivery from blood vessels, but without passing through the endothelial cell layer. The apical side will be covered with the gastric mucosa by realizing the ALI cell culture.

- **Optical transparency of the microfluidic device:** transparency is required to monitor cell concentrations by optical means, such as the microscope and fluorescent analysis. PDMS offers inherent optical transparency and thus is useful for optical monitoring, in contrast to other alternative polymers suitable for biomedical applications, such as Ostemer$^©$, Flexdym^{TM}, Polyethylene, Polystyrene and Polypropylene that are not optically transparent.

- **Absorption in the microfluidic chip:** ideally, microfluidic chips would have 0% molecular absorption. Nevertheless, all polymers can adsorb molecules, each at a different rate. Due to the undesired non-specific absorption of proteins and other molecules by PDMS, a portion of the analyte transport gets absorbed by the chip body [107, 108]. Therefore, it cannot be determined whether drug concentration is reduced due to contact with the cells or due to the unwanted absorption by PDMS. Therefore, optical means are the only way to monitor the number of apoptotic cells and free drug concentration in cell culturing during therapeutic drug testing experiments. To overcome the disadvantage of undesired absorption, several novel solutions have been reported recently in the literature, e.g., surface modification by surface segregation of smart polymers for biomicrofluidics [36]. In the case of chips designed for gastric cell culture, we can neglect PDMS absorption due to the flow conditions and continuous drug delivery.

- **Gas permeability of the microfluidic device:** the availability of oxygen and carbon dioxide is required to maintain sustainable conditions for cells to proliferate. Therefore, culturing cells inside the channels requires a capability for gas to penetrate from outside of the microfluidic structure through the chip material to the inner side

of the channel compartment. This requirement is fulfilled by PDMS, as it inherently offers gas permeability of the chip. Without this property, cells would die within a very short time (less than 20 min), making it impossible to conduct drug observation over a longer period of time (e.g. of several days).

- **Laminar flow:** laminar flow ensures no-stress conditions for the cell culture. This flow condition can be enabled by the channel size. In microfluidic structures the Reynolds number, which is proportional to the channel diameter, is sufficiently low and fluid flows without any turbulence [109].

- **Pore sizes:** the influence of the membrane's pore size on cell culture is still an open research question. Due to our application and cell type, it is beneficial to provide the maximal percent of the open area and simultaneously prevent cell migration to the bottom channel. Therefore, the 3 µm pore size is chosen for the polyester membrane. Furthermore, to increase porosity, a femtosecond laser structure was designed to print in the closed microfluidic channel.

- **The elasticity of the microfluidic chip:** flexibility of the chip is not necessary but is advantageous for the cell culture in microfluidics. It reduces mechanical stress for the cells and enables soft deformations similar to the body conditions. Also, this feature is fulfilled inherently by PDMS, as it offers very high flexibility which can be tuned for a specific application.

All of the aforementioned requirements - continuous flow, separate but connected-through-the-membrane cell culture compartments, flexibility, gas permeability of the chip material, optical transparency etc., can be fulfilled by a microfluidic chip made of Polydimethylsiloxane (PDMS). PDMS combines all of the necessary properties required for the realization of Organ-on-Chip devices, making this material an unbeatable solution compared to other alternatives. Regarding the geometry, the best chip structure for the aforementioned purposes is two channels which are divided by the porous membrane, as shown in Figure 4.4. This concept is used in numerous studies for realization of many human organ parts on chip [110–112], but it has not yet been reported for Stomach-on-Chip. In this work, the focus is on the 2D Stomach-on-Chip application. A concept with two channels divided by a porous membrane is optimized for the gastric cells and a novel bonding technology is developed, as described below. Moreover, the microfluidic chip is a great platform for sensor integration. Therefore, the Stomach-on-Chip model proposed in this work is also equipped with sensors and actuators, which are described in Chapter 7. As a preview example, the in-vitro microfluidic model enables the possibility for non-invasive sensing by measurement of the transepithelial electrical resistance (TEER) (Figure 4.4, yellow color), which provides valuable information about 2D organoid or cell monolayer confluence.
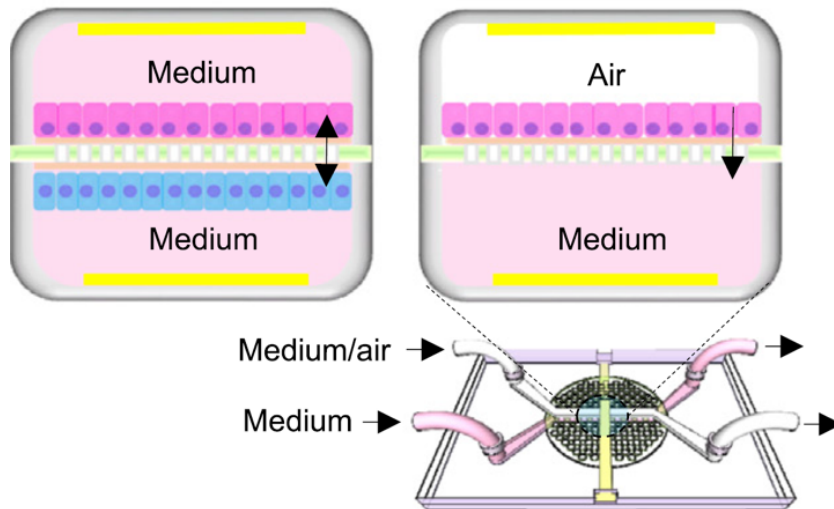
Figure 4.4: 2D organoids on-a-chip with top and bottom channels connected by a porous membrane covered with an extracellular matrix. The top channel functions as an air–liquid interface (ALI), which mimics the medium-free and luminal (apical side towards the lumen) localization of a 2D organoid. Alternatively, the top channel contains cells with medium and on the bottom of the porous membrane there is medium and added fibroblasts. The chip contains integrated noninvasive sensing of the barrier function by measuring the transepithelial electrical resistance (TEER); electrodes are shown by the yellow color [101].

Figures 4.3 and 4.4 show the design of the microfluidic structure, in which the gastric epithelium cells or stomach organoids are cultured in the top channel. Medium with drugs or any another substance for test is pumped through the bottom microfluidic channel. It reproduces the body conditions, while the drug is provided from the basolateral side under dynamic conditions. In the top channel the air-liquid interface (ALI) can be realized. As discussed previously, a physical implementation of a microfluidic device has been designed and fabricated for realization of cell line monolayers, cell co-culture and for a 2D gastric organoids culture. Fabrication of these microfluidic devices is discussed in the following Section 4.1.2. Drug testing performed using this chip with cultured gastric cells is described in the Section 4.2.

4.1.2 Microfluidic Chip Fabrication

Based on the considerations in Section 4.1.1 and technology described in Chapter 3, this section presents the fabricated microfluidic chips, suitable for 2D cell culture.

After considering all the necessary features of the microfluidic chip needed to address a specific biological question (in our case, stomach modeling), appropriate materials have to be chosen. Due to all the considerations listed above, PDMS was selected as a chip material and polyester as a membrane polymer. According to this choice, the technological process is based on molding and bonding procedures. Therefore, to mold the PDMS structures,

the master mold has to be designed and fabricated. Employed materials and the developed technological process are given in Section 3.1.1. The first generation of the master mold was designed with different sizes of microfluidic channels (Figure 4.5) to compare and select the right one for gastric cells. The main variable parameter was channel width: 3 mm, 2 mm, 1 mm, 0.5 mm, and 0.1 mm. The CAD design of this master mold is given in Figure 3.1. Also, the first master mold was fabricated out of photoresist SU-50 with a resulting structure height of 50 µm. The microfluidic PDMS devices were fabricated (the process is described in Chapter 3) from this mold and tested for the cell culture. The cells were cultured successfully in 1 mm, 0.5 mm, and 0.1 mm wide channels. Nevertheless, the cultured cellular layer significantly reduced the channel height by approximately 40 %, and the cells showed degraded life activities after 3 or more days. Therefore, the height of the structure was changed to 100 µm, and new master molds were developed, shown in Figure 4.5. For this purpose the photoresist SU-100 was utilized.
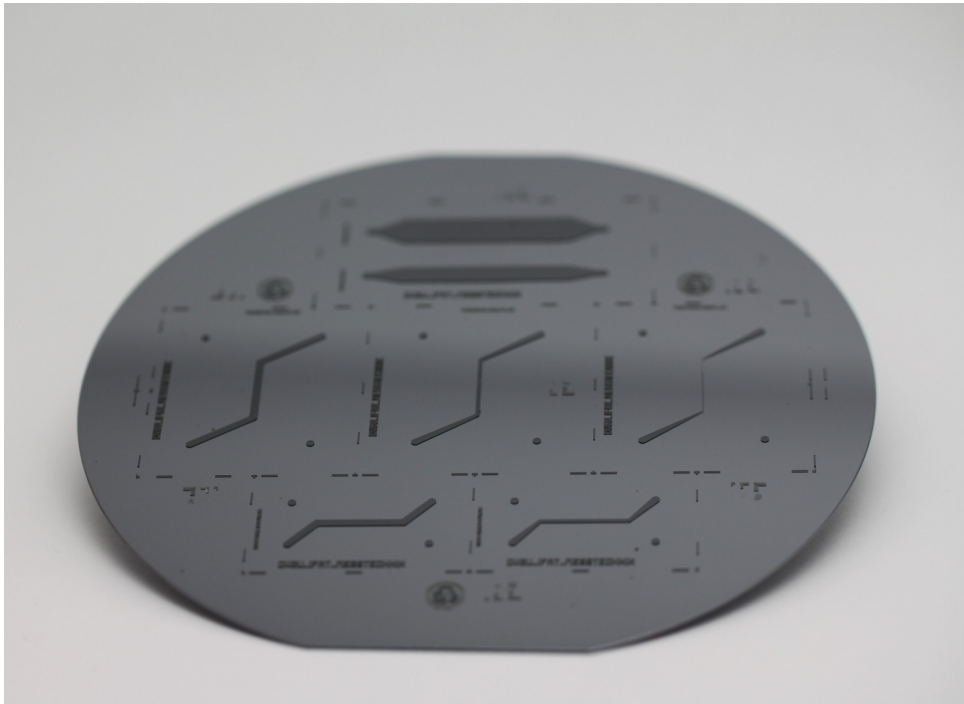
Figure 4.5: Photograph of the master mold (first generation), made by the soft lithographic process. Various micro-channel widths are fabricated: 100 µm, 500 µm and 1000 µm. The height of the structures is 100 µm.

Thereafter, the PDMS-based microfluidic devices had to be fabricated with the master mold. The molding process is described in Section 3.2. Once the replicas are prepared, they can be aligned and bonded to the porous membrane.

A microfluidic chip can contain membranes realized from various types of polymers. The bonding ability of various materials differs because of their chemical composition. The most efficient bonding can be realized using membranes implemented from the same

material as the chip body. However, fabricating a membrane of PDMS requires special equipment and might be costly. Therefore, producing the membrane from other polymers apart from PDMS makes sense, for example, polyester or polycarbonate. Compared to PDMS, these materials offer an advantage compared for the realization of the membrane since the surface of these materials enhances cellular growth thanks to the following effect: due to their hydrophilic surface these materials can be covered by a water-based solution with proteins, for example, collagen. The combination of the hydrophilic surface and the coverage by collagen will enhance cell adherance and growth. In case two different materials are used to implement the membrane and the channel, e.g., polyester and PDMS, it becomes much more complex and cumbersome to bond these parts to each other. This requires additional effort and more advanced technology steps.

The first PDMS-Polyester bonding process to be tested was realized by polyester membrane surface modification with the (3-Aminopropyl)triethoxysilan (APTES) solution [113]. Bonding strength was verified by a leakage test. The concept is to detect the maximal time and flow rate at which the leakage appears and the two polymer layers delaminate. The maximal "breakdown" flow rate for PDMS and polyester layers bonded by chemical surface modification was 5 µl/min, which is not sufficient for microfluidic devices used with continuous flow. Furthermore, 24 samples were developed by means of chemical surface modification for bonding between the replicas and the membrane, and all of them delaminated at the average flow rate of 5 µl/min. Therefore, a novel fabrication technology and adhesive PDMS-based bonding process were proposed in this work.

For this reason, we have developed a novel general-purpose methodology applicable for bonding of any porous material to PDMS through an adhesive PDMS sublayer in this work. It is desired to implement a microfluidic chip from the least number of materials as possible. Therefore, to realize the aforementioned adhesive sublayer-based bonding, we proposed to use PDMS in liquid phase, which fills the pores in the membrane and cures subsequently.

Using PDMS is a natural choice which provides better mechanical stability and higher bonding force. Furthermore, the chip remains functional over a longer period of time and can sustain much higher flow rates compared to other solutions. The leakage test of the chips fabricated with the proposed method shows excellent stability. Samples were tested up to 83.2 µl/min and only two out of 50 fabricated chips showed leakage after several days of pumping at the maximal flow rate.

Once the liquid PDMS in the pores hardens, it constitutes a continuous 3D structure made of PDMS connecting the lower chip part to the upper chip part. Therefore, it simply encompasses the membrane and, in addition to this, creates an inherent natural array of PDMS vias, which are shown in Figure 4.6.
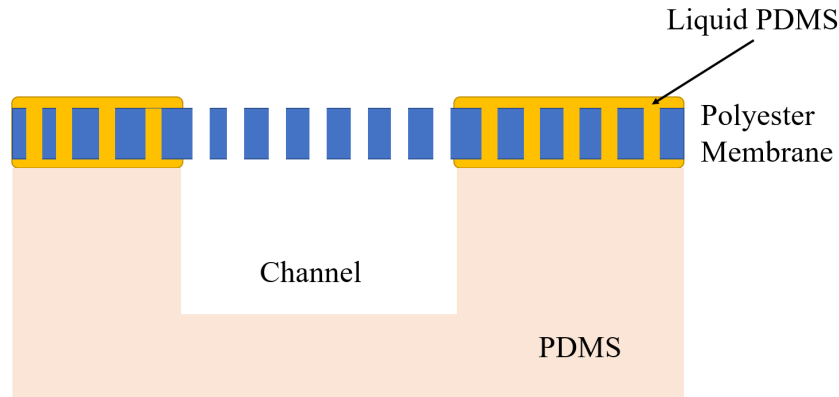
Figure 4.6: Schematic description of the adhesive bonding concept with liquid PDMS. The polymer fills the membrane's pores and ensures reliable bonding, combined with mechanical support that holds the membrane from top and bottom.

Since the microfluidic chip should enable protein exchange between the lower and the upper channels and drug penetration from one channel to another, it is important that the pores in the membrane, which are located over the channel, remain hollow, i.e., unfilled with PDMS or any other material. Therefore, we use a "doctor-blade" technique to cover with liquid PDMS only those parts of the membrane which participate in the bonding process of the chip. As shown in Figure 4.7, according to the technology proposed in this work, the part of the polyester located above the channel remains untouched by liquid PDMS.

High resolution is achieved thanks to the channel wall acting as an inherent natural boundary. Liquid PDMS applied as a thin layer to the lower part of the chip cannot leak into the channel due to the surface tension forces. These forces ensure that the liquid is halted at the edge of the microfluidic channel since the edge acts as a defect and presents a barrier in the way to the liquid. Thanks to this effect, we achieve a highly accurate separation between the polyester area with liquid PDMS and the one without it, as shown in Figure 4.7 (upper right part).

As discussed in Chapter 3, the fabrication steps of a microfluidic chip must take into account that, after application of the liquid PDMS on top of the lower part of the chip, a polyester membrane must be placed upon it. The interaction between the surfaces of the two materials having different phases (the PDMS layer is liquid whereas the polyester membrane is solid) results in wetting effects. Note that polyester is a hydrophilic material and PDMS has low surface tension (20.4 mN/m). These are basic conditions for the wetting process to take place. Therefore, when the membrane is placed on top of the thin liquid PDMS layer, wetting forces occur. Wetting is the ability of a liquid to maintain contact with a solid surface, resulting from inter-molecular interactions when the two are brought together. This happens in the presence of a gaseous phase or another liquid phase
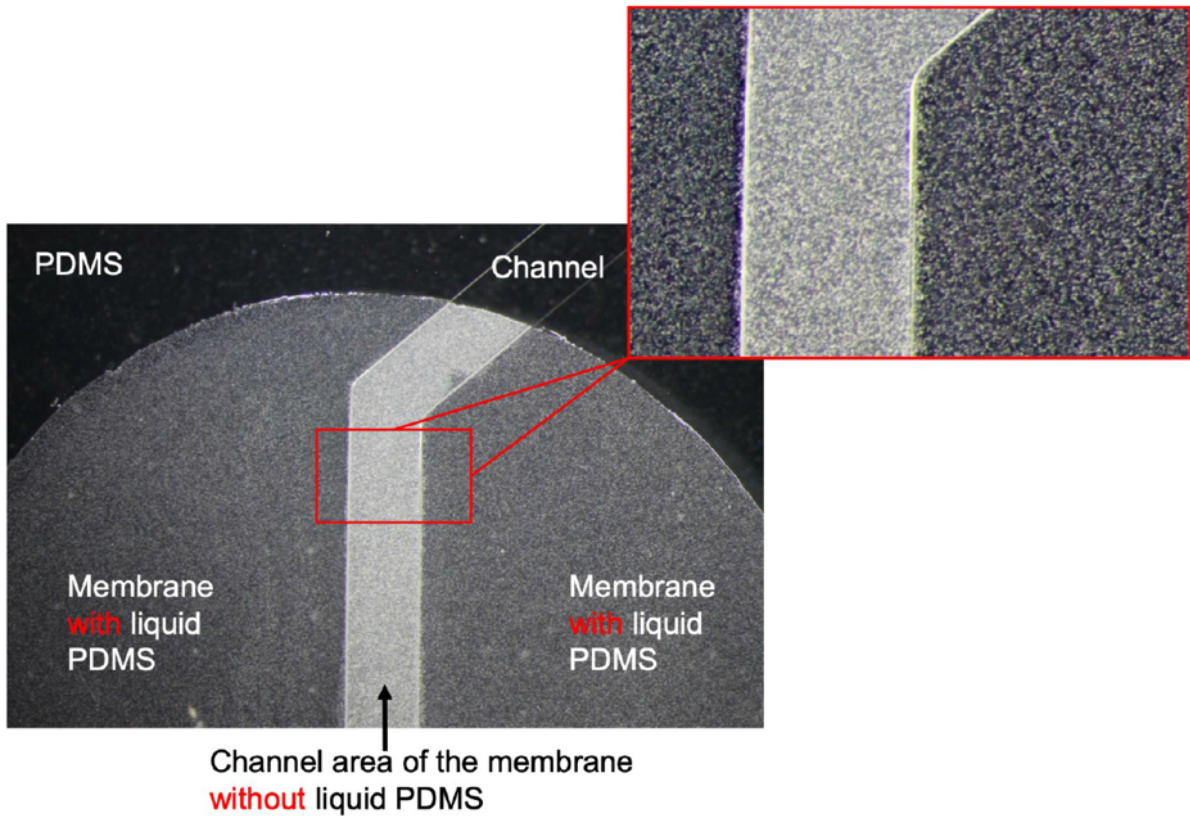
Figure 4.7: Microphotograph of the "doctor-blade" technique. Porous polyester membrane located on the structured PDMS layer with a 1 mm wide microfluidic channel. Liquid PDMS was applied to all areas except for the channel area. The magnification shows that the membrane is clean and liquid PDMS does not clog the pores [96].

not miscible with the first one. The degree of wetting (wettability) is determined by a force balance between adhesive and cohesive forces. Wetting is important in the bonding or adherence of two materials [114]. Wetting and the surface forces that control it are also responsible for other related effects, including capillary effects.

The layer thickness must be chosen very carefully to force the liquid PDMS to stay within the boundary by means of surface tension. The goal is to prevent wetting of the polyester by the liquid PDMS in the vicinity of the channel. At the same time, wetting in the area which participates in the bonding process, as shown in Figure 4.7, must be preserved. Liquid PDMS fills the volume of the pores in the polyester membrane by means of capillary motion. Capillary motion is the process of a liquid flowing in a narrow space without the assistance of, or even in opposition to, any external forces like gravity. Manipulating the amount of the liquid PDMS as the parameter for process optimization provides an instrument to control the wetting forces. The amount should be sufficiently low to prevent PDMS from flowing into the channel, yet at the same time, it should be sufficient to fill the 3 µm pores of a 10 µm thick polyester membrane. The amount of liquid PDMS

was determined empirically in this work, and it resulted in an optimal layer thickness of 2-6 μm. The "doctor-blade" technique provides layer thickness controllability in the range of $\pm$ 2 μm. The thickness of the liquid PDMS was measured by the spectrophotometer F20-UVX (Fimmetrix, KLA Corporation, USA). In case more exact controllability is desired, other potentially expensive machinery and steps might be required, such as spin coating. In this work, we chose the "doctor-blade" technique to keep the chip fabrication as inexpensive as possible. Also, spin-coating requires covering of the channel area to prevent its filling by liquid PDMS.

During chip fabrication particular care must be exercised, because before application of the liquid PDMS each layer is activated by oxygen plasma to enhance the bonding ability, as described in Section 2.1.5. As a result of this activation, the surfaces of both polymers (polyester and PDMS) become highly hydrophilic. This is related to an increase of the surface energy, which results in a much smaller contact angle ($\leq 40°$). For such obtuse angles, verification can only be conducted qualitatively by placing a droplet on the surface and observing how the droplet spreads over the surface. Therefore, a plasma-treated surface of the polyester membrane becomes highly hydrophilic and reactive wetting takes place [115]. Wetting forces become stronger and require much higher attention during fabrication steps to avoid undesired leakage of the liquid PDMS into the channel area of the polyester membrane. Therefore, the amount of liquid PDMS used as an adhesive layer for one chip was 0.01 g. A detailed description of the technological steps for microfluidic chip assembly is given in Table 3.10. Thus, an alternative bonding technology for Organ-on-Chip applications was developed. This method is highly universal, allows the bonding of any porous material to PDMS and does not require the use of additional components which can adversely impact the biological experiments. A successfully bonded microfluidic PDMS/Polyeste-based chip is shown in Figure 4.8.

Also, the cross-section of the chip and the porous membrane are shown in Figure 4.9. Filling the membrane pore with liquid PDMS and subsequent curing and then bonding achieves the desired result, i.e. sufficient bonding force to enable sufficient flow rate without leakages.

The cell culture experiments showed the best performance with the microfluidic chip with a channel width of 1 mm. Compared to the chips with channel widths of 100 μm and 500 μm, cells have more room to grow into a layer, create tight junctions, and still be able to sense the channel walls, which helps them to polarize. The bigger size of the cell tissue also means that there is a larger cell amount and, therefore, more factors and proteins of interest are released. It increases the concentration and gives the opportunity to measure the amount of the released factors, after collection of the medium with these proteins from the outlets. Therefore, the biological parameters of the cultured cells can be detected. Also, in the microfluidic device with the channel dimensions of 100 μm $\times$ 1000 μm, laminar flow is present and the liquid velocity is lower compared to 100 μm $\times$ 100 μm
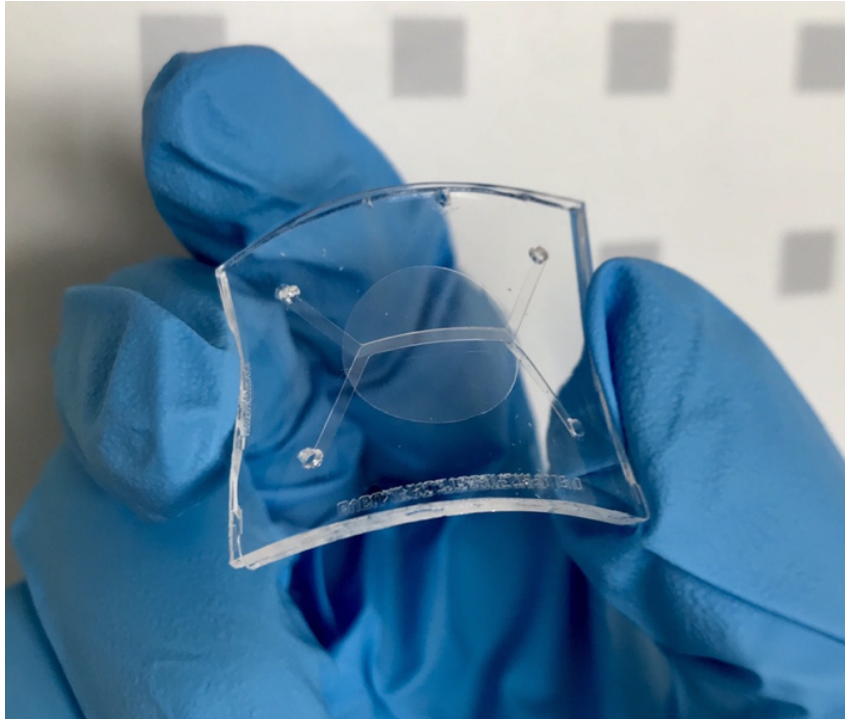
Figure 4.8: Micro-fabricated flexible structure with two channels divided by a porous polyester membrane. The device is designed and developed for in-vitro cell culture and drug screening on gastric mono-layers and human stomach organoids.
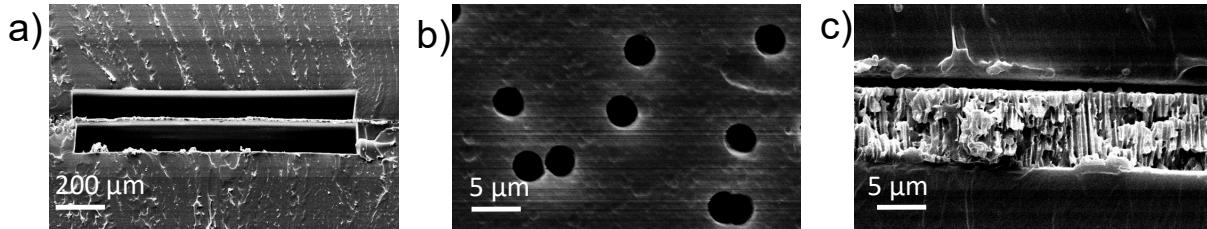
Figure 4.9: SEM microphotographs of (A) the chip cross-section, (B) membrane surface, and (C) membrane bonded to the two layers of PDMS in a cross-section [96].

and $100\,\mu\text{m} \times 500\,\mu\text{m}$ wide channels. The velocity in the $1\,\text{mm}$ channel was calculated as $0.09\,\text{mm/s}$, in the $500\,\mu\text{m}$ channel as $0.17\,\text{mm/s}$ and in the $100\,\mu\text{m}$ channel as $0.9\,\text{mm/s}$. The calculations were made for the flow rate of $0.5\,\mu\text{l/min}$ ($v = Q/A$, where v is a flow velocity, Q is a volumetric flow rate, A is a cross-sectional area). Therefore, the stress from the medium speed for the cells in a $1\,\text{mm}$ wide channel is lower, which is beneficial for the biological experiment.

Thus, the most favorable channel geometry was tested and chosen. Cell culture experiments require sufficient data samples for statistical analysis. Therefore, a large number of chips was fabricated. To improve fabrication efficiency, multiple structures of $1\,\text{mm}$ width were placed on a single lithography shadow mask design (Figure 3.2).

Next, the second generation master mold was fabricated with a structure height of 200 µm. The channel's height was increased to provide sufficient space not only for epithelial cell lines, but also for stomach organoids. These geometrical parameters were found empirically. From a single master wafer with 10 microfluidic channels (Figure 4.10), we obtain 5 chips with channel characteristics width × length × height of 1 mm × 1 cm × 200 µm, respectively. These characteristics are optimal for gastric cell and organoid culture because they offer sufficient space in the microfluidic channel and yet cells can sense the physical borders. These borders help to simulate the body conditions and expedite cell polarization.
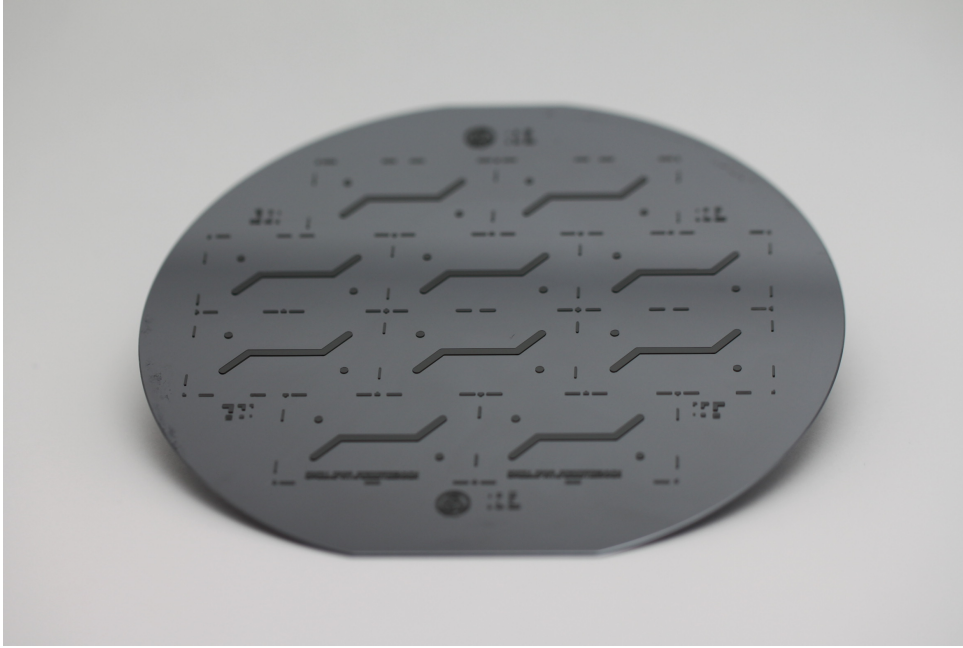
Figure 4.10: Photograph of the master mold (second generation), made by the soft lithographic process. The width of the micro-channels is 1000 µm and the height of the structures is 200 µm.

To sum up, a novel method for bonding the porous membranes to PDMS was developed to meet the requirements of the Stomach-on-Chip application. It ensures the chip's long-term stability and allows for continuous pumping of cell culture medium over the course of weeks. Furthermore, compared to the existing publications, the chip fabrication time was decreased from several days [94] to only 5 hours. This became possible thanks to the bonding method and utilization of the commercial membrane and compact master mold. The optimal geometry parameters for the gastric cell culture were determined empirically.

4.2 Proof of concept and gastric cell culture in microfluidic chip

Previously, we explored the design of a microfluidic chip tailored for both 2D organoid culture and gastric epithelial cell culture. The primary differentiation centers on the channel height, driven by the increased spatial requirements during organoid growth. Therefore, in this thesis, microfluidic structures with channel height of 50 µm, 100 µm and 200 µm were developed. The proof of concept is performed by culturing human gastric epithelial cells NCI-N87.

As mentioned previously, to operate microfabricated chips for cell culturing, a highly precise pumping system is required. Therefore, the microfluidic chips were connected to a pressure-driven pumping system, which consists of a low-pressure generator (FLPG PLUS), pressure controller (MFCS-EZ, Fluigent GmbH, Germany), flow rate platform, flow sensors (flow units) and reservoirs for the cell culture medium, as shown in Figure 4.11.
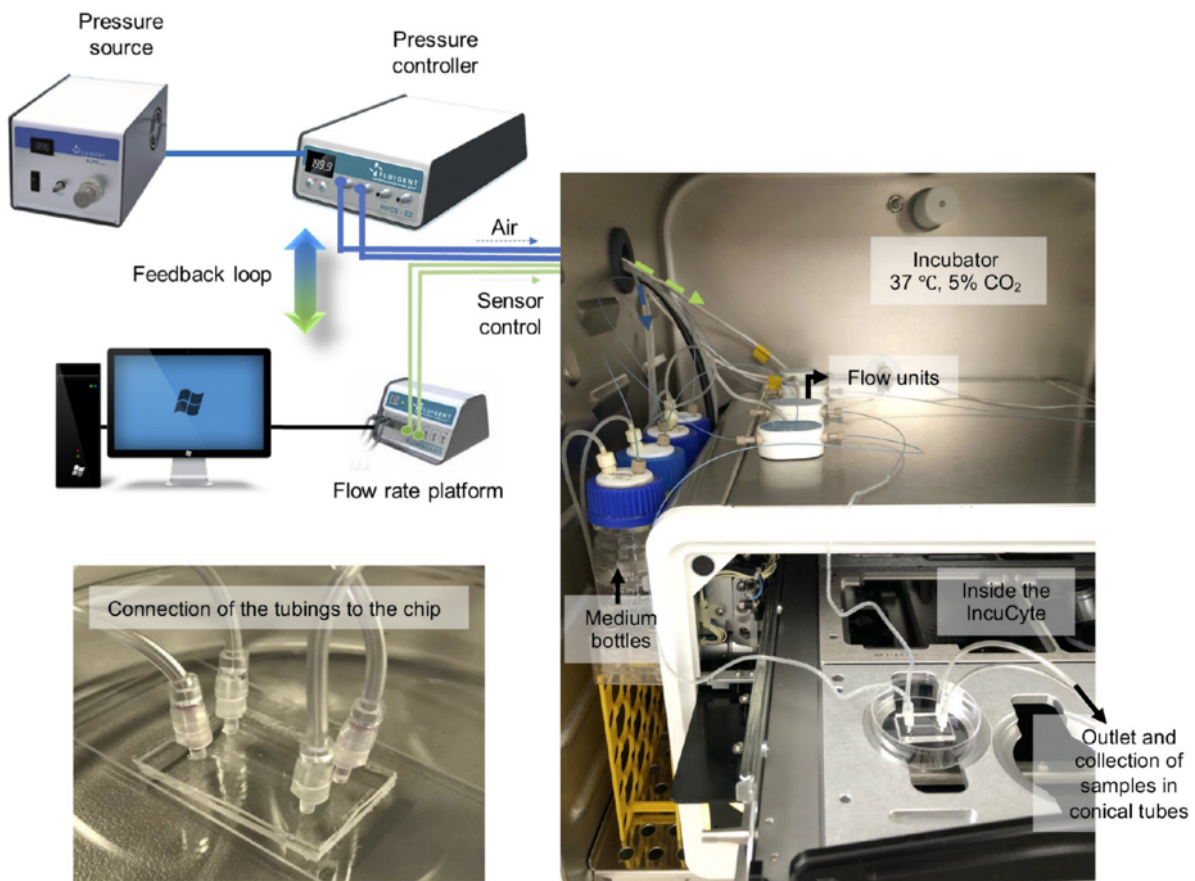
Figure 4.11: Schematic view of the built system to operate the microfluidic devices. It consists of the pump (Fluigent, GmbH), incubator and IncuCyte automated fluorescence microscope [96].

This system is not designed to work in an incubator; thus, the electronic devices were placed outside while reservoirs, flow sensors and chips were placed inside the sterile environment. These component parts of the system were connected by wires and tubes,

which were passed through the opening in the incubator. Furthermore, the microfluidic devices were placed in an automated fluorescence microscope to detect the influence of the chemotherapeutic drug and cell death. Therefore, the flow sensors were connected to the chips by a soft tube with an inner diameter (ID) of 0.13 mm.

In the developed microfluidic devices, gastric epithelial cells were cultured and a chemotherapeutic anticancer drug in clinical use (CPT) was tested.

In this work, a polarized epithelial cell monolayer was created by culturing the human gastric epithelial cell line NCI-N87 in a chip under dynamic conditions with a flow rate of 0.5 µl/min. These conditions ensured a continuous supply of fresh medium to the gastric epithelium monolayer without affecting the cells. In this thesis, gastric epithelial cells were grown on-a-chip also under static conditions and showed the formation of a cell layer but failed to develop a continuous confluent monolayer over two days (Figure 4.12).
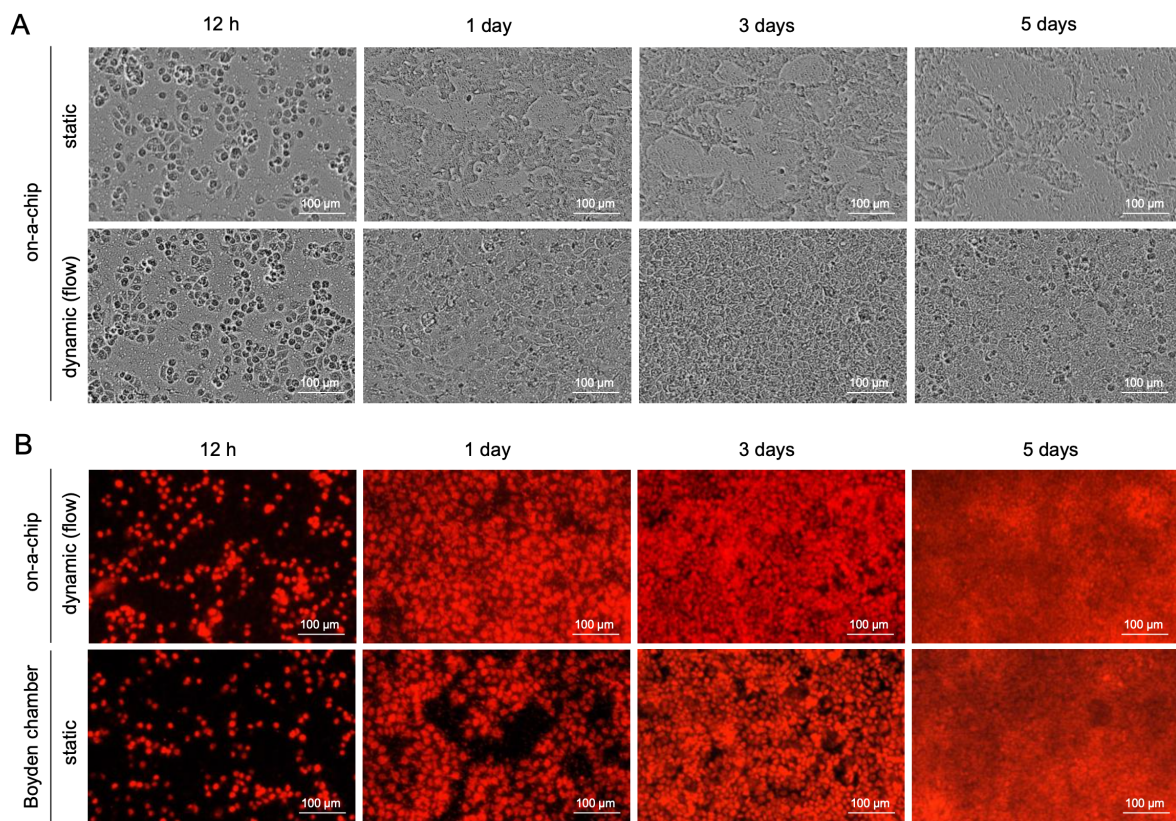
Figure 4.12: Formation of a continuous gastric epithelial monolayer on-a-chip. (A) Representative phase-contrast images of gastric epithelial cells on-a-chip. NCI-N87 cells were seeded at a density of 1800 cells/mm², and cells were analyzed with a continuous media flow at 0.5 µl/min after 0.5, 1, 3, and 5 days. Tayshe cells in the static chip were cultured without media flow. (B) Red fluorescent stained live cells on-a-chip or cells in the Boyden chamber. Cells were cultured in the media containing Incucyte Nuclight Rapid Red Dye and analyzed after the indicated time [96].

In contrast, cells on-a-chip with continuous media flow developed a nearly confluent monolayer after one day, which showed stable growth over seven days. The comparison of the cell culture in the Boyden chamber and in the chip under static and dynamic conditions is shown in Figure 4.12. Living cells on the chip and in the Boyden chamber were stained with red fluorescence and analyzed after the indicated time.

Also, the number of cells was counted at every control point of time, and measurements show more efficient mitosis in the chip (Figure 4.13).
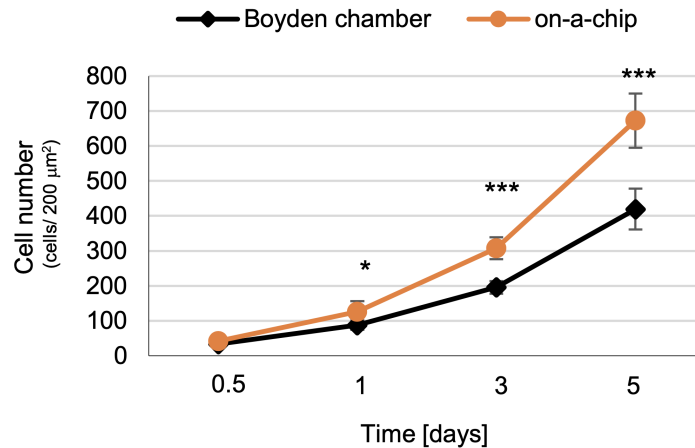
Figure 4.13: Comparison between number of cells on-a-chip and those in the Boyden chamber. Average numbers of cells from five fields were calculated at each time point and the values are presented as *$p < 0.05$, ***$p < 0.001$ [96].

After three days, a fully confluent monolayer was observed. It is noteworthy that the cells grown on-a-chip exhibited significantly faster growth compared to those grown in the Boyden chamber. This implies that a continuous media flow in a microfluidic chip is superior in facilitating the formation of a continuous confluent gastric epithelial monolayer. It is important to note that the cells require a specific period for optimal attachment to the collagen-coated membrane surface. Hence, the gastric epithelial cells were incubated without media flow for at least 4 hours after seeding. This duration may vary for other cell types and should be determined experimentally. The gastric epithelium acts as a barrier in the gastric mucosa, and it is composed of intercellular contacts that seal the paracellular space between epithelial cells. To assess the barrier integrity, the paracellular permeability of the gastric epithelial monolayer was evaluated using fluorescent probe for fluorescein isothiocyanate (FITC) dextran. Measurements showed the formation of a completely confluent cell layer on the fifth day in the chip and on the seventh day in the Boyden chamber.

This discovery indicated that the gastric epithelial monolayer was able to develop faster in the microfluidic device when exposed to dynamic flow conditions. Figure 4.14 confirmed the intercellular contact of the continuous cell monolayer through Immunofluorescence

(IF) staining of E-cadherin within the cell monolayer after 5 days of culturing on-a-chip or in the Boyden chamber.
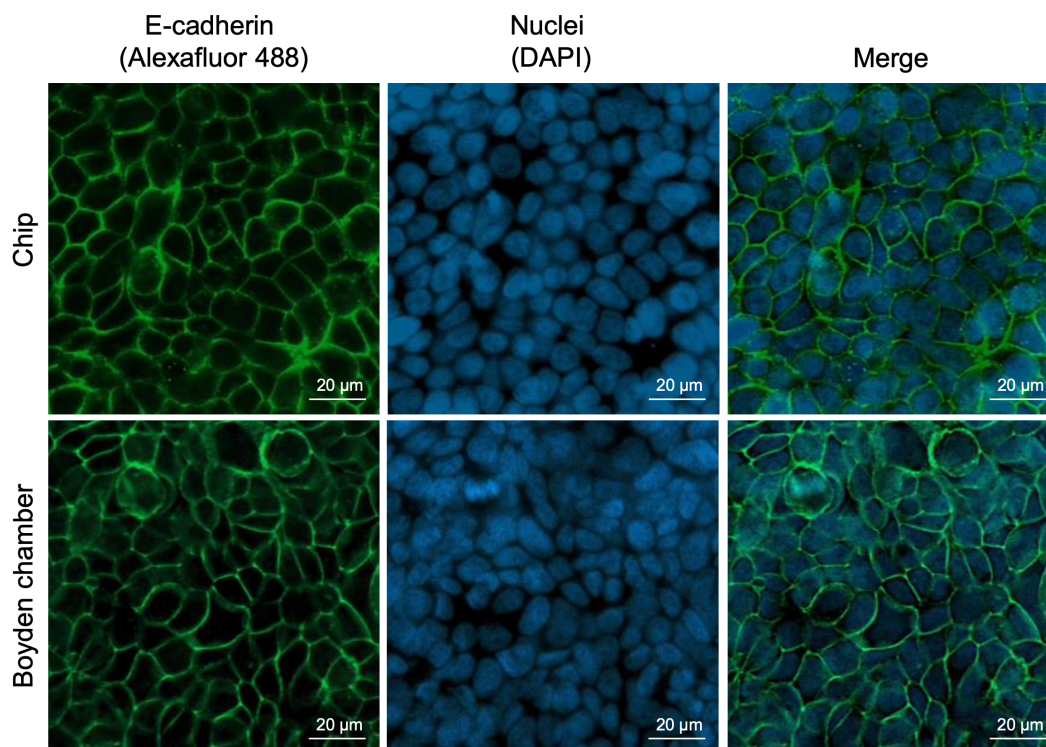
Figure 4.14: Immunofluorescent images of E-cadherin (green) in gastric epithelial monolayer grown for 5 days on-a-chip and in the Boyden chamber. Blue colour marks the nucleas of the cells and green shows the tight junctions between them [96].

Furthermore, the microfluidic device was found to be suitable for analyzing apoptotic cell death in IncuCyte (Figure 4.11). To demonstrate this, the responsiveness of the gastric epithelial monolayer on the chip to external stimuli was assessed through the analysis of apoptotic cell death following treatment with CPT, a gastric anticancer drug. CPT was found to stabilize the topo I-DNA covalent complex, leading to DNA damage.

In the microfluidic device, the media flow from the bottom channel imitates cellular uptake from the bloodstream and facilitates the delivery of nutrients, therapeutic drugs, and other compounds to the basolateral side of the gastric epithelial monolayer. To assess the effects of CPT, a gastric anticancer drug, on the monolayer, CPT was applied to the bottom channel, exposing the cells to CPT from the basolateral side only. The top channel's media flow contained a green fluorescent dye, caspase-3/7 green reagent, and activated caspase-3/7 recognition motifs (DEVD) to monitor CPT-induced apoptotic cell death over time (Figure 4.15).

Upon activation of caspase-3/7 in an apoptotic cell, the reagent is cleaved at the DEVD recognition motif, releasing a DNA binding dye that labels the nuclear DNA of apoptotic cells, which can be quantified through fluorescence imaging. The microfluidic chips were
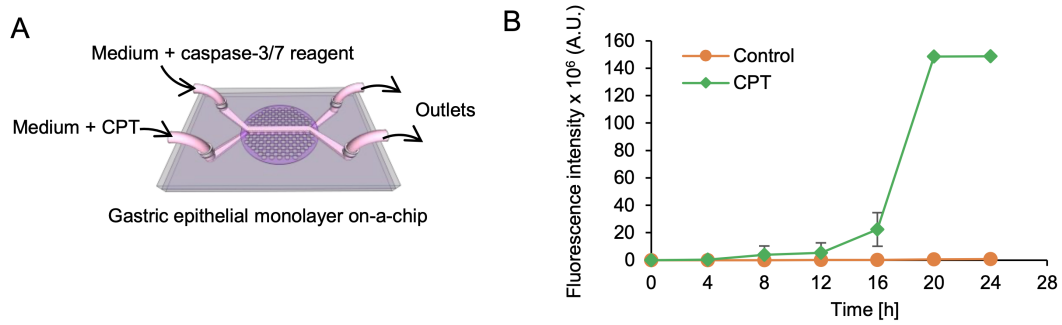
Figure 4.15: Real-time monitoring of the apoptotic cell death of the gastric epithelial mono-layer on-a-chip using the IncuCyte automated fluorescence microscope. (A) The schematic overview on the assay performed on-a-chip. (B) Fluorescence intensity of CPT-treated cells compared to control [96].

then placed inside the IncuCyte and connected to the flow system, enabling real-time monitoring of apoptotic cell death of the gastric epithelial monolayer on the chip. The results showed that apoptotic cell death was induced after exposure to CPT within 8 hours and increased in a time-dependent manner, as shown in Figure 4.16.
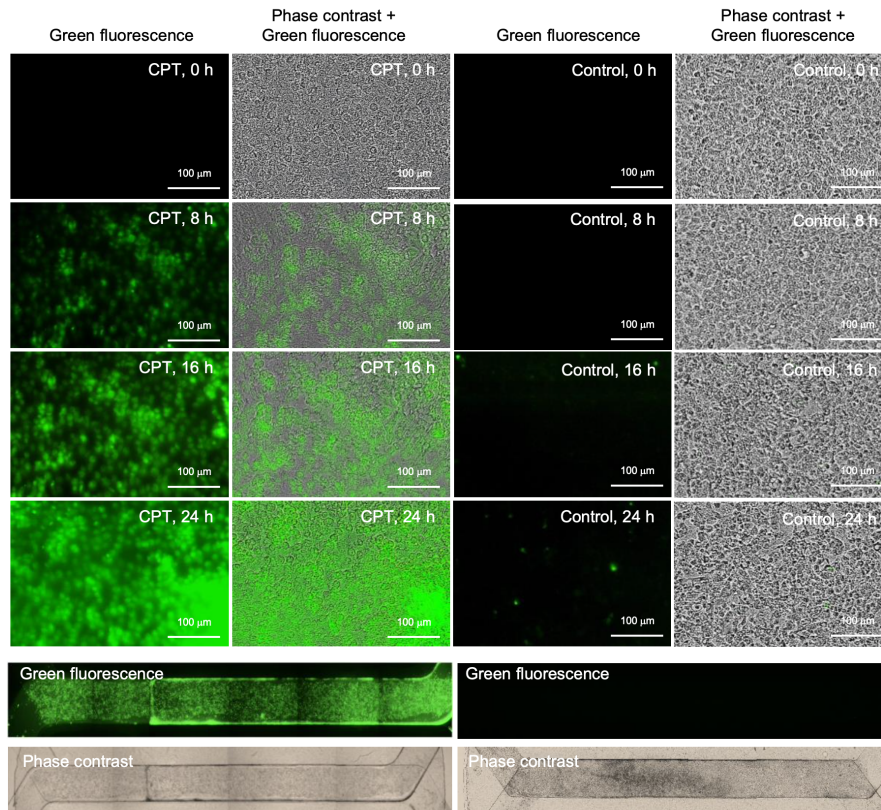
Figure 4.16: Fluorescent and phase-contrast images of the gastric epithelial monolayer on-a-chip after 24 h of exposure to continuous media flow containing CPT, automated capturing by the IncuCyte [96].

No apoptotic cell death was observed in the nontreated gastric epithelial monolayer. A stitched image of the gastric monolayer on the chip exposed to a continuous media flow containing CPT for 24 hours demonstrated cell death across all growth areas on the chip. These findings suggest that the gastric epithelial monolayer on the chip provides a suitable platform for studying drug responses. Importantly, the two-channel chip setup enables the detection of various end points triggered by chemotherapeutic processes, such as inflammasome activation, in addition to apoptotic cell death.

4.3 Femtosecond laser structured membrane in closed microfluidic channel

In order to improve the open-to-closed area ratio of the membrane in the cell culture microfluidic structure, we printed this membrane inside a finished transparent chip [25]. This might enhance cell culture and drug screening because cells could have better accessibility to the bottom channel where the nutrition and drug supply are located. Technology developed for this purpose is described in Subchapter 3.4. The main objective of this study was to utilize 3DLL technology for incorporating the SZ2080 membrane into a PDMS channel system for Organ-on-a-Chip applications, which requires precise fabrication of the membrane and structural stability. The alternative name for femtosecond laser structuring is Three Dimensional Laser Lithography (3DLL). The setup for 3DLL is provided in work [95]. The membrane is typically a perforated plate with numerous circular or rectangular pores, ranging from $5\,\mu m$ to $10\,\mu m$, for inter-cellular communication (Figure 4.17 a and c). This type of porous filter was utilized in the previous subchapter for Stomach-on-Chip application. However, indicated pore arrangement may restrict fabrication throughput from a 3DLL perspective due to the need for sharp turns at a sub-μm scale and frequent open/close laser shutter movements. Thus, an alternative wire-based structure is proposed in Figure 4.17 (b and d), requiring fewer stage movements than the previous structure. The wire structure has a width of $2.5\,\mu m$ with wires separated by $1.5\,\mu m$ and a porosity of $60\,\%$, allowing proteins and nutrients to pass through while preventing cell migration. This wire-based structure is equally suitable for OoC applications, facilitating intercellular communication.

Prior to performing Three Dimensional Laser Lithography (3DLL) in a closed microfluidic channel, it is necessary to load and dry the photoresist within the channel. These two steps significantly impact the printability and mechanical quality of the produced membrane. A critical challenge that arises during closed channel fabrication is the presence of gas bubbles in the channel which can cause defects in the fabricated structure due to incomplete polymerization of the photoresist. Air bubbles can appear in a closed channel by two mechanisms. Firstly, they may arise during the loading of the liquid polymer due to non-uniform flow of the resin. Secondly, bubbles may occur during the drying of the photoresist
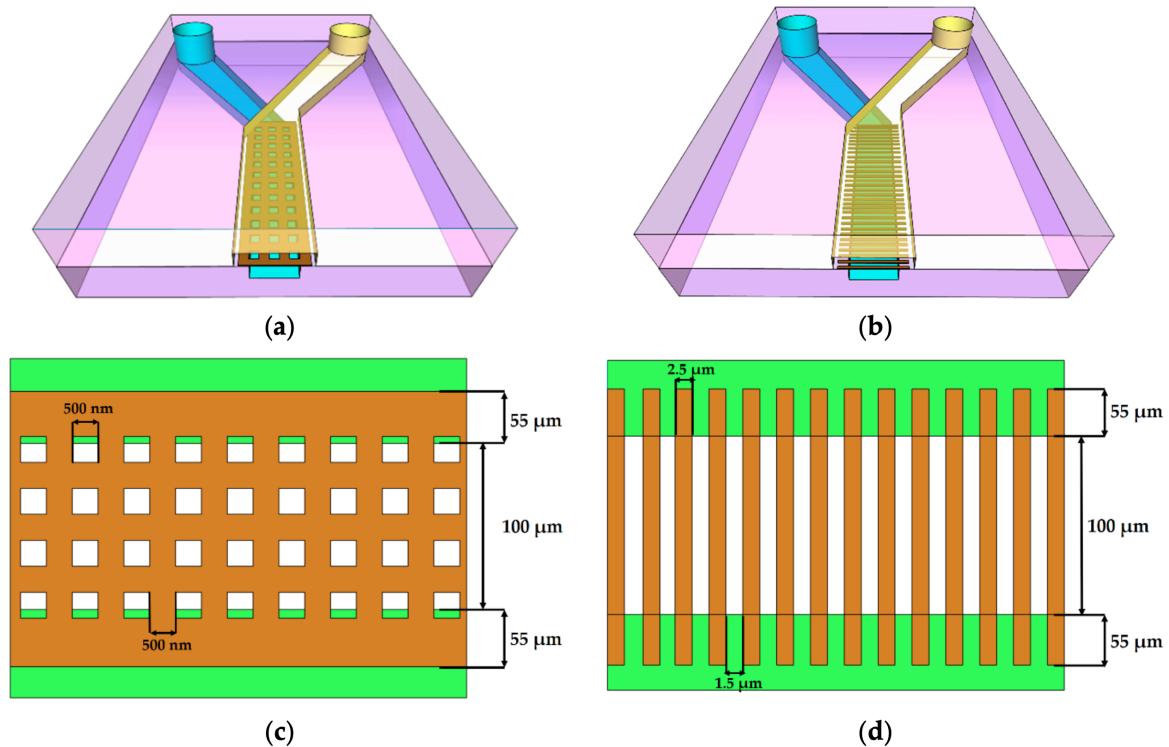
Figure 4.17: Designs of the μ-structures for printing in microfluidic channels. First model is a square grid membrane and second is wire-shaped, where (a and b) are the 3D models of the entire structure between the two microfluidic channels, (c and d) are the 2D top views of the membranes with the annotated dimensions of the periodic structure [25].

in the channel. Therefore, it is crucial to determine the optimal curing time as part of the overall process preparation. This issue is not a concern in standard sample preparation where gas can escape freely from the resin drop on a glass substrate. Attempting to print structures in a non-fully cured photoresist leads to mechanically unstable structures that misalign during fabrication (Figure 4.18, left). Conversely, an excessively long pre-baking time can cause volumetric changes in the loaded material, creating empty spaces and bubbles. Our empirical investigations have determined that the optimal curing time is 45 min at 50 °C, which is 15 min less than the drying time for photoresist in an open environment. A fully aligned structure with stable and accurately repeated separation between the wires, such as the periodic wire array shown in Figure 4.18 (right), can be achieved by carefully avoiding bubbles during the fabrication process.

In this thesis, direct-laser-writing was employed to print membranes that separated two microfluidic channels along a length of 1 cm. Longer channel lengths are advantageous in Organ-on-Chip applications as they provide more surface area for cell culture. Due to limitations in imaging, only a portion of the 1 cm structure is shown in Figure 4.18 (right). During the drying process, the SZ2080 material experiences volume loss and hardening,
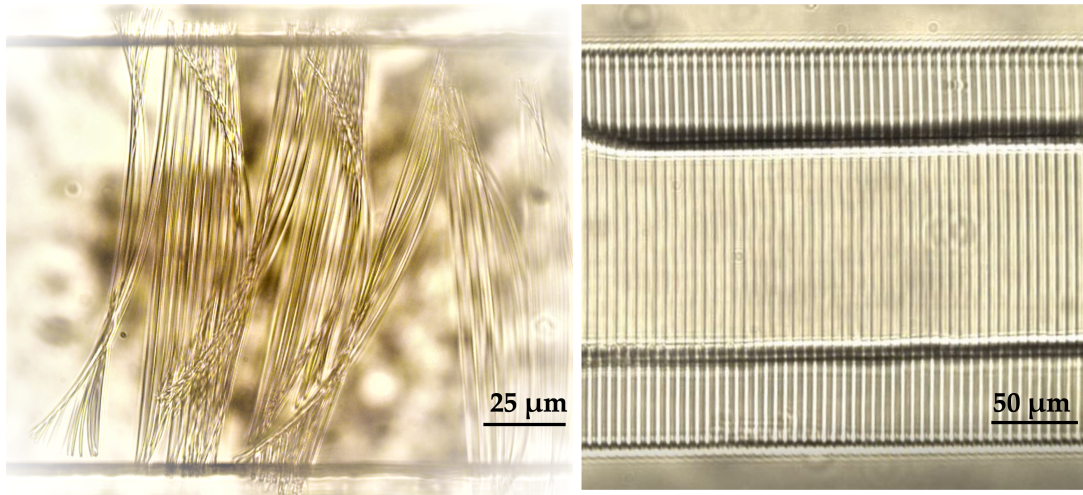
Figure 4.18: Microstructured wire-shaped membrane in microfluidic channel by femtosecond laser. Left side shows the case with incomplete curing of the photoresist in the channel and right side shows the case with a completely cured photoresist [25].

leading to the deformation of the PDMS carrier chip-body. This deformation must be accounted for during fabrication. However, if the condensation (soft bake) process is performed correctly, the overall deformation rarely exceeds 1 µm [25].

As previously mentioned, printing structures inside a closed microfluidic channel poses several challenges. The choice of PDMS wall thickness presents a trade-off between the mechanical stability of the sample and the resolution of the printed structures due to the limited working distance of high-precision, high-NA objectives. Several experiments with different lenses were conducted to determine the best objective for achieving high-resolution printing. The 1.4 NA objective, with a focusing distance of around 300 µm, would be the best option for achieving the highest resolution. Nevertheless, the fabricated chip for printing had a PDMS thickness of approximately 1 mm. This wall thickness is required by the Organ-on-Chip application and ensures the microfluidic chip stability for cell culture and medical experiments. Therefore, due to the PDMS thickness, we used a 0.4 NA objective with a focusing distance of 1.5 mm. Thus, we reached the correct focal plane, precisely between the top and bottom channels (Figure 4.19).

The printing time and complexity of the structure are additional challenges that must be considered for in-situ printing. The 3DLL technique writes the structure point-by-point. This can be time-consuming for complex structures with many geometrical features. For example, the fabrication of a square-grid membrane (Figure 4.17 (a and c)) over a 1-centimeter-long channel using the 3DLL technique takes 13 hours. Over this time, additional deformations could appear due to the over-dry of the loaded photoresist in the microfluidic channel. Due to the gas permeability of PDMS, continuous evaporation of the solvent from the photoresist through the channel's walls occurs. Thus, we decided
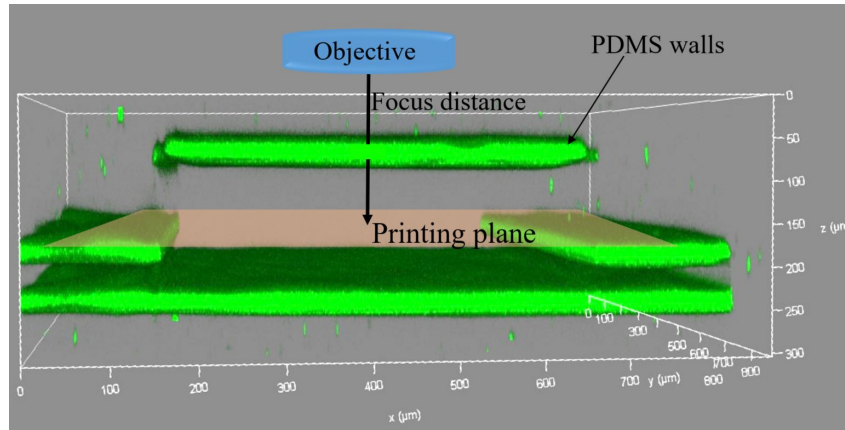
Figure 4.19: Confocal 3D image of the bottom, middle and top PDMS channel's walls with schematically shown objective, focus distance and focal plane. The green color is represented by the PDMS's autofluorescence in the spectral range of 581–695 nm.

to pursue the second approach with the wire-shaped membrane (Figure 4.17 (b and d)), which reduces the fabrication time to 7 hours without negatively affecting the structure's functionality. Moreover, it has another advantage over the classical square-grid membrane since it emulates the natural stomach interface more closely. An interesting observation was made regarding the proposed wire-membrane configuration. Nano-wire connections between the printed wires, which act as additional support for organic substances, were unintentionally formed due to the self-polymerization process that occurs if two lines are made sufficiently close to each other (Figure 4.20). Nevertheless, this effect is highly beneficial, as it provides additional mechanical stability for the membrane.

Also, an additional step in the process preparation, which can be time-consuming, is z-coordinate compensation. If the PDMS chip is deformed significantly, then this procedure can ensure the correctness of the printing (focal) plane over the entirety of the 1 cm long channel. Therefore, before initiation of printing, a manual or software check of the focus over the complete laser path is required. In this work, the tilt of the sample was marginal, and straightforward fabrication without any compensation was possible. Therefore, each PDMS chip was placed on the glass slide and adhered to it due to the sticky properties of PDMS. The microfluidic chip was removed from the glass slide only after completion of the printing process. This saved preparation time, prevented over-dry of the photoresist SZ2080 and eliminated PDMS chip deformations.

Nevertheless, the most intense deformation appears in the following technological step. The development of printed structures in a closed microfluidic channel using the "ship-in-a-bottle" method is a challenging process due to the limited access of the liquid developer. Removal of the un-polymerized substrate during the development step opens the channels, and 4-Methyl-2-pentanone is a gentle solvent that is suitable for developing non-
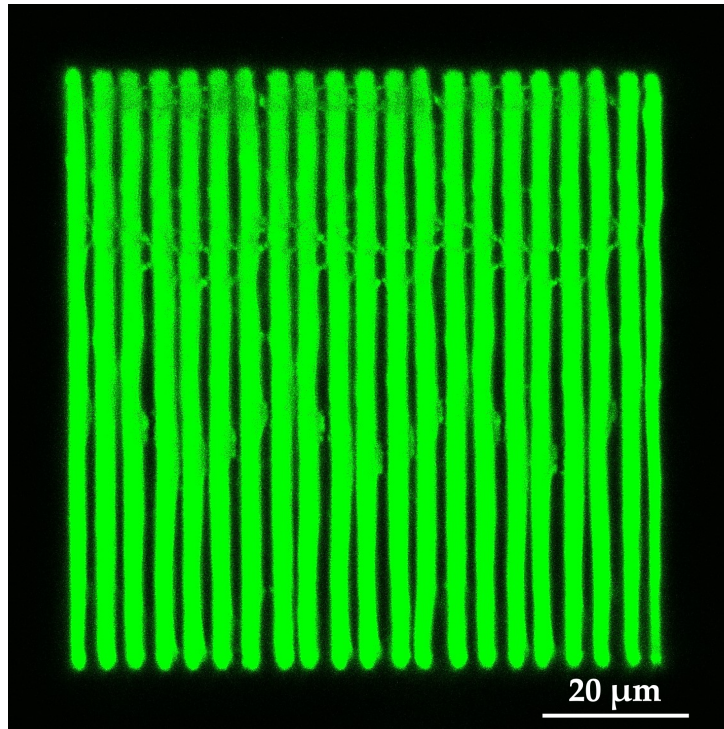
Figure 4.20: Femtosecond laser structured membrane with the nano-sized interconnection between the "wires" [25].

polymerized photoresist SZ2080 in open structures. However, both 4-Methyl-2-pentanone and 2-propanol are not suitable for development in closed microfluidic channels due to the swelling of the PDMS, which poses a major challenge in maintaining the mechanical stability of the printed structures, and they can break (Figure 4.21)

Acetone is the most aggressive solvent that can develop residual non-polymerized photoresist, even with low accessibility, but it also causes deformation and damage to the printed structures. This deformation also affects the adhesion of the printed membrane to the PDMS. One possible solution is to physically fix the PDMS chip to the glass to prevent deformation. Therefore, the membrane can be printed inside the closed microfluidic channel with minimal deformations, which even with mechanical fixation could not be excluded. Nevertheless, most of these deformations are in the range of the cell size (Figure 4.22). The biocompatibility of the photoresist SZ2080 [116] and the negligible nature of these defects yield a membrane that is suitable for Organ-on-Chip applications. The realized wire membrane is effectively a one-dimensional periodic structure, similar to a 1D diffraction grating. Figure 4.23 confirms this effect, as we see the separation by colors corresponding to different wavelengths thank to the periodic membrane structure, which in turn confirms the accuracy of the fabricated periodic device.

To summarize, a 1 cm long membrane was printed inside the closed PDMS microfluidic channel by the femtosecond laser or two-photon polymerization method. Such additive manufacturing of the structure for cell culture opens a wide range of opportunities to tune
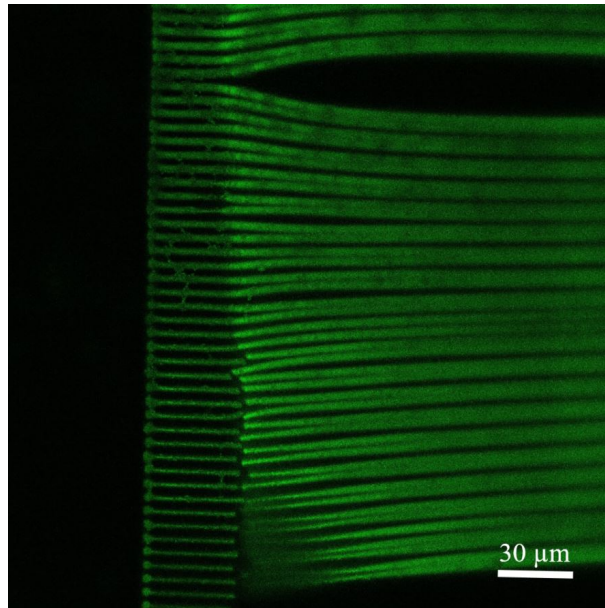
Figure 4.21: Confocal microscope images of the membrane in microfluidic channel printed by femtosecond laser, developed in 2-propanol [25].
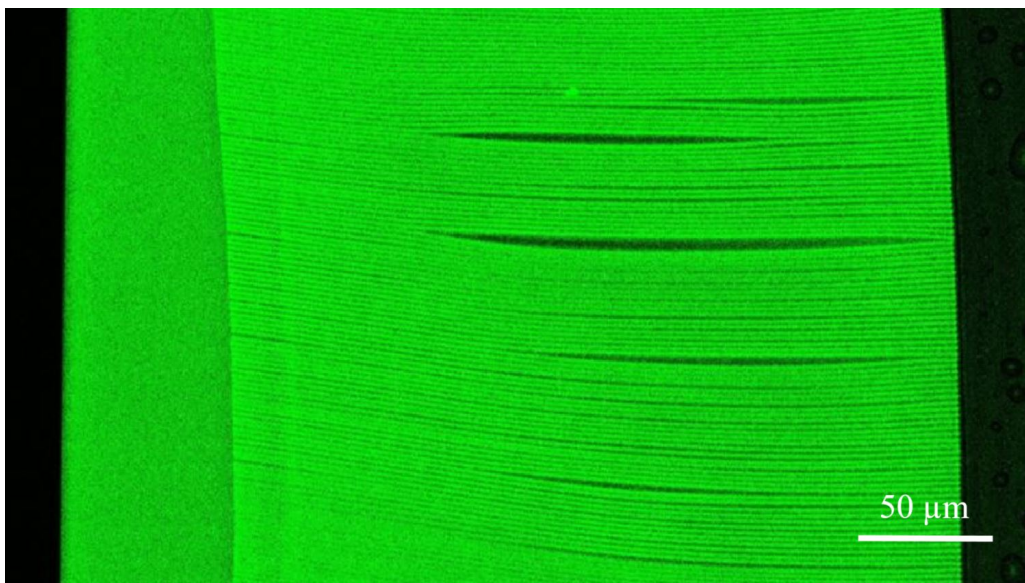
Figure 4.22: Confocal microscope images of the membrane in microfluidic channel printed by femtosecond laser and developed in acetone.

the membrane's properties according to the cell type and biological inquiry. Nevertheless, the completely-optimized printing process still has room for improvement, despite the fact that an already-functional printed structure was developed. The goal of this further improvement is to eliminate any PDMS chip deformation in order to keep the printed structure safe from damage and deformation. Also, the adhesion force between the PDMS andstructures printed by 3DLL can be improved with a surface plasma treatment before loading the photoresist or with chemical modification of the inner surface of the

channel with (3-Aminopropyl)triethoxysilane. Another solution is to use three-dimensional laser lithography (3DLL) to print the entire microfluidic system. However, suitable elastomers for 3DLL are currently limited and tend to shrink substantially after fabrication. Nevertheless, this approach allows for more flexibility and the integration of functional elements, such as valves, during the same printing step. The results presented in this study provide a foundation for further research in expanding the use of 3DLL in Organ-on-Chip manufacturing.
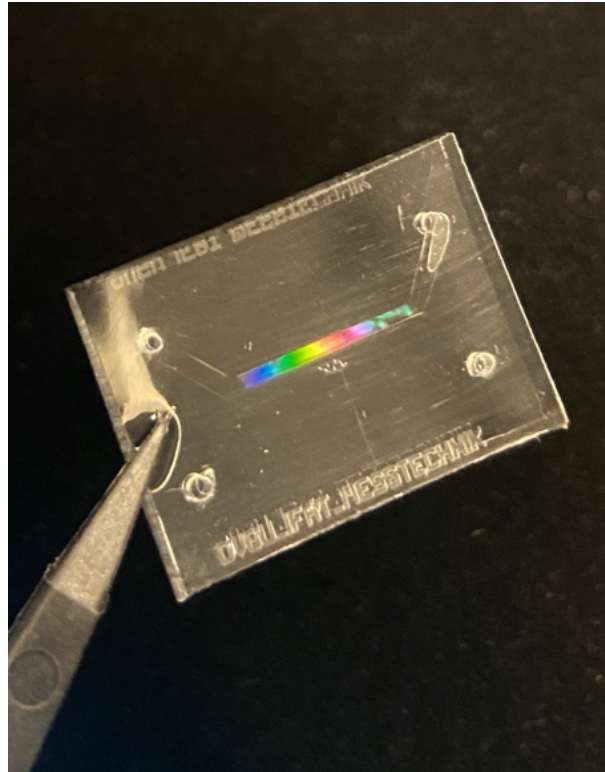
Figure 4.23: Microfluidic PDMS-based chip with the femtosecond laser structured membrane. The light dispersion points to the nano-resolution of the structure printed in closed microfluidic channels [25].

4.4 Conclusions and future outlook

This chapter presented a microfluidic chip for cell culture and tissue engineering. A novel bonding technology for bonding a porous filter to silicone was developed based on a state-of-the-art concept with two microfluidic channels divided by a membrane. This technology allows bonding any porous material to structured layers for assembly of the microfluidic chip. Compared to state-of-the-art technologies, this method ensures flexibility in choice of the consumed materials and reduces the fabrication time from days to several hours. This means, the ability to use thin filters with a wide range of pore size and density, thicknesses, and material properties as a membrane becomes straightforward. Therefore,

it is possible to realize corresponding surroundings that are specific for a given cell type. These are beneficial advantages for every Organ-on-Chip application, since this is an ongoing field of research. Various cell types, representing different organs, can be cultured in microfluidic devices. Therefore, the work in this chapter describes a microfluidic chip design and fabrication for the purpose of mimicking the parts of the human stomach. The proof of concept was successfully achieved by culturing human gastric epithelial cancer cells and by testing a chemotherapeutic drug on the cultured tissues. These experiments will be conducted on human stomach organoids in the future. Therefore, the channel height was already adjusted to accommodate the larger volume required by the organoids. Also, the optimal channel width for Stomach-on-Chip was found experimentally and is 1 mm. For fabrication of the microfluidic chip, a master mold for the silicone was optimized and developed by soft lithography. Consequently, further cell culture and drug screening experiments can be done in the developed microfluidic devices. Models, such as the one presented here, could become an alternative for pre-clinical drug testing on animals, if sufficient statistics are gained for approval by the approval agencies. Furthermore, a 1 cm long membrane with nano-resolution was printed inside a closed microfluidic chip. Regarding the optimal printing time, a wire-shaped membrane's geometry was chosen. This geometry is also beneficial for the Stomach-on-Chip application since it emulates the wrinkled stomach surface. Every "wire" in this membrane is 2.5 μm wide and the distance between the wires is 1.5 μm. To the best of author's knowledge, this is the first membrane in a microfluidic channel structured by femtosecond laser. The complete structuring process was developed and optimized in this work. The most challenging part is structure development inside the closed microfluidic channel, due to the limited access to the liquid which removes residual non-polymerized photoresist. In addition, tPDMS, due to its material properties, swells in different solvents. This could cause deformation of the printed membrane. Therefore, this part of the process could be further optimized. Moreover, additional 3D geometries could be tested. Also, as was mentioned previously in Chapter 2 and will be described in Chapter 7, a microfluidic chip is a suitable platform for sensor embedding. This could enable measurements which are not accessible via a microscope and must be done in the cell's nearest surroundings. Therefore, such a microfluidic chip with an adjustable assembly process can be equipped with a broad variety of micro-sensors for physiological conditions, cell-cell communication, and released biological substances.

5 ImmunoChip

5.1 Microfluidic chip for studying the immune cells

T cells are part of the body's immune system and play a significant part in protecting the organism from infections. The communication between macrophages and T cells is crucial for the immune system to defend the host. Mistakes in this communication can lead to immunodeficiency, autoimmunity, failure to destroy invading pathogens, and cancer [117]. Intraperitoneal (IP) macrophages are required to initiate the immune response by activating T cells, since they eliminate bacteria, pathogens, and malignant cells. A deeper understanding of T cells' detection and interaction processes with macrophages can significantly improve the healthcare system, since the human body's immune system is a natural protection mechanism that is much more advanced than any existing therapy. Therefore, a promising research direction is to find ways to assist the immune response. The investigation of interactions involving moving T cells and stationary macrophages was carried out within Petri dishes. However, a challenge arose during the process of pipetting T cells into wells containing IP macrophages. Some T cells fortuitously landed near macrophages, leading to unexpected interactions that hindered the analysis of the initial cell interactions. To address this, it was necessary to prevent these coincidental contacts before imaging. As a solution, a microfluidic chip was developed in collaboration with Prof. Dr. A. Müller's group, Institute for Molecular and Clinical Immunology, Otto-von-Guericke University. The device concept is based on three parallel glass bottom channels connected by perpendicular microchannels with a subcellular diameter, yet large enough for active transmigration. The setup must allow imaging of the initial interactions between T cells and intraperitoneal (IP) macrophages and simultaneously prevent undesired cell-cell contact.

To realize this system, a novel microfluidic device was developed and fabricated during the course of this work. Therefore, the following sub-section presents a detailed view on the development, fabrication and applicability of the PDMS-based microfluidic channels for study of the interactions between T cells and intraperitoneal (IP) macrophages under various circumstances. Chapter 5 is structured as follows:

- Section 5.1.1 presents detailed design considerations of the microfluidic chips for experiments with immune T cells, providing biomedical insight, discussion of the microfluidic device with a high level of integration, and qualitative specifications,

- Section 5.1.2 provides a detailed description of the physical design, layout, and manufacturing of the 3D microfluidic device,

- Section 5.2 describes the application of the PDMS microfluidic chip manufactured in Section 5.1.2 for study of the interactions between T cells and intraperitoneal (IP) macrophages under different circumstances,

- Section 5.3 summarizes this chapter, provides an outlook into the future and emphasizes the key novel results reported in this section.

5.1.1 Chip Design Considerations for ImmunoChip

The main goal is to create a microfluidic system without active pumping for two cell types: macrophages obtained from the peritoneal cavity of a mouse infected with Leishmania major and $CD4^+$ T cells. In this microfluidic system, macrophages must proliferate and stay in a stable position. Simultaneously, the immune T cells must be able to migrate, but not in clusters. Only single-cell motion is desired so that T-cell motion toward the macrophages can be tracked and a single fluorescence signal, which appears during contact between macrophages and T cells, can be recognized.

Thus, the system must include channels for storing the cells and channels for the active migration of a single-cell. The size of the $CD4^+$ T cells is approximately 5 - 7 µm in diameter. The tiny interconnecting channels must be the sub-cell size to ensure the active migration of the single cells toward the macrophages. At the same time, storage channels have to contain the complete amount of cells and the required medium volume to provide the cells with nutrition and life-supporting components. Thus, the following dimensions were chosen: 150 µm and 100 µm wide for large channels and 6 µm wide for small microfluidic channels. The 3D CAD design of the microfluidic chip is shown in Figure 5.1.

Generally designed experiments with cells can be described by the following steps. First, the macrophages are seeded in the middle of a 150 µm wide channel (see Figure 5.2). Then, T cells are loaded into the side microfluidic channels which have a width of 100 µm. Additional fluorescence components assist in tracking the cells during migration through the interconnecting channels. For detection and analysis of cells' behavior, optical investigations using high-resolution optical and fluorescence microscopes were planned.

To provide the cavity for the macrophage's proliferation and for time-limited hosting of $CD4^+$ T cells andto provide for channels for active movement of T cells towards the macrophage, the experimental setup must consider and fulfill the following requirements.
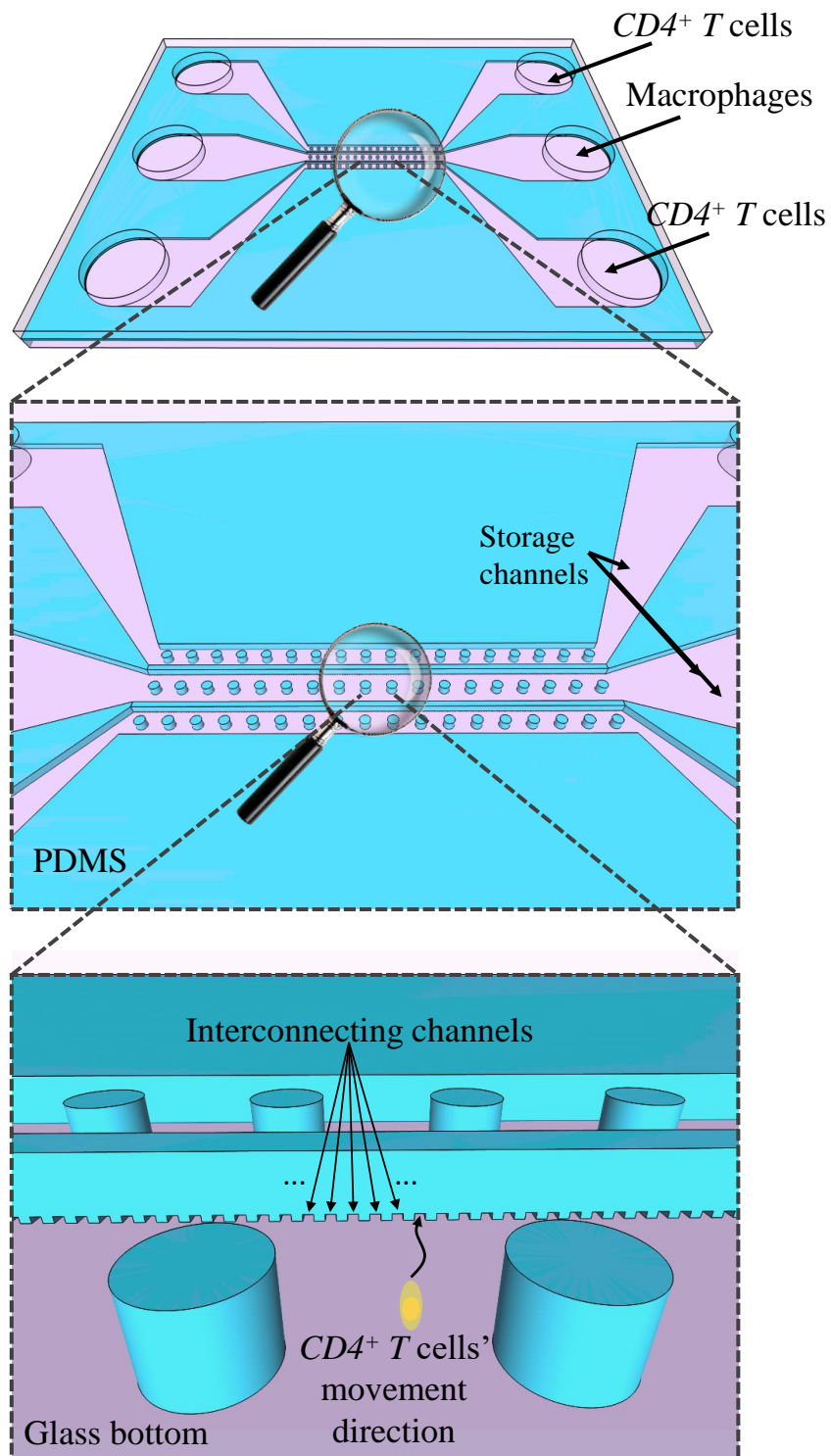
Figure 5.1: 3D schematic view of the ImmunoChip.
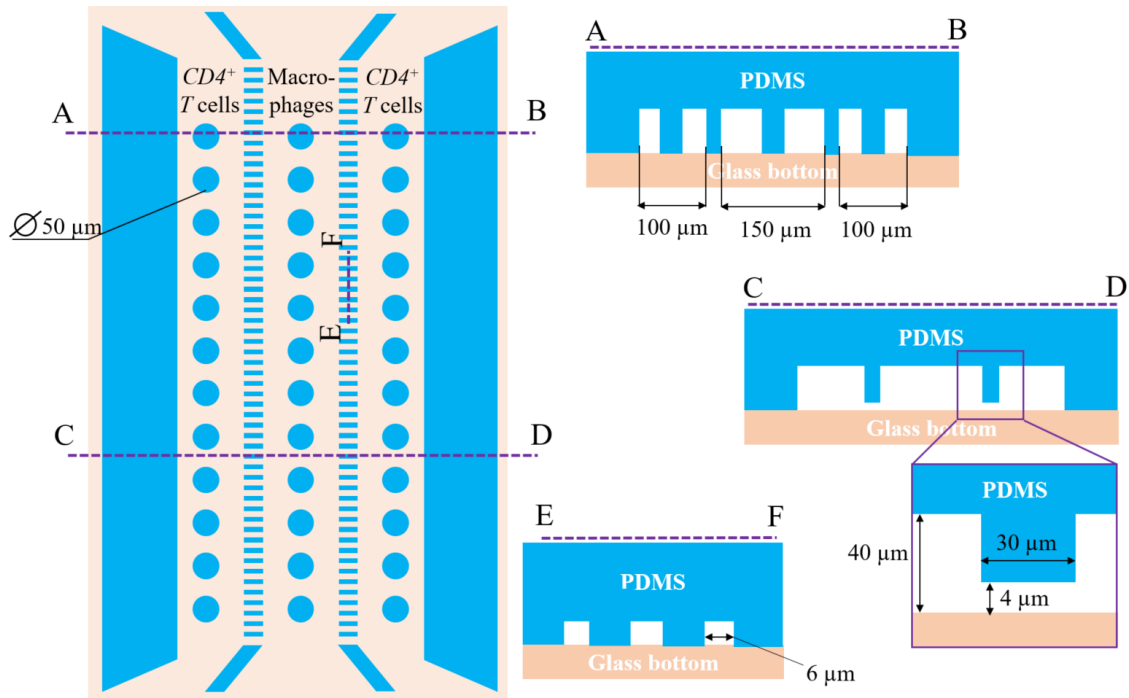
Figure 5.2: 2D schematic view of the ImmunoChip with the specified dimensions.

This can be translated into specifications for the microfluidic chip and address the following design properties:

- **3D configuration of the channels:** As was previously discussed, the microfluidic system includes two clusters of channels: storage channels and interconnecting channels (see Figure 5.2). The width of these channels is $100\,\mu m$, $150\,\mu m$ for a storage cluster and $6\,\mu m$ for interconnecting. The soft lithographic process can realize the different widths according to the shadow mask design. The challenging part lies in the z-coordinate or height differences of the microfluidic channels. As the interconnecting channels are required to ensure single-cell migration, their height should not exceed $4\,\mu m$. Nevertheless, the storage channels have to be at least ten times higher to ensure a sufficient amount of cell culture medium. To summarize, the ImmunoChip has to consist of the three storage channels with a width of $100\,\mu m$, $150\,\mu m$ and $100\,\mu m$ and a height of $40\,\mu m$. They have to be interconnected by smaller channels, which are $6\,\mu m$ wide, $4\,\mu m$ high and $30\,\mu m$ long (see Figure 5.2). Therefore, the microfluidic structure is three-dimensional, as storage and interconnecting channels are different in height.

- **Gas permeability of the microfluidic device:** Since the experiment runs over 4 hours without induced flow, the cells must receive the necessary gas, such as oxygen and CO_2, through the chip material. Therefore, at least one side of the microfluidic chip has to be made of a gas-permeable material. PDMS has a clear advantage due to its high gas permeability. A challenge related to high gas permeability is liquid

evaporation and air bubble appearance in the microfluidic channel. This can be bypassed with droplets of the medium placed on the chip's inlets and outlets, which will ensure an additional liquid volume and that evaporation from the chip will not dramatically impact the appearance of air bubbles.

- **Possibility for high-resolution microscopy:** As specified in the last item, only one part of the chip must be made out of PDMS to ensure gas permeability. This layer will be specified as a top part. In turn, the bottom layer has to serve another requirement - high-resolution microscopy. Therefore, the bottom wall of the chip has to be thinner or equal to the thickness of the microscopy slide, which is 170 µm, since fluorescence analysis and microscopy will be used to detect the cell's interaction and motion. Also, it is desirable to have the glass slide at the bottom because cells, affected by gravity, will launch on the bottom layer. Thus, the bottom layer should be non-structured to avoid any unnecessary barriers for the cells.

- **Optical transparency of the complete microfluidic device:** As long as one side of the microfluidic chip is transparent, microscopic imaging of the cells can be done, e.g., by an inverted microscope. Nevertheless, complete transparency of the chip is required as well. Complete transparency allows cellular biologists to observe the pipetting process while cell loading, ensure the absence of air bubbles, and perform phase contrast imaging. Also, complete transparency is required to monitor cell concentrations by optical means, such as the microscope and fluorescent analysis. The combination of a bottom thin glass slide and a PDMS structured top part of the microfluidic device ensures its full transparency. Considering the first requirement of gas permeability, PDMS is the best choice of material in this case, while it offers inherent optical transparency as well.

- **Adsorption in the microfluidic chip:** PDMS has a known drawback of molecular adsorbance. However, in this particular case, this disadvantage can be disregarded since the critical or must-measure components are absent. The fluorescence components responsible for highlighting the cell's location only emit light through targeted reactions. Consequently, even if PDMS adsorbs some of these components, it will not emit light within the chip material, as there are absent cells for reaction. Therefore, the analysis will remain uninterrupted.

- **The elasticity of the microfluidic chip:** Although not strictly necessary, flexibility and elasticity in the microfluidic structure provide significant advantages. While elasticity focuses on the capacity of a stretched material to regain its initial form after stretching forces are eliminated, flexibility pertains to a material's ability to bend readily without fracturing. It distinguishes flexibility from elasticity, as they represent different material properties. These characteristics reduce mechanical

stress on the cells during loading (seeding) and allows soft deformations resembling natural conditions. Additionally, as cells actively migrate through the interconnecting channels, elasticity, flexibility, and stretchability aid in overcoming the migration obstacle created by the narrow channel. It is not an easy task for cells to migrate, as the channels' size is approximately 1 μm smaller than the cell's size. PDMS inherently provides these advantageous features due to its high flexibility and elasticity, which can be adjusted per the needs of the specific application.

- **High level of integration:** This experiment is designed for investigation on the single-cell level of the active migration of several hundred cells. All T cells and macrophages are first located in storage channels, which are connected via the interconnecting migration channels. It is exactly these interconnecting channels that have to be realized in a sufficient number so that most of the T cells can penetrate simultaneously. This leads to a requirement for large-scale integration of the microfluidic channels [118]. In this case, the microfluidic channels must be realized in both a large number and also planar on a limited surface. The complete ImmunoChip channel area must also be simultaneously visible to the microscope. To meet these requirements, the width can not exceed 0.6 mm, but the length of the structure could be extended to gain broad statistical data. A length of 2 mm was chosen. Therefore, the chip will be shifted four times during the experiment to obtain imaging of the complete structure.

- **Optimized liquid flow:** To ensure the complete filling of the interconnecting channels, the chip has to be filled with MilliQ or DI water directly after fabrication. In the following 30 min after oxygen plasma treatment, PDMS is highly hydrophilic, and the chip can be filled by the capillary forces. There is no active pumping designed for the experiment except for pipetting of the medium with cells and macrophages. Therefore, wetting the PDMS surface when it is hydrophilic is essential. Otherwise, the appearance of air bubbles would be unavoidable. Nevertheless, during the loading of cells into the chip using a pipette, the applied forces have to be carefully controlled to avoid mechanical forces which could over-stress the cells and macrophages.

5.1.2 Microfluidic Chip Fabrication

A microfluidic device for studying immune cells (ImmunoChip) was fabricated by the methods described in the Sections 3.1.2, 3.2 and 3.3 according to the requirements listed in Section 5.1.1.

The main challenge in microstructuring for this application is the 3D master mold fabrication (Section 3.1.2), since PDMS will replicate the complete structure fabricated on the wafer. The channels differ in all three coordinates, which is not the case for the

other microfluidic devices reported herein. To realize this structure, a two step fabrication technology was developed: the first step is a lithographic process with optimized parameters, and the second step is femtosecond laser direct writing on the pre-structured wafer. The complete master mold concept is shown in Figure 5.3.
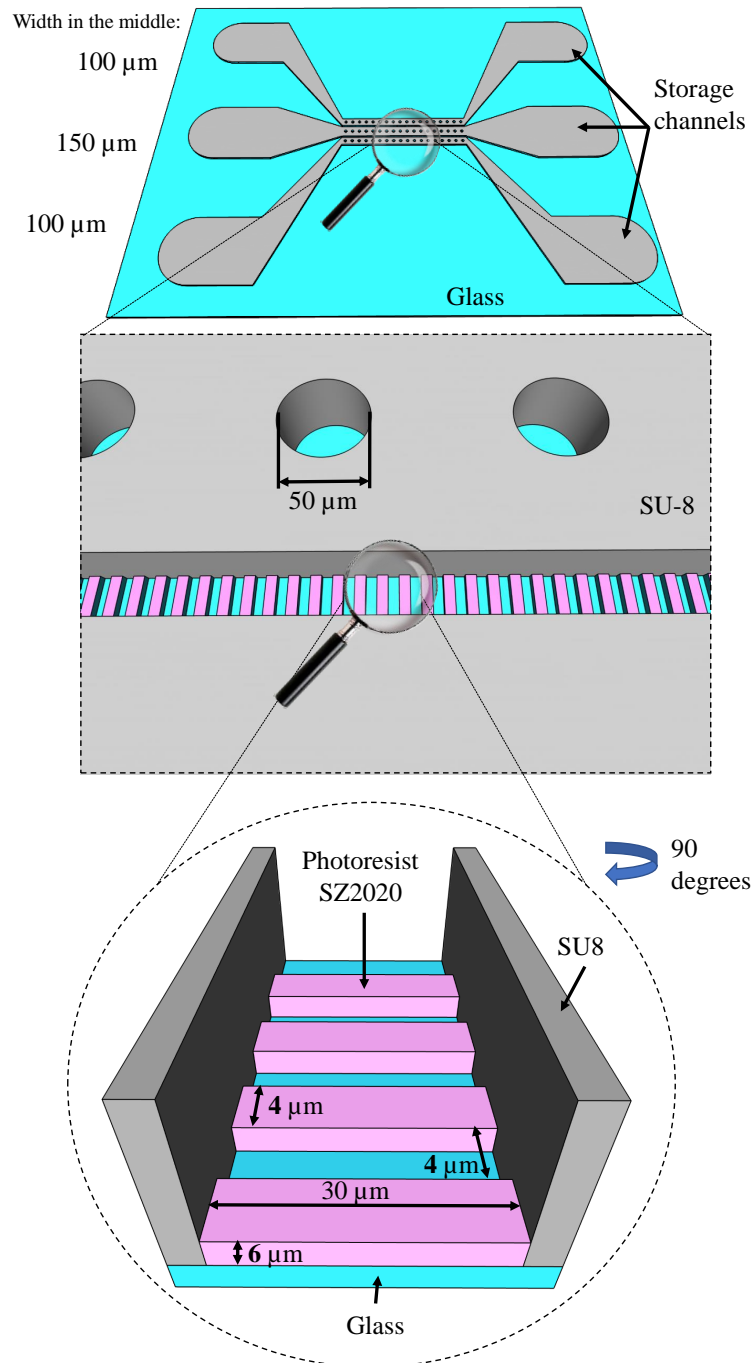
Figure 5.3: Schematic view of the master wafer design for ImmunoChip. Pink colour represents the femtosecond structured patterns for micro-channels. The grey color is for SU-8 structures (width 100 mm, 150 mm and 100 mm), blue color represents the glass wafer.

As shown, the structures for replicating storage channels (grey color) are relatively large and could be obtained with the soft lithographic process. In this case, photoresist structuring parameters must be optimized considering the subsequent processing, e.g., femtosecond laser direct writing (3D laser lithography, pink color in Figure 5.3).

The first step is the photolithographic process, parameters of which are listed in Tables 3.3 and 3.4. A glass wafer is chosen as a carrier for the master mold structure. This is a necessary requirement for femtosecond laser structuring, which can subsequently be done only through the wafer, because the 40 mm high walls of the storage channels would result in shadowing and make 3D laser lithography impossible. In its turn, the soft lithographic process on the glass wafer has to be optimized according to a balance between the exposure dose and the efficient development of the unexposed photoresist. An alternative carrier is a silicon wafer, where UV light reflected at the wafer surface comes back into the photoresist layer and ensures its complete exposure. Therefore, the adhesion of the SU-8 exposed photoresist and silicon wafer is achieved. In the case of the glass wafer, the top layer of the photoresist is exposed and the rest of the light energy is transmitted through the wafer to the mask alignment machine holder. Moreover, this holder causes undesired reflections which can lead to partial exposure in regions where the photoresist needs to stay unexposed. Therefore, fabrication of the structure can be unsuccessful, as shown in Figure 5.4. As seen, the layer is partially undeveloped, resulting in the presence of photoresist debris, and a part of the layer in contact with the wafer remains unexposed. In this case, the channel structures tended to delaminate even after short development.
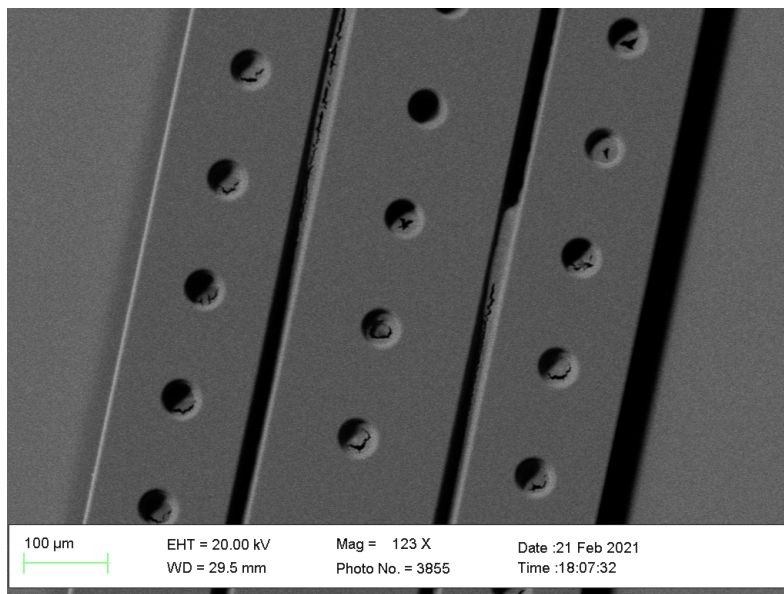
Figure 5.4: SEM microscope image of the SU-8 structures made by soft lithography without underlayer. The residual photoresist debris is visible in this image.

To improve the exposure step, the glass wafer can be placed on a carrier, which reflects the UV light back into the photo-reactive layer or, alternatively, absorbs the light energy

and prevents the random return of photons into the spin-coated photoresist. The first technological trial was based on the use of a silicon wafer as a carrier under the glass wafer for the exposure step. During exposure on the silicon/glass wafer, the exposure dose is kept similar to the dose for exposure on the silicon wafer. Otherwise, overexposure causes loss of the structural shape. Nevertheless, undesired reflection occurred due to the silicon/glass interface and the thickness of the glass wafer. The resulting structures were determined to be unsuitable for further processing. The subsequent approach was to place a black body under the glass wafer and expose the photo-reactive layer with an increased exposure dose. In this case, the UV light passes through the photoresist layer only once and is adsorbed when it leaves the substrate. This significantly improved the quality of the fabricated structures, and only a few debris were left inside of the cylindrical structures, which in the replica will serve as columns for holding the roof of the microfluidic channels. Possible reasons for the residual debris are the refractive surface at the bottom of the glass wafer, the glass/black body interface, and the non-ideality of the black body. Therefore, to improve the photolithographic process and successfully fabricate the structures on a glass wafer which will be suitable for subsequent processing, a layer of ZnO nanoparticles dissolved in toluene was spin-coated on the bottom side of the wafer. The maximal ZnO light adsorption occurs at 367 nm [119]. Hence, this layer absorbs all of the light transmitted through the photoresist and glass wafer, preventing any undesired reflections. In this case, a higher exposure dose has to be set to ensure the complete exposure of the necessary areas. The parameters for this process are given in Section 3.1.2. The optimized process positively impacted the integrity of the fabricated micro-structures, as shown in Figure 5.5.
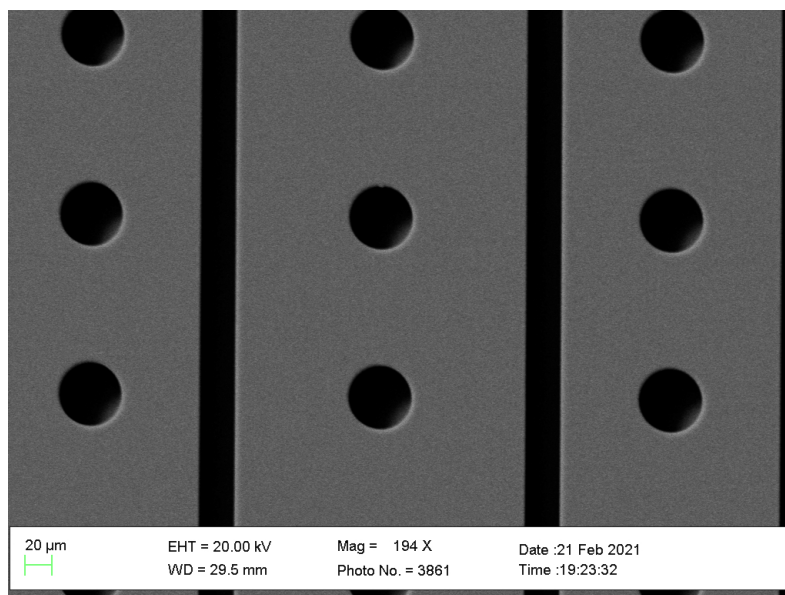
Figure 5.5: SEM image of the SU-8 structures made by soft lithography on Borofloat glass wafer with ZnO underlayer. The residual photoresist debris is fully removed.

After optimization of the soft lithography process and obtaining the structured elevations for replicating the microfluidic channels, the subsequent step of structuring can proceed. As previously mentioned, this next phase of processing is carried out using the femtosecond laser. Producing the required microfluidic masters with two highly different feature sizes is a challenging task for standard lithographic techniques. As a result, it was decided to pair one-step lithography, used to acquire the master part needed for larger channels, with the 3D laser lithography (3DLL), which can be employed to integrate smaller features into the master [120]. Indeed, 3D laser lithography is an ideal tool for such a task, as it combines sub-micron level precision/resolution with the capability to create structures within other structures.

One of the key aspects of integrating features using 3DLL is choosing the proper configuration of the sample in relation to the focusing direction. Intuitively, it would seem that shining through the material drop to the sample is the simplest solution. However, in this case the pre-polymer drop de-focuses the laser beam and additional uneven aberrations occur due to the curved shape and varying depth of the material, distorting voxel shape and size [121, 122]. Also, SU-8 present in the pre-polymer would induce further shadowing, potentially making features close to the original master of lower mechanical quality [123]. Thus, to accommodate proper focusing, the sample is placed in a drop-down configuration. Then, the laser beam needs to pass just the 350 μm thick glass substrate, resulting in constant and well-predictable aberrations and no shadowing.

It was determined that the laser-made structure matched requirements within 1 μm tolerance. Furthermore, photoresist SZ2080 showed excellent adhesion to both glass substrate and SU-8, resulting in an excellent master suitable for PDMS molding. Additionally, the process ended up being highly efficient, with each integration only taking 30 min or less. Once the master mold with 7 identical structures for replication (Figure 5.6) was obtained, liquid PDMS can be poured thereon and cured, as described in Chapter 3. The best way to avoid creation of air bubbles in the fabricated structures is to cure PDMS at room temperature over 48 hours. This long curing time ensures that all bubbles created during mixing of the PDMS are naturally removed. Figure 5.7 shows the microscopy images of the master mold fabricated by soft lithography (a), then the same structure over-printed by the femtosecond laser to create migration channels (b) and the resulting PDMS replica of this mold (c). As it is seen, bubbles or defects are absent in the replicated PDMS part.

The challenging process in ImmunoChip fabrication is release of the cured PDMS from the master mold. Two photoresists (SU-8 and SZ2080) and two technologies (soft lithography and 3DLL) were used for fabrication. Therefore, the adhesion between SU-8 and SZ2080 is sufficient but not ideal, as opposed to the case where only a single material is utilized. Thus, the PDMS layer has to be removed extra slowly and carefully to ensure the stability of the master mold and the completeness of the replicated structures. Adhesion of the PDMS to the glass wafer, in this case, is minimal and does not interrupt the release
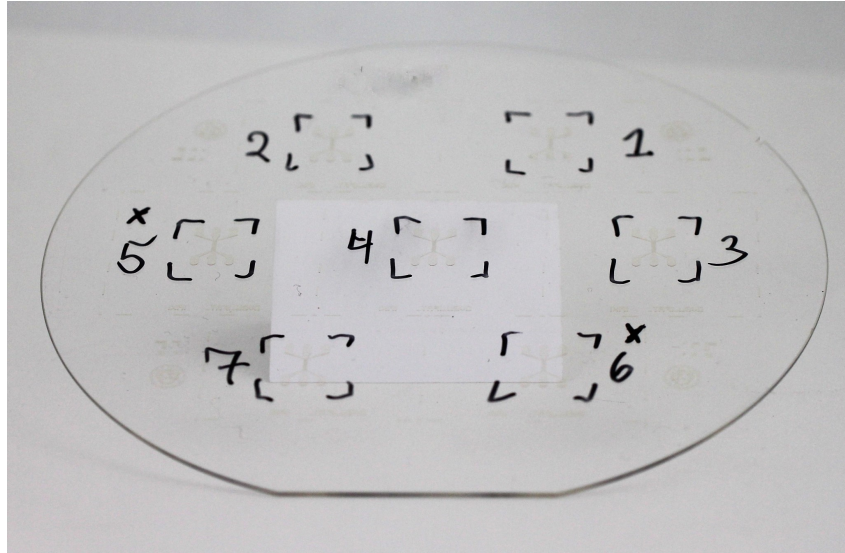
Figure 5.6: Photograph of the completed master mold wafer for ImmunoChip. There are 7 identical structures (marked by the black squares) on the wafer made by a soft lithography process and overprinted by the femtosecond laser.
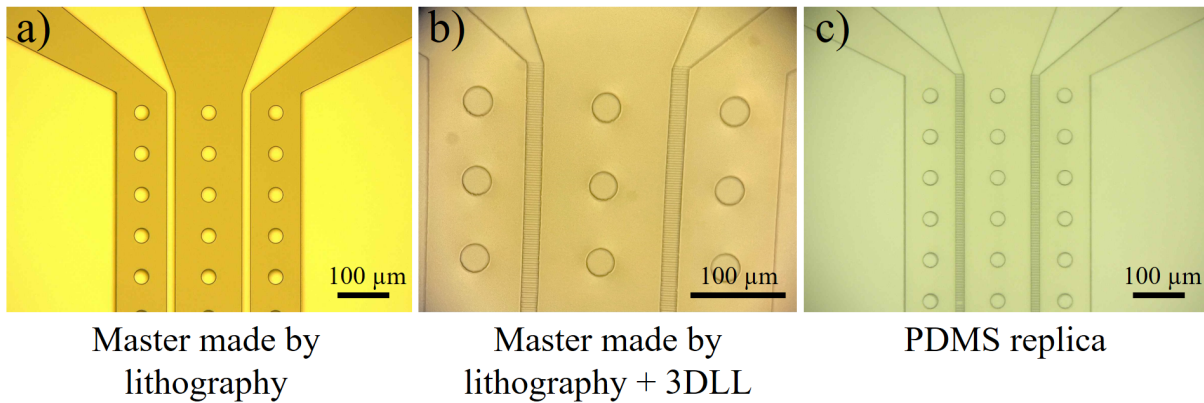
Figure 5.7: Microphotograph of the pre-structured master wafer created by soft lithography with three structures for molding the storage channels (a), the same wafer with structures overprinted by femtosecond laser for molding of migration channels (b) and PDMS replica made employing the shown master mold (c).

process. This is a consequence of processing the wafer with SU-8 photoresist, which possesses a low adhesion to PDMS. The released PDMS layer is cut and each chip is bonded to the 170 µm thick microscopy cover glass slide. The process parameters are listed in Section 3.3.

The completed ImmunoChip is shown in Figure 5.8 (a).
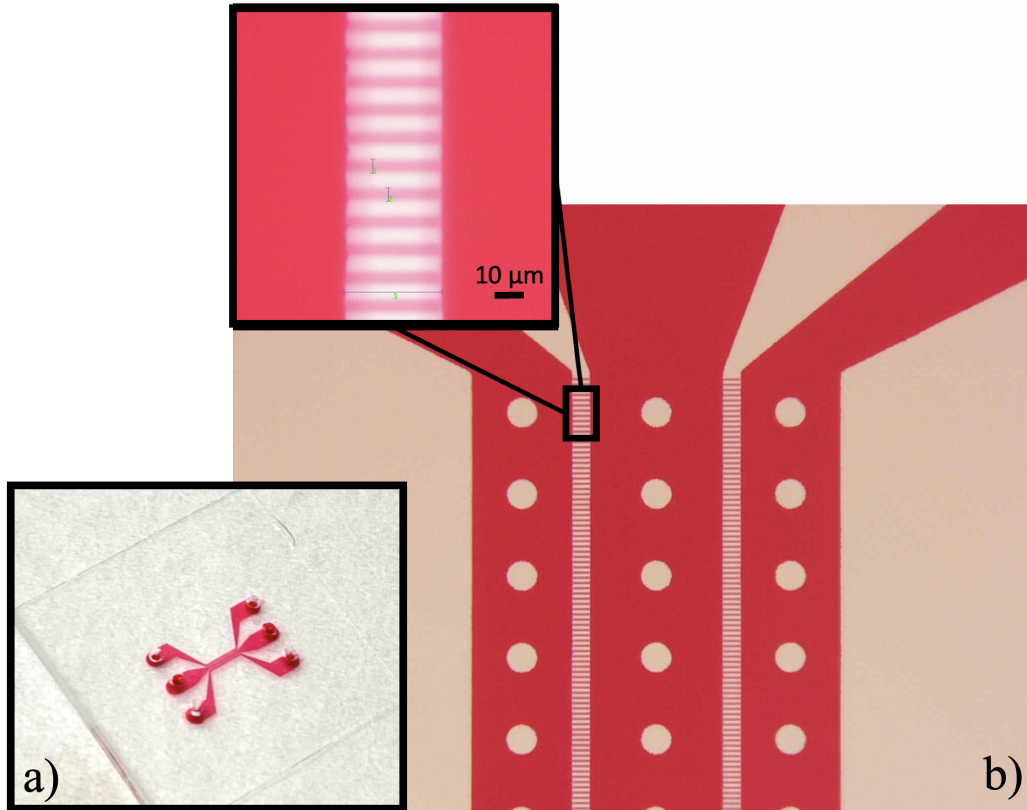
Figure 5.8: Photograph of the fabricated PDMS/glass microfluidic chip for immunology applications (ImmunoChip) (a) and magnification of the $100\,\mu$m and $150\,\mu$m wide channels for storage of macrophages and T cells (b). In insert are shown micro-channels for interconnection, which are $4 \times 6 \times 30\,\mu$m^3. The chip is filled with red ink to visualize the channels.

For the PDMS/glass bonding process, oxygen plasma was employed. Oxygen plasma changes the PDMS surface to hydrophilic. Therefore, the chip has to be filled with DI water directly after fabrication to ensure a homogeneous fill and to avoid air bubbles in the microfluidic channels. Subsequently, the liquid can be replaced by the cell culture medium or any other liquid. Therefore, pipetting has to be done carefully and in the aqueous environment, e.g., with the liquid drop on each inlet and outlet. An example of homogeneous chip filling and the absence of air bubbles is shown in Figure 5.8 (b). The chip is filled with colored DI water directly after completing the bonding process.

5.2 Proof of concept: PDMS microfluidic chip for T cells and macrophages

The study of immune cell behavior and interactions during infections is crucial for understanding the complexities of the immune response. To investigate these interactions at a microscale level, the microfluidic chip shown in Figure 5.8 was used. It is a crucial tool for conducting a series of groundbreaking experiments aimed at study of the interactions between infected macrophages and immune cells. The design and functionality of the chip allowed for precise control and visualization of cell behavior within a confined environment, mimicking aspects of the in vivo conditions. In this experiment, macrophages obtained from the peritoneal cavity of mice were infected with Leishmania major and pipetted into the middle storage channel. Additionally, $CD4^+$ T cells were introduced into the side storage channels (Figure 5.1). The aim was to understand the migration and interaction dynamics of $CD4^+$ T cells with infected macrophages using advanced imaging techniques, including CellTracker Deep Red (CTDR) staining and Fluo-4 calcium imaging. Also, in order to visualize these interactions, a Leica DMi8 video microscope for real-time imaging was employed. Time-lapse microscopy allowed researchers to track the migration of $CD4^+$ T cells towards the infected macrophages and observe the dynamic interactions between these immune cells in real-time.

To begin the experiments, macrophages were isolated from the peritoneal cavity of mice and subsequently infected with Leishmania major, a parasitic protozoan responsible for the disease Leishmaniasis. These infected macrophages were then gently pipetted into the inner channel of the microfluidic chip. Due to the carefully designed surface chemistry within the inner channel and use of the hydrophilic glass coverslips as a bottom layer, the macrophages were encouraged to attach to the ground layer and extend.

Meanwhile, in the outer channels of the microfluidic chip, $CD4^+$ T cells were introduced. $CD4^+$ T cells are a crucial component of the adaptive immune system and play a central role in orchestrating immune responses against pathogens. The outer channels were filled with a suspension of $CD4^+$ T cells, and through the tiny connections between the inner and outer channels, the T cells could access the infected macrophages.

Figure 5.9 shows the ImmunoChip loaded with the $CD4^+$ T cells, where the first row represents the phase contrast microscopy images. Next, to visualize the movement and location of the T cells, the CellTracker Deep Red (CTDR) fluorescent dye, which stained the T cells a distinct purple color (second row), and Fluo-4, a calcium-sensitive fluorescent dye that emits green fluorescence upon calcium influx (third row), were employed. Thus, staining with Fluo-4 enables measurement of T cell activation and calcium signaling. The fourth row is the combination of previous ones.

One of the primary objectives of these experiments was to investigate how the infected macrophages and $CD4^+$ T cells communicate with each other during the immune response.

Phase contrast microscopy

Stained with CellTracker Deep Red (CTDR) T cells

Stained with Fluo-4 (green) T cells

Combination of three rows above
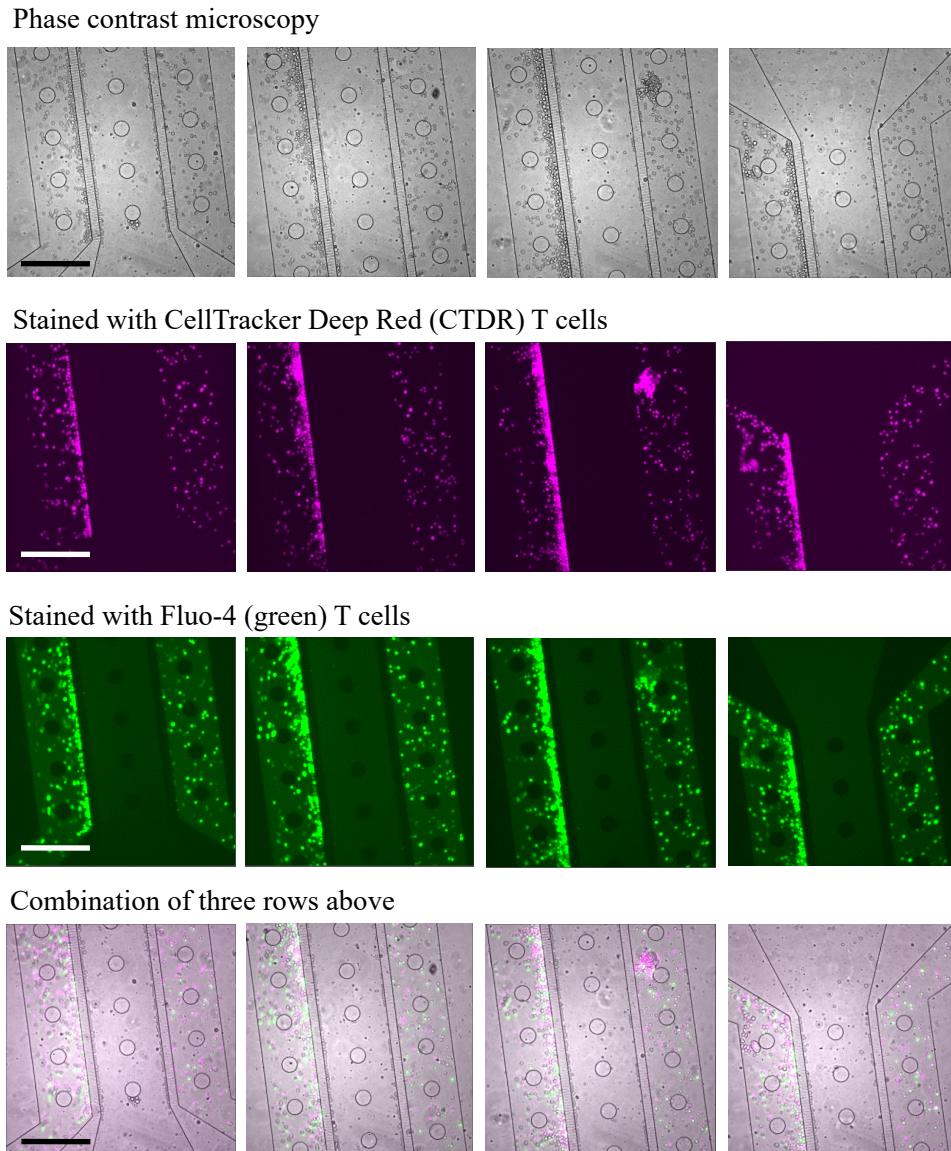
Figure 5.9: Microscope image of the T cells in side channels of ImmunoChip. In the first row are the phase contrast microscopy images, in the second row - stained by CellTracker Deep Red (CTDR, purple) T cells, third row shows the T cells treated with Fluo-4 (green), and the fourth row is a combination of previous ones. The scale bar is 150 μm. Courtesy of Prof. A. Müller, IMKI, OvGU Magdeburg.

The presence of the parasite Leishmania major triggered an immune reaction, leading to the activation of $CD4^+$ T cells. Upon encountering the infected macrophages, the $CD4^+$ T cells should respond by forming specific immune synapses and moving toward the macrophages.

Due to the limited fluid circulation inside of the chip, the signaling of the macrophages appeared weak and the T cells required additional stimulus to move towards the middle channel. Therefore, the chemokine CXCL9 was added into the 150 μm wide channel.

Figure 5.10 shows the desired result with the migration of the $CD4^+$ T cells through the $4 \times 6 \times 30\,\mu m^3$ channels. It is important to mention that PDMS possesses self-fluorescence in the green spectrum. Therefore, the chip in the third row is better visualized.

Phase contrast microscopy

Stained with CellTracker Deep Red (CTDR) T cells

Stained with Fluo-4 (green) T cells

Combination of three rows above
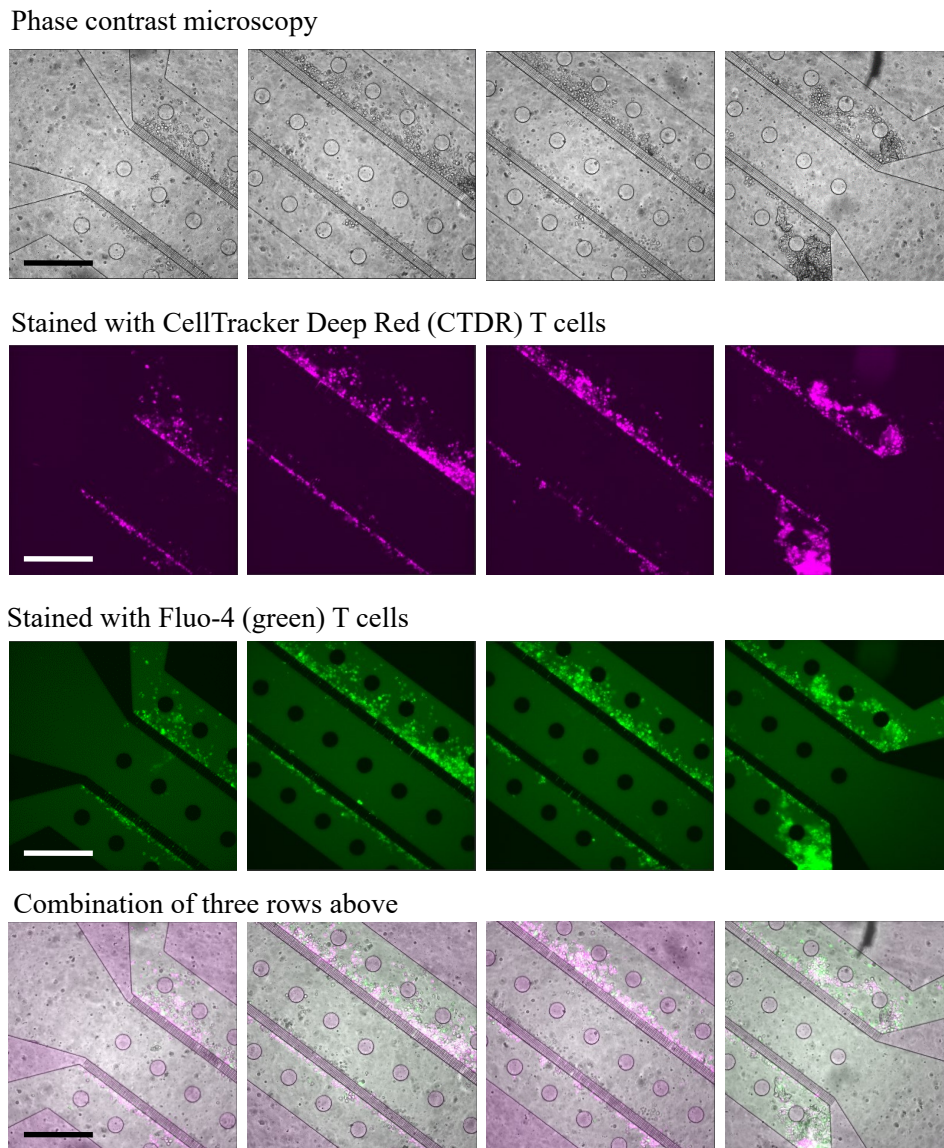
Figure 5.10: Microscope image of the T cells, which migrate from the side to the center channel in ImmunoChip due to the presence of the infected macrophages and the chemotactic gradient of CXCL9. In the first row are the phase contrast microscopy images, in the second row - stained by CellTracker Deep Red (CTDR, purple) T cells, the third row shows the T cells treated with Fluo-4 (green), and the fourth row is a combination of previous ones. The scale bar is 150 μm. Courtesy of Prof. A. Müller, IMKI, OvGU Magdeburg.

Upon reaching the inner channel, the $CD4^+$ T cells began to form immune synapses with the infected macrophages. Immune synapses are specialized cell-to-cell interfaces that allow for an exchange of signaling molecules and cytokines, which are crucial for coordinating the immune response against infections.

Furthermore, the use of Fluo-4 allowed researchers to observe changes in intracellular calcium levels within the $CD4^+$ T cells. Increased calcium influx indicated cell activation, demonstrating that the T cells were responding to the presence of the infected macrophages and the chemotactic gradient of CXCL9. The migration process is shown in magnification in Figure 5.11.

Stained by CellTracker Deep Red (CTDR) T cells

Stained by Fluo-4 (green) T cells
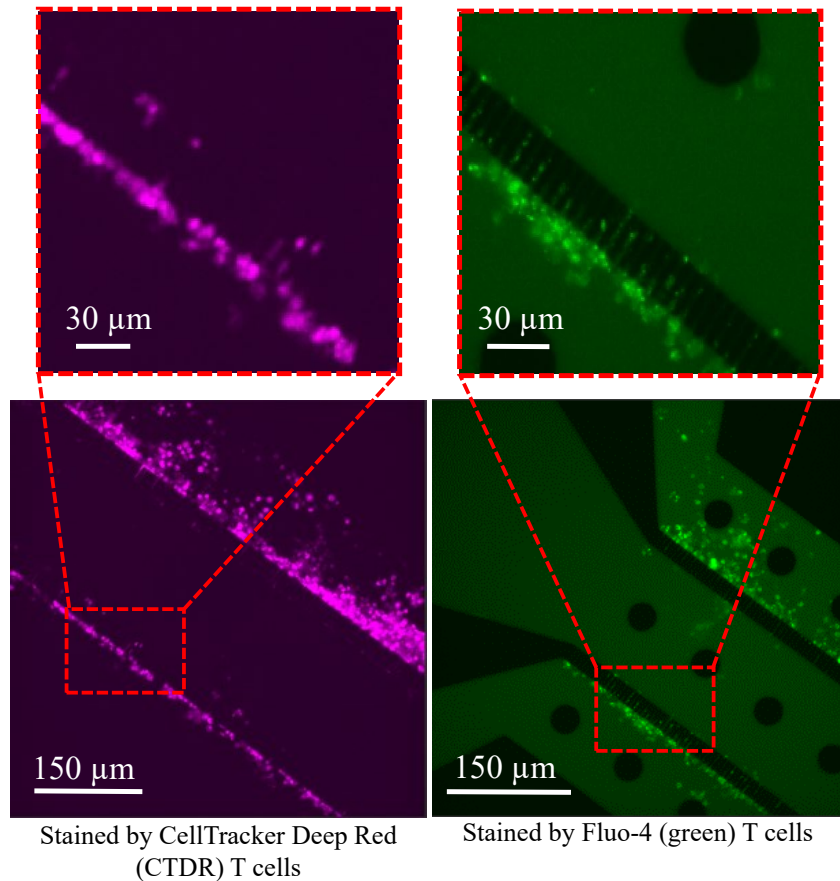
Figure 5.11: Microscope images of the T cells, which migrate from the side to the center channel through the $4 \times 6 \times 30\,\mu\text{m}^3$ channels in ImmunoChip, due to the presence of the infected macrophages and the chemotactic gradient of CXCL9. Purple color points the cells stained by CellTracker Deep Red (CTDR, purple), and green stands for T cells treated with Fluo-4. Courtesy of Prof. A. Müller, IMKI, OvGU Magdeburg.

Upon reaching the inner channel, the T cells began to interact with the infected macrophages. These interactions were dynamic and complex, involving the formation of immune synapses and exchange of signaling molecules. The Fluo-4 calcium imaging provided valuable insights into the activation status of the T cells during these interactions. We observed a calcium influx in the T cells upon contact with the infected macrophages, indicating their activation in response to the pathogen.

In summary, the microfluidic chip employed in experiments with infected macrophages and immune cells can revolutionize the field of immunology research. Its unique design

allows precise control of cellular interactions, enabling researchers to gain valuable insights into immune responses during infection. The chip's potential applications in studying various diseases and developing personalized treatments hold promise for advancing our understanding of the immune system and improving patient care in the future.

5.3 Conclusions and future outlook

The microfluidic chip provided a powerful platform for investigating the dynamic interactions between infected macrophages and $CD4^+$ T cells. By introducing chemokines and fluorescent dyes, it was possible to monitor cell behavior within a controlled microenvironment.

The experiment's results highlighted the importance of chemokines in orchestrating immune cell migration and interactions during infections. The migration of $CD4^+$ T cells towards infected macrophages demonstrated the role of CXCL9 in guiding immune cells to the site of infection. The experiments conducted with the microfluidic chip opened up new avenues of research in the field of immunology and infectious diseases. The chip's ability to precisely mimic in vivo conditions at a microscale level provided a deeper understanding of the complexities of the immune system and allowed for more accurate predictions of immune responses to various infections and treatments.

Overall, the study contributed to a deeper understanding of immune responses in the context of infectious diseases. The microfluidic chip, in combination with advanced imaging techniques, holds significant potential for further investigations into immune cell behavior and the development of targeted immunotherapies. The findings from this experiment have implications for the development of novel therapeutic strategies aimed at enhancing the immune response and combating infectious diseases.

In addition to studying the immune response against Leishmania major, the microfluidic chip's versatility could allow for exploration of a wide range of other pathogenic infections and immune-related processes. It enables the investigation of how various pathogens influence immune cell behavior and how different immune cell types interact with each other.

The chip also presents a platform for testing potential immunotherapies and drugs that could modulate immune responses. By introducing candidate compounds into the microfluidic chip, one can evaluate their effects on infected macrophages, $CD4^+$ T cells, and other immune cell types, gaining insights into their potential therapeutic value.

6 LabyrinthChip

6.1 Microfluidic chip for studying the single cell microswimmers Chlamydomonas

Chlamydomonas reinhardtii are motile (insert in Figure 6.1), unicellular microalgae that swim in the low Reynolds number hydrodynamic regime. The biflagellated microorganisms propel through aqueous fluids at typical velocities of 50 to 100 μm/s and are classic examples of puller-type microswimmers. Chlamydomonas possess eyesight that enables them to exhibit phototactic behavior, i.e., to react to light stimuli and seek optimal conditions for photosynthesis. In their natural habitat, wet soil, the algae frequently encounter suspended and sedimented particles and rough surfaces. Therefore, navigation through complex environments is an essential task for microswimmers.

In laboratory settings, researchers often examine microswimmers either in bulk or in specialized quasi-two-dimensional structures, such as thin films, narrow Hele-Shaw cells, or confined interfaces, which enable easier observation. However, the natural environments where microorganisms swim are highly complex. Microscopic organisms like Chlamydomonas reinhardtii found in soil or E. coli residing in the guts of mammals encounter rough, non-planar surfaces and interact with suspended and settled passive particles. Due to these constraints, the dynamics of microswimmers are profoundly influenced by such complex environments. Understanding how microswimmers navigate through these intricate surroundings is crucial for comprehending phenomena like groundwater contamination and the spread of infections in animals or plants. Various applications involving self-propelled particles, such as bacterial bioremediation or tumor treatment, would greatly benefit from a deep understanding of how heterogeneous media impact the movement of microswimmers.

The mechanisms underlying the scattering behavior of Chlamydomonas reinhardtii have been investigated through a series of experimental and simulation studies. Unlike the simple reflection of light, the scattering of active swimmers by obstacles is influenced by intricate hydrodynamic and steric interactions and involves the non-equilibrium phenomenon of self-propulsion. Experimental examination of the interactions between the motile puller-type algae and a flat wall revealed a consistent outgoing angle determined by the geometry of the swimmer. Interactions with cylindrical obstacles are more complex and can be purely hydrodynamic in nature. In arrays of large symmetric pillars, Chlamydomonas reinhardtii exhibit preferred swimming directions as a collective. Thin microchannels with a thickness

slightly larger than the cell diameter (about 20 µm) restrict the movement of swimming algae to a single plane, simplifying the analysis of their trajectories and facilitating the study of confinement effects.

In this study, the transfer of Chlamydomonas reinhardtii microswimmers between two compartments separated by a labyrinth represented by an array of cylindrical and elongated pillars is presented (Figure 6.1).
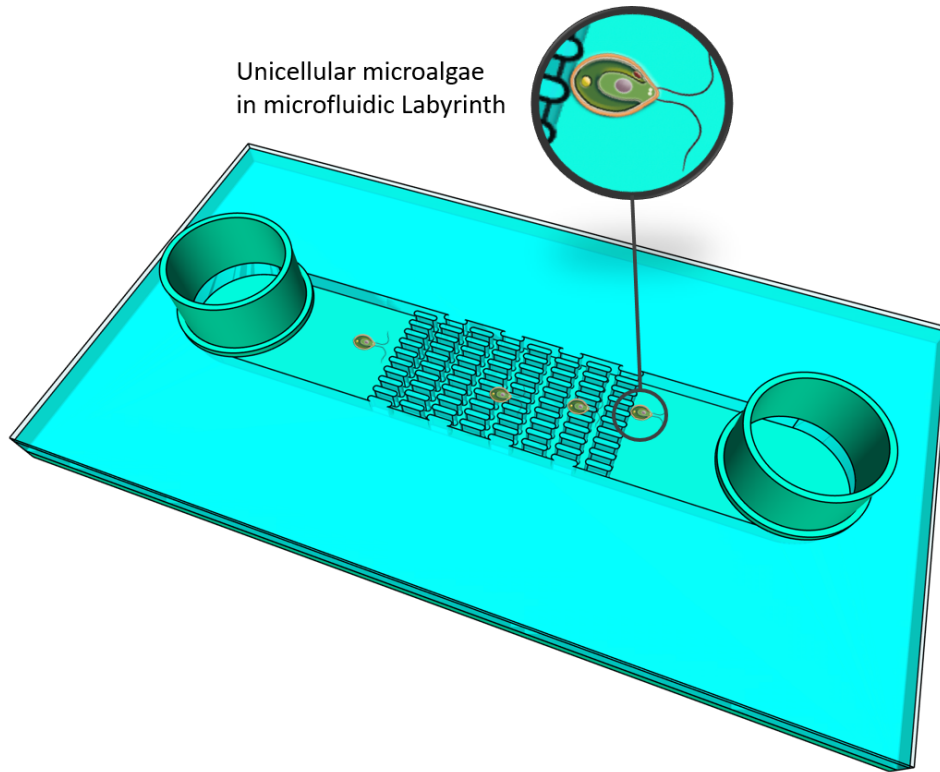
Figure 6.1: CAD model of the microfluidic structure for unicellular microalgae Chlamydomonas (in magnification).

By selecting pillars with rounded and elongated shapes, we can examine the impact of anisotropy on the kinetics of transfer and the directional characteristics of microswimmers' motion. These findings demonstrate that the shape and orientation of the pillars significantly influence the transmission and reflection coefficients of swimming algae, as well as the directional anisotropy of their movement. To study the effect of heterogeneous surroundings on the motion of Chlamydomonas, microstructured PDMS channels that act as an artificial porous environment can be employed.

To realize the study of Chlamydomonas motion, a novel microfluidic device was created during the course of this work. Therefore, the following sub-section presents a detailed view on the development, fabrication and applicability of the PDMS-based microfluidic channels for the study of the motion of algae in the different labyrinth-like structures.

Chapter 6 is structured as follows:

- Section 6.1.1 presents detailed design considerations for microfluidic chips for algae experiments,

- Section 6.1.2 provides a detailed description of the physical design, layout, and manufacturing of the 3D microfluidic device,

- Section 6.2 describes the application of the PDMS microfluidic chip manufactured in Section 6.1.2,

- Section 6.3 summarizes this chapter, provides an outlook into the future and emphasizes the key novel results reported in this section.

6.1.1 Chip Design Considerations for LabyrinthChip

While designing the LabyrinthChip, requirements were taken into consideration not only for microswimmers Chlamydomonas, but also for general conditions for all single-cell active species of approximately $10\,\mu$m size. The purpose of this microchip is to create a labyrinth-like barrier inside the microfluidic channel and to study the movement behavior of the algae in it.

- **Channel configuration and dimensions:** The microfluidic chip needs to be designed for single-cell organisms. Therefore, the height of the channel is set for $20\,\mu$m, which ensures exclusively planar motion of the microswimmers. Moreover, the labyrinth-like structures are planned to be located in the middle of the channel. Therefore, they create a porous wall or an obstacle for the Chlamydomonas and divide the channel into three areas: a loading chamber, a labyrinth compartment, and the area reached by algae that passes through the labyrinth. The purpose is to study the influence of the different geometries of the obstacles on the algae motion. Therefore, five chips are designed with differences in the shape, amount, orientation and distance between the structures (Figure 3.5 and Subchapter 3.1.3). Channels should consist of two obstacle-free regions separated by the porous wall (labyrinth). Thus, algae that interact with the obstacle array can either get to the other side of the channel (transmission) or exit the region with obstacles to the side of the channel from which it came (reflection).

- **Gas permeability of the microfluidic device:** Same as many living creatures, Chlamydomonas requires gas exchange. Therefore, PDMS is an optimal material for the upper part of the chip, which is structured.

- **Possibility for high-resolution microscopy:** Similar to the previously described ImmunoChip, the LabyrinthChip is used for single-cell moving organisms. Therefore,

at least one side of the microfluidic device has to be made of a microscopy glass slide, which is 170 µm thick, if microscopy and motion recording is to be employed.

- **Optical transparency of the complete microfluidic device:** The algae are sensitive to light and react to changes in wavelength in the visible spectrum [124]. Therefore, complete transparency of the chip is necessary. One side of the chip is utilized for microscopy and motion recording. Thus, the opposite side is used to illuminate microswimmers with the different wavelengths.

- **Absorption in the microfluidic chip:** In this work, the microfluidic chip is employed solely for optical experiments and motion analysis. Due to the absence of chemical components which could otherwise be absorbed, PDMS remains an optimal choice for replicating labyrinth-like structures and microfluidic channels.

- **Elasticity of the microfluidic chip:** In the case of the LabyrinthChip, elasticity of the layer with the labyrinth structure is required. TCollision of the microswimmers with the pillars can cause mechanical deformations and shear stress for the living creatures. In the case that the labyrinth is relatively soft, algae could transmit through or be reflected without damage. In its turn, the bottom layer does not need to be flexible or elastic because the chip will not be flexed or bent during the experiments with algae.

- **Optimized liquid flow:** The flow and wetting forces in the microfluidic chip have to be optimized, and the experimental protocol has to be designed accordingly. Algae can move by themselves in the channel, so no additional flow is required. Moreover, air bubbles are highly undesired in the microfluidic channel. Therefore, chips must be loaded with DI water directly after fabrication. In this case, capillary forces ensure a sufficient wetting force and no bubbles appear. Next, the chip is stored in the aqueous solution until loading of the algae. The microswimmers with the medium are pipetted into the microfluidic channel and replace the DI water. This design is intended to ensure sufficient wetting, the absence of air bubbles, and provide for solely capillary flow of the liquid.

6.1.2 Microfluidic Chip Fabrication

According to the design considerations listed above, PDMS and microscopy glass slides are the most relevant materials for the fabrication of microfluidic chips for Chlamydomonas reinhardtii microswimmers. To structure PDMS, the master mold was fabricated by the soft lithographic process. Thus, the technical drawing of the shadow mask and simultaneously master mold is given in Figure 3.5.

The photograph of the resulting 4″ master wafer with the structures for replication is shown in Figure 6.2.
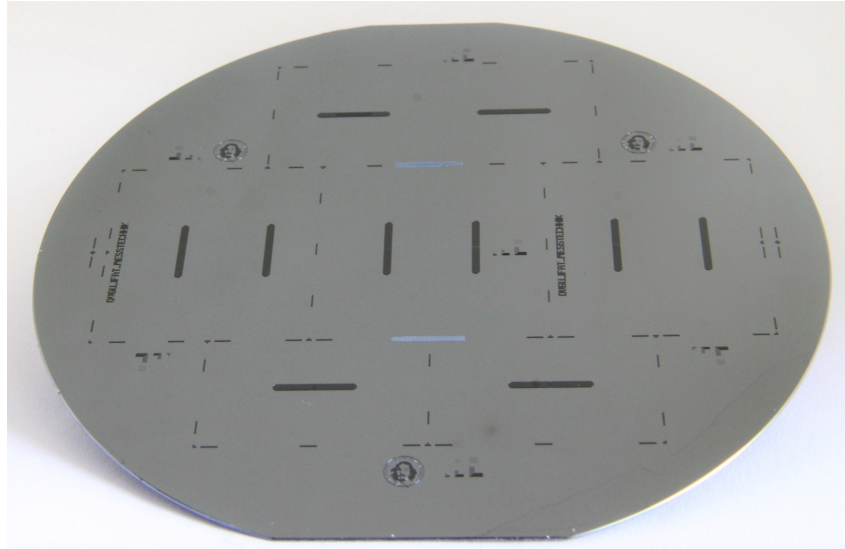
Figure 6.2: Photograph of the completed master mold wafer for LabyrinthChip. There are ten structures for replicating the microfluidic channels, with labyrinths positioned in the middle of each channel. Labyrinths differ in shape, amount of pillars, orientation, and distance between them. Every channel is doubled to increase the output from the molding process.

As mentioned before, five types of labyrinth-like structures are present on the wafer (2 times each). Pillars with circular geometry are located in the middle, and each structure is doubled to increase the yield of the fabrication process. Elongated pillars are situated in the bottom and top parts of the mold.

In the fabrication of the master mold, the technical question that needed to be resolved is the development of the residual photoresist from the $10\,\mu m$ radial circular wells. The complication is realization of unhindered access of the developer into the wells. To improve the development process, the development time was significantly increased to 1 hour 35 minutes. It is a very long development time compared to the standard 10 minutes. In this case, the adhesion of the SU-8 photoresist-based structures has to be ideal, and exposed photoresist has to stay on the wafer after development. Therefore, the wafer was pre-cleaned with KOH solution before spin-coating of the photoresist to improve adhesion. The result of the process is shown in Figure 6.3, which presents the master wafers' SEM images with circular wells and their replications by the PDMS, which appear as pillars. As can be seen, the resulting PDMS structures have a very good quality.

The configuration of the labyrinth with the elongated pillars is less challenging to fabricate. With continuous stirring, the developer can easily access the bottom of the elongated wells and the residual photoresist in the well is already fully removed after $10\,min$ of the development process. The result is shown in Figure 6.4.
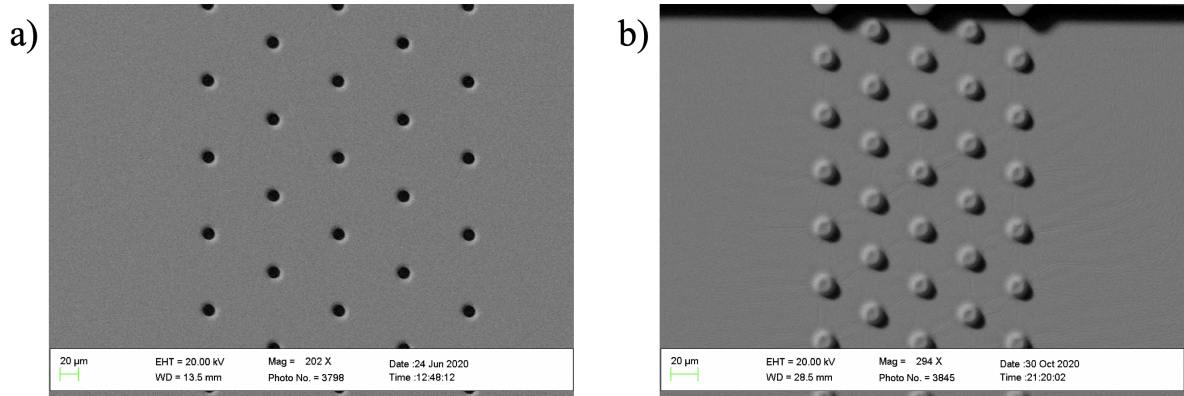
Figure 6.3: SEM images of the structured master mold with circular pillars in the middle of the channel structure; fabricated with soft lithography (a) and its replication in PDMS (b).
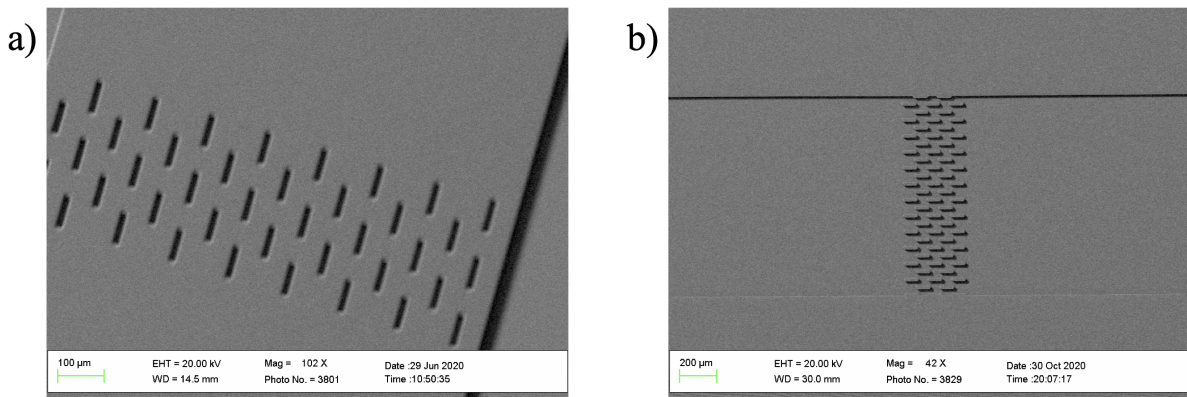
Figure 6.4: SEM images of the structured master mold with elongated pillars in the middle of the channel structure; fabricated with soft lithography (a) and its replication in PDMS (b).

Once the master mold is fabricated, subsequent steps such as molding and bonding can proceed. All the steps and parameters are given in Sections 3.2 and 3.3. PDMS replicas obtained from the master mold exhibit variations in their geometrical parameters, attributed to design differences and fabrication tolerances. PDMS, being an elastic polymer, undergoes deformation upon release from the master mold structure, as detailed in Table 6.1, where w is the pillars' width, l - length, a and b are the distance between elongated pillars, r is the radius of the circular pillar and d is the distance between the centers of circular pillars (Figure 3.5). Sample numbers correspond to Figure 6.5. It illustrates the diverse configurations of the fabricated PDMS/glass microfluidic chips.

Each structure is placed multiple times on the wafer. Obstacle orientation and the porosity affect the transmission/reflection probability. For example, elongated obstacles oriented perpendicularly to the channel walls suppress the transmission of the swimmers.

Table 6.1: Specifications of the LabyrinthChips.

Sample No.	Type of pillars	Set dimensions	Resulted in replica dimensions
1 ($\perp$)	Oblong, perpendicular to the channel wall	$w = 20\,\mu\text{m}$, $l = 80\,\mu\text{m}$, $a = 40\,\mu\text{m}$, $b = 40\,\mu\text{m}$	$w = 21 \pm 0.5\,\mu\text{m}$, $l = 80 \pm 0.6\,\mu\text{m}$
2 ($\parallel$)	Oblong, parallel to the channel wall	$w = 20\,\mu\text{m}$, $l = 80\,\mu\text{m}$, $a = 40\,\mu\text{m}$, $b = 40\,\mu\text{m}$	$w = 21 \pm 0.5\,\mu\text{m}$, $l = 80 \pm 0.6\,\mu\text{m}$
3 ($\parallel$)	Oblong, parallel to the channel wall	$w = 20\,\mu\text{m}$, $l = 80\,\mu\text{m}$, $a = 40\,\mu\text{m}$, $b = 20\,\mu\text{m}$	$w = 21 \pm 0.5\,\mu\text{m}$, $l = 80 \pm 0.6\,\mu\text{m}$
4 ($\circ$)	Circular	$r = 10\,\mu\text{m}$, $d = 80\,\mu\text{m}$	$r = 10 \pm 0.6\,\mu\text{m}$, $d = 60\,\mu\text{m}$
5 ($\circ$)	Circular	$r = 10\,\mu\text{m}$, $d = 60\,\mu\text{m}$	$r = 10 \pm 0.6\,\mu\text{m}$, $d = 60\,\mu\text{m}$

Therefore, the perpendicular configuration of the elongated pillars is present only in one geometry configuration.
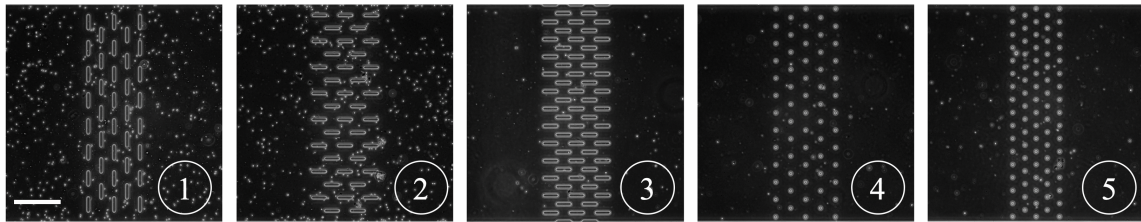
Figure 6.5: Microscope images of the labyrinth types. (1) elongated structures perpendicular to fluid flow; (2) elongated structures parallel to fluid flow; (3) elongated structures parallel to fluid flow with a high density of the columns; (4) cylindrical columns; (5) cylindrical columns with high density. Scale bar is $200\,\mu\text{m}$.

For further experiments with microswimmers, it is highly important to avoid bubbles in the microfluidic channels because bubbles can play a role in creating additional obstacles for the microswimmers. Therefore, the chip is filled with DI water directly after fabrication. The water is pulled inside of the labyrinth by the capillary forces so that no bubbles are created. The chips are stored subsequently in an aqueous environment and careful pipetting is conducted to transfer the microswimmers into the microchannel.

6.2 Proof of concept and Chlamydomonas motion detection in a microfluidic chip

Fabricated channels with five different labyrinths, shown in Figure 6.5, were utilized to detect and analyze the motion of Chlamydomonas. In the microchannels, a set of pillars or labyrinth is employed as a model to simulate a porous wall, effectively dividing two

compartments by the obstacles. These compartments in the chip are shown in the insert of Figure 6.6 and specified with numbers as follows. The compartment (1) is with algae, (2) is without them and (3) is a labyrinth area. To conduct the experiment, algae are pipetted into the channels, and their motion is self-guided without influence of external pumping. When a microswimmer traverses the porous wall, two outcomes are possible: either the microswimmer permeates through the labyrinth and transitions from one compartment to the other (referred to as "transmission"), or it returns back to the region from which it originated (referred to as "reflection").
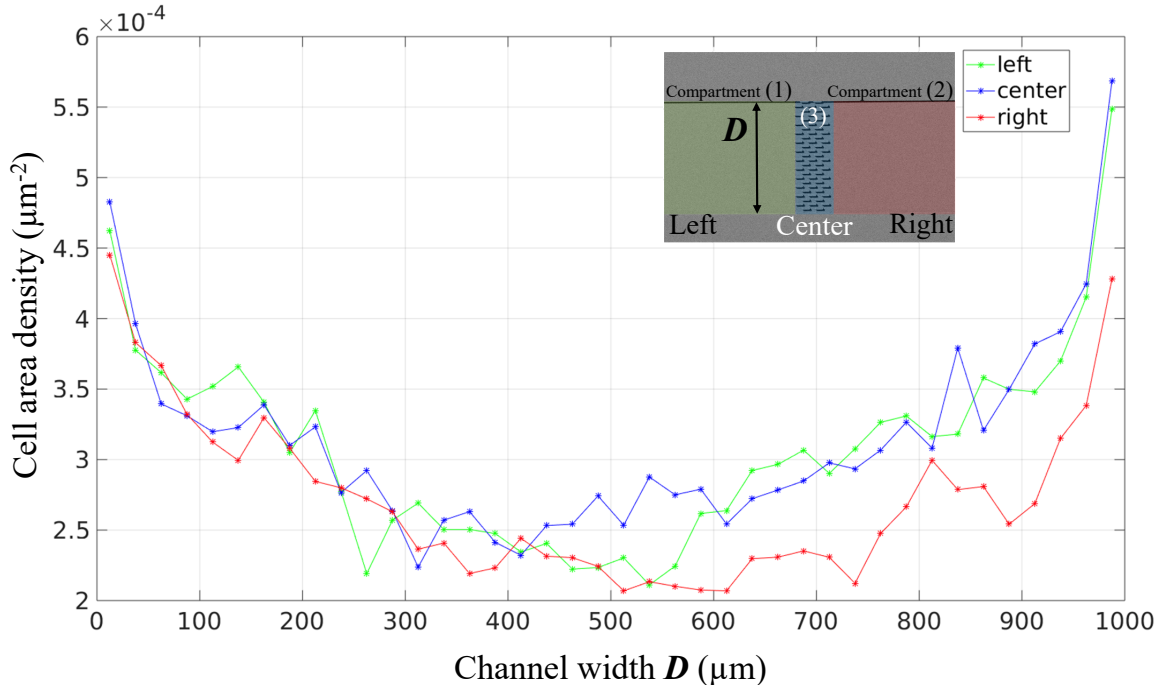
Figure 6.6: The cell number density averaged over time, is plotted as a function of the distance from the upper wall of the microchannel (denoted as D) for sample 2 (Table 6.1). In this case, the compartment with labyrinth (represented by the blue curve) consists of pillars that are aligned parallel to the walls of the channel. The inset diagram provides a visual representation of how D is defined and illustrates the division of the channel into three compartments. With permission of Prof. A. Eremin, IfP, OvGU Magdeburg.

It is important to mention that, unlike the rapid equalization of the number of mobile cells between compartments, an imbalance exists in cell concentration across the width of the microchannel due to the accumulation of swimmers at the walls of the channel. This effect is shown in Figure 6.6. This phenomenon was previously reported for Chlamydomonas reinhardtii by Williams et al. [125].

Next, to induce a discrepancy in the distribution of microswimmers, localized illumination is applied. In thin microchannels with a thickness of approximately $20\,\mu m$, no significant phototaxis (movement in response to light) was observed. However, when exposed to blue light ($480\,nm$), the microswimmers adhered to the glass substrate due to the phenomenon

of adsorption. These adhered microswimmers are referred to as immotile, although they maintain slow gliding motility. Upon termination of the localized illumination, the cells desorb from the substrate and transition back into the motile state. The equalization process occurs within a time frame of approximately 200 seconds. However, there is an initially induced imbalance in the total cell density caused by light exposure. The rate of the desorption process is approximately 500 s. During detachment, the number of adhered cells follows an almost exponential decay pattern, ultimately reaching a number determined by the overall intensity of the illumination and other cell-related conditions. The characteristic time for desorption can be obtained by fitting the decay curve with a single exponential function.

Excursions of microswimmers through the compartment with the obstacle array can be categorized as transmission or reflection events, allowing us to define reflection and transmission coefficients (R and T) as the ratio of the number of reflection/transmission events to the total number of observed excursions through the labyrinth. The boundaries of the center compartment are positioned 17 µm away from the outermost obstacle row, representing the distance below which steric swimmer-obstacle interactions can occur. This assumption is based on a swimmer body radius of 5 µm and a 12 µm flagellar length. Transmission and reflection events occurring close to the lateral channel walls are discarded to exclude the influence of steric swimmer-wall interactions that might mask the effects of obstacle geometry and arrangement.

The behavior of motile algae is influenced by the geometry of their surroundings, as evident from the distributions of path lengths observed in permeating trajectories. When comparing path lengths, two aspects should be considered: the availability of short paths and the probability of swimmers finding them. The former aspect is solely determined by geometric factors, while the latter involves interactions between the swimmers and the obstacles. Table 6.2 provides the reflection and transmission coefficients for different channels and obstacle porosities of Chlamydomonas reinhardtii (labyrinth geometries are provided in Figure 6.5).

Table 6.2: Reflection/Transmission events of the algae due to the porosity of the labyrinth structure in microfluidic channel.

Sample No.	Porosity, %	Transmitted, %	Reflected, %
1 ($\perp$)	78	1	99
2 ($\parallel$)	83	22.4	77.6
3 ($\parallel$)	77	18.7	81.3
4 ($\circ$)	97	32.1	67.9
5 ($\circ$)	94	30.2	69.8

The transmission is greatly suppressed when elongated obstacles are oriented perpendic-

ular to the channel's main axis, resulting in the reflection of nearly all algae (see sample no. 1 in Table 6.2). Transmission coefficients for the parallel oriented elongated obstacles (samples 2 and 3) and cylindrical pillars (samples 4 and 5) are significantly higher than those for the perpendicular oriented elongated obstacles.

The suppression of transmission for perpendicularly oriented oblong obstacles can be attributed to two factors. Firstly, this geometry has a small aperture, meaning that the obstacles occupy a substantial portion of the channel's cross-section. Secondly, the preferred swimming direction of Chlamydomonas reinhardtii within the porous wall is unfavorable for transmission.

Although perpendicular obstacles direct algae toward the lateral microchannel walls, it is important to address concerns regarding the potential distortion of transmission/reflection statistics due to the exclusion of trajectories approaching the channel walls. While including trajectories in the vicinity of the channel walls significantly increases the absolute number of transmission events, the transmission coefficient for perpendicular obstacle orientation remains remarkably small at $T = 4\%$. Furthermore, a higher porosity leads to a greater transmission probability for channels with the same obstacle shape and orientation. This observation can be seen by comparing samples 5 and 4 or samples 2 and 3 in Table 6.2.

Additionally, the impact of geometric constraints on the swimming behavior of microswimmers is evident in the characteristics of their trajectories. When encountering obstacles, the algae undergo scattering, leading to a reduction in their swimming persistence. Moreover, when regularly ordered obstacles are present, they influence the alignment of the microswimmers' trajectories as they slide over the surface of the pillars. Figure 6.7 illustrates typical trajectories observed in labyrinth area which contains an array of pillars, specifically for sample 4 (given in Figure 6.5 and Table 6.2). These trajectories generally exhibit small undulations.

Chlamydomonas reinhardtii are known to swim along helical paths in bulk fluid, which is attributed to the nonplanar beating of their flagella and slight asymmetry in flagellar driving forces. However, confinement within the microchannel restricts the rotation of the algae, suppressing their helical motion and instead resulting in undulated trajectories. The combined hydrodynamic and steric interactions between the algae and the pillars cause scattering, as studied by Contino et al. [126]. When the impact angles are small, the algae slide along the pillars with minimal changes in orientation. As a result, they align themselves along the paths formed between the periodically arranged pillars. Figure 6.7 (b) exemplifies trajectories that initiate in one compartment and terminate in the other compartment, representing transmission through the labyrinth to move from compartment 1 to compartment 2 (or vice versa). Some algae even reverse direction and return to the same compartment from which they originated after traversing compartment 3, as shown in Figure 6.7 (a). This scenario is referred to as reflection.

While any algae can undergo transmission or reflection, these events differ significantly
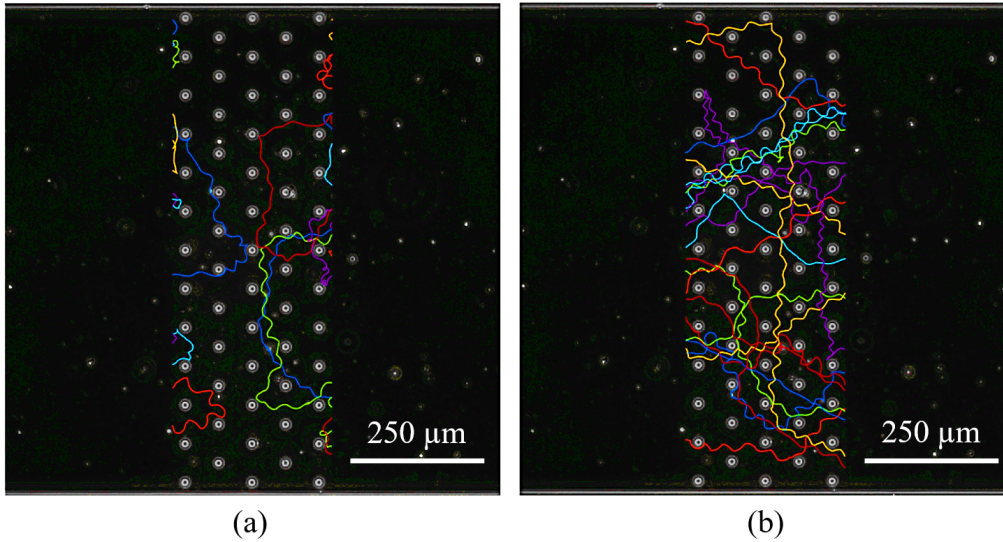
Figure 6.7: Microscope image with marked examples of the algae trajectories for reflection (a) and transmission (b) events. Courtesy of Prof. A. Eremin, IfP, OvGU.

in their statistical properties, as depicted in Figure 6.8. Algae involved in reflection exhibit considerably shorter average time in the labyrinth than those involved in transmission. This difference can be attributed to the fact that most algae scatter back at the first row of pillars. This observation is clearly illustrated in Figure 6.8, where the distribution of maximal penetration depth for reflecting trajectories is presented. The distribution function displays multiple peaks corresponding to the positions of the pillar planes, indicating that scattering effects play a significant role in the reflection process rather than tumbling or meandering of individual cells.

The dynamics of microswimmers in compartments with pillars are strongly influenced by shape-anisotropic obstacles, specifically elongated pillars, resulting in distinct behavior compared to the case of cylindrical pillars. The shape and orientation of the pillars also impact the exchange rates between compartment 1 and compartment 2. Figure 6.9 showcases exemplary trajectories of motile algae in the porous environment of the labyrinth, in which elongated obstacles are present with their long axes either perpendicular or parallel to the microchannel walls.

Similar to the scenario with cylindrical pillars, reflections of the algae in a labyrinth with elongated pillars frequently occur at the outermost row of obstacles (as depicted in Figure 6.10). This observation is particularly prominent when the pillars are oriented orthogonally. It should be noted that trajectories associated with reflection events can exhibit additional complexity. The microswimmers can penetrate deeper into the obstacle array, as illustrated in Figure 6.9. Algae that successfully traverse the porous environment may follow a straight path (Figure 6.9 b) or navigate through the labyrinth of pillars (Figure 6.9 a, c and d). Consequently, there is a wide range of transmission path lengths
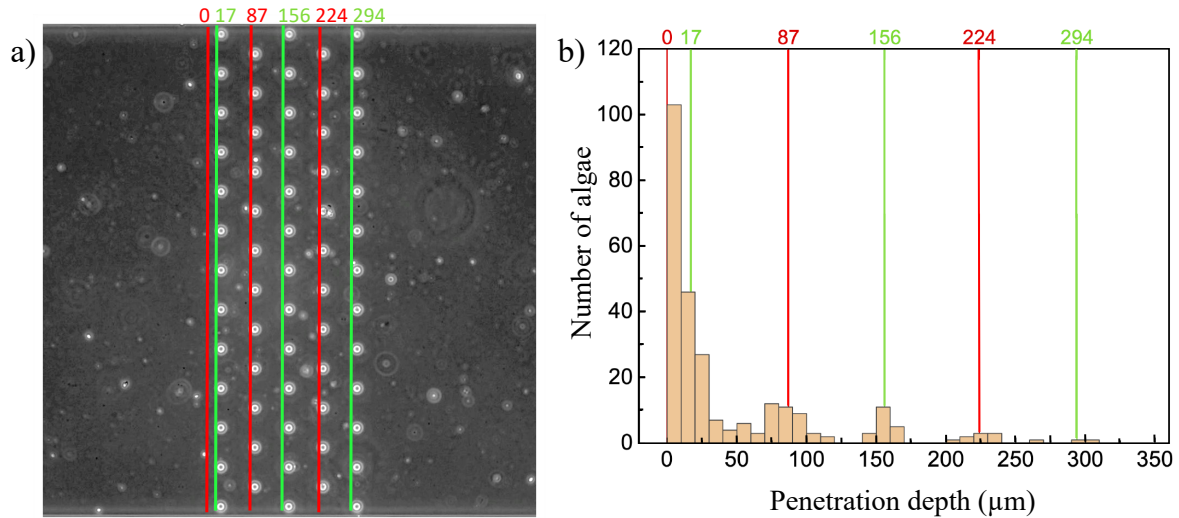
Figure 6.8: Graphical representation of the statistical algae penetration depth for reflection events in the labyrinth with circular pillars (labyrinth geometry is number four in Figure 6.5) The swimming direction is from left to right and (a) shows the physical penetration depth at each row of pillars, while (b) is the statistical graph of algae penetration. Courtesy of Prof. A. Eremin, IfP, OvGU.
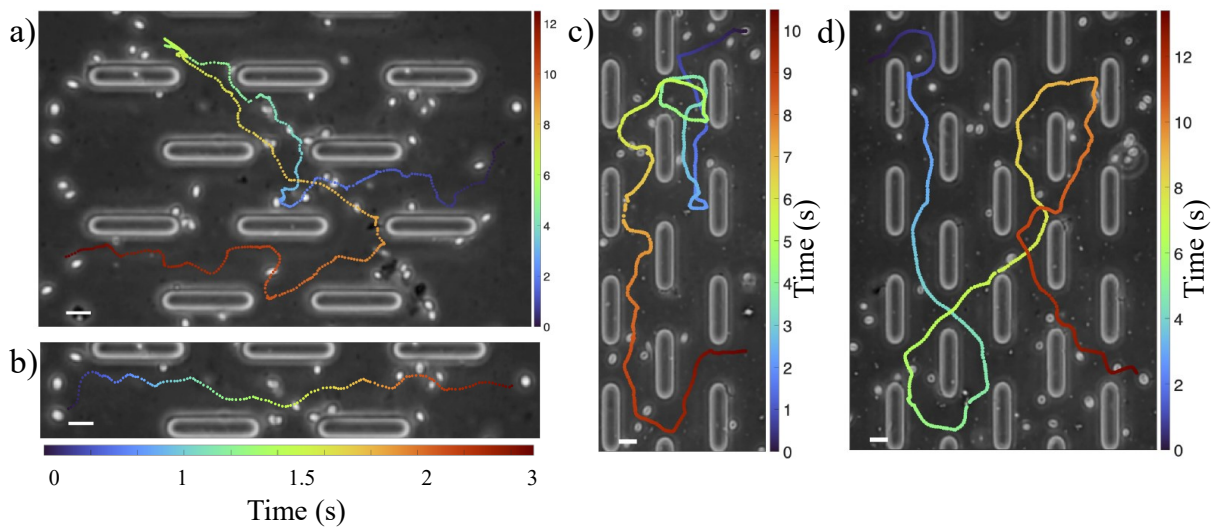
Figure 6.9: Microscope image with marked examples of algae trajectories for reflection (c) and transmission (a, b, d) events in the labyrinths with parallel (a, b) and perpendicular (c, d) obstacles as referred to the wall of the microfluidic channel. Labyrinth geometries are number two and one in Figure 6.5). Courtesy of Prof. A. Eremin, IfP, OvGU.

and durations spent within the obstacle array until reaching the other compartment.

The trajectory shown in Figure 6.9 (a) demonstrates transient adhesion for a duration of less than 2 seconds. Due to the confined nature of the microchannel, characterized by close proximity to the upper and lower walls, this phenomenon, along with periods of slow translation accompanied by a 'jiggle motion', is occasionally observed.
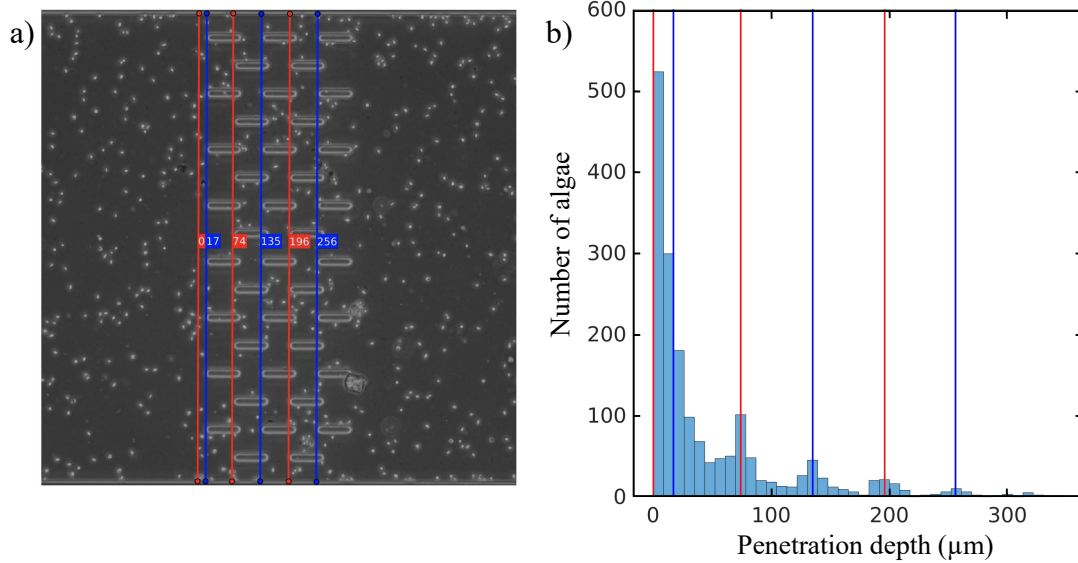
Figure 6.10: Graphical representation of the statistical algae penetration depth for reflection events in the labyrinth with elongated pillars (labyrinth geometry is number two in Figure 6.5). The swimming direction is from left to right and (a) shows the physical penetration depth at each row of pillars, while (b) is the statistical graph of algae penetration. Courtesy of Prof. A. Eremin, IfP, OvGU.

For sample 2, where parallel elongated obstacles are present, reflected algae exhibit significantly shorter mean labyrinth times ($t_{\mathrm{ref}} \approx 1.3\,\mathrm{s}$) in compartment 3 compared to transmitted algae ($t_{\mathrm{trans}} \approx 3.5\,\mathrm{s}$). The reflections predominantly occur at the tips of the pillars, which is where the maxima in the distribution function of penetration lengths occurs (Figure 6.10 b).

In the case of sample 1, with elongated pillars oriented perpendicular to the capillary axis, the wall detention time for transmitted algae ($t_{\mathrm{trans}} \approx 7.2\,\mathrm{s}$) becomes longer than that observed with parallel aligned pillars. This can be attributed to trapping caused by the pillar alignment of trajectories in the orthogonal direction (as seen in Figure 6.9 c and d). Notably, the distribution of angular displacements is highly anisotropic, with maxima aligned orthogonally to the capillary axis.

It is important to mention that trajectories with distances to the lateral microchannel walls that are smaller than the steric interaction distance are excluded from the dataset. In the case of sample 1, this results in a small subset of only 30 translation trajectories, which makes claims about the transmission time through the labyrinth less definitive. However, when relaxing this constraint and considering trajectories that may involve steric wall interactions, the amount of time algae are observed in the labyrinth is still remarkably high, with $t_{\mathrm{trans}} \approx 6.2\,\mathrm{s}$ (based on 283 trajectories). Also, the shortest available paths are straight lines following obstacle-free lanes from compartment 1 to compartment 2. In some cases, algae may find slightly smaller paths by utilizing the finite lane width to travel

at a smaller angle to the horizontal, although this deviation appears to be negligible in practice.

6.3 Conclusions and future outlook

This chapter presented the design, fabrication, and proof of concept of a microfluidic chip for the study of the one-cell creature Chlamydomonas reinhardtii. The Chlamydomonas microswimmers can swim in 2D space, as the chip channel is only $20\,\mu\mathrm{m}$ high. In this transparent microstructure the motion of the algae was observed and analyzed. The findings show the significant impact of shape anisotropy in porous medium obstacles on the diffusion of microswimmers. Reflection and transmission coefficients demonstrate that the geometric constraints and obstacle density strongly influence the transmission of microswimmers through the porous wall and their reflections.

A decrease in the porosity of the wall hinders the transmission of microswimmers while promoting their reflection. The shape anisotropy of the obstacles, combined with steric and hydrodynamic interactions between the microswimmers and pillars, leads to an alignment of themicroswimmer trajectories. This alignment introduces a bias in the diffusive process, with scattering at the pillar arrays playing a significant role in the reflection events.

The alignment effect depends on the orientation of the pillars and is mediated by interactions with the microchannel walls. In the case of orthogonally oriented pillars (perpendicular to the channel wall of the labyrinth), this alignment can even result in trapping, as observed in the experiments.

The findings presented in this chapter provide valuable insights into the design and behavior of microfluidic chips tailored for one-cell organisms like Chlamydomonas reinhardtii. Thus, several exciting directions for future research and development emerge:

- Enhanced microswimmer manipulation and detection of physiologycal parameters: Explore advanced techniques to further manipulate and control the motion of microswimmers within microfluidic channels. This could involve integration of the actuators and sensors into a microfluidic channel with labyrinth.

- Optimizing Porous Structures: Continuing to fine-tune the design of porous structures within microfluidic chips to optimize the transmission and reflection of microswimmers. This could involve experimenting with different obstacle densities, shapes, and orientations.

- Multi-Species Interactions: Investigate how multiple microswimmer species interact within the same microfluidic environment. Understanding how different species influence each other's motion and behavior could have significant implications in various fields.

- Real-World Applications: Explore potential real-world applications for this research, such as use of microfluidic chips to study the impact of environmental factors on microorganisms or development of innovative diagnostic tools to analyze microswimmer behavior.

In summary, this chapter lays the foundation for an exciting future in microfluidic research and offers a deeper understanding of microswimmer dynamics and their interactions with geometric constraints. These insights have the potential to drive advances in both fundamental scientific knowledge and practical applications in diverse fields.

7 Sensor implementation

Organ-on-Chip and numerous biomedical applications require multiple types of sensors to monitor the physiological state of cells cultured inside a microfluidic channel. For example, oxygen sensors provide information about cellular oxygen consumption. Oxygen concentration measurements are beneficial to determine if different cells consume different amounts of oxygen, giving also an indication about cancerous cells.

Another example is transepithelial electrical resistance (TEER) measurements, which provide an indication whether or not cells have formed a tight junction and have grown into a tissue.

Furthermore, the integration of a temperature sensor onto a thin PDMS membrane holds potential for monitoring inflammation models in close proximity to the cells. Nevertheless, it should be noted that the realization of any of these electric sensors necessitates the incorporation of metal electrodes onto the elastic polymer, which remains a broad area of ongoing research.

Certainly, there exist numerous other sensors with relevance to biomedical applications. However, this research work focuses primarily on the three aforementioned sensor types, which are expounded upon in greater detail within this chapter. Additionally, this chapter addresses several noteworthy research challenges pertaining to micro-structuring, particularly within the context of soft materials like Polydimethylsiloxane (PDMS) that are equipped with metal structures.

An intriguing prospect lies in the integration of sensors into each of the aforementioned microfluidic chips. As of now, the Stomach-on-Chip platform has been selected as the primary host for sensor integration. Nevertheless, it is worth noting that the technology for oxygen sensor integration described below could potentially be applied to the ImmunoChip and LabyrinthChip, as could the meander-shaped thermo-electric element as well.

The chapter is organized as follows: Section 7.1 discusses oxygen sensors and conditions for oxygen concentration measurement. Section 7.2 presents TEER sensors and their applicability to cell layer resistance measurements. Next, Section 7.3 analyzes in detail properties of a thermo-electric meander-shaped element on a PDMS membrane which can be used in multiple ways, such as temperature sensors and heat elements and is mechanically deformed under applied current. Finally, Section 7.4 summarizes this chapter, provides a review of presented learning and gives an outlook on suggested future research directions.

7.1 Oxygen concentration in-situ measurements

Oxygen in different concentrations is required in any microfluidic chip that contains a biological substance, since oxygen is involved in most cellular biologic processes. For example, tumorous tissues generate an oxygen gradient. Cancerous cells consume more oxygen than healthy cells, thereby generating the hypoxia effect, which is one of the prominent properties of cancer, including hematological cancers. Hypoxia is the oxygen deficiency of the cell.

Another effect of cancerous cells that can be monitored by oxygen sensors is aerobic glycolysis, which is considered to be a universal property of malignant cells, and it is found that one of the causes of cancer is impaired mitochondrial metabolism. Mitochondria also produces reactive oxygen species (ROS), which are responsible for many physiological processes and can be harmful if produced excessively [127].

Therefore, oxygen sensors are absolutely necessary in microfluidic based Organ-on-Chip investigations of cancer related questions. However, commercially available oxygen sensors are not designed to be used in a microfluidic environment. Therefore, use of such sensors for Organ-on-Chip applications is a non-standard use case. Hence, the purpose of this section is to study the feasibility of use of a commercially available PreSens (PreSens GmbH, Germany) luminescence oxygen sensor [98] for Organ-on-Chip applications.

This section presents a comparison of results of this oxygen sensor measured in a beaker, in a microfluidic chip without a membrane, and in a microfluidic chip with a membrane.

Figure 7.1 shows the PreSens sensor principle of operation based on the dynamic quenching mechanism. Miniature circular sensor spots, 1 mm of diameter and 40-70 μm thick, are placed inside a microfluidic channel and are excited externally by a low-power Light Emitting Diode (LED).

Thanks to the transparency of PDMS, light reaches the sensor spot without attenuation. The spot absorbs the light and moves into an excited state. In the absence of oxygen, the sensor spot re-emits light with the same intensity, which again can go through the transparent PDMS wall and be detected externally by the contactless read-out. However, when oxygen is present in the channel, some of the received energy is transferred by collision into the oxygen molecules, which quenches the emission of light at the molecular level (as is shown in Figure 7.1, 2b). Therefore, the light intensity at the macro level is reduced dependent upon the concentration of oxygen molecules in the sensor region, and the light intensity can be converted into oxygen concentration values. In this fashion, one can quantify the amount of oxygen in the microfluidic channel.

The main advantage of this solution is that the sensor spots (shown on the top left-hand side of Figure 7.1) are not physically attached to the read-out device. This enables placement of the sensor spots inside the microfluidic channel (Figure 7.2), which is essential for Organ-on-Chip applications. The optical fiber end must be pointed at the sensor spot
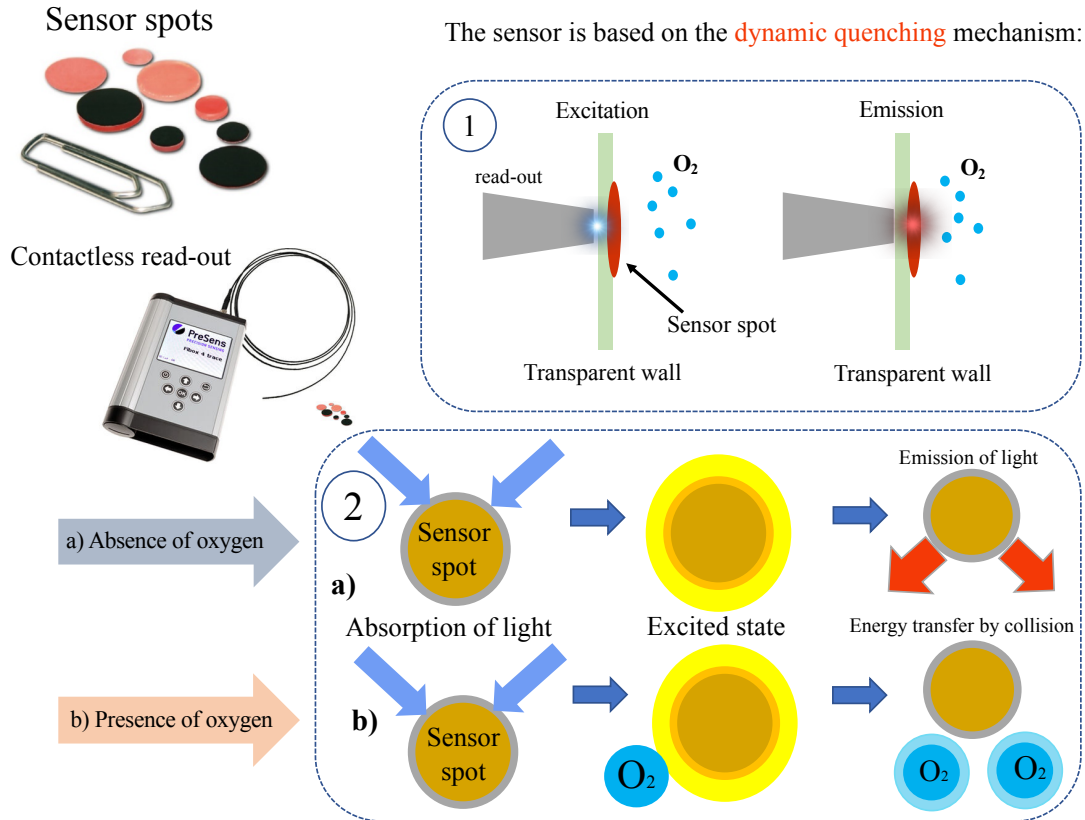
Figure 7.1: Oxygen sensor based on a dynamic quenching mechanism. Part (1) shows the sensor spot and read-out system location with respect to the chip's transparent wall. Part (2) describes the sensing principle at the molecular level, where (a) shows light emission in the absence of oxygen. In (b) in the presence of oxygen, energy transfer to the oxygen molecules results in less intense light emission on a macro-scale.

at the outer side of the PDMS wall, and the read-out is then performed wirelessly.

The sensor spot is located inside the PDMS chip, as shown in Figure 7.2. The main research question to be investigated is whether the microfluidic chip fabrication process affects the sensor spot. The sensor spot was glued to the master wafer and then covered by liquid PDMS on top, as specified in Section 3.6.1. The initial oxygen measurements were conducted with DI water, since DI water is a standard natural solvent. Oxygen concentration was measured under "conventional" conditions (beaker) and two different non-conventional conditions (microfluidic channel with/without membrane). Each measurement was repeated three times. The target is to exclude additional factors which might cause measurement errors. In cell measurements, we would like to be sure that the difference in measured oxygen values is only related to cell activity.

By comparing the measurements in a microfluidic chip and in a beaker, we determine if the commercial PreSense sensor is applicable in a microfluidic chip.
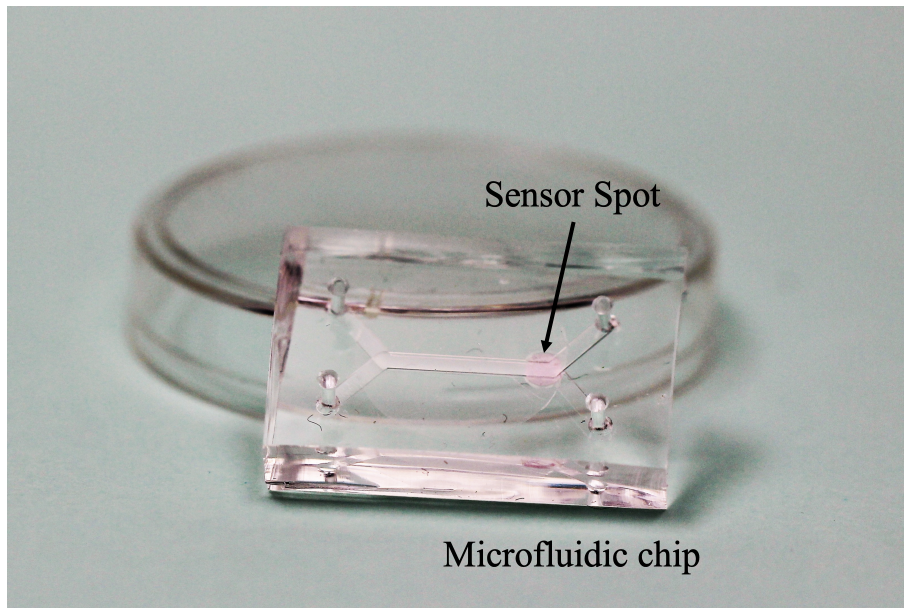
Figure 7.2: Photograph of the PreSense luminescence sensor spot what has been integrated into the microfluidic device (Chapter 4). The sensor spot has a thickness of 40 µm and a diameter of approximately 1 mm.

The graphs in Figure 7.3 show the real-time measurements of the oxygen concentration in DI water, and Table 7.1 contains the average values for every measurement with standard deviation.

Table 7.1: Standard deviation of the oxygen concentration measurements in DI water. Measurements were conducted in a beaker, in a microfluidic chip, and in a microfluidic chip with a membrane.

Meas. No.	Beaker	Chip	Chip with membrane
1	8.606 ± 0.0119 ppm	10.095 ± 0.0119 ppm	9.763 ± 0.0142 ppm
2	8.59 ± 0.0116 ppm	10.079 ± 0.0143 ppm	9.743 ± 0.0115 ppm
3	8.573 ± 0.0123 ppm	10.076 ± 0.0146 ppm	9.740 ± 0.0121 ppm

Oxygen was measured for 30 seconds with a 1-second step, and measurements were repeated three times. Within all three measurement series, the concentration of oxygen in the beaker varied between 8.54 ppm and 8.63 ppm. Slight changes in the measured oxygen concentration were seen in measurements on the microfluidic chip. However, the standard deviation, as indicated in Table 7.1, serves as confirmation that the PreSens sensor exhibits stable measurements of oxygen concentration over time in deionized water within the microfluidic chip. These values align closely with the accuracy level specified in the sensor's datasheet, which is approximately 15 ppb [98].

Furthermore, it's essential to consider the integration of the sensor into Organ-on-Chip applications. In these applications, a frequently used fluid is the cell culture medium, which
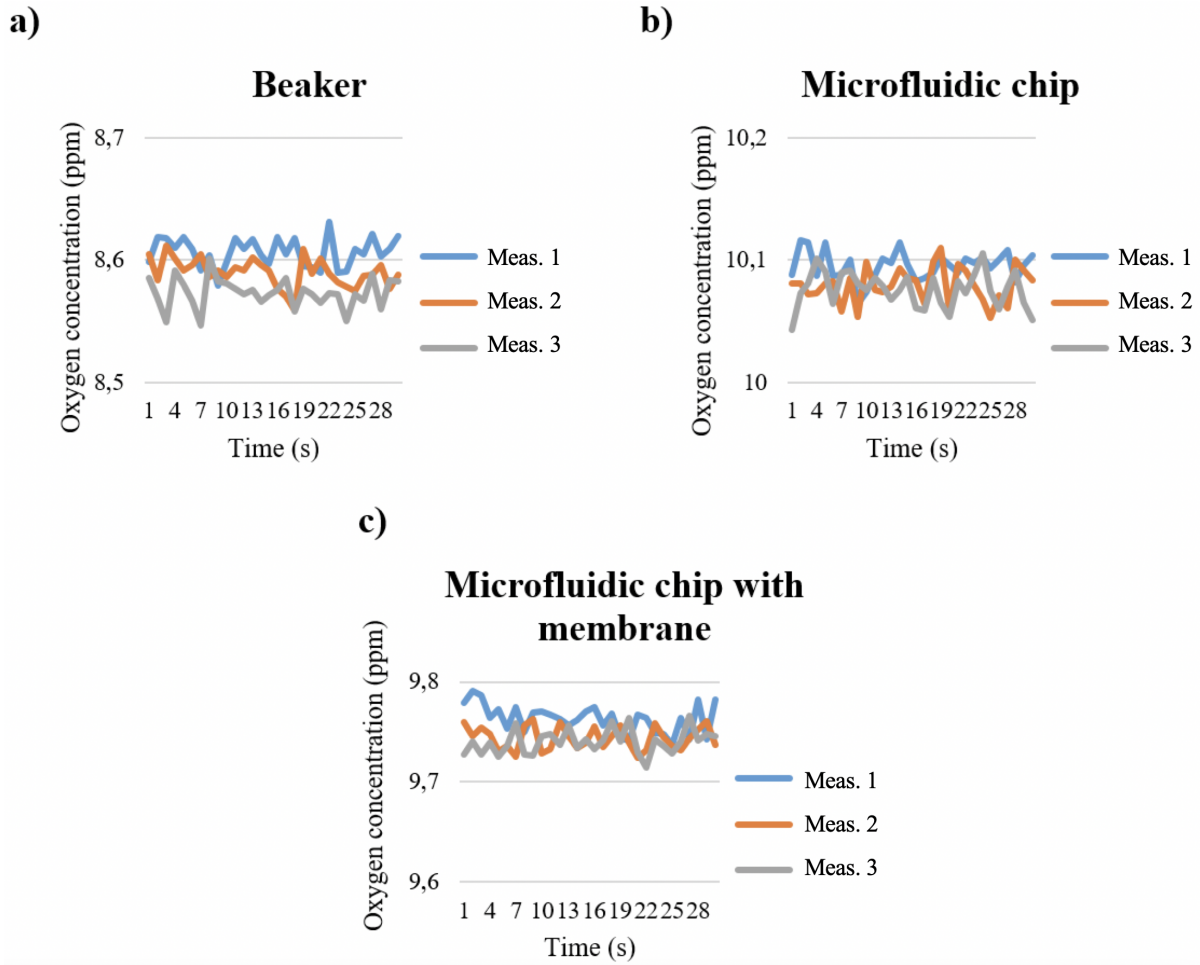
Figure 7.3: Oxygen measurements conducted on DI water: a) in a beaker, b) within a microfluidic chip, c) within a microfluidic chip with a porous membrane.

provides the cell with essential organic components, e.g., nutrients and growth factors required for cell proliferation. One of the critical constituents of cell culture medium is serum, which is a vital source of amino acids, proteins, vitamins (especially fat-soluble vitamins like A, D, E, and K), carbohydrates, lipids, hormones, growth factors, minerals, and trace elements.

However, it's worth noting that, as mentioned in the sensor's datasheet [98], potential cross-sensitivity with organic solvents could be observed. To address this concern, subsequent measurements were performed using the same setups but this time with deviations in serum content of the cell culture medium. Measurements were taken with nominal cell culture medium and with a medium containing a higher concentration of serum.

Figure 7.4 shows the investigation of oxygen concentration in a cell culture medium in the channel using the proposed setup under three different conditions: a) in the beaker, b) in a microfluidic channel and c) microfluidic chip with a membrane. It is worth mentioning that the initial channel height within the chip was set at 400 µm. When the membrane was introduced, the channel height was subsequently reduced by half. As demonstrated by

the measurements in DI water and subsequently specified in the case of the cell culture medium (Figure 7.4, b, c), the volume reduction does not impact the accuracy of the measurements. This is seen clearly in Table 7.2, which shows the standard deviation of the measurements.
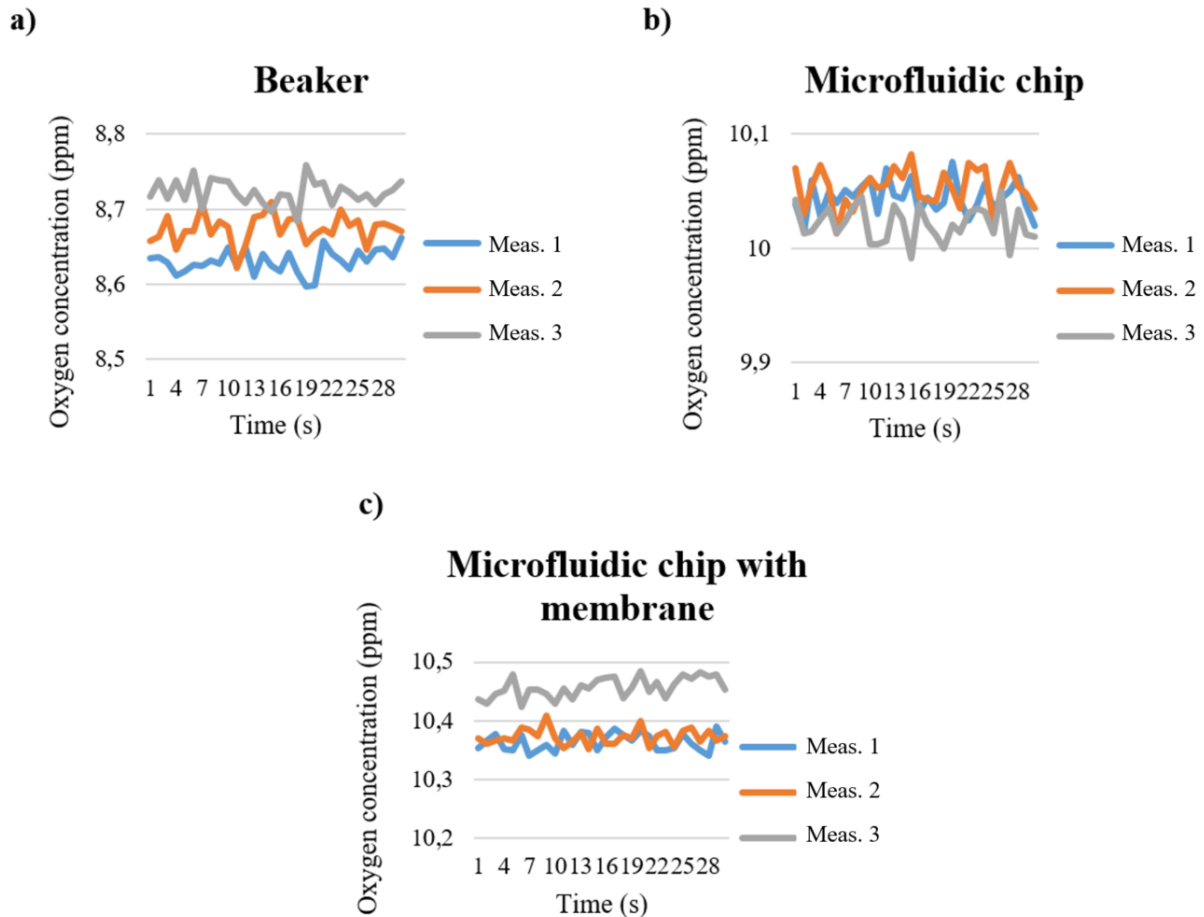
Figure 7.4: Oxygen measurements conducted in cell culture medium without serum under different conditions: in a beaker (a), within a microfluidic chip (b), and within a microfluidic chip with a porous membrane (c).

Table 7.2: Standard deviation of the oxygen concentration measurements in cell culture medium. Measurements were conducted in a beaker, microfluidic chip, and microfluidic chip with the membrane.

Meas. No.	Beaker	Chip	Chip with membrane
1	8.630 ± 0.0155 ppm	10.044 ± 0.0141 ppm	10.363 ± 0.0146 ppm
2	8.673 ± 0.0185 ppm	10.052 ± 0.0168 ppm	10.372 ± 0.0132 ppm
3	8.722 ± 0.0164 ppm	10.021 ± 0.0152 ppm	10.456 ± 0.0172 ppm

The difference in the absolute values between the oxygen concentration measured in the beaker and in the microfluidic chip can be explained by open versus closed environments.

The oxygen concentration in the microfluidic channel was slightly higher compared to that in the beaker, with an absolute value of about 10 ppm instead of 8 ppm, respectively. This effect can be attributed to the pressure-driven pump used to propel the liquid in the microfluidic chip, leading to increased oxygen dissolution in the fluid. The standard deviation values confirm the stability of the approach and its applicability to measurement of the oxygen concentration of a cell culture medium in the microfluidic chip.

Moreover, as observed in Figure 7.5 and detailed in Table 7.3, a minor elevation in oxygen concentration is evident in the cell culture medium when additional serum is introduced. This may suggest the presence of cross-sensitivity with the organic components, which are at a higher concentration with the increased serum content. This implies that a portion of the energy was transferred, but not to the oxygen molecules; nevertheless, it resulted in a reduction of emitted light intensity which the readout interpreted as an increase in the measured oxygen concentration. Nevertheless, the stability in terms of the standard deviation of the measurements stayed at the same satisfactory level (compareing Tables 7.3, 7.2 and 7.1), and these findings are beneficial for cell culture protocol. Measurement comparison confirms the stability of the sensor and proves the feasibility of detecting oxygen in medium + serum in the microfluidic channel.

Table 7.3: Standard deviation of the oxygen concentration measurements in cell culture medium with serum. Measurements were conducted in a beaker, microfluidic chip, and microfluidic chip with the membrane.

Meas. No.	Beaker	Chip	Chip with membrane
1	9.084 ± 0.0151 ppm	10.207 ± 0.0147 ppm	10.241 ± 0.0149 ppm
2	9.106 ± 0.016 ppm	10.205 ± 0.0152 ppm	10.252 ± 0.0171 ppm
3	9.122 ± 0.0155 ppm	10.181 ± 0.0176 ppm	10.297 ± 0.0167 ppm

By comparing these three use cases, one can make conclusions on the intrusiveness of this approach. Since the sensor spot is in direct contact with the material under test (MUT), this might affect the results. A possible impact mechanism is as follows: as the cells grow within the microfluidic channel, the volume they occupy gradually increases, displacing the liquid medium. Therefore, it is important to check whether the difference in measurements is not dominated by the change in the microfluidic channel's height and volume capacity (Figure 3.8) in order to eliminate systematic offset error caused by the environment. This is verified by a comparison of the measured values in the chip with membrane and without membrane. Since the measured values are almost identical, there is no need for de-embedding of the results.

Obviously, as in any measurement technique, oxygen measurements must be calibrated and bench-marked against reference measurements. The reference measurements were performed by means of an oxygen sensor FireStingO$_2$, manufactured by PyroScience GmbH
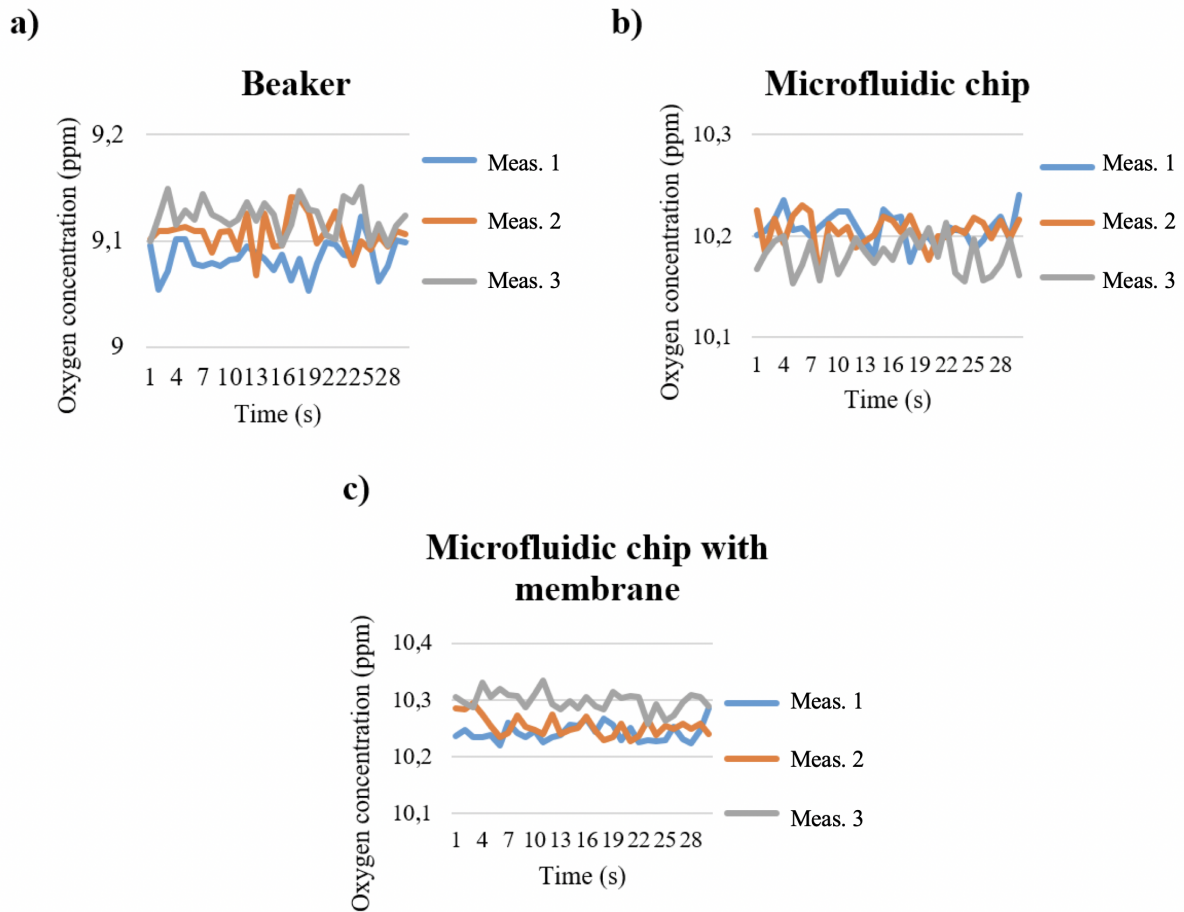
Figure 7.5: Oxygen measurements conducted in cell culture medium with serum under different conditions: in a beaker (a), within a microfluidic chip (b), and within a microfluidic chip with a porous membrane (c).

(Figure 7.6). FireStingO$_2$ utilizes the same as PreSens principle of light excitation by an LED to excite a fluorescence response.

Figure 7.6: FireStingO$_2$ chopstick oxygen sensor [128].

Unfortunately, the available configuration of the FireStingO$_2$ was only in a chopstick sensor which can not be placed into the microfluidic chip. Therefore, FireStingO$_2$ can only be used for the standard use case of oxygen measurement in a beaker. Hence, the reference measurements could only be performed in the beaker, and comparison between the two measurement techniques could be done only on this measurement set.

Table 7.4 shows a comparison of the measured values performed using FireStingO$_2$ and PreSens oxygen sensors. Additionally, the standard deviation, given in this table, shows that the measurements performed with the PreSens sensor exhibit a lower statistical spread.

Table 7.4: Comparison of maximum and minimum values and standard deviation of oxygen concentration measured by FireStingO$_2$ and PreSens sensors in two different liquids - DI and medium. All values are in ppm.

Nr.	Sensor	Liquid	Minimum	Maximum	Range
1	**FireStingO$_2$**	DI water	8.713	8.929	8.833 ± 0.0499
2			8.692	8.918	8.813 ± 0.0530
3			8.689	8.880	8.797 ± 0.0415
4		Medium	9.068	9.349	9.224 ± 0.0644
5			8.745	9.493	9.303 ± 0.0992
6			9.363	9.612	9.459 ± 0.0597
7	**PreSens**	DI water	8.579	8.649	8.606 ± 0.0119
8			8.558	8.627	8.589 ± 0.0116
9			8.547	8.612	8.577 ± 0.0123
10		Medium	8.597	8.662	8.630 ± 0.0155
11			8.622	8.710	8.673 ± 0.0185
12			8.681	8.759	8.722 ± 0.0164

The values obtained by both sensors in DI water differ only in a decimal region. Also, the measured values with the PreSens sensor have less variability, as evidenced by the smaller standard deviation. Nevertheless, the difference in measurements of cell culture medium is more pronounced. One possible reason is cross-sensitivity of the organic components. Obviously, the FireSting sensor molecules release energy to the oxygen and to some organic molecules, which results in a higher measured oxygen concentration. Therefore, one can conclude that the PreSense sensor spot possesses less cross-sensitivity to the organics. The results are shown graphically in Figure 7.7. Measurements were collected over a 30 second interval, having a one measurement per second. Measurements were repeated three times.

The reference measurement results prove that PreSens is a stable and reliable sensor solution. Results are comparable with those obtained by the FireStingO$_2$ sensor. Additionally, measurement results in the beaker can be considered to be a reference, unaffected by
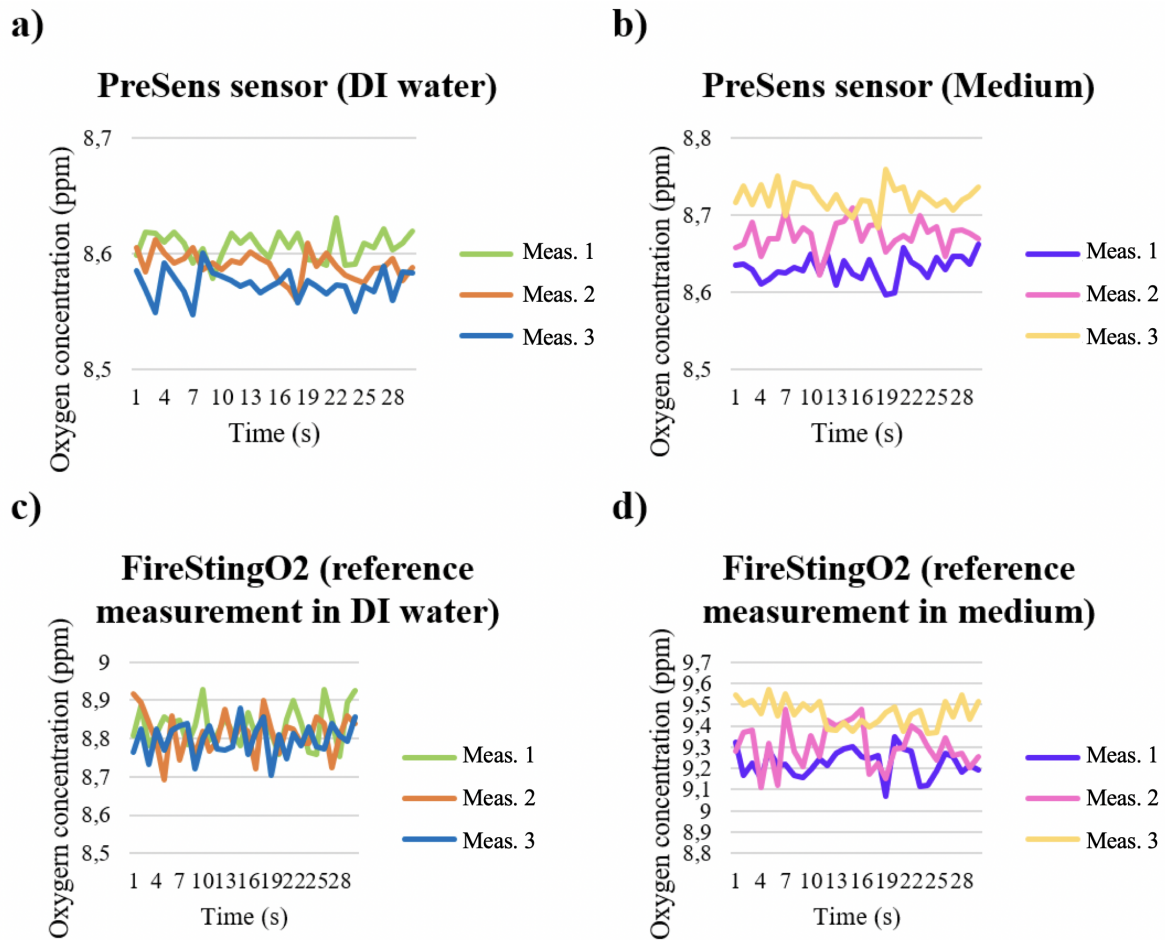
Figure 7.7: Oxygen measurements conducted in a beaker under the following conditions: a) DI water measured using PreSens sensor; b) cell culture medium without serum measured using PreSens sensor; c) DI water measured using FireStingO$_2$ sensor; (d) cell culture medium without serum measured using FireStingO$_2$ sensor.

the sensor surroundings. The fact that the standard deviation of the oxygen concentration measurements obtained in microfluidic channels does not deviate much from those obtained in a beaker gives high confidence that oxygen measurements using PreSens in a microfluidic chip are also reliable.

7.2 Transepithelial Electrical Resistance Measurements

Recent advances in microfluidic technologies have enabled the development of Organ-on-Chip systems that mimic the physiological microenvironment of human organs. One such system is the Stomach-on-Chip, which offers a promising platform for studying gastrointestinal diseases, drug responses, and cell behavior in a controlled and representative manner. In this study, a novel approach to provide in-situ measurements of cell confluency within the Stomach-on-Chip device by integrating transepithelial electrical resistance

(TEER) electrodes is presented. The TEER-based method allows real-time monitoring of cell growth and confluency, offering valuable insights into the behavior of gastric epithelial cells. Also, confluence measurements by TEER sensing can provide information on the ideal time duration for drug testing.

A microfluidic chip with embedded TEER electrodes that come into direct contact with the cell culture medium was designed and developed. Positioning of the electrodes close to the cultured cells ensures stable measurements of the resistance between them, which changes as cells grow and form a confluent layer with tight junctions. Compared to measurements conducted using chopstick electrodes, the stable positioning of electrodes within a microfluidic channel eliminates measurement uncertainties associated with human factors that can arise during the manual insertion of electrodes into a Boyden chamber. The microfluidic chip was fabricated using the method described in Section 3.6.2, enabling precise control over its features and dimensions. Electrodes (14 mm long, 1 mm wide and 200 ± 5 nm thick, of gold) on PDMS (1mm thick) were realized by sputtering through an accordingly designed shadow mask.

Figure 7.8 illustrates the Computer-Aided Design (CAD) model of the microfluidic chip with integrated TEER electrodes. The electrodes are strategically placed to maximize cell-electrode interactions while minimizing any interference with the flow dynamics. This design allows for seamless monitoring of cell confluency in real-time.
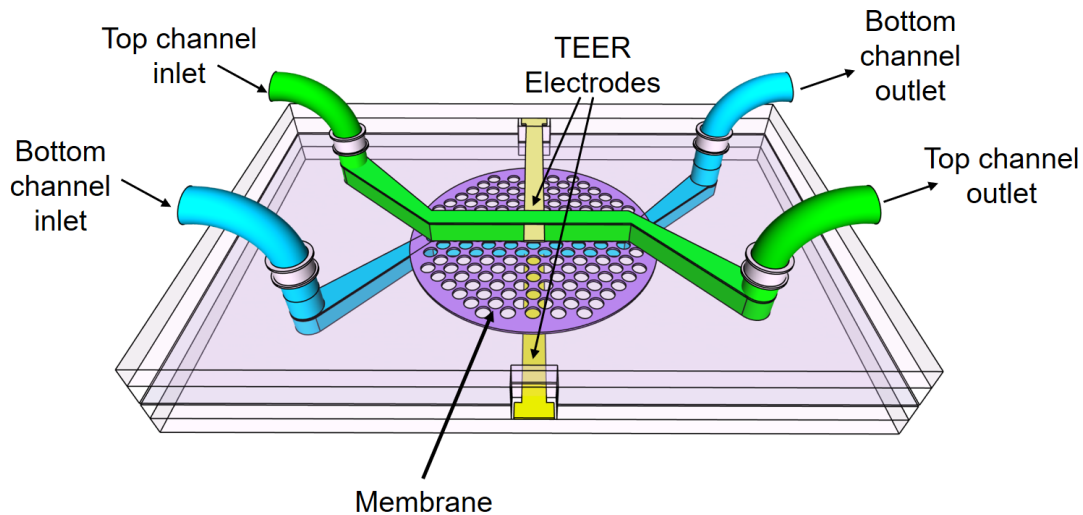
Figure 7.8: CAD designed model of the microfluidic chip with embedded transepithelial electrical resistance (TEER) electrodes.

The TEER resistance measurements provide valuable information about cell growth and confluency over time. When cells undergo mitosis and proliferate, the number of cells on the membrane increases, leading to a denser cell layer. Consequently, the resistance between the TEER electrodes rises proportionally, as tight junctions represent the resistors in the cell layer equivalent circuit Fig. 2.19. A blank resistance R_{blank} was measured by an

ohmmeter. A measured value of approximately $9.5\,\Omega\,\mathrm{cm}^2$ corresponds to a membrane area of $0.1\,\mathrm{cm}^2$. This is a resistance of the cell culture medium and a porous membrane. Then the resistance was measured while cells grew and data reflecting the confluency status of the gastric epithelial cells was obtained, as specified in Subsection 3.6.2.

As demonstrated in Figure 7.9, the TEER measurements track the progress of cell confluency over time. During the initial days of cell seeding, the resistance is low as the cells are sparsely distributed on the membrane. However, as the cells continue to divide and create tight junctions, the resistance steadily increases. On the 7$^{\mathrm{th}}$ day after cell seeding, the curve reaches a saturation region, indicating that the epithelial cancer gastric cells have formed a confluent layer. The measured values exhibit a strong correlation with the existing literature [99], [68].
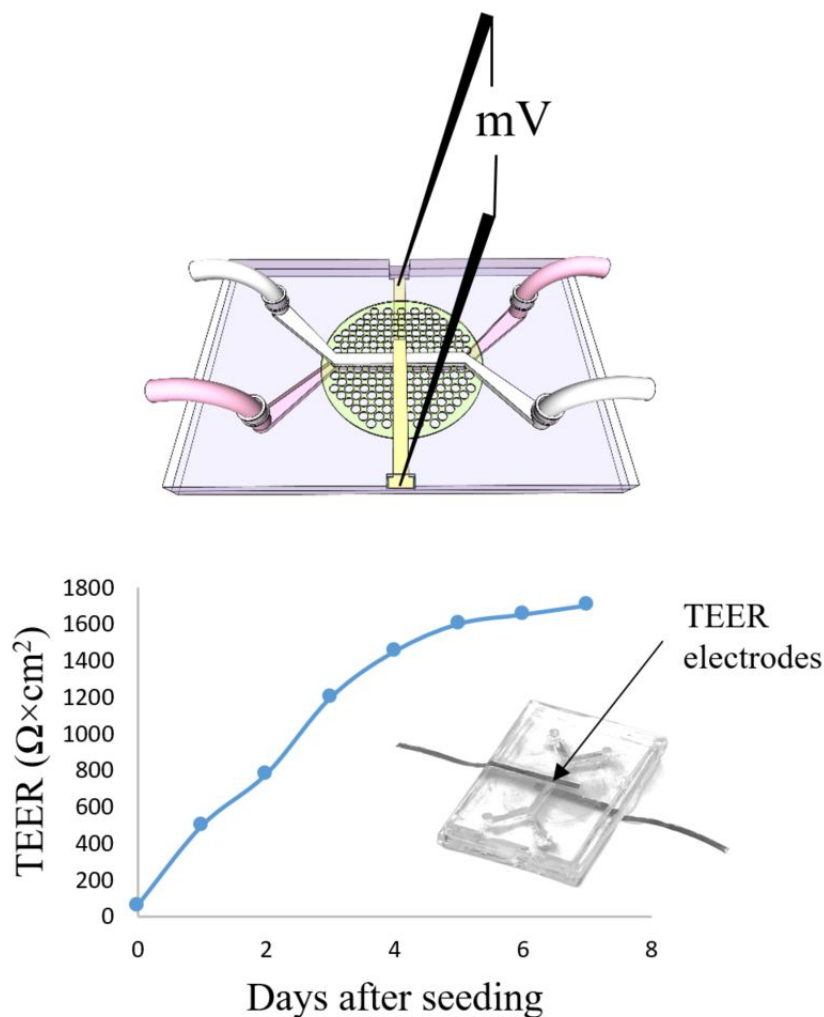
Figure 7.9: The upper part of the figure illustrates the schematic representation of the microfluidic structure, featuring two channels, a membrane, and TEER electrodes. The lower part of the figure shows the recorded resistance between the electrodes throughout the cell growth process, accompanied by a photograph of the manufactured microfluidic device [68].

One crucial aspect of the TEER-based method is the impact of temperature on resistance measurements. To ensure accurate data acquisition without compromising cell viability, a simple temperature stabilization procedure was employed. During the measurements, the microfluidic chip is temporarily removed from the incubator. However, the chip remains inside the incubator for cell culturing at all other times. Before data acquisition, the chip is allowed to stabilize at room temperature for approximately 15 minutes. This step ensures that temperature-related effects do not interfere with the resistance measurements. This short period of temperature stabilization does not negatively affect the cultured cells. This careful approach guarantees reliable TEER measurements and provides a robust platform for study of cell behavior in a Stomach-on-Chip environment. However, resistance measurements can also be done directly in incubator at the stable temperature therein. For this purpose the microfluidic chip has to be equipped with humidity- stable and sterile electronics. In this case, TEER sensor is beneficial for the designed experimental setup for Stomach-on-Chip (Figure 4.11), since the chip has to be located in the automated fluorescence microscope inside the incubator and connected to the pressure-driven pump.

Upon completion of the TEER measurements, the microfluidic chip is reconnected to the pumping system. A flow rate of 0.5 µl/min is maintained to ensure proper medium exchange and provide a stress-free environment for the cultured cells. The laminar flow within the 1 cm long channel ensures that the cells experience minimal shear stress, which is essential for maintaining cell integrity and functionality. Liquid flow in the microfluidic chip did not influence the transepithelial electrical resistance measurements.

Moreover, as described before, electrodes have been sputtered on PDMS through a shadow mask. The surface of these electrodes, along with their magnification, is depicted in Figure 7.10, revealing the presence of elongated two-directional wrinkles labeled as $\vec{x}$ and $\vec{y}$.
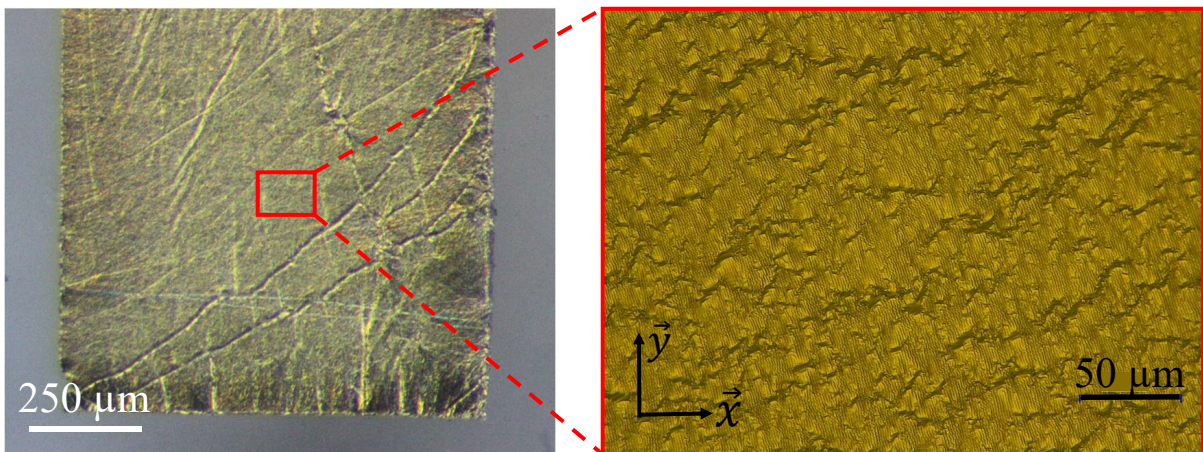
Figure 7.10: Microscope image of gold electrodes, sputtered on PDMS, and its magnification in the inset.

Wrinkled electrodes on elastic silicone surfaces have recently sparked significant interest in the field of flexible electronics and microfluidics. The intriguing observation of wrinkling on these surfaces, despite the absence of pre-stretching procedures, has opened up new avenues for understanding the complex behavior of metal layers on elastic and viscoelastic materials.

The origin of these wrinkles can be traced back to the metal deposition process, where the PDMS thin near-surface layer undergoes thermo-mechanical expansion. The grooves and wrinkles emerge as a result of this expansion, leading to wrinkling patterns on the electrode surface. Remarkably, similar surface defects were observed even without the pre-stretching the PDMS before sputtering, and the temperature during the interval metal deposition process was kept below $50\,°C$, contrary to earlier assumptions that elevated temperatures might be necessary for wrinkle formation [83, 86, 87].

The appearance of wrinkles on the metal electrodes significantly influences their electrical properties. The resistance of the wrinkled electrodes was found to be three times higher than the calculated value for a planar thin film, which is typically around $1.7\,\Omega$. As a consequence, the measured resistance of the wrinkled electrodes was $5 \pm 0.1\,\Omega$. This deviation from the expected resistance can be attributed to the altered geometrical characteristics induced by the wrinkling phenomenon. This aspect is investigated in further detail in following Section 7.3.

During the fabrication of the microfluidic chip, the sputtered electrodes' resistance might increase slightly, reaching approximately 7 - $8\,\Omega$. This is due to the handling of the flexible PDMS layers, which can sometimes lead to minor fractures in the electrodes. Despite these challenges, the measurements using the developed microfluidic device with TEER electrodes (Figure 7.9, 7.10) were successfully conducted, proving the feasibility of this approach.

The wrinkling of metal layers on elastic and viscoelastic materials is a captivating and complex research direction that holds tremendous promise for numerous applications. However, the natural formation of wrinkles on these surfaces remains relatively unexplored. Delving deeper into the underlying mechanisms driving wrinkle formation and evolution can unlock valuable insights into the behavior of these materials under various conditions.

Understanding and controlling wrinkle formation without resorting to PDMS pre-stretching would be a game-changer in the field of flexible electronics. This could lead to the development of more robust and efficient devices, as well as simplify the manufacturing process. Furthermore, improved control over wrinkling could potentially enhance the performance and reliability of devices, making them suitable for a broader range of applications, including wearables, biomedical sensors, and soft robotics.

Therefore, this phenomena was investigated in additional detail and is reported in the next Section 7.3. In contrast to this section, the electrodes are placed on a thin freestanding PDMS membrane since the strategic placement of the electrodes on the PDMS membrane

could offer exciting possibilities for in-situ measurements. By keeping the cell layer visible during experiments, researchers can gain real-time insights into biological processes, cellular behavior, and dynamic interactions at the interface between the cells and the electrode surface. Moreover, the influence of PDMS hardness and thickness on the wrinkling behaviour of electrodes was investigated and will be described in the following section. This case has not been reported in the literature yet.

7.3 Thermo-Electric Meander-shaped Element on the membrane

In the previous Subchapter 7.2, a sensor based on TEER electrodes was presented. As was shown, electrodes that are sputter deposited on the elastic silicone possess wrinkles which result in higher resistance compared to electrodes without wrinkles. This investigation has led to fascinating findings and promising applications. The emergence of surface defects, even with PDMS stretching, highlights the need for a deeper understanding of wrinkling phenomena on elastic materials. Such knowledge could pave the way for enhanced control and manipulation of wrinkles, leading to the development of a wider variety of possible innovations.

Additionally, it is of high interest to embed sensors and actuators directly on a thin membrane that can serve as a carrier for cell culturing (Figure 4.4). Every sensor requires electrodes and metal traces to conduct signals to and from the outer world.
In the previous subchapter, the electrodes were realized on a thick PDMS structure. To bring an electric element even closer to the cell layer, e.g. as the one discussed in the Subchapter 4.1, the electrodes must be implemented on a thin membrane.

As opposed to Chapter 4.1, in which a polyesther membrane and femtosecond laser structured membrane were described, in this subchapter a PDMS membrane is considered. To obtain a continuous conducting path, electrodes must first be deposited, and only then can pores be fabricated. Consequentially, this method is not applicable to the membranes presented in Chapter 4.1, because:

a) in the case of a polyesther membrane, the membrain was already a pre-structured commercially available filter;

b) in case of the femtosecond laser fabricated structure, the microstucturing was performed in a closed microfluidic channel.

Therefore, in this subchapter a thin freestanding PDMS layer is fabricated and used as a substrate for the metal electrodes. This functionalized membrane can be implemented in the microfluidic chip. Such a thin PDMS membrane can be useful in numerous applications described in Chapter 2.

The methods presented in Chapter 3 were used to realize a thin PDMS membrane equipped with a meander-shaped metal thin film that exhibits thermo-electric properties (Figure 3.10 and 7.13). The reported membrane has several beneficial characteristics which can make it useful for numerous applications, such as e.g. Organ-on-Chip or sensing applications. The properties are listed below:

a) the membrane is quite thin and can be realized with any thickness in the range from $2.5\,\mu m$ to $50\,\mu m$. The thickness of a film can be adjusted by altering the spin speed during the spin-coating process. These values plus the fact that it is composed of PDMS make it suitable for various Organ-on-Chip applications;

b) thanks to a very careful derivation of the optimal dimensions for width, length and thickness, minimal power dissipation and highest efficiency can be achieved with regard to the thermo-electric properties of the device proposed in this subsection;

c) despite the thinness of the structure, it is still very stiff and suitable for handling with a supportive ring.

In this section, we discuss the thermo-electrical and thermo-mechanical behavior of a novel Cr/Au thermo-electric structure on a thin freestanding PDMS membrane. Meander-shaped elements with varying wire lengths were developed to achieve different resistance values. The investigation also covers the natural wrinkle formation that occurs during magnetron sputtering on soft layers of different thicknesses. Furthermore, temperature-current and resistance-current characteristics of the meanders on both freestanding and fixed PDMS layers are provided.

To our knowledge, this study is the first so far to explore the influence of PDMS substrate hardness on the thermo-electric characteristics of metal structures. The impact of different mixing ratios of PDMS base and curing agents on the thermo-electrical characteristics of the meanders is examined.

Moreover, the PDMS/Cr/Au interface is analyzed with regard to naturally created wrinkles, and the underlying physical mechanisms driving wrinkle formation are discussed. Finally, this research investigates the mechanical deformation of the PDMS freestanding membrane and the movement of the meanders under the application of DC current.

The proposed membranes have been fabricated, and subsequently the surface was investigated by visual inspection, as shown in Figure 7.11.

On the left-hand side of the figure, Figure 7.11(a), one can see that the structure exhibits a smooth surface which translates the profile of the underlying material. In this case we have a silicon carrier with a photoresist on top. Based on our previous research findings and reports in the literature [129], pre-treating PDMS with oxygen plasma enables superior adhesion of PDMS and conducting structures. Furthermore, the surface becomes hydrophilic.
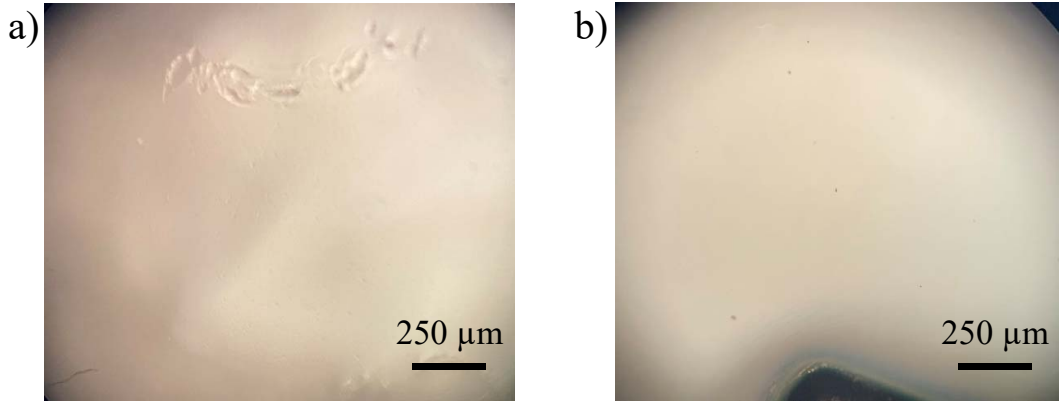
Figure 7.11: Microscope pictures of the bare PDMS membrane surface - (a) before oxygen plasma treatment; (b) 20 s after the treatment [100].

Hence, on the right-hand side of the Figure, 7.11(b), one can see a picture taken 20 s after treatment of the surface by oxygen plasma. It is expected that during the plasma treatment, wrinkles and deformations will arise due to thermal effects throughout the entire process duration. However, it appears that after the plasma treatment is completed, PDMS resumes its original wrinkle-free form. Therefore, the surface is flat and homogeneous. Moreover, PDMS membrane thickness tolerance did not exceed 2% of the original thickness at any point. Table 7.5 shows measured in detail thickness parameters. As one can see from this table, the inhomogeneity is minimal and remains within $\pm 0.16 \, \mu m$.

Table 7.5: Targeted PDMS thickness and measured variation over the membrane: P1 - value at the center; P3 - edge; P2 - in the middle between P1 and P3.

Sample No.	Intended thickness	P1	P2	P3	Average
	µm	µm	µm	µm	µm
1	20	20.3	20.4	20.5	20.4
2	20	20.34	20.37	20.4	20.37
3	40	40.08	40.09	40.11	40.09
4	40	40.11	40.12	40.14	40.12
5	20	40.38	40.45	40.7	40.51
6	20	40.29	40.31	40.6	40.4
7	40	19.9	20.1	20.3	20.1
8	40	20	20.2	20.4	20.2

As discussed previously in Chapter 3, the subsequent processing step is the deposition of a metalization layer on top of the PDMS carrier. In this case, two meander structures of different lengths were sputter deposited using a shadow mask. Figure 7.12 shows the two structures with lengths 29 mm and 48 mm. Also, the figure provides a view of the wrinkled deformations that form on the surface of the thermo-electric meander elements sputtered onto the PDMS carrier.

The final chromium (Cr) layer thickness is 25 nm, while the gold (Au) layer thickness was measured to be 409 nm. It is important to mention that Cr is acting as an adhesive material in this case. Pull-off test was conducted and showed excellent bonding between the Cr/Au layer and the oxygen plasma pre-treated PDMS carrier. An outstanding breaking strength value of 1.4 MPa was achieved.

The exact detailed dimensions of the meandered thermo-electric structure depicted in Figure 7.12 are shown in Figure 7.13.
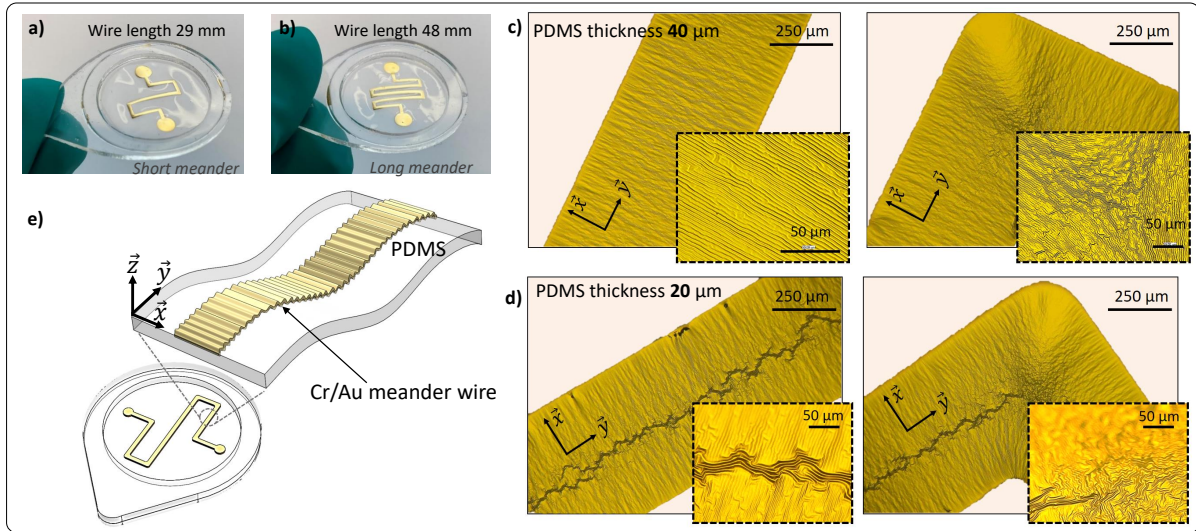
Figure 7.12: Microphotographs of standalone PDMS devices with (a) short meander structure (29 mm) and (b) long meander structure (48 mm). (c), (d) depict microscope pictures of the meander structures sputtered on PDMS carrier with 40 µm and 20 µm thickness; finally, (e) presents a 3D model of the structure with the thermo-electric passive device. The wrinkling is visible in the zoom-in inset in the figure [100].

Upon the completion of the sputtering step, which involved argon gas in plasma state, a large number of mechanical deformations were formed covering the entire surface of the metal wires. Both one-dimensional $\vec{x}$ and two-dimensional deformations were observed (in $\vec{x}$ and $\vec{y}$), as shown in Figure 7.12, sub-figures (c) and (d), respectively. The one-dimensional deformations, which run transverse to the wire parallel to the $\vec{x}$ axis with a horizontal periodicity of 5 µm and vertical wrinkle elevations of 0.26 µm, as can be read from the annotated profilometer measurement results shown in Figure 7.14.

By careful observation of the wrinkles in the meander wire Figure 7.12 one can observe an interesting behaviour: the two wrinkle directions are lateral to the structure's horizontal dimension and then they converge to a singularity. This leads two-dimensional wrinkle formations on the surface.

A physical explanation for this could come from the thermo-electrical properties of a metal layer placed on a PDMS surface:
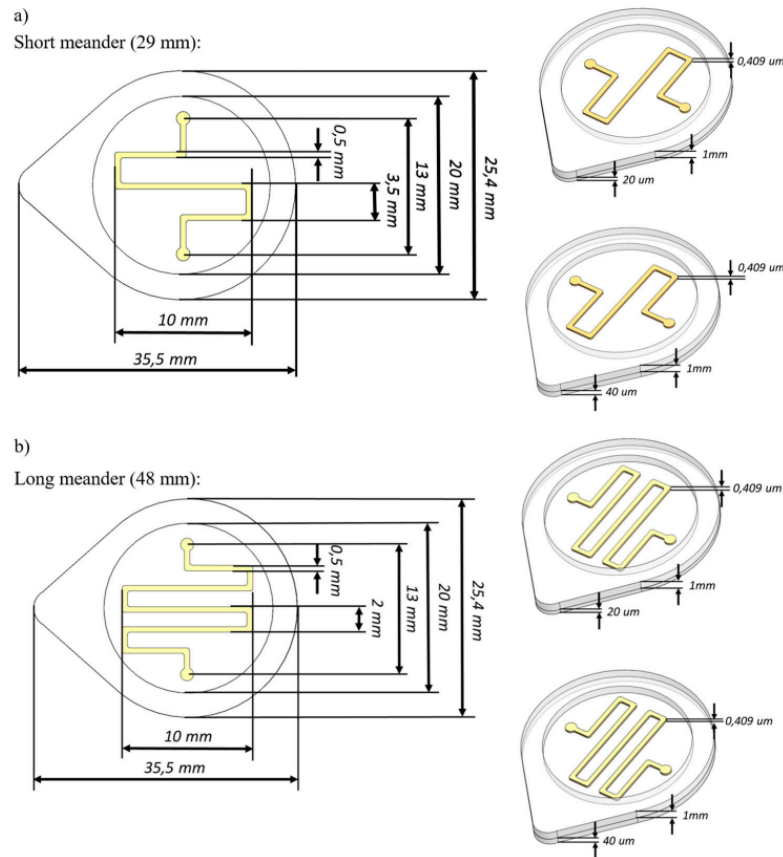
Figure 7.13: Annotated drawings of the fabricated devices with exact physical dimensions. Both 2D and 3D description of the structures are shown for the (a) short meander structure (29 mm) and (b) long meander structure (48 mm) [100].
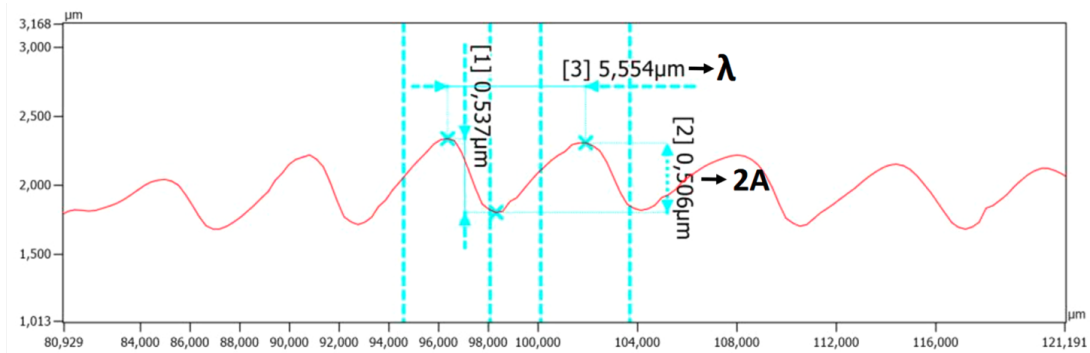
Figure 7.14: Annotated structure topography measurements obtained with a Profilometer Keyence VK-X3000 [100].

- the metal meander structure acts as a very good thermal conductor, therefore relaying any thermal variations directly into the PDMS carrier by direct physical contact;

- the polymer structure deforms and the surface expands even under minimal thermal stress conditions.

It needs to be mentioned that this effect can be used intentionally, as discussed later, by

applying a DC current to heat the meander structure.

Since the magnetron sputtering process was not continuous but followed a duty cycle, the ambient temperature in the chamber remained below 30 °C at all times during the metal deposition process. The reason for PDMS carrier deformation seems to be ballistic injection of the target metal atoms during sputtering. These atoms possess high kinetic energy, enabling them to reach the PDMS carrier. During impact with the surface, kinetic energy is converted to thermal energy and leads to a rise in PDMS surface temperature. This, in turn, results in thermo-mechanical deformation and expansion of the structure. The same effect was observed on both thicker and thinner PDMS carriers, having 20 μm and 40 μm thickness.

Hence, under thermo-mechanical stress conditions, the PDMS structure is deformed. After the structure cools, the PDMS reverts to its original form. At this point, wrinkle patterns form on the metal surface due to the mechanical forces tearing the metal trace structure, which is attached by adhesion to the PDMS carrier substrate. This finding is in accordance with observations reported in the literature that confirm and support this effect [85, 129–133]. To sum up, the wrinkles depicted in Figure 7.12 (c),(d) are caused by the thermal stress during the plasma sputtering process. This means that wrinkles are created intrinsically during the sputtering process, without any specific additional micromechamical processing steps such as pre-streching. This is an interesting observation that can be of high practical relevance for metallization of PDMS substrates.

Next, wrinkle formation on two metal trace structures fabricated on PDMS substrates of different thicknesses (Figure 7.12 (c),(d), with 20 μm and 40 μm thick PDMS substrates, respectively) are systematically compared to each other. For a valid comparison, the metallization thickness is equal in both cases.

One can clearly see that on the 20 μm thick PDMS structure in Figure 7.12 (d) there are longitudinal wrinkles along the $\vec{y}$ direction. Interestingly, the metallization of the 40 μm thick PDMS structure does not exhibit such wrinkles. This can be explained according to the theory presented in [134], which states that systematic periodic surface deformations occur in the presence of metallization thickness gradients. Such a metallization gradient is likely to show up as a result of deposition by means of the shadow mask. In this study, metallization gradients were present at the opposite edges of the metal structure. Hence, the wrinkles were generated concurrently in a periodic manner advancing from each edge towards each other and the center of the metal trace, meeting at the symmetry axis. This results in generation of perpendicular ditches due to the mismatch in periodicity and intensity of the two converging wrinkle waves. Yet, interestingly, this phenomenon is not present at all in the case of the 40 μm thick PDMS structure. Neither does it takes place in thicker substrates, e.g. of 1 mm thickness, as shown in Figure 7.15.

Clearly, the difference between the two cases is that in the case of 20 μm thickness, the PDMS substrate is soft, while above a certain threshold, which seems emprically to be
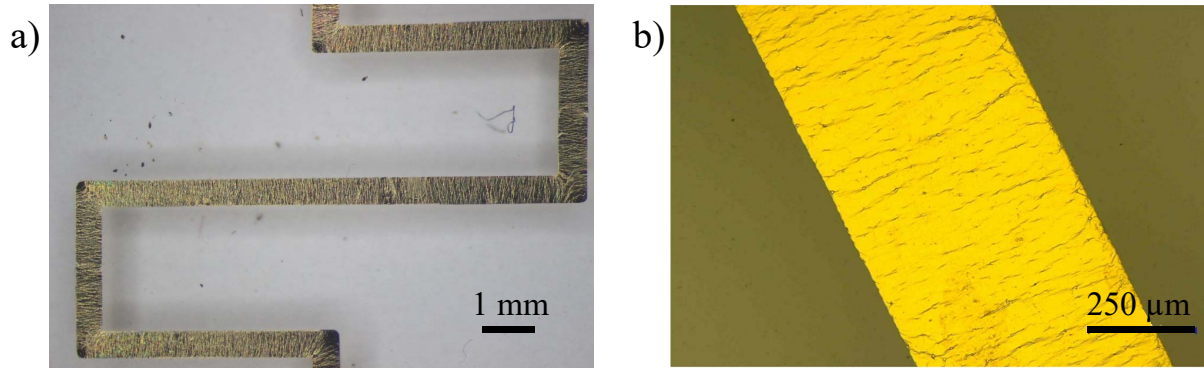
Figure 7.15: Microphotographs of a) meander structure on a 1 mm thick PDMS substrate; b) measured one-directional wrinkle arrangement [100].

40 µm, the PDMS substrate is sufficiently hard to prevent this effect from taking place. Curiously, the wrinkling theories from the literature do not account for substrate as a variable and therefore cannot predict the effect reported here. Both the continuum elasticity approach [85] and the non-linear wrinkle formation theory [134] employ a simplification that assumes the substrate is a thin slab placed on a semi-infinite substrate under the influence of elastic mechanical stress.

Moreover, there is another noteworthy observation related to wrinkle formation. At the large contact pad elements, located at the start and end terminals of the meandered structure and having a circular shape of 3 mm diameter, labyrinth-shaped wrinkle formation (both in $\vec{x}$ and $\vec{y}$ directions) arose, as shown in Figure 7.16.

There are two simultaneous counteracting thermo-mechanical effects occurring at the interface between the PDMS carrier and the metal wire which are responsible for such a complex labyrinthine wrinkling pattern on the circular pad surface:

- Radial compression

- Isotropic thermal expansion

It is noteworthy to mention that the hierarchical wrinkle formation at the pad edges, as seen in Figure 7.16 (a),(b) resembles the radial shape corresponding to use of a solvent evaporation method in the fabrication process, as discussed in [135]. Simultaneously, the center area of the pad is covered by a labyrinthine wrinkle topography, which is determined by the carrier elasticity properties and the physical dimensions of the metallization, as analyzed in [130, 135–137].

Interestingly, a similar phenomenon was investigated specifically for this purpose with fabricated circular metal layers, obtained by sputtering without the use of shadow masks. To study this effect in a systematic manner, ten test structures were fabricated by full-area metal deposition on circular PDMS (mixing ratio 10:1) carrier substrates of various

a) 10:1   b) 10:4

Contact pad   Contact pad

100 µm   100 µm

c) 10:1   d) 10:4

100 µm   100 µm
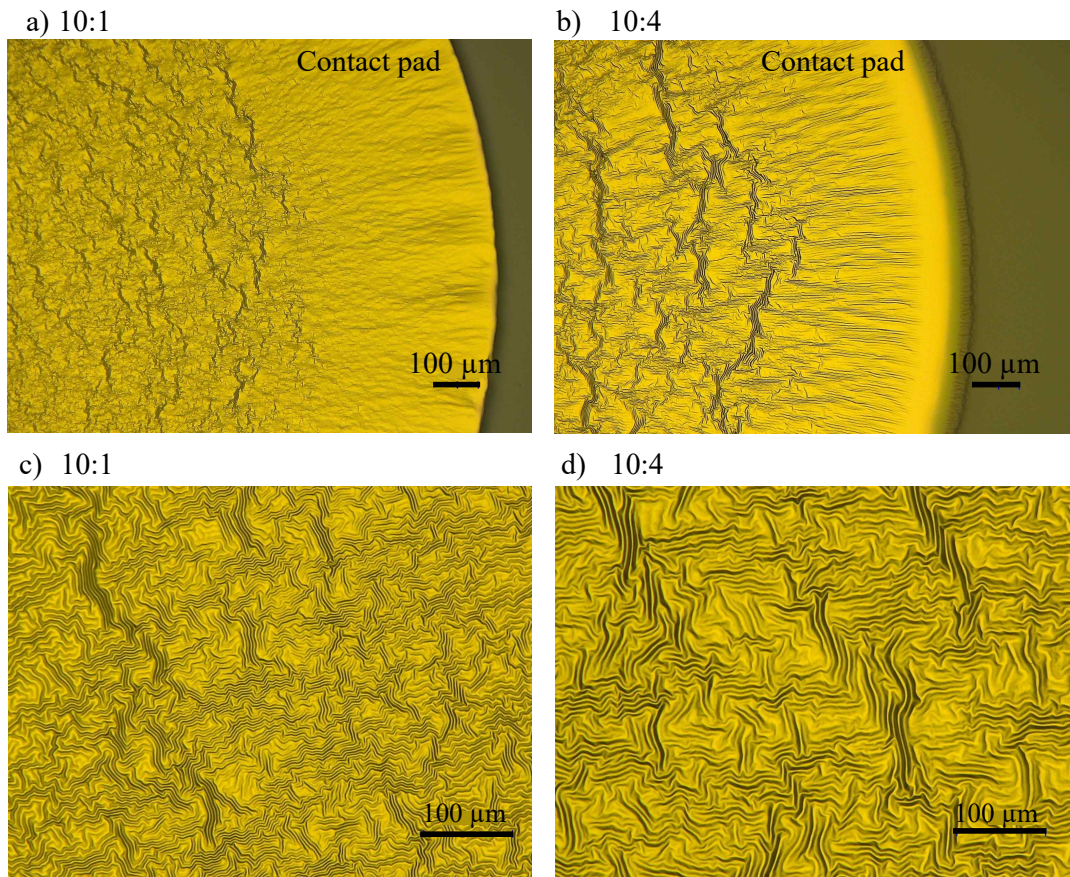
Figure 7.16: Microphotographs of contact pads, exhibiting labyrinth-shaped wrinkles, located at the ends of the meander structure on a 40 µm PDMS substrate a), c) formulated with mixing ratio of 10:1; b), d) formulated with mixing ratio of 10:4. The sub-figures c) and d) are a magnification of the center part of the images in sub-figures a) and b) [100].

thicknesses. The thickness was varied in steps of 100 µm from 0.1 mm to 1 mm. All of these structures on relatively thick PDMS substrates exhibited radial hierarchical wrinkling, as shown in Figure 7.17.

In the previous discussion, it was shown that the dimensions (more precisely: the thickness) of the PDMS carrier have an influence on the wrinkling behavior and the resultant pattern shapes on the metallization surface. In addition, it was also observed that the hardness of the polymeric support material not only improves the mechanical stability properties but also has an influence on the surface properties after metallization. To investigate this further, additional carriers with identical geometric dimensions but utilizing a different mixing ratio of 10:4 were prepared (10 parts base, 4 parts crosslinker). For comparison, Table 7.6 shows the measured hardness levels obtained for the two mixing ratios. As expected, the PDMS in the 10:4 ratio exhibits a higher hardness in contrast to the 10:1 ratio.

On a stiffer substrate, the surface of the metallization was flat in some areas, as shown
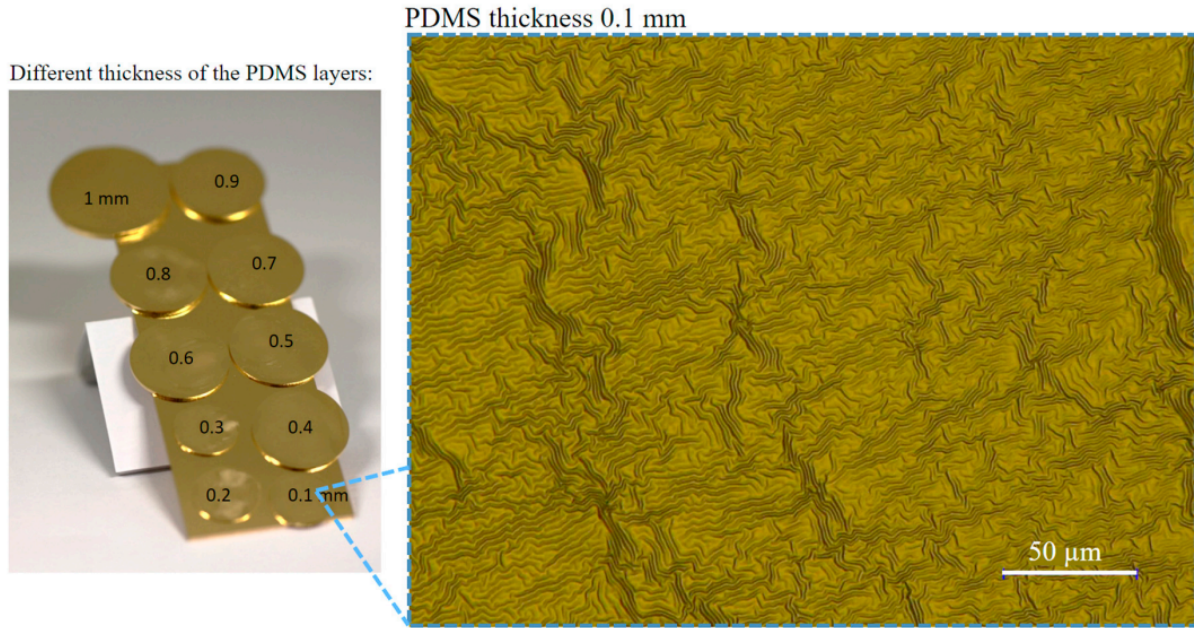
Figure 7.17: Chip photograph of circular test structures of Cr/Au deposited on PDMS carrier formulated with a 10:1 mixing ratio. The substrate thickness is increased from 0.1 mm to 1 mm in steps of 0.1 mm. The zoomed view shows the surface of a 0.1 mm thick structure. Identical wrinkle patterns were observed on all the structures, fabricated without shadow mask [100].

Table 7.6: Measured PDMS hardness levels for two values of PDMS mixing ratios.

Mixing ratio (base : curing agent)	Hardness (HC)	Wrinkle Height (µm)
10:1	70.4 ± 0.1	0.26
10:4	74.6 ± 0.1	0.437

in Figure 7.18. However, other regions also exhibited wrinkle formation. As can be seen, the average wrinkle height on a 10:4 substrate was measured to be 0.437 µm, while on a 10:1 substrate it is only 0.26 µm.

Additionally, Figure 7.19 compares the roughness of the surface for the structures with a 10:1 and with a 10:4 mixed PDMS substrate. The profile measurements were done using a 3D profilometer (Keyence Corp., 3D-Profilometer VR-6000).

As discussed previously, wrinkles are formed as a result of thermo-mechanical stress at the interface between PDMS and a metal thin film. Hence, the wrinkle formations are present over the entire volume of the metal wire, resulting in alteration of its length compared to the planar non-wrinkled state, as shown in Figure 7.12 (e). The structure becomes effectively longer. This leads to a considerable deviation of the effective measured resistance compared to the design target calculation. As shown in Table 7.7, there is a large discrepancy between measured and calculated resistance values.

For example, the shorter meander device, denoted as sample 3 in Table 7.7 and shown in Figure 7.19 (b), exhibits a ratio of 3.14 between the measured value of 11 Ω and calculated
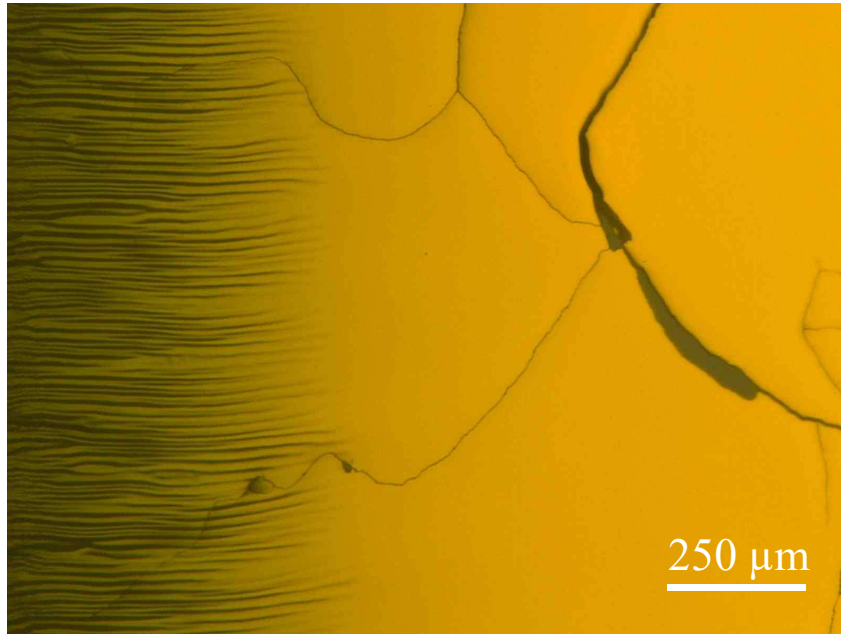
Figure 7.18: Microscope photo of the metal trace surface on a 20 µm thick hard PDMS substrate formed with a 10:4 mixing ratio. Both flat and wrinkled regions can be identified. The miniature cracks are clearly visible in the flat region. Yet, in the wrinkled region these appear to be self healing [100].
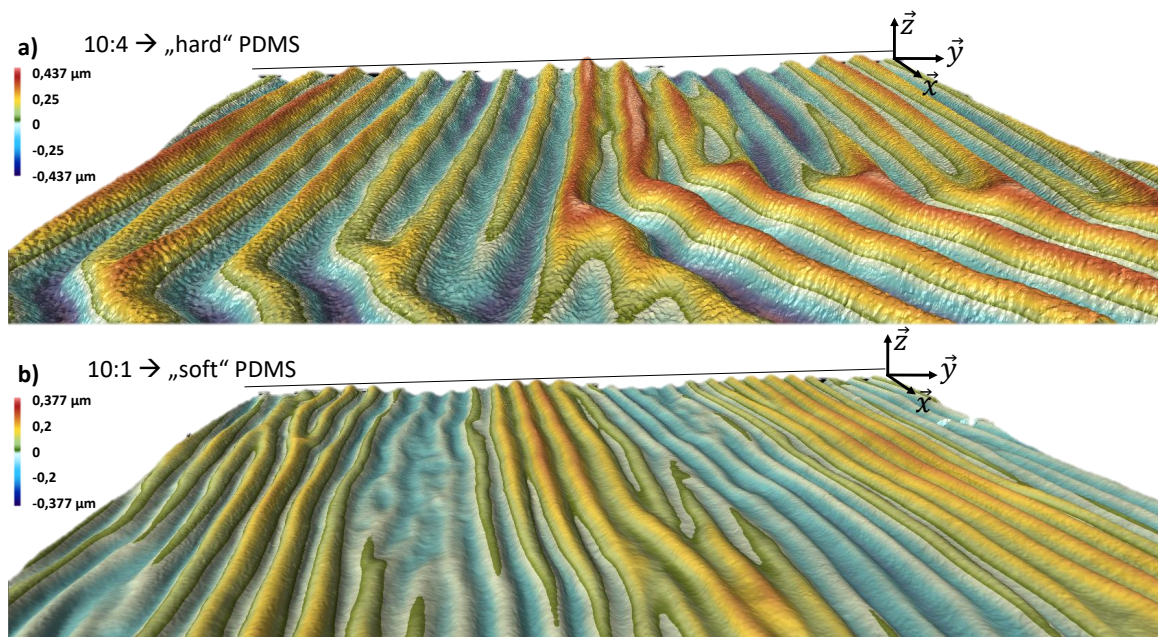
Figure 7.19: Profile measurement of the meander on a 40 µm thick PDMS membrane with two mixing ratio values: a) 10:4 "hard"; b) 10:1 "soft" [100].

value of $3.46\,\Omega$. Similarly, the longer meandered device, shown in Figure 7.12 (b), exhibits a ratio of 2.44 between the measured resistance value of $14\,\Omega$ and the calculated value of $5.73\,\Omega$. The measured value is always higher than calculated by a factor that varies

Table 7.7: Detailed parameters of the thermo-electric meander-shaped elements on thin freestanding PDMS membranes.

Sample	Meander length	PDMS mixing ratio	PDMS thickness[1]	R_calc	R_meas	Wrinkles wavelength
No.	mm	base : curing agent	µm	Ω	Ω	µm
1	29	10:1	20.4	3.46	10.8	5.1
2	48	10:1	20.37	5.73	13.5	5.07
3	29	10:1	40.09	3.46	11	5.05
4	48	10:1	40.12	5.73	14	5.08
5	29	10:4	20.1	3.46	15.4	5.33
6	48	10:4	20.2	5.73	20.5	5.34
7	29	10:4	40.51	3.46	15.42	5.34
8	48	10:4	40.4	5.73	20.7	5.36

[1] PDMS thickness value obtained at three coordinates along the structure. The entry in the table represents the average value of the three measured values.

between roughly 2.5 to 4. This effect was empirically confirmed for all of the structures, with the assumption that wire thickness and width do not change. Obviously, it is also assumed that the metal specific resistivity (ρ) remains unvaried.

The meandered wire becomes extended due to wrinkling, resulting in a longer effective length which leads to a higher effective DC resistance. This can be easily explained by the well-known Pouillet's law

$$R = \rho \cdot \frac{l}{A}, \tag{7.1}$$

where ρ is the resistivity in Ω·m, A is the cross-sectional area and l is the wire length. Larger l leads to a higher resistance R.

Additionally, Figure 7.20 (a),(b) present measured heatmaps of several Cr/Au meander structures on a 10:1 PDMS carrier.

A DC current was applied and the temperature response was studied using an infrared (IR) camera. At a DC current of 180 mA, the short wire reached a temperature of 160 °C, while the long wire heated up to 230 °C.

The measured temperature dependence on applied DC current exhibits a parabolic behaviour. This can be intuitively explained by Joule's first law $P = I^2 \cdot R$, under the assumption of perfect conversion of electrical power to thermal energy on the conducting meandered element. Since two different lengths result in differing resistance values, the curvature of the two curve arrays is different. Figure 7.20 (b) proves empirically that the thermal behaviour is nearly independent of the PDMS thickness. The current-temperature curves for 20 µm and 40 µm thick membranes overlap almost perfectly.

Yet, Figure 7.20 (c) shows that the mixing ratio, and thereby hardness of the PDMS substrate has a significant impact. As discussed above and described in Figure 7.19, the structures formed with a PDMS mixing ratio 10:1 (soft) and 10:4 (hard) exhibit different
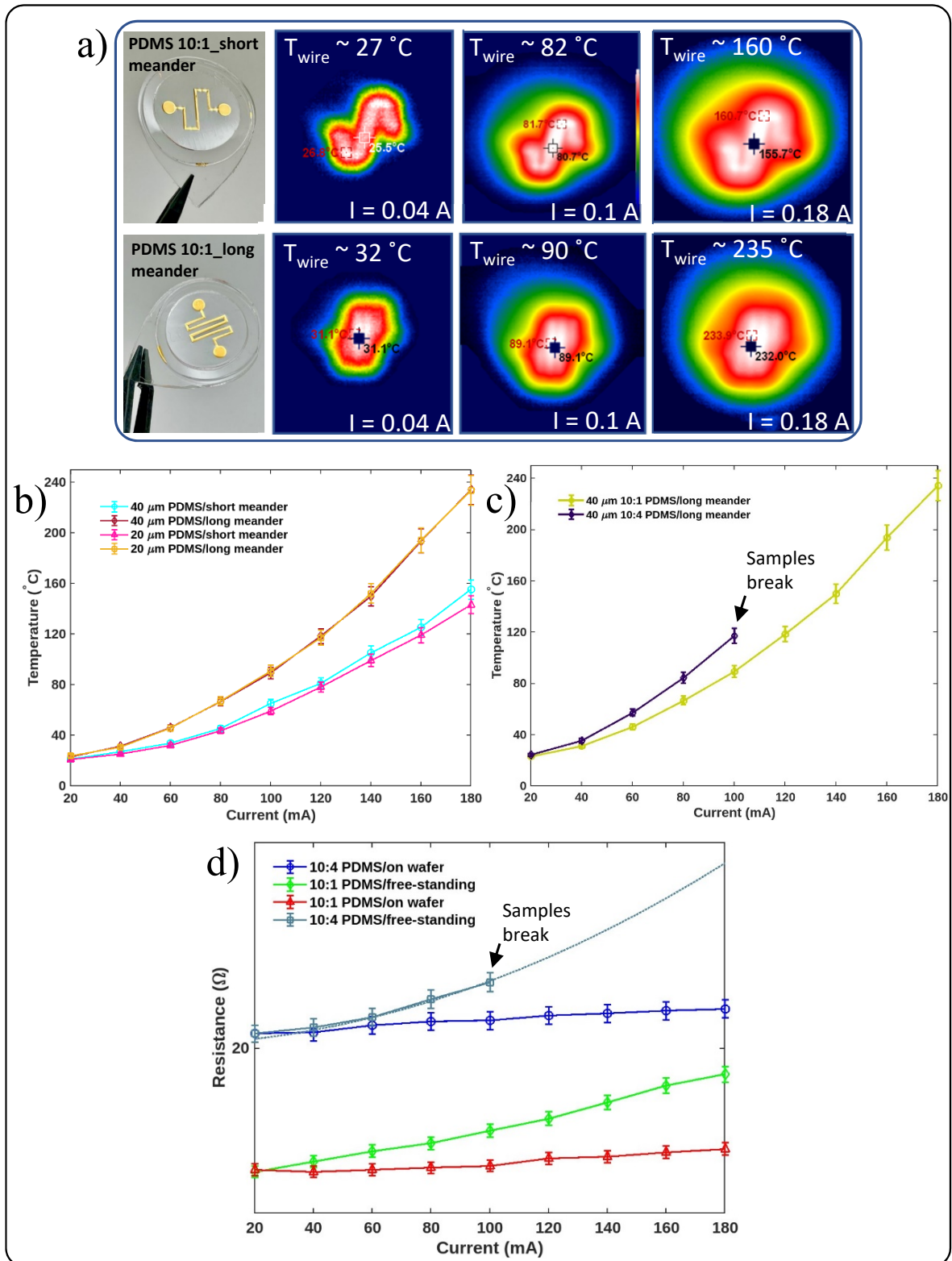
Figure 7.20: Images obtained using an infra-red camera (a) of short (left) and long (right) meander structures on a 20 μm PDMS carrier. Various levels of DC current were applied. The three heatmaps from left to right correspond to the applied currents of 0.04 A, 0.1 A, and 0.18 A; (b) Measured temperature vs. applied DC current behaviour of both long and short meanders (all structures on 10:1 PDMS substrate); (c) Comparison of measured temperature vs. applied DC current properties for long meander structures realized on 10:1 and 10:4 PDMS carriers. (d) Measured resistance vs. applied DC current properties of long meander elements on a 20 μm tall PDMS carrier [100].

wrinkle heights. According to Figure 7.14,the average wrinkle height was measured to be 522 µm for a 10:1 PDMS structure (soft), while the full-swing wrinkle height achieves 874 µm for a 10:4 PDMS structure (hard). Therefore, the wrinkle height exhibits a ratio of 1.68 between the two mixing rates. Therefore, even when the as-deposited dimensions of the meander structure are identical, the effective length of the meander line on the 10:4 substrate is longer because of the higher wrinkles compared to the 10:1 element.

Hence, the resistance for the structure on 10:4 PDMS is also higher (measured value of 20.7 Ω) compared to that of the device on the 10:1 carrier (measured value of 14.1 Ω). The two resistances differ by a factor of 1.46. Consequently, due to the higher effective resistance, the 10:4 structure heats up to a higher temperature compared to that of the 10:1 structure for the same applied DC current, as shown in Figure 7.20 (c). The temperature difference is related to different resistance values.

Another important point to be mentioned is that resistance measurements were performed under two measurement conditions:

a) devices placed on a silicon wafer prior to releasing;

b) in freestanding condition after releasing.

Figure 7.20 (d) compares the resistance measurements of two structures, one on 10:4 PDMS and the other on 10:1 PDMS, measured a) on a silicon wafer; b) freestanding. Interestingly, without DC current applied, the wire resistance value is independent of the mounting (on a silicon wafer or freestanding), and the curves have a similar initial value. Yet, when a DC current is applied, the presence of a silicon wafer under a membrane makes a difference. The freestanding thin PDMS membrane exhibits considerable mechanical bending, while affixed to the silicon wafer PDMS membrane does not move. This leads to a conclusion that applied DC current heats the wire which results in thermal expansion of the structure.

In detail, the mechanism can be described as follows: the meander heats up, the generated heat is conducted to the PDMS membrane, which in turn deforms and this leads to a deformation of the metal wire, i.e. it expands. Due to this expansion, the resistance of the wire increases with increasing temperature. The wire resistance is non-linearly dependent on the DC current. As shown in Figure 7.20 (d), for a *freestanding* 10:1 PDMS device, the resistance changes from 14.1 Ω to 18.7 Ω as the applied current is varied from 20 mA to 180 mA, described by the green curve. An identical device, was measured under different conditions, in this case mechanically fixed to a silicon wafer as opposed to freestanding. Thus, the structure cannot expand freely with application of DC current. Additionally, the generated heat is absorbed in part by the silicon wafer underneath the PDMS structure. Therefore, the change of resistance in this case is more linear and the gradient is lower. For the same variation of input current from 20 mA to 180 mA, the resistance only increases to to 15.3 Ω, as shown by the red curve.

A very similar effect is observed on 10:4 PDMS samples (hard PDMS). The intrinsic resistance value with no current applied is $20.7\,\Omega$. When applied current is increased to $100\,\text{mA}$, the meander resistance on a *freestanding* PDMS membrane increases to $23.2\,\Omega$, while on a *non-freestanding* membrane affixed to a silicon wafer, the resistance reaches only $21.3\,\Omega$. As opposed to the fixed structure, which could be measured to a higher current of $180\,\text{mA}$ resulting in an increased resistance value of $22.3\,\Omega$, the *freestanding* 10:4 PDMS samples could not be measured at higher applied current. Unfortunately, above a certain current level, the structures break. To understand this effect, one can consider Figure 7.18 which shows that the device has an inhomogenous nature, comprising intermixed wrinkled and planar regions. Miniature mechanical cracks emerge in the process of PDMS stretching and leads to mechanical rupture of the entire structure. Typically, the presence of a wrinkled region protects the structure from breaking in the presence of thermally-induced mechanical deformations. This can be attributed to the self-healing effect. However, a combination of wrinkled and planar areas reduce the efficacy of wrinkled regions in structural self-healing.

Moreover, meanders on a 10:1 PDMS substrate exhibit an excellent self-healing property. The measured resistance and the wrinkle periodicity are well repeatable even after 60 on/off cycles, as can be seen in Table 7.8.

Table 7.8: Meander resistance and wavelength of the wrinkles, for the $40\,\mu\text{m}$ thick PDMS membrane with $29\,\text{mm}$ meander, after multiple on/off cycles (the number of cycles is specified by the indices). The intermediate time is 5 minutes.

$\mathbf{I}$ (A)	$\mathbf{R_{10}}$ (Ω)	λ_{10} (μm)	$\mathbf{R_{20}}$ (Ω)	λ_{20} (μm)	$\mathbf{R_{30}}$ (Ω)	λ_{30} (μm)	$\mathbf{R_{40}}$ (Ω)	λ_{40} (μm)	$\mathbf{R_{50}}$ (Ω)	λ_{50} (μm)	$\mathbf{R_{60}}$ (Ω)	λ_{60} (μm)
0	11	5.05	11	5.05	11	5.05	11	5.05	11	5.05	11	5.05
0.18	12.76	5.26	12.7	5.39	12.76	5.31	12.66	5.3	12.73	5.24	12.73	5.39

Due to the thermo-mechanical expansion of the thermo-electric element, the entire PDMS membrane undergoes displacement. PDMS membrane movement is induced by the heat distribution from the wire into the bulk of the PDMS substrate. Figure 7.21 depicts the variation of the vertical deformation of a $40\,\mu\text{m}$ 10:1 PDMS membrane as function of applied DC current through the meander wire. For small current values below $40\,\text{mA}$ the deviation is negligible. Beyond this threshold, at medium current values between $40\,\text{mA}$ to $120\,\text{mA}$, there is a considerable increase in the wire vertical deflection, as shown in inlet b) in Figure 7.21. The structure is planar for small currents, while it increasingly deflects and bends with higher DC current passed through the meander wire.

This effect can be attributed to the temperature difference between the conducting material and the PDMS bulk. The area around the metal wire expands faster due to heating, causing the structure to bend in a circular manner. The center of the wire has the highest heat density and deflects upwards with higher current, while PDMS at a lower

temperature holds the edges and does not permit deformation, holding the meander inthe original position. This results in vertical deformation and a height difference between edge and the center of the structure of up to 70 µm. Further current increases beyond 120 µA (high-current) result in bending of the entire PDMS membrane structure with the wire. This is likely due to the fact that beyond a certain value, the thermal-mechanical force of the wire exceeds the PDMS forces holding the wire edges. Interestingly, the wrinkles remain despite the bending of the structure.

Finally, its worthwhile mentioning that a meander structure on a 20 µm thin freestanding PDMS membrane exhibits different thermo-mechanical vertical deformation behaviour as a function of applied DC current. As opposed to meander structures on the thick PDMS carrier, e.g. 40 µm which exhibit wrinkles only in the $\vec{x}$ transvers dimension, meander structures on a thin PDMS carrier exhibit wrinkles both in $\vec{x}$ transverse and $\vec{y}$ longitudinal axes, as described in Figure 7.12(d). Therefore, when such a structure on a 20 µm PDMS is heated by a DC current, the $\vec{y}$ wrinkles along the structure bend in a triangular shape, as opposed to dome-shaped deformations for structures on the 40 µm thick PDMS.
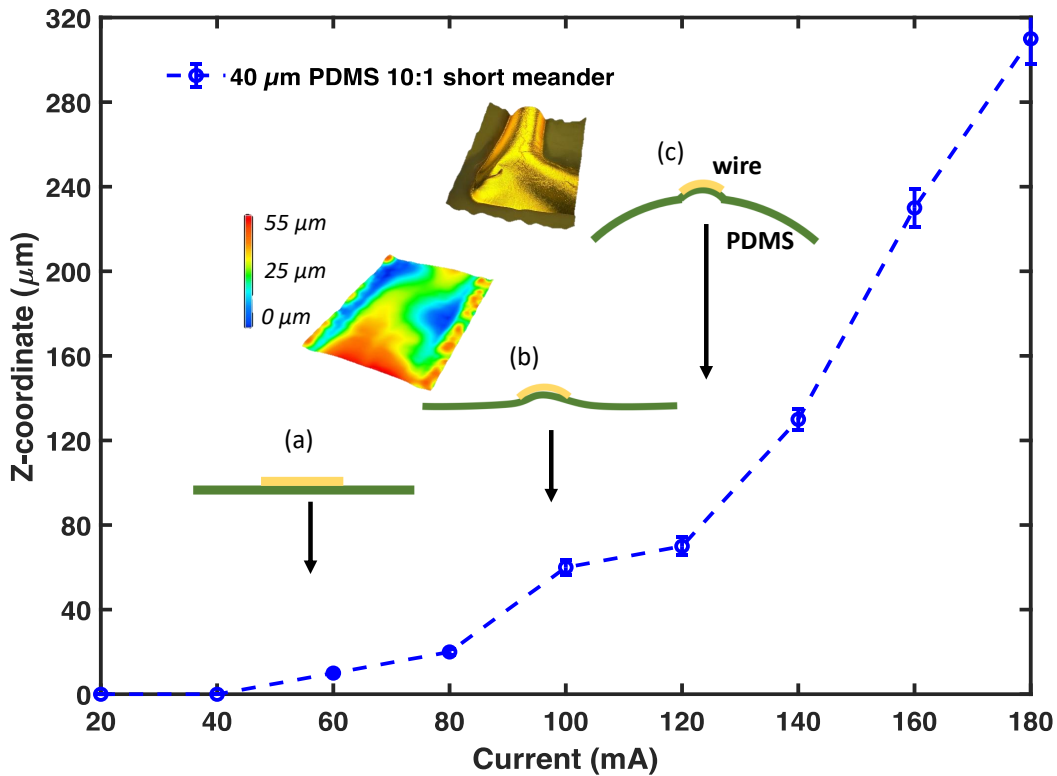
Figure 7.21: Vertical displacement of a meander on a 40 µm free-standing PDMS membrane. Inset figures: a) small current - no wire deviation; b) medium current - meander wire bending; c) high current - wire bending is very large causing PDMS membrane deformation [100].

7.4 Conclusions and future outlook

Integrating sensors into Lab-on-Chip systems holds great promise for biological and medical applications. Real-time measurement of physiological parameters directly at the cell culture, such as oxygen levels and cell confluence, can provide crucial information and enhance our understanding of biological processes. In this regard, a commercial luminescence sensor was successfully incorporated into a flexible Organ-on-Chip structure.

First, a PreSens oxygen sensor was integrated into a PDMS microfluidic chip, and oxygen measurements were taken. The results were compared with measurements in a beaker. Additionally, these measurements were compared with measurements obtained by a FireStingO$_2$ (reference sensor). The presented results confirm the feasibility of using the PreSens sensor for oxygen measurements in organ-on-a-chip applications. It was shown that a commercial luminescence sensor can be successfully integrated into a flexible Organ-on-Chip structure.

The oxygen concentration measurements were stable and reproducible. Relatively low standard deviation signified that the measured absolute values have minimal dispersion. Oxygen concentration was measured in a beaker, in a microfluidic chip and in a microfluidic chip with a membrane. Oxygen level varies due to the system setup. It was observed that the oxygen concentration in the microfluidic channel was slightly higher compared to that in the beaker, with a difference in absolute values of about 10 ppm instead of 8 ppm, respectively. This effect can be attributed to the pressure-driven pump used to propel the liquid in the microfluidic chip, leading to increased oxygen dissolution in the fluid.

Furthermore, TEER electrodes were designed and implemented on the polymer surface. The increase in measured TEER resistance over time indicated consistent cell growth and the formation of tight junctions between the cells. These measurements were conducted at room temperature, necessitating the cooling of the chip after removing it from the 37°C incubator.

Next, this chapter presented a thorough investigation of the thermo-mechanical properties of conductive meander structures on PDMS membranes. Two meander lengths of 29 mm and 48 mm have been fabricated on 20 µm and 40 µm freestanding PDMS membranes. Interesting effects were studied related to the properties of PDMS being a soft silicon-based polymer. These properties lead to the creation of natural wrinkles during the magnetron sputtering process of chromium (Cr) and gold (Au) metallization. Curiously, wrinkled metallization maintains electrical conductivity, providing additional new beneficial properties, such as self-healing and prevention of mechanical cracking even in the presence of substrate deformation. Self-healing enables reproducible measurement results even after 60 cycles of heating and cooling.

The dependence on wrinkle properties and substrate thickness was investigated in detail. Properties of conducting meanders realized on 20 µm and 40 µm thick PDMS substrates

were thoroughly compared. On a "thick" 40 µm substrate wrinkles appeared only in a single $\vec{x}$ transverse direction, while on a "thin" 20 µm substrate, wrinkles appeared in both $\vec{x}$ transverse and $\vec{y}$ longitudinal directions over the entire metal structure. This phenomena can be explained with existing models.

However, none of the wrinkle theories have considered the PDMS thickness to date. Yet, the research in this chapter shows that the PDMS thickness does strongly affect wrinkle properties and thus must be take into account.

This chapter presented another interesting effect of wrinkling on wire resistance. Due to an effective surface lengthening of the metal wires with wrinkle formation, the resistance increases. For a 29 mm long meander, the simulated resistance was 3.5 Ω as compared to 11 Ω measured in the fabricated structure, while for the 48 mm long meander had a measured value of 14 Ω compared to a simulated value of 5.73 Ω.

Additionally, in this chapter the impact of PDMS mixing ratio on the thermo-electric properties of meander-shaped conducting elements was investigated. The wrinkle height of a stiffer PDMS (with mixing ratio of 10:4) is higher, as compared to the softer 10:1 PDMS structure, resulting in an absolut values difference of 0.437 µm to 0.26 µm. As mentioned previously, the effective length is stretched due to wrinkles, resulting in higher resistance. Thus, the effective resistance and temperature is higher for wires on a "harder" 10:4 membrane, as opposed to the "softer" 10:1 membrane for the same applied DC current. Another effect that was shown is the surface inhomogeneity, i.e. alternating wrinkled and planar areas on "hard" PDMS substrate. This results in micro-sized cracks at a high applied current of 100 mA, which are not present in meanders realized on a "soft" 10:1 PDMS structure. This proves the self-healing property of the wrinkled metal.

Finally, this chapter analyzed the thermo-mechanical deformation properties of meander wires and the PDMS membrane under applied DC current conditions. Wires on a 40 µm membrane deformed in a dome-shape, while on a 20 µm membrane, a triangular shape is realized. Wire deformation is related to the wrinkle shape and positioning.

As we look ahead, this research opens exciting avenues for the integration of sensors into Lab-on-Chip systems, particularly in the domain of biological and medical applications.

The successful incorporation of the PreSens oxygen sensor underscores its potential utility in many Organ-on-a-Chip platforms. The potential for continuous oxygen monitoring within microfluidic systems extends its applicability to various biomedical contexts, offering enhanced insights into critical biological processes, such as those in tissue engineering and single-cell analysis. Based on the developed technology reported herein, future chip fabrication could include the integration of additional sensors spots, such as those for pH or carbon dioxide (CO_2) monitoring, further enhancing the versatility and utility of the Lab-on-Chip platforms. This presents exciting prospects for more comprehensive and multifaceted analyses in the field of biomedical research and diagnostics.

For future improvements in in-situ TEER measurements, it is important to develop a

read-out system capable of providing wireless data and power transfer within the incubator setting. This advancement would enhance convenience and efficiency in monitoring TEER values during cell culture experiments by eliminating the need to remove the system from the incubator for readouts.

Also, an additional future research direction would be investigation of meander-shaped thermo-electrical conducting structures on PDMS membranes for use as a sensor or actuator in Lab-on-Chip applications. The properties of resistance dependence on applied current, wrinkle formation in the fabrication process and thermo-mechanical displacement can be further investigated for use in multiple applications.

Finally, disruptive innovation can be achieved by sensor fusion of numerous sensors in a single microfluidic channel. Obviously, this requires miniature sensors with integrated readout chips. Yet, by combination of several sensors one can achieve continuous monitoring of the well-being of the cultured cells inside the channel in real-time. Additionally, by integrating thermo-electric-mechanical actuators in the channels, one can manipulate the cell layer and control what happens inside the channel. This opens a vast number of opportunities for medical research and studies which would not be possible using the classical Boyden chamber environment and chopstick electrodes.

8 Summary and Outlook

This thesis redefines the landscape of microfluidic device development with integrated sensors for in-channel monitoring. These innovations lay the foundation for interdisciplinary research endeavors and foster the accumulation of knowledge and the creation of tools with the potential to revolutionize healthcare and environmental sciences. A motivation for the pioneering spirit of this work is a desire to develop models which could enhance the healthcare of humans and reduce the number of animal death in the labs.

Given the intricate nature of biology, specific biological inquiries often necessitate tailored bespoke solutions. Consequently, commercially-available pre-made microfluidic devices frequently prove inadequate when confronted with the complexities inherent in addressing such specialized biological questions. Also, integration of the sensors for in-situ measurements in the microfluidic devices is impossible with prefabricated commercial devices. Moreover, these structures are usually incompatible with the read-out systems (usually optical) typically used at medical institutes today.

Therefore, this thesis has presented a systematic approach for development of custom-designed PDMS microfluidic chips. Obviously, the amount of imaginable applications is infinite. Therefore, this thesis researched and presents only several selected examples of custom- designed PDMS-based microfluidic chips: a) Stomach-on-Chip for gastric organ/organoid emulation; b) ImmunoChip for immunology investigations and c) LabyrinthChip for microswimmer studies.

First, Chapter 1 presented the motivation for microfluidic engineering and discussed some potential research fields that can be analyzed by these means. Chapter 2 systematically discussed in depth PDMS material properties, such as biocompatibility, gas permeability, optical transparency, mechanical flexibility, stretchability, robustness, surface properties and micro-structuring approaches. These beneficial properties are the reason for such high popularity of this material. Yet, there are some disadvantages such as molecular adsorption, difficulties in realization of metal electrodes on its surface and hydrophobicity. Therefore, alternative materials to PDMS were also briefly discussed.

Chapter 3 describes in detail the processing methods for fabrication of microfluidic chips using PDMS and complementary materials. The first step is master mold fabrication, which is the most critical step in chip development. Since this work focuses on three distinct chips for differing applications, each master mold is described separately. Next, PDMS mixing and bonding is described. Additionally, for targeted biomedical applications that require a custom design of the membrane pores with different sizes and nano-resolution,

femtosecond laser structuring techniques can be utilized, as described in Section 3.4. This is a highly powerful technology for membrane structuring. Finally, sensors and actuators are required to monitor and manipulate what happens inside the microfluidic channel. Therefore, Section 3.6 showed possible approaches to modify processing techniques to accommodate sensors or actuators.

Chapter 4 showed in depth a microfluidic chip for cell culture and tissue engineering. The chosen organ of interest is stomach, since the complexity of the human gastro-intestinal tract can not be represented by any animal and thus an alternative model is required for drug screening.

In this chapter, a microfluidic chip designed for cell culture and tissue engineering was introduced. An innovative bonding technology, inspired by cutting-edge concepts, which enables the attachment of a porous filter to silicone was developed. This technology effectively divides the microfluidic chip into two channels separated by a membrane. Notably, this method offers the flexibility to bond various porous materials to structured layers, streamlining the microfluidic chip assembly process. In contrast to conventional techniques, the reported approach allows for the use of a wide range of materials and significantly reduces fabrication time from days to just a few hours. Consequently, employment of thin filters with diverse pore sizes, densities, thicknesses, and material properties as membranes becomes a straightforward endeavor. The proof of concept was successfully validated by culturing human gastric epithelial cancer cells and conducting chemotherapeutic drug tests on the cultured tissues. Furthermore, through experimental exploration it was determined that the optimal channel width for the Stomach-on-Chip was 1 mm. As a result, the master mold for silicone replication was optimized and developed via soft lithography. The findings presented here have the potential to guide forthcoming research avenues. For instance, they may pave the way for investigations into co-culturing bacteria or exploring immunotherapy as a form of cancer treatment. Additionally, there is scope for evaluation of various drugs and their combinations on patient-derived gastric organoids cultured within microfluidic chips. These experiments hold the promise of refining patient treatment strategies and enhancing our comprehension of the protective barriers within the human stomach. Furthermore, by leveraging the developed technology, it is feasible to expand microfluidic chip structures into multiple layers. This will provide an opportunity to culture more cell types in proximity but each on separate membranes and split them for future analysis.

Additionally, printing of a 1 cm long membrane with nano-resolution within a sealed microfluidic chip was accomplished. To achieve the desired membrane geometry, a wire-shaped design was selected. This particular geometry, in addition to its potential for Stomach-on-Chip applications, emulates the wrinkled surface of the stomach. Each "wire" within this membrane measures 2.5 µm in width, with a 1.5 µm spacing between wires. To the best of the authors' knowledge, this represents the first instance of such a

membrane structured within a microfluidic channel using femtosecond laser technology. The complete structuring process was developed and optimized in this work. Notably, the most challenging aspect of this process occurs within the enclosed microfluidic channel, where access to the liquid is limited, and removal of the remaining non-polymerized photoresist can be particularly tricky. Moreover, the PDMS material has distinct swelling characteristics in different solvents, which could potentially lead to deformation of the printed membrane. Thus, there is room for further optimization in this phase of the process. In the future, femtosecond laser structuring inside of the closed microfluidic channel can be used to fabricate different membrane geometries. This technology enables the detailed study of the influence of porosity on the co-cultured cell layers. Moreover, various organic photo-reactive materials can be used for the realization of a degradable membrane which can enable closer cell proximity over time.

Next, Chapter 5 showed a novel custom- developed microfluidic device enabling the study of dynamic interactions between $CD4^+$ T cells and infected traperitoneal (IP) macrophages. A dedicated 3D microfluidic structure (ImmunoChip), consisting of 378 interconnected channels, was developed. The master mold fabrication for PDMS was done in two steps: first, soft lithography for big micro-channels (two channels $100\,\mu m$ and one $150\,\mu m$) and second, femtosecond direct write process for $6\,\mu m \times 4\,\mu m \times 30\,\mu m$ perpendicular channels. This is a powerful platform which opens new possibilities in immunology research. By introducing chemokines and fluorescent dyes, it became feasible to intricately manipulate and closely monitor cell behavior within a meticulously controlled microenvironment.

The presented chip can precisely mimic in vivo conditions for the study of the human immune system. To the author's knowledge, this chapter presented for the first time a 3D master mold, which was fabricated by a combination of soft lithographic processing and femtosecond laser structuring. These technologies complement each other and compensate for the drawbacks of each other. Again, this result strongly advances the state of the art in the microstructuring of microfluidics. Moreover, femtosecond laser microstructuring inside of the closed microfluidic channel, presented herein, can be a highly beneficial approach for ImmunoChip. The expansion of this technology can used to create more complex membranes (3D) and movable parts in the channel, such as micro-gates or micro-pumps. As an example, such gates will be useful in an ImmunoChip, since the loading of this chip has room for improvement with respect to keeping the middle channel undisturbed while pipetting the medium with $CD4^+$ T cells into side channels. Also, it would be interesting to study different geometries of the microfluidic structures in ImmunoChip since active penetration of the $CD4^+$ T cells is highly dependent on the channel size.

Further, Chapter 6 presented a custom-developed microfluidic chip (LabyrinthChip) to study the motion of Chlamydomonas reinhardtii, unicellular algae (microswimmers) that require laminar conditions. Round and elongated shape pillars were fabricated inside a

PDMS chip to create a labyrinth for Chlamydomonas. Various labyrinth geometries and patterns were developed to study the behaviour of microswimmers in different environments. The main technological challenge to be solved was removal of residual photoresist in the development process step. The proposed solution was the optimization of lithography parameters so that photoresist remains soft and can be easily washed out yet still hard enough to be exposed. Thereby, the walls of circular pillars of $10\,\mu m$ radius were realized as straight 90° perpendicular structures. Novel in this chapter is the proposed microstructured patterns of obstacles for the microswimmers. The furtherance of this research may involve exploration and evaluation of various labyrinth designs and shapes. Additionally, investigation of microswimmer interactions with other organisms or substances within these channels could offer a valuable avenue for environmental research. Single-cell organisms possess the remarkable capability to transform harmful elements into harmless ones. Consequently, gaining a deeper insight into this mechanism and identifying new methods to enhance it could contribute to environmental restoration efforts on a global scale.

Sensor implementation (Chapter 7) into Lab-on-Chip systems holds significant promise for biological and medical applications. Real-time monitoring of physiological parameters, such as oxygen levels and cell confluence, directly within cell cultures is a means to provide critical information and to enhance our comprehension of biological processes. In this context, the successful incorporation of a commercial luminescence sensor into a flexible Organ-on-Chip structure was achieved. Initially, integration of the PreSens oxygen sensor into a PDMS microfluidic chip enabled the measurement of oxygen levels. These measurements were subsequently compared with readings obtained in a beaker and with those acquired using a FireStingO$_2$ reference sensor. The outcomes presented confirm the viability of employment of the PreSens sensor for recording oxygen levels in organ-on-a-chip applications. It was demonstrated that a commercial luminescence sensor can be effectively embedded into a flexible Organ-on-Chip structure. The oxygen concentration measurements were found to be stable and reproducible, with relatively low standard deviations indicating minimal dispersion in the measured absolute values. Notably, variations in oxygen concentration were observed among different settings, with the oxygen concentration within the microfluidic channel found to be slightly higher (approximately $10\,ppm$) compared to that in the beaker (8 ppm). This effect is attributed to the use of a pressure-driven pump for liquid propulsion within the microfluidic chip, leading to increased oxygen dissolution in the fluid. Furthermore, electrodes for transepithelial electrical resistance (TEER) measurements were devised and implemented on the polymer surface. The progressive increase in resistance over time indicated consistent cell growth and the formation of tight junctions between the cells. Notably, these measurements were conducted at room temperature, necessitating chip cooling after removal from the $37\,°C$ incubator. Subsequently, this chapter conducted a comprehensive exploration of the thermomechanical properties of meander conducting structures on PDMS membranes. Meander

structures of two different lengths, 29 mm and 48 mm, were fabricated on freestanding PDMS membranes of 20 µm and 40 µm thicknesses. Intriguing effects related to the properties of PDMS, being a soft silicon-based polymer, were examined. These effects included the natural formation of wrinkles during the magnetron sputtering process of chromium (Cr) and gold (Au) materials. Remarkably, wrinkled metallization maintained structural conductivity, offering additional advantageous properties such as self-healing, even in cases of substrate deformation and mechanical cracks. This self-healing property enabled consistent measurement results even after 60 cycles of heating and cooling. The relationship between substrate thickness and wrinkle properties was thoroughly investigated. Wrinkles appeared solely in a single $\vec{x}$ transverse direction on the "thick" 40 µm substrate, while on the "thin" 20 µm substrate, wrinkles manifested in both directions, $\vec{x}$ transverse and $\vec{y}$ longitudinal, across the entire metal structure. This phenomenon was explained using existing models. It is noteworthy that none of the existing wrinkle theories had previously considered PDMS thickness. However, the research in this chapter demonstrates that PDMS thickness significantly affects wrinkle properties and must therefore be taken into account. Additionally, this chapter highlighted another notable effect: resistance variation due to wrinkling. The effective extension of the metal wires during production led to an increase in resistance. For instance, a 29 mm long meander exhibited an increase in measured resistance from a simulated value of $3.5\,\Omega$ to $11\,\Omega$, while a 48 mm long meander increased from a simulated value of $5.73\,\Omega$ to a measured value of 14 ohms. Furthermore, the chapter delved into the impact of PDMS mixing ratios on the thermo-electric properties of meander-shaped conducting elements. Wrinkle heights were observed to be higher for a stiffer PDMS structure (mixing ratio of 10:4) compared to a softer 10:1 PDMS structure, resulting in an elevation from 0.437 µm to 0.26 µm. As previously mentioned, the effective length was stretched due to wrinkles, resulting in higher resistance. Consequently, the effective resistance and temperature were higher for wires on the "harder" 10:4 membrane compared to the "softer" 10:1 membrane under the same applied DC current. Another noteworthy effect observed was surface inhomogeneity on the "hard" PDMS substrate, featuring alternating wrinkled and planar areas. This resulted in micro-sized cracks at a high applied current of 100 mA, which were absent in meanders realized on the "soft" 10:1 PDMS structure, thereby confirming the self-healing property of the wrinkled metal. Finally, this chapter conducted an analysis of the thermo-mechanical deformation properties of meander wires and PDMS membranes under applied DC current conditions. It was observed that wires on a 40 µm membrane deformed in a dome-like shape, whereas on a 20 µm membrane, a triangular shape was recognized. The deformation of the wires was found to be closely related to the shape and positioning of the wrinkles. Based on the research presented in this chapter, one can embed different sensor types in the microfluidic chips based on PDMS. For example, more sensor spots, such as sensors for CO_2 or pH detection, could be implemented into Stomach-on-Chip, ImmunoChip, or LabyrinthChip

thanks to the developed technology for oxygen sensor implementation. Furthermore, when sputtered onto PDMS, wrinkled thin metal films exhibit a remarkable "self-healing" attribute that shields them against cracking and detachment from the flexible substrate. Moreover, the creation of biosensors necessitates the immobilization of antibodies onto the surface. However, it's important to note that antibody immobilization is a well-established protocol for flat metal thin films. Consequently, a promising avenue for future research could involve refining the precise orientation of antibody immobilization on the wrinkled electrodes for enhanced biosensor applications.

Looking into the future, there are many ways to carry on the research discussed in this thesis. First, the microfluidic models for Organ-on-Chip applications or drug testing have not been approved by authorities worldwide yet. The regulation process is ongoing. There is still a long way to go towards standardization. Yet, once approved, such models that mimic organs for drug testing shall in the long-term become a viable alternative to animal experiments. Therefore, several efforts can be spent to support the standardization of microfluidic chips, such as generation of statistical databases of comparison for in vivo and in-chip drug screening. Second, a combination of the lithographic techniques with a femtosecond laser gives a high degree of flexibility and is a very powerful processing platform. Further development of technologies based on a combination of both may advance the state of the art in microstructuring.

Third, integration of read-out systems (for example optical) with the sensors would enhance the measurement capabilities and provide more information about cell conditions and functions in the microfluidic channel. Finally, use of additive manufacturing to simplify the fabrication of microfluidic chips is a promising field of study. By further development of the algorithms for 3D printers and optimization of the materials, one can achieve high accuracy at a low price. This can give increase the use and mass market applicability of microfluidic chips that can accordingly be produced in large quantities and at low cost. This will pave the way for consumer use of microfluidics devices and could become great success.

Bibliography

[1] Michael J. Workman, John P. Gleeson, Elissa J. Troisi, Hannah Q. Estrada, S. Jordan Kerns, Christopher D. Hinojosa, Geraldine A. Hamilton, Stephan R. Targan, Clive N. Svendsen, and Robert J. Barrett. Enhanced Utilization of Induced Pluripotent Stem Cell–Derived Human Intestinal Organoids Using Microengineered Chips. *Cellular and Molecular Gastroenterology and Hepatology*, 5(4):669–677.e2, 2018.

[2] Hyuna Sung, Jacques Ferlay, Rebecca L. Siegel, Mathieu Laversanne, Isabelle Soerjomataram, Ahmedin Jemal, and Freddie Bray. Global Cancer Statistics 2020: GLOBOCAN Estimates of Incidence and Mortality Worldwide for 36 Cancers in 185 Countries. *CA:A Cancer Journal for Clinicians*, 71(3):209–249, 2021.

[3] Bruce K. Gale, Mark A. Eddings, Scott O. Sundberg, Andrew Hatch, Jungkyu Kim, and Tammy Ho. Low-Cost MEMS Technologies. In Yogesh B. Gianchandani, Osamu Tabata, and Hans Zappe, editors, *Comprehensive Microsystems*, pages 341–378. Elsevier, Oxford, 2008.

[4] Nico Tucher. *Analysis of photonic structures for silicon solar cells*. PhD thesis, 12 2016.

[5] C. White, K. Tan, A. Wolf, and L. Carbary. 4 - Advances in structural silicone adhesives. In David A. Dillard, editor, *Advances in Structural Adhesive Bonding*, Woodhead Publishing in Materials, pages 66–95. Woodhead Publishing, 2010.

[6] Craig Sturgess, Christopher Tuck, Ian Ashcroft, and Ricky Wildman. 3D Reactive Inkjet Printing of Polydimethylsiloxane. *J. Mater. Chem. C*, 5, 08 2017.

[7] Mohamad Riduwan, Muhammad Bisyrul Hafi Othman, Azlan Arifin, and Zulkifli Ahmad. Cross-link network of polydimethylsiloxane via addition and condensation (RTV) mechanisms. Part I: Synthesis and thermal properties. *Polymer Degradation and Stability*, 96:2064–2070, 12 2011.

[8] Ruslan Yu. Lukin, Aidar M. Kuchkaev, Aleksandr V. Sukhov, Giyjaz E. Bek-mukhamedov, and Dmitry G. Yakhvarov. Platinum-Catalyzed Hydrosilylation in Polymer Chemistry. *Polymers*, 12(10), 2020.

[9] Byung Hwi. Kim Sujin. Lee Kangwon. Choy Young Bin. Heo Chan Yeong. Shin, Byung Ho. Kim. Silicone breast implant modification review: overcoming capsular contracture. *Biomaterials Research*, 37(22), 12 2018.

[10] Yoav Barnea, Dennis C Hammond, Yuval Geffen, Shiri Navon-Venezia, and Keren Goldberg. Plasma Activation of a Breast Implant Shell in Conjunction With Antibacterial Irrigants Enhances Antibacterial Activity. *Aesthetic Surgery Journal*, 38(11):1188–1196, 01 2018.

[11] International Organization for Standardization. Biological evaluation of medical devices, October 2009.

[12] Sarah-Sophia D. Carter, Abdul-Raouf Atif, Sandeep Kadekar, Ingela Lanekoff, Håkan Engqvist, Oommen P. Varghese, Maria Tenje, and Gemma Mestres. PDMS leaching and its implications for on-chip studies focusing on bone regeneration applications. *Organs-on-a-Chip*, 2:100004, 2020.

[13] Jessamine Ng Lee, Cheolmin Park, and George M. Whitesides. Solvent Compatibility of Poly(dimethylsiloxane)-Based Microfluidic Devices. *Analytical Chemistry*, 75(23):6544–6554, 2003. PMID: 14640726.

[14] A. Lamberti, S. L. Marasso, and M. Cocuzza. PDMS membranes with tunable gas permeability for microfluidic applications. *RSC Adv.*, 4:61415–61419, 2014.

[15] G. Firpo, E. Angeli, L. Repetto, and U. Valbusa. Permeability thickness dependence of polydimethylsiloxane (PDMS) membranes. *Journal of Membrane Science*, 481:1–8, 2015.

[16] Aigars Piruska, Irena Nikcevic, Se Hwan Lee, Chong Ahn, William R. Heineman, Patrick A. Limbach, and Carl J. Seliskar. The autofluorescence of plastic materials and chips measured under laser irradiation. *Lab Chip*, 5:1348–1354, 2005.

[17] Maria Cazacu, Carmen Racles, Mirela-Fernanda Zaltariov, Mihaela Dascalu, Adrian Bele, Codrin Tugui, Alexandra Bargan, and George Stiubianu. From Amorphous Silicones to Si-Containing Highly Ordered Polymers: Some Romanian Contributions in the Field. *Polymers*, 13(10), 2021.

[18] Hong Huy Tran, Bharath Venkatesh, Youngjin Kim, Daeyeon Lee, and David Riassetto. Multifunctional Composite Films with Vertically Aligned ZnO Nanowires by Leaching-enabled Capillary Rise Infiltration. *Nanoscale*, 11, 10 2019.

[19] Jihoon Lee, Jungwoo Kim, Hyoungsub Kim, Young Bae, Kyeong-Hee Lee, and Hyoung Jin Cho. Effect of thermal treatment on the chemical resistance of polydimethylsiloxane for microfluidic devices. *Journal of Micromechanics and Microengineering*, 23:035007, 01 2013.

[20] Han Gao, Haifeng Hu, Yong Zhao, Jin Li, Ming Lei, and Yong Zhang. Highly-sensitive optical fiber temperature sensors based on PDMS/silica hybrid fiber structures. *Sensors and Actuators A: Physical*, 284:22–27, 2018.

[21] Dnyandeo Pawar, Ajay Kumar, Rajesh Kanawade, Samir Mondal, and Ravindra K. Sinha. Negative axicon tip micro-cavity with a polymer incorporated optical fiber temperature sensor. *OSA Continuum*, 2(8):2353–2361, Aug 2019.

[22] Austin R. Van Sickle, Joseph B. Miller, Christopher Moore, Rebecca J. Anthony, Uwe R. Kortshagen, and Erik K. Hobbie. Temperature Dependent Photoluminescence of Size-Purified Silicon Nanocrystals. *ACS Applied Materials & Interfaces*, 5(10):4233–4238, 2013. PMID: 23627320.

[23] N.E. Stankova, P.A. Atanasov, Ru.G. Nikov, R.G. Nikov, N.N. Nedyalkov, T.R. Stoyanchov, N. Fukata, K.N. Kolev, E.I. Valova, J.S. Georgieva, and St.A. Armyanov. Optical properties of polydimethylsiloxane (PDMS) during nanosecond laser processing. *Applied Surface Science*, 374:96–103, 2016. E-MRS 2015 Spring Meeting Symposium CC: "Laser and plasma processing for advanced applications in material science", 11-15 May 2015, Lille (France).

[24] Hans Rudolf Christen. *Chemie*. Diesterweg, Salle, 1984.

[25] Liubov Bakhchova, Linas Jonušauskas, Dovilė Andrijec, Marharyta Kurachkina, Tomas Baravykas, Alexey Eremin, and Ulrike Steinmann. Femtosecond Laser-Based Integration of Nano-Membranes into Organ-on-a-Chip Systems. *Materials*, 13(14), 2020.

[26] Emel Yilgör and Iskender Yilgör. Silicone containing copolymers: Synthesis, properties and applications. *Progress in Polymer Science*, 39(6):1165–1195, 2014. Topical issue on Polymer Chemistry.

[27] James E. Mark. Some Interesting Things about Polysiloxanes. *Accounts of Chemical Research*, 37(12):946–953, 2004. PMID: 15609986.

[28] I D Johnston, D K McCluskey, C K L Tan, and M C Tracey. Mechanical characterization of bulk Sylgard 184 for microfluidics and microengineering. *Journal of Micromechanics and Microengineering*, 24(3):035017, feb 2014.

[29] S. Johari, H. Fazmir, A.F.M. Anuar, M.Z. Zainol, V. Nock, and W. Wang. PDMS young's modulus calibration for micropillar force sensor application. In *2015 IEEE Regional Symposium on Micro and Nanoelectronics (RSM)*, pages 1–4, 2015.

[30] G Camino, S.M Lomakin, and M Lazzari. Polydimethylsiloxane thermal degradation Part 1. Kinetic aspects. *Polymer*, 42(6):2395–2402, 2001.

[31] G Camino, S.M Lomakin, and M Lageard. Thermal polydimethylsiloxane degradation. Part 2. The degradation mechanisms. *Polymer*, 43(7):2011–2015, 2002.

[32] T. S. Radhakrishnan. Thermal degradation of poly(dimethylsilylene) and poly(tetramethyldisilylene-co-styrene). *Journal of Applied Polymer Science*, 99(5):2679–2686, 2006.

[33] Wei Wang, Sehoon Chang, and Ayrat Gizzatov. Toward Reservoir-on-a-Chip: Fabricating Reservoir Micromodels by in Situ Growing Calcium Carbonate Nanocrystals in Microfluidic Channels. *ACS Applied Materials & Interfaces*, 9(34):29380–29386, 2017. PMID: 28792207.

[34] Godfrey Pasirayi, Vincent Auger, Simon M. Scott, Pattanathu K.S.M. Rahman, Meez Islam, Liam O'Hare, and Zulfiqur Ali. Microfluidic Bioreactors for Cell Culturing: A Review. *Micro and Nanosystemse*, 3(2):137–160, July 2011.

[35] Xueping Jiang, Haipeng Zheng, Shoshana Gourdin, and Paula T. Hammond. Polymer-on-Polymer Stamping: Universal Approaches to Chemically Patterned Surfaces. *Langmuir*, 18(7):2607–2615, 2002.

[36] M.L. Yarmush O.B. Usta Goekaltun A., Y.B. Kang and A. Asatekin. Simple Surface Modification of Poly(dimethylsiloxane) via Surface Segregating Smart Polymers for Biomicrofluidics. *Scientific Reports*, 9(1):7377, 5 2019.

[37] Shambhulinga Aralekallu, Rajamouli Boddula, and Vijay Singh. Development of glass-based microfluidic devices: A review on its fabrication and biologic applications. *Materials & Design*, 225:111517, 2023.

[38] Flexdym Materials. Accessed on April 04, 2023.

[39] Alexander H. McMillan, Emma K. Thomée, Alessandra Dellaquila, Hussam Nassman, Tatiana Segura, and Sasha Cai Lesher-Pérez. Rapid Fabrication of Membrane-Integrated Thermoplastic Elastomer Microfluidic Devices. *Micromachines*, 11(8), 2020.

[40] Akitaka Senuma. Gas permeability coefficients of ethylene-vinyl acetate copolymer-modified poly(dimethylsiloxane) membranes. Double-column approach for two-phase materials. *Macromolecular Chemistry and Physics*, 201(5):568–576, 2000.

[41] Flexdym Materials. Accessed on April 04, 2023.

[42] Drago Sticker, Mario Rothbauer, Sarah Lechner, Marie-Therese Hehenberger, and Peter Ertl. Multi-layered, membrane-integrated microfluidics based on replica molding of a thiol–ene epoxy thermoset for organ-on-a-chip applications. *Lab Chip*, 15:4542–4554, 2015.

[43] J.M. Lin. *Microfluidics for Single-Cell Analysis*. Integrated Analytical Systems. Springer Singapore, 2019.

[44] Jose A. del Rio and Isidre Ferrer. Potential of Microfluidics and Lab-on-Chip Platforms to Improve Understanding of "prion-like" Protein Assembly and Behavior. *Frontiers in Bioengineering and Biotechnology*, 8, 2020.

[45] Florian Lapierre, Yuan Gao, John Oakeshott, Thomas S. Peat, and Yonggang Zhu. *Enzyme Assay in Microfluidics*, pages 1–8. Springer US, Boston, MA, 2013.

[46] Robert Langer and Joseph P. Vacanti. Tissue Engineering. *Science*, 260(5110):920–926, 1993.

[47] David C. Duffy, J. Cooper McDonald, Olivier J. A. Schueller, and George M. Whitesides. Rapid Prototyping of Microfluidic Systems in Poly(dimethylsiloxane), journal = Analytical Chemistry. 70(23):4974–4984, 1998. PMID: 21644679.

[48] A. Folch, A. Ayon, O. Hurtado, M. A. Schmidt, and M. Toner. Molding of Deep Polydimethylsiloxane Microstructures for Microfluidics and Biological Applications. *Journal of Biomechanical Engineering*, 121(1):28–34, 02 1999.

[49] B.-H. Jo, L.M. Van Lerberghe, K.M. Motsegood, and D.J. Beebe. Three-dimensional micro-channel fabrication in polydimethylsiloxane (PDMS) elastomer. *Journal of Microelectromechanical Systems*, 9(1):76–81, 2000.

[50] Terai H. King Kevin R. Weinberg E.J. Kaazempur-Mofrad M.R. Vacanti J.P. Borenstein, Jeffrey T. *Biomedical Microdevices*, 4(3):167–175, 2002.

[51] Jamil El-Ali, Peter K. Sorger, and Klavs F. Jensen. Cells on chips. *Nature*, 442(7101):403–411, 2006.

[52] Divya Nalayanda, Mahendran Kalukanimuttam, and David Schmidtke. Micropatterned surfaces for controlling cell adhesion and rolling under flow. *Biomedical microdevices*, 9:207–14, 05 2007.

[53] Dongeun Huh, Akiko Mammoto, Martin Montoya-Zavala, and Donald E. Ingber. A human breathing lung-on-a-chip. *The FASEB Journal*, 24(S1):1065.22–1065.22, 2010.

[54] Julia A. Boos, Patrick M. Misun, Giulia Brunoldi, Lea A. Furer, Leonie Aengenheister, Mario Modena, Nassim Rousset, Tina Buerki-Thurnherr, and Andreas Hierlemann. Microfluidic Co-Culture Platform to Recapitulate the Maternal–Placental–Embryonic Axis. *Advanced Biology*, 5(8):2100609, 2021.

[55] Alexander Peyton Nesmith, Ashutosh Agarwal, Megan Laura McCain, and Kevin Kit Parker. Human airway musculature on a chip: an in vitro model of allergic asthmatic bronchoconstriction and bronchodilation. *Lab Chip*, 14:3925–3936, 2014.

[56] Feng Zhang, Kai-Yun Qu, Bin Zhou, Yong Luo, Zhen Zhu, De-Jing Pan, Chang Cui, Yue Zhu, Ming-Long Chen, and Ning-Ping Huang. Design and fabrication of an integrated heart-on-a-chip platform for construction of cardiac tissue from human iPSC-derived cardiomyocytes and in situ evaluation of physiological function. *Biosensors and Bioelectronics*, 179:113080, 2021.

[57] Mosha Abulaiti, Yaxiaer Yalikun, Kozue Murata, Asako Sato, Mustafa Sami, Yuko Sasaki, Yasue Fujiwara, Kenji Minatoya, Yuji Shiba, Yo Tanaka, and Hidetoshi Masumoto. Establishment of a heart-on-a-chip microdevice based on human iPS cells for the evaluation of human heart tissue function. *Scientific Reports*, 10:19201, 11 2020.

[58] Denise Marrero, Ferran Pujol-Vila, Daniel Vera, Gemma Gabriel, Xavi Illa, Aleix Elizalde-Torrent, Mar Alvarez, and Rosa Villa. Gut-on-a-chip: Mimicking and monitoring the human intestine. *Biosensors and Bioelectronics*, 181:113156, 2021.

[59] Onur Kilic, David Pamies, Emily Lavell, Paula Schiapparelli, Yun Feng, Thomas Hartung, Anna Bal-Price, Helena T. Hogberg, Alfredo Quinones-Hinojosa, Hugo Guerrero-Cazares, and Andre Levchenko. Brain-on-a-chip model enables analysis of human neuronal differentiation and chemotaxis. *Lab Chip*, 16:4152–4162, 2016.

[60] Jose A. del Rio and Isidre Ferrer. Potential of Microfluidics and Lab-on-Chip Platforms to Improve Understanding of "prion-like" Protein Assembly and Behavior. *Frontiers in Bioengineering and Biotechnology*, 8, 2020.

[61] Wei Wei, Fernando Cardes, Andreas Hierlemann, and Mario M. Modena. 3D In Vitro Blood-Brain-Barrier Model for Investigating Barrier Insults. *Advanced Science*, 10(11):2205752, 2023.

[62] Shabir Hassan, Shikha Sebastian, Sushila Maharjan, Ami Lesha, Anne-Marie Carpenter, Xiuli Liu, Xin Xie, Carol Livermore, Yu Shrike Zhang, and Ali Zarrinpar. Liver-on-a-Chip Models of Fatty Liver Disease. *Hepatology*, 71(2):733–740, 2020.

[63] Kyung-Jin Jang, Monicah A. Otieno, Janey Ronxhi, Heng-Keang Lim, Lorna Ewart, Konstantia R. Kodella, Debora B. Petropolis, Gauri Kulkarni, Jonathan E. Rubins, David Conegliano, Janna Nawroth, Damir Simic, Wing Lam, Monica Singer, Erio Barale, Bhanu Singh, Manisha Sonee, Anthony J. Streeter, Carl Manthey, Barry Jones, Abhishek Srivastava, Linda C. Andersson, Dominic Williams, Hyoungshin Park, Riccardo Barrile, Josiah Sliz, Anna Herland, Suzzette Haney, Katia Karalis,

Donald E. Ingber, and Geraldine A. Hamilton. Reproducing human and cross-species drug toxicities using a Liver-Chip. *Science Translational Medicine*, 11(517):eaax5516, 2019.

[64] Chak Leung, Pim de Haan, Kacey Ronaldson-Bouchard, Ge-Ah Kim, Jihoon Ko, Hoon Suk Rho, Zhu Chen, Pamela Habibovic, Noo Jeon, Shuichi Takayama, Michael Shuler, Gordana Vunjak-Novakovic, Olivier Frey, Elisabeth Verpoorte, and Yi-Chin Toh. A guide to the organ-on-a-chip. *Nature Reviews Methods Primers*, 2:33, 05 2022.

[65] Samith Hettiarachchi, Haotian Cha, Lingxi Ouyang, Amith Mudugamuwa, Hongjie An, Gregor Kijanka, Navid Kashaninejad, Nam-Trung Nguyen, and Jun Zhang. Recent microfluidic advances in submicron to nanoparticle manipulation and separation. *Lab Chip*, pages –, 2023.

[66] Hyungseok Lee and Dong-Woo Cho. One-step fabrication of an organ-on-a-chip with spatial heterogeneity using a 3D bioprinting technology. *Lab Chip*, 16:2618–2625, 2016.

[67] Jiaming Li, Zhenying Cai, Laura Pontano Vaites, Ning Shen, Dylan C. Mitchell, Edward L. Huttlin, Joao A. Paulo, Brian L. Harry, and Steven P. Gygi. Proteome-wide mapping of short-lived proteins in human cells. *Molecular Cell*, 81(22):4722–4735.e5, 2021.

[68] Liubov Bakhchova and Ulrike Steinmann. In-Situ Measurements of the Physiological Parameters in Lab-on-Chip Systems. *tm - Technisches Messen*, 89(s1):61–65, 2022.

[69] Stefanie Fuchs, Sofia Johansson, Anders Ø. Tjell, Gabriel Werr, Torsten Mayr, and Maria Tenje. In-Line Analysis of Organ-on-Chip Systems with Sensors: Integration, Fabrication, Challenges, and Potential. *ACS Biomaterials Science & Engineering*, 7(7):2926–2948, 2021. PMID: 34133114.

[70] Wesley J. Eaton and Michael G. Roper. A microfluidic system for monitoring glucagon secretion from human pancreatic islets of Langerhans. *Anal. Methods*, 13:3614–3619, 2021.

[71] Mostafa Azimzadeh, Patricia Khashayar, Meitham Amereh, Nishat Tasnim, Mina Hoorfar, and Mohsen Akbari. Microfluidic-Based Oxygen (O2) Sensors for On-Chip Monitoring of Cell, Tissue and Organ Metabolism. *Biosensors*, 12(1):6, December 2021.

[72] Bernhard Müller, Philipp Sulzer, Manuel Walch, Helene Zirath, Tomáš Buryška, Mario Rothbauer, Peter Ertl, and Torsten Mayr. Measurement of respiration and

acidification rates of mammalian cells in thermoplastic microfluidic devices. *Sensors and Actuators B: Chemical*, 334:129664, 2021.

[73] Birgit Ungerböck, Siegfried Fellinger, Philipp Sulzer, Tobias Abel, and Torsten Mayr. Magnetic optical sensor particles: a flexible analytical tool for microfluidic devices. *The Analyst*, 139(10):2551–2559, 2014.

[74] Pei-Hsun Wu, Dikla Raz Ben Aroush, Atef Asnacios, Wei-Chiang Chen, Maxim Dokukin, Bryant Doss, Pauline Durand-Smet, Andrew Ekpenyong, Jochen Guck, Natali Guz, Paul Janmey, Jerry Lee, Nicole Moore, Albrecht Ott, Yeh-Chuin Poh, Robert Ros, Mathias Sander, Igor Sokolov, Jack Staunton, and Denis Wirtz. A comparison of methods to assess cell mechanical properties. *Nature Methods*, 15, 07 2018.

[75] Marta Urbanska, Hector Munoz, Josephine Bagnall, Oliver Otto, Scott Manalis, Dino Di Carlo, and Jochen Guck. A comparison of microfluidic methods for high-throughput cell deformability measurements. *Nature Methods*, 17:1–7, 06 2020.

[76] Ana Moya, Enrico Sowade, Francisco J. del Campo, Kalyan Y. Mitra, Eloi Ramon, Rosa Villa, Reinhard R. Baumann, and Gemma Gabriel. All-inkjet-printed dissolved oxygen sensors on flexible plastic substrates. *Organic Electronics*, 39:168–176, 2016.

[77] Johannes Dornhof, Jochen Kieninger, Harshini Muralidharan, Jochen Maurer, Gerald A. Urban, and Andreas Weltin. Microfluidic organ-on-chip system for multi-analyte monitoring of metabolites in 3D cell cultures. *Lab Chip*, 22:225–239, 2022.

[78] Stefanie Fuchs, Ruben W.J. van Helden, Maury Wiendels, Mees N.S. de Graaf, Valeria V. Orlova, Christine L. Mummery, Berend J. van Meer, and Torsten Mayr. On-chip analysis of glycolysis and mitochondrial respiration in human induced pluripotent stem cells. *Materials Today Bio*, 17:100475, 2022.

[79] Olivier Y. F. Henry, Remi Villenave, Michael J. Cronce, William D. Leineweber, Maximilian A. Benz, and Donald E. Ingber. Organs-on-chips with integrated electrodes for trans-epithelial electrical resistance (TEER) measurements of human epithelial barrier function. *Lab Chip*, 17:2264–2271, 2017.

[80] Noa Renous, Mark D. Kiri, Ronny A. Barnea, Rossana Rauti, Yael Leichtmann-Bardoogo, and Ben M. Maoz. Spatial trans-epithelial electrical resistance (S-TEER) integrated in organs-on-chips. *Lab Chip*, 22:71–79, 2022.

[81] Bo Tang, Mengxi Liu, and Andreas Dietzel. Low-Cost Impedance Camera for Cell Distribution Monitoring. *Biosensors*, 13(2), 2023.

[82] Tiffany Baëtens, Emiliano Pallecchi, Vincent Thomy, and Steve Arscott. Cracking effects in squashable and stretchable thin metal films on PDMS for flexible microsystems and electronics. *Scientific Reports*, 8, 06 2018.

[83] Yu Wang, Zhengwei Li, and Jianliang Xiao. Stretchable Thin Film Materials: Fabrication, Application, and Mechanics. *Journal of Electronic Packaging*, 138(2):020801, 04 2016.

[84] Jinting Song, Hanqing Jiang, W. Choi, D. Khang, Y. Huang, and J. Rogers. An analytical study of two-dimensional buckling of thin films on compliant substrates. *Journal of Applied Physics*, 103:014303 – 014303, 02 2008.

[85] Senjiang Yu, Yong Ni, Linghui He, and Quan-Lin Ye. Tunable formation of ordered wrinkles in metal films with controlled thickness gradients deposited on soft elastic substrates. *ACS applied materials & interfaces*, 7(9):5160–5167, 2015.

[86] Chenxi Lu, Huihua Li, Sen-Jiang Yu, Zhiwei Jiao, and Lingwei Li. Ridged Zn/PDMS smart surface with wide-range reversible wettability and high sensitivity responsive to mechanical strain. *Materials & Design*, 193:108857, 06 2020.

[87] Sen-Jiang Yu, Yao-Peng Du, Sun Ya-Dong, Quan-Lin Ye, and Hong Zhou. Wrinkling patterns in metal films sputter deposited on viscoelastic substrates. *Thin Solid Films*, 638, 07 2017.

[88] M. Berber, V. Bulto, R. Kliß, and H. Hahn. Transparent nanocrystalline ZnO films prepared by spin coating. *Scripta Materialia*, 53(5):547–551, 2005.

[89] Aleksandr Ovsianikov, Jacques Viertl, Boris Chichkov, Mohamed Oubaha, Brian MacCraith, Ioanna Sakellari, Anastasia Giakoumaki, David Gray, Maria Vamvakaki, Maria Farsari, and Costas Fotakis. Ultra-Low Shrinkage Hybrid Photosensitive Material for Two-Photon Polymerization Microfabrication. *ACS Nano*, 2(11):2257–2262, 2008.

[90] Linas Jonušauskas, Tomas Baravykas, Dovilė Andrijec, Tomas Gadisauskas, and Vytautas Purlys. Stitchless support-free 3D printing of free-form micromechanical structures with feature size on-demand. *Scientific Reports*, 9, 11 2019.

[91] Alexandra Borók, Kristóf Laboda, and Attila Bonyár. PDMS Bonding Technologies for Microfluidic Applications: A Review. *Biosensors*, 11(8), 2021.

[92] Bor-han Chueh, Dongeun Huh, Christina R. Kyrtsos, Timothée Houssin, Nobuyuki Futai, and Shuichi Takayama. Leakage-Free Bonding of Porous Membranes into Layered Microfluidic Array Systems. *Analytical Chemistry*, 79(9):3504–3508, 2007. PMID: 17388566.

[93] Pouya Rezai, P Ravi Selvaganapathy, and Gregory R Wohl. Plasma enhanced bonding of polydimethylsiloxane with parylene and its optimization. *Journal of Micromechanics and Microengineering*, 21(6):065024, 2011.

[94] Dongeun Huh, Hyun Jung Kim, Jacob P Fraser, Daniel E Shea, Mohammed Khan, Anthony Bahinski, Geraldine A Hamilton, and Donald E Ingber. Microfabrication of human organs-on-chips. *Nature protocols*, 8(11):2135–2157, 2013.

[95] Linas Jonušauskas, Tomas Baravykas, Dovilė Andrijec, Tomas Gadišauskas, and Vytautas Purlys. Stitchless support-free 3D printing of free-form micromechanical structures with feature size on-demand. *Scientific Reports*, 9:17533, 2019.

[96] Liubov Bakhchova, Phatcharida Jantaree, Anubhuti Gupta, Berend Isermann, Ulrike Steinmann, and Michael Naumann. On-a-Chip-Based Sensitive Detection of Drug-Induced Apoptosis in Polarized Gastric Epithelial Cells. *ACS Biomaterials Science & Engineering*, 7(12):5474–5483, 2021. PMID: 34704732.

[97] Florian von Rüling, Liubov Bakhchova, Ulrike Steinmann, and Alexey Eremin. Permeation dynamics of active swimmers through anisotropic porous walls. *arXiv preprint arXiv:2306.12866*, 2023.

[98] PreSense oxygen sensor spot. Accessed on August 20, 2023.

[99] Balaji Srinivasan, Aditya Reddy Kolli, Mandy Brigitte Esch, Hasan Erbil Abaci, Michael L. Shuler, and James J. Hickman. TEER Measurement Techniques for In Vitro Barrier Model Systems. *SLAS Technology*, 20(2):107–126, April 2015.

[100] Liubov Bakhchova, Liudmila Deckert, and Ulrike Steinmann. Wrinkled Thermo-Electric Meander-Shaped Element on a Thin Freestanding PDMS Membrane. *Membranes*, 13(5), 2023.

[101] Phatcharida Jantaree, Liubov Bakhchova, Ulrike Steinmann, and Michael Naumann. From 3D Back to 2D Monolayer Stomach Organoids-on-a-Chip. *Trends in Biotechnology*, 39(8):745–748, 2021. Special Issue: Microphysiological Systems.

[102] Francesco Boccellato, Sarah Woelffling, Aki Imai-Matsushima, Gabriela Sanchez, Christian Goosmann, Monika Schmid, Hilmar Berger, Pau Morey, Christian Denecke, Juergen Ordemann, and Thomas F Meyer. Polarised epithelial monolayers of the gastric mucosa reveal insights into mucosal homeostasis and defence against infection. *Gut*, 68(3):400–413, 2019.

[103] Kang Kug Lee, Heather A. McCauley, Taylor R. Broda, Matthew J. Kofron, James M. Wells, and Christian I. Hong. Human stomach-on-a-chip with luminal flow and peristaltic-like motility. *Lab Chip*, 18:3079–3085, 2018.

[104] Michael Naumann, Olga Sokolova, Nicole Tegtmeyer, and Steffen Backert. Helicobacter pylori: A Paradigm Pathogen for Subverting Host Cell Signal Transmission. *Trends in Microbiology*, 25(4):316–328, 2017.

[105] Constanze Nossol, A-K Diesing, N Walk, H Faber-Zuschratter, Roland Hartig, A Post, Jeannette Kluess, H-J Rothkötter, and Stefan Kahlert. Air–liquid interface cultures enhance the oxygen supply and trigger the structural and functional differentiation of intestinal porcine epithelial cells (IPEC). *Histochemistry and cell biology*, 136:103–15, 06 2011.

[106] Kousei Ito, Hiroshi Suzuki, Toshiharu Horie, and Yuichi Sugiyama. Apical/Basolateral Surface Expression of Drug Transporters and its Role in Vectorial Drug Transport. *Pharmaceutical research*, 22:1559–77, 11 2005.

[107] B.J. van Meer, H. de Vries, K.S.A. Firth, J. van Weerd, L.G.J. Tertoolen, H.B.J. Karperien, P. Jonkheijm, C. Denning, A.P. IJzerman, and C.L. Mummery. Small molecule absorption by PDMS in the context of drug response bioassays. *Biochemical and Biophysical Research Communications*, 482(2):323–328, 2017.

[108] Michael W. Toepke and David J. Beebe. PDMS absorption of small molecules and consequences in microfluidic applications. 6(12):1484, 2006.

[109] Pavel Sengupta, Kalap Khanra, Amit Roy Chowdhury, and Pallab Datta. 4 - Lab-on-a-chip sensing devices for biomedical applications. In Kunal Pal, Heinz-Bernhard Kraatz, Anwesha Khasnobish, Sandip Bag, Indranil Banerjee, and Usha Kuruganti, editors, *Bioelectronics and Medical Devices*, Woodhead Publishing Series in Electronic and Optical Materials, pages 47–95. Woodhead Publishing, 2019.

[110] N Jusoh, J Ko, and NL Jeon. Microfluidics-based skin irritation test using in vitro 3D angiogenesis platform. APL Bioeng. 2019; 3 (3): 036101.

[111] Dongeun Huh, Yu-suke Torisawa, Geraldine A Hamilton, Hyun Jung Kim, and Donald E Ingber. Microengineered physiological biomimicry: organs-on-chips. *Lab on a Chip*, 12(12):2156–2164, 2012.

[112] Hiroshi Kimura, Yasuyuki Sakai, and Teruo Fujii. Organ/body-on-a-chip based on microfluidic technology for drug discovery. *Drug metabolism and pharmacokinetics*, 33(1):43–48, 2018.

[113] Hongyu Guo, Shengyi Liu, Bingyan Jiang, and Mingyong Zhou. Irreversible bonding of PDMS-LiNbO3 heterostructure for microfluidic application by stepwise plasma modification. *Surface and Coatings Technology*, 445:128718, 2022.

[114] G. Agrawal, Y.S. Negi, S. Pradhan, M. Dash, and S.K. Samal. 3 - Wettability and contact angle of polymeric biomaterials. In Maria Cristina Tanzi and Silvia Farè, editors, *Characterization of Polymeric Biomaterials*, pages 57–81. Woodhead Publishing, 2017.

[115] Girish Kumar and K. Narayan Prabhu. Review of non-reactive and reactive wetting of liquids on surfaces. *Advances in Colloid and Interface Science*, 133(2):61–89, 2007.

[116] Aleksandr Ovsianikov, Jacques Viertl, Boris Chichkov, Mohamed Oubaha, Brian MacCraith, Ioanna Sakellari, Anastasia Giakoumaki, David Gray, Maria Vamvakaki, Maria Farsari, and Costas Fotakis. Ultra-Low Shrinkage Hybrid Photosensitive Material for Two-Photon Polymerization Microfabrication. *ACS Nano*, 2(11):2257–2262, November 2008.

[117] Jennifer L. Guerriero. Chapter Three - Macrophages: Their Untold Story in T Cell Activation and Function. In Lorenzo Galluzzi and Nils-Petter Rudqvist, editors, *Biology of T Cells - Part B*, volume 342 of *International Review of Cell and Molecular Biology*, pages 73–93. Academic Press, 2019.

[118] Ismail Emre Araci and Philip Brisk. Recent developments in microfluidic large scale integration. *Current Opinion in Biotechnology*, 25:60–68, 2014. Analytical biotechnology.

[119] Dhananjay Singh, D. Pandey, R. Yadav, and Devraj Singh. A study of nanosized zinc oxide and its nanofluid. *Pramana*, 78:759–766, 05 2012.

[120] Linas Jonušauskas, Saulius Juodkazis, and Mangirdas Malinauskas. Optical 3D printing: bridging the gaps in the mesoscale. *Journal of Optics*, 20(5):053001, apr 2018.

[121] Julian Hering, Erik H. Waller, and Georg Von Freymann. Automated aberration correction of arbitrary laser modes in high numerical aperture systems. *Opt. Express*, 24(25):28500–28508, Dec 2016.

[122] Gabrielius Kontenis, Darius Gailevičius, Linas Jonušauskas, and Vytautas Purlys. Dynamic aberration correction via spatial light modulator (SLM) for femtosecond direct laser writing: towards spherical voxels. *Opt. Express*, 28(19):27850–27864, Sep 2020.

[123] Linas Jonušauskas and Sima Rekštyte. Augmentation of direct laser writing fabrication throughput for three-dimensional structures by varying focusing conditions. *Optical Engineering*, 53:125102, 12 2014.

[124] Yoshifumi Ueno, Shimpei Aikawa, Akihiko Kondo, and Seiji Akimoto. Adaptation of light-harvesting functions of unicellular green algae to different light qualities. *Photosynthesis Research*, 139(1-3):145–154, May 2018.

[125] Stephen Williams, Raphael Jeanneret, Idan Tuval, and Marco Polin. Confinement-induced accumulation and de-mixing of microscopic active-passive mixtures. *Nature Communications*, 13, 08 2022.

[126] Matteo Contino, Enkeleida Lushi, Idan Tuval, Vasily Kantsler, and Marco Polin. Microalgae Scatter off Solid Surfaces by Hydrodynamic and Contact Forces. *Phys. Rev. Lett.*, 115:258102, Dec 2015.

[127] Lisa M. Coussens and Zena Werb. Inflammation and cancer. *Nature*, 420(6917):860–867, December 2002.

[128] FireSting oxygen sensor. Accessed on August 20, 2023.

[129] Andreas Schedl, Christian Neuber, Andreas Fery, and Hans-Werner Schmidt. Controlled Wrinkling of Gradient Metal Films. *Langmuir*, 34(47):14249–14253, 2018.

[130] Senjiang Yu, Yongjie Guo, Huihua Li, Chenxi Lu, Hong Zhou, and Lingwei Li. Tailoring Ordered Wrinkle Arrays for Tunable Surface Performances by Template-Modulated Gradient Films. *ACS Applied Materials & Interfaces*, 14(9):11989–11998, 2022.

[131] Joel YY Loh, Ali Zeineddine, Moein Shayegannia, Robyn McNeil, Liam McRae, and Nazir P Kherani. A one-step, tunable method of selective reactive sputter deposition as a wrinkling approach for silver/polydimethylsiloxane for electrically conductive pliable surfaces. *Microsystems & Nanoengineering*, 8(1):89, 2022.

[132] Ting Zhu, Kai Wu, Yun Xia, Chao Yang, Jiaorui Chen, Yaqiang Wang, Jinyu Zhang, Xiong Pu, Gang Liu, and Jun Sun. Topological Gradients for Metal Film-Based Strain Sensors. *Nano Letters*, 22(16):6637–6646, 2022.

[133] Yutaka Yamada, Kazuma Isobe, and Akihiko Horibe. Droplet motion on a wrinkled PDMS surface with a gradient structural length scale shorter than the droplet diameter. *RSC advances*, 12(22):13917–13923, 2022.

[134] Long Ma, Linghui He, and Yong Ni. Tunable hierarchical wrinkling: From models to applications. *Journal of Applied Physics*, 127(11):111101, 2020.

[135] Hugues Vandeparre, Sylvain Gabriele, Fabian Brau, Cyprien Gay, Kevin Kit Parker, and Pascal Damman. Hierarchical wrinkling patterns. *Soft Matter*, 6(22):5751–5756, 2010.

[136] Sen-Jiang Yu, Yao-Peng Du, Ya-Dong Sun, Quan-Lin Ye, and Hong Zhou. Wrinkling patterns in metal films sputter deposited on viscoelastic substrates. *Thin Solid Films*, 638:230–235, 2017.

[137] Senjiang Yu, Yadong Sun, Yong Ni, Xiaofei Zhang, and Hong Zhou. Controlled formation of surface patterns in metal films deposited on elasticity-gradient PDMS substrates. *ACS applied materials & interfaces*, 8(8):5706–5714, 2016.